Advanced Gas Turbine

AGT

Technology Project

DOE/NASA 0168-11
NASA CR-182127
EDR 13295

Final Report

Allison
GAS TURBINE DIVISION
General Motors Corporation
P.O. Box 420
Indianapolis, Indiana 46206-0420

AUGUST 1988

Prepared for
National Aeronautics
and Space Administration
Lewis Research Center
Cleveland, Ohio 44135
Contract DEN 3-168

For U.S. Department of Energy
Conservation and Renewable Energy
Office of Transportation Systems

DOE/NASA 0168-11
NASA CR-182127
EDR 13295

Advanced Gas Turbine AGT Technology Project

Final Report

Allison Gas Turbine Division
General Motors Corporation
Indianapolis, Indiana 46206-0420

AUGUST 1988

Prepared for
NATIONAL AERONAUTICS AND SPACE ADMINISTRATION
Lewis Research Center
Under Contract DEN 3-168

for
U.S. Department of Energy
Conservation and Renewable Energy
Office of Transportation Systems

FOREWORD AND ACKNOWLEDGMENTS

This final report provides overall summary documentation of the Advanced Gas Turbine Technology Project conducted by the Allison Gas Turbine Division of General Motors Corporation under contract to the NASA-Lewis Research Center (contract DEN3-168). Funding and sponsorship of this project came from the Heat Engine Propulsion Division, Office of Transportation Systems, in the Office of Conservation and Renewable Energy of the Department of Energy (DOE). This program's period of performance (technical) spanned October 1979 through June 1987. This document especially emphasizes program activities during 1986 and 1987; earlier semiannual and annual reports, listed as references, present further details of earlier years.

Several General Motors divisions and other companies were major contributors to this effort. They are: Allison Gas Turbine Division—prime contractor and team leader, with overall powertrain, ceramic components, and controls responsibilities; Pontiac Motor Division—vehicle and cost studies; Delco Remy Division—starter/boost motor development; Standard Oil Engineered Materials Company (formerly Carborundum)—ceramic components; Corning Glass Works—ceramic components; GTE Laboratories—ceramic components; and The Norton company—ceramic components.

Allison wishes to recognize the invaluable contributions made to the success of this program by key personnel at the DOE and NASA. Specific acknowledgments are to:

- Mr. Saunders B. Kramer, DOE, program manager, for overall program guidance
- Messrs. Richard Alpaugh and Albert Chesnes, DOE, for management support, guidance, and strategic project direction
- Mr. Paul T. Kerwin, NASA-Lewis, project manager, for professional, consistent, thorough, and understanding technical and programmatic guidance
- Mr. Robert Evans, NASA-Lewis, for management support, counsel, and encouragement
- Mr. William Sanders, NASA-Lewis, for ceramic materials assessment and coordination

The Allison program manager for this project was H. E. (Gene) Helms. Project efforts were directed by R. A. Johnson and P. J. Haley. Materials efforts were directed by Dr. P. W. Heitman. Design effort was directed by L. C. Lindgren, D. L. Vaccari, and R. L. Holtman.

TABLE OF CONTENTS

LIST OF ILLUSTRATIONS

LIST OF ILLUSTRATIONS (CONT.)

LIST OF ILLUSTRATIONS (CONT.)

LIST OF ILLUSTRATIONS (CONT.)

LIST OF ILLUSTRATIONS (CONT.)

LIST OF ILLUSTRATIONS (CONT.)

LIST OF ILLUSTRATIONS (CONT.)

LIST OF TABLES

LIST OF TABLES (CONT.)

ABBREVIATIONS

AGT	advanced gas turbine; automotive gas turbine
AFBMA	Anti-Friction Bearings Manufacturer's Association
AS	aluminum silicate
ATTAP	Advanced Turbine Technology Applications Project
BALCO	Balancing Company, Inc.
BMAS	barium magnesium aluminosilicate
BOT	burner outlet temperature
BU	build
BVG	burner variable geometry
CAS	calcium aluminosilicate
CATE	Ceramic Applications in Turbine Engines
CBO	Carborundum (Sohio)
CO	carbon monoxide
COSMIC	computation of swirl/mixing in combustors
CrVTi	chrome vanadium titanium
CT	computed tomography
CTE	cyclic thermal exposure
CVI	chemical vapor infiltration
CVT	continuously variable transmission
DOE	Department of Energy
ECU	electronic control unit
EPS	equivalent penetrameter sensitivity
FEM	finite element model
FOD	foreign object damage
FPI	fluorescent penetrant inspection
GMC	General Motors Corporation
GMCM	General Motors Custom Microprocessor
GT	gas turbine; gasifier turbine
HIP	hot isostatic press
IGT	industrial gas turbine
IGV	inlet guide vane
IQI	image quality indicator
IR&D	independent research and development
KS	key slots
LAS	lithium aluminum silicate
LeRC	Lewis Research Center
MAS	magnesium aluminosilicate
MOR	modulus of rupture
$MoSi_2$	molybdenum disilicide
NASA	National Aeronautics and Space Administration
NDE	nondestructive evaluation
NGK	Spark Plug Co., Ltd.
NO_x	oxides of nitrogen
o.d.	outer diameter
ORNL	Oak Ridge National Laboratory
PMD	Pontiac Motor Division
POS	probability of survival
PSZ	partially stabilized zirconia
PT	power turbine
RB SiC	reaction-bonded silicon carbide
r.f.	radio frequency
RIT	rotor inlet temperature
RP	Rochester Products
RPD	reference powertrain design
SASC	sintered alpha-silicon carbide
SCG	slow crack growth
SEM	scanning electron microscope
SENB	single-edged notch beam
SEP	Societe Europeene de Propulsion
SFD	squeeze film damper
SI	spark-ignition
Si_3N_4	silicon nitride
SiSiC	siliconized silicon carbide
SiC	silicon carbide
SLS	sea level static
S/N	serial number
Sohio	Standard Oil (Carborundum)
SSN	sintered silicon nitride
TEM	transmission electron microscopy
TIT	turbine inlet temperature
TS	thickness sensitivity
VP	vane pockets
WC	tungsten carbide

I. INTRODUCTION AND SUMMARY

1.1 PROGRAM BACKGROUND, SCOPE, AND SCHEDULE

The Allison Gas Turbine Division of General Motors Corporation (GMC) completed the Advanced Gas Turbine Technology Project in the summer of 1987 under contract to the National Aeronautics and Space Administration (NASA) Lewis Research Center (LeRC) using funding received from the Heat Engine Propulsion Division, Office of Transportation Systems in the Office of Conservation and Renewable Energy of the Department of Energy (DOE). This advanced, high risk work was initiated in the fall of 1979 under charter from the U. S. Congress to promote an engine for transportation that would provide an alternative to reciprocating spark-ignition (SI) engines for the U. S. automotive industry and simultaneously establish the feasibility of advanced ceramic materials for hot section components to be used in an automotive gas turbine (AGT).

The AGT selected by Allison for development was designated the AGT 100 to be compatible with other vehicular gas turbines developed by GMC. This 100 hp, two-shaft engine was chosen for development because of its potential to meet government designated performance goals, including: higher miles per gallon (30% improvement) than projected 1985 SI engines; multifuel capability (demonstrate four fuels); and 1985 Federal Emission Standards for automobiles. In addition, it was desirable that the engine be competitive in initial and life cycle costs and meet safety and noise standards and acceleration requirements. The vehicle selected in 1979 to meet the performance goals was the projected 3000 lb 1985 Pontiac Phoenix automobile equipped with a six-cylinder advanced SI engine that would achieve 28 mpg using gasoline.

Changes were made in contract emphasis after contract initiation due to evolving budget and technology considerations. The largest consideration was the rate of progress in developing ceramic components to satisfy the 3500 hr design life requirement for an AGT. This ceramic component requirement was estimated to be achievable in the planned 66-month activity. However, because this scheduled development has proven to be more difficult, expensive, and rigorous than anticipated, emphasis in the program was changed to recognize the magnitude of these technological challenges. Subsequently, the vehicle development was eliminated, the performance objectives were changed to goals, and the project objective became a proof-of-concept demonstration for ceramic hot section components of an AGT.

The resulting AGT 100 engine is shown in Figure 1. Figure 2 shows the final objective and goals for the program. The full ceramic hot section flow path includes the combustor, gasifier turbine scroll and vanes, gasifier turbine rotor, power turbine scroll and vanes, power turbine rotor, regenerator bulkhead, regenerator, and miscellaneous supporting and connecting pieces. The insulation in the hot section is also ceramic fiber. The only metal in the hot portion of the engine is the external pressure vessel and metal parts for the combustor variable geometry mechanism. The engine weight of 300 lb and the engine dimensions enable a direct replacement in the Pontiac Phoenix engine compartment using a standard automatic or manual transmission.

Figure 3 shows the final schedule for the AGT 100 program that evolved by successive interaction and integrated planning with NASA/DOE. This 84-month schedule identifies dates for ceramic component processing and engine testing, development of aerodynamic and mechanical components for the engine, and key build and test dates for the AGT 100 engine. Approximately sixty percent (60%) of funds expended in the program were devoted to ceramic component development, either with ceramic suppliers or to in-house evaluation of ceramics in rigs and engines. The remaining 40% of the funds were devoted to aerodynamic and mechanical design, fabrication of rig and engine parts, and reporting and dissemination of data generated in the program.

The feasibility of using ceramic components in AGTs is considered to have been shown by rig and engine data generated in the program.

1.2 AGT 100 PROGRAM ACHIEVEMENTS

The AGT 100 program successfully achieved project objectives with significant technology advances. The initial data base for design, material characterization, problem identification, and approach to problem solving is already being applied in the technical community.

Specific AGT 100 program achievements are considered to be as follows:

- Ceramic component feasibility for use in gas

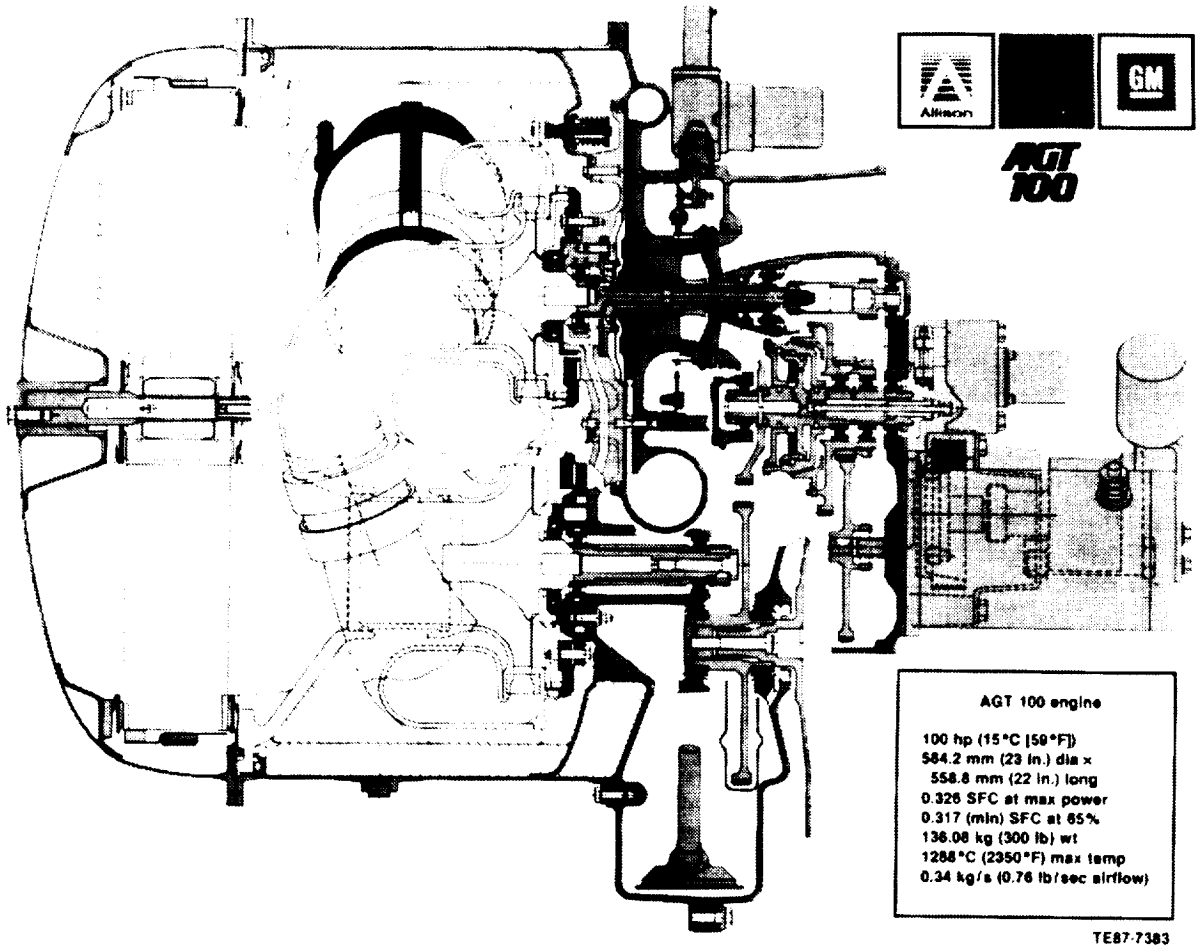

Figure 1. *AGT 100 engine cross section.*

turbine engines has been demonstrated.

- A new engine was designed, fabricated, and tested for 572 hr at operating temperatures to 2200°F.
- Statistical design methodology has been applied and correlated to experimental data acquired from over 5500 hr of rig and engine testing.
- Ceramic component processing capability has progressed from a rudimentary level able to fabricate simple parts to a sophisticated level able to provide complex geometries such as rotors and scrolls.
- Required improvements for monolithic and composite ceramic gas turbine components to meet automotive reliability, performance, and cost goals have been identified.
- The combustor design demonstrated lower emissions than 1986 federal standards on methanol, JP-5, and diesel fuel. Thus, the potential for meeting emission standards and multifuel capability has been demonstrated.
- Small turbine engine aerodynamic and mechanical design capability has been initiated.
- An infrastructure of manpower, facilities, materials, and fabrication capabilities has been established which is available for continued development of ceramic component technology in gas turbine and other heat engines.

1.3 AGT 100 ENGINE SELECTION AND PROGRAM DEVELOPMENT ACTIVITIES

The AGT is very different from aircraft and industrial turbines in design and usage. The driving cycle of an automobile requires only a small fraction of operating time (less than 0.1%) at full power. Over 95% of the driving cycle is achieved at less than 35% of the rated engine horsepower, and 99%

OBJECTIVE:
DEMONSTRATE PROOF-OF-CONCEPT WITH ALL CERAMIC HOT SECTION COMPONENTS

POTENTIAL FOR:
- **42.5 MPG — 3000 LB CAR**
- **EMISSIONS — 1985 STDS**
- **ALTERNATE FUELS**
- **2350°F (UNCOOLED) OPERATING TEMPERATURE**

TE87-7483

Figure 2. *AGT 100 program objective and goals.*

of the driving cycle is accomplished at less than 50% of the rated engine horsepower. Thus, the AGT is truly a "part power" engine. For the combined automotive driving cycle (55% city miles, 45% highway miles), the average horsepower used is 14 when the engine is rated at 100 hp, which includes 3 hp to drive engine accessories such as power steering and air conditioning. This part power usage of the AGT makes it necessary to recover exhaust heat to achieve desired fuel economy. A regenerator (rotary heat exchanger) was used in the AGT 100 engine to achieve a design thermal efficiency of 42% (as compared to less than 25% thermal efficiency in SI engines). The ceramic regenerator components are shown in Figure 4.

The merits of single shaft, two-shaft, and three-shaft engines were carefully weighed in selecting the AGT 100 engine. A two-shaft or three-shaft engine can be combined easily with either an automatic or manual transmission to achieve a powertrain. A single shaft engine is a higher risk because a continuously variable transmission (CVT) or equivalent is required to make a powertrain. Since no CVT transmissions are in common automotive production (either in 1979 or 1987), the single shaft AGT requires invention for practical application in the future. The three-shaft engine requires more bearings and turbomachinery aerodynamic matching to achieve a wide range efficiency. Thus, the two-shaft

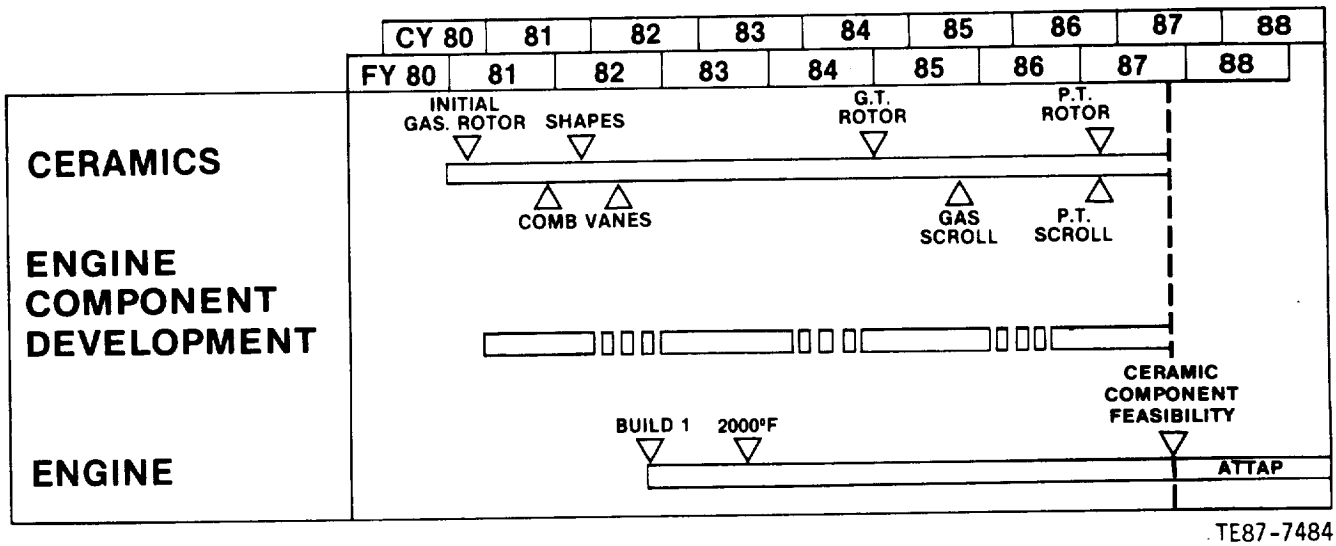

Figure 3. *AGT 100 development schedule.*

engine was selected because of transmission compatibility, reasonable turbomachinery matching, high part power efficiency, and reasonable stress levels in the ceramic turbine rotors.

The AGT 100 compressor pressure ratio was selected by performance analysis and optimized at 4.5. The engine airflow was set at 0.76 lb/sec to achieve the desired 100 hp at 100% design. Other parameters such as efficiencies, leakages, pressure losses, and mechanical losses are shown in the reference powertrain design (RPD) column in Table I. The operating turbine inlet temperature (TIT) design condition was set at 2350°F for the RPD. This was the lowest TIT to meet an optimum performance engine goal while maintaining the lowest possible temperature target for ceramic components and simultaneously minimizing the formation of oxides of nitrogen (NO_x) to meet emission standards. In Table I, current engine performance using the best component performances demonstrated in the program is shown compared to the RPD. This comparison reflects the need for additional development to meet RPD engine design values. RPD overall performance goals are considered achievable in the same time frame as structurally satisfactory ceramic components.

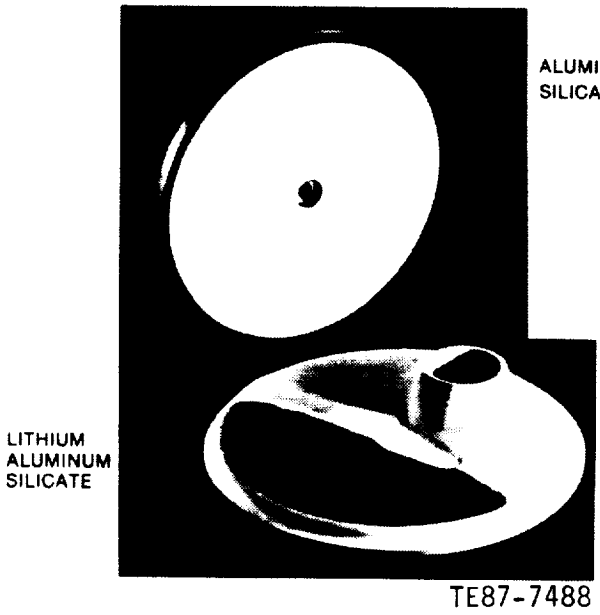

Figure 4. *Regenerator ceramic components.*

Two AGT 100 engines (plus spare parts) were built and tested in the AGT 100 program. Forty-five separate engine builds and 572 engine test hours were accomplished to demonstrate engine feasibility and verify ceramic components. Figure 5 shows an initial AGT 100 engine on a dynamometer test stand.

Key problems identified with ceramic components relate to early failure identification, compliant materials at interfaces between parts, tolerance control between hot and cold running conditions, and foreign object damage (FOD). The FOD problem has highlighted the need for combustion in transient engine operation free of carbon formation. Of sev-

Table I.
AGT 100 engine reference powertrain design potential and current achieved component performances.

Engine		Current	Reference powertrain design
Rotor inlet temperature	°F	2200	2350
Maximum power	hp	66.5	100
Specified fuel consumption	lb/hp/hr	0.457	0.325
Components			
Compressor:	Airflow rate—lb/sec	0.726	0.760
	compression ratio	4.34	4.50
	η (%)	77.1	82.8
Gasifier turbine:	η (%)	80.2	84.6
Power turbine:	η (%)	86.1	86.7
Regenerator:	η (%)	91.2	94.7
	Leakage (%)	5.3	5.2
Parasitic losses			
Engine leakage	%	4.1	2.5
Cycle total pressure loss	%	14.6	14.1
Mechanical loss	hp	10.5	7.8

eral rotor blade failures experienced, at least two failures were traced to carbon deposits forming on the ceramic combustor wall, "flaking" off, and being ingested into the turbine.

The major structural problem identified in engine running with ceramic components is FOD to rotors and vanes. Other ceramic components have either been successful or have problems that are correctable with improved design, processing, or control of environment in the engine. Monolithic ceramic rotors with fewer flaws and/or tougher ceramic rotors (possibly composite materials) combined with improved combustion and more rugged hot flow-path airfoil geometries offer potential solutions to the FOD problem.

Table II identifies rigs and engines designed, built, and used to conduct the AGT 100 program. As indicated in Table II, rigs and engines were devoted largely to the ceramics technology development, the exception being the aerodynamic development of the compressor, combustor, turbine, and the regenerator. A mechanical development rig was used to study rotor dynamics, and a regenerator seal rig was employed to achieve geometry that met leakage criteria. The combustor and regenerator rigs were used for both performance and proof testing of ceramic components.

Table II.
Program rigs and engines.

	Used for ceramic testing
Compressor rig	No
Combustor rig	Yes
Turbine rig	No
Regenerator disk/seal hot-flow rig	Yes
Static components hot proof rig	Yes
Turbine rotor foreign object damage rig	Yes
Engines	Yes
Regenerator cyclic thermal exposure rig	Yes
Rotordynamics rig	No
Rotor cold spin rigs	Yes
Vane thermal shock rig	Yes
Bulkhead pressure test rig	Yes
Regenerator seal leaf rig	No
Regenerator flow distribution rig	Yes
Total test hr: 5540	

An overview of the testing evaluation conducted in the AGT 100 program shows rig and engine qualification activity relative to introducing ceramic materials into gas turbine engines.

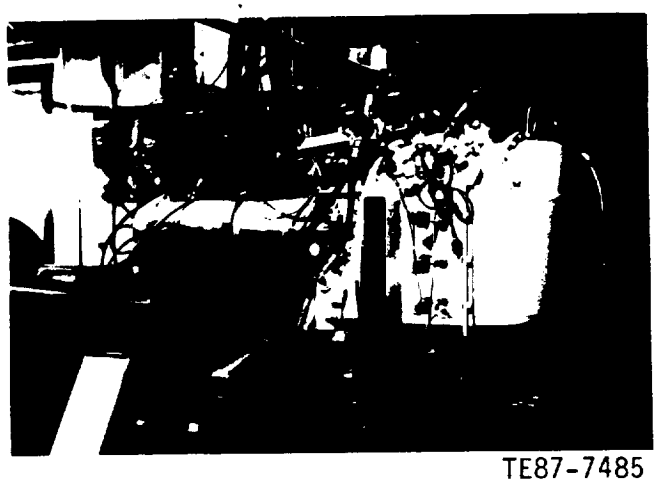

TE87-7485

Figure 5. *AGT 100 engine on a dynamometer test stand.*

The unique rigs used to proof test ceramic components for engine testing and their uses are as follows:

- Regenerator disk/seal hot-flow rig (792 test hours)
  - Qualification of regenerator disk for heat transfer effectiveness, pressure drop, and carry-over leakage
  - Qualification of hot and cold side seals for bypass leakage under face and leaf seal surfaces
  - Qualification of disk and seals for temperature capability
- Combustor rig (150 test hours)
  - Qualification of combustor parts relative to both transient and steady-state temperature capability and for variable geometry function
  - Combustor performance and emissions measurements
- Static component hot proof rig (25 test hours)
  - Qualification of scrolls, vanes, and inner and outer backplates relative to steady-state pressure and temperature capability
- Turbine rotor spin rigs (69 test hours)
  - Qualification of turbine rotors for centrifugal stress capability at engine operating speeds (86,500 rpm-gasifier and 68,500 rpm-power turbine)
- Vane thermal shock rig (150 test hours)
  - Qualification of vanes for transient and steady-state temperature capability

Table III.
AGT 100 engine test hours on ceramic components.

	Ceramic component	Engine test time (hr) High-time part	Total time
Combustor:	Dome	135	401
	Body	214	572
	Pilot tube	119	572
	Dilution band	247	572
Turbine:	Vane	71	192
	Rotor	100	142
	Scroll	30	77
	Inner backplate	53	152
	Outer backplate	22	77
Regenerator:	Disk	267	572
	Bulkhead	161	572
Miscellaneous:	Shim, gasifier turbine	126	572
	Shim, power turbine	126	572
	Coupling, interior turbine	37	69
	Coupling, power turbine exhaust	18	23

- Regenerator cyclic thermal exposure rig (2100 test hours)
- Qualification of regenerator matrix material relative to chemical stability at engine operating conditions

In total, 5540 test hours were accumulated on AGT 100 rigs and engines. The balance of this time (subtracting above rigs' times) accrued in engine testing, other ceramic component testing, and mechanical and aerodynamic evaluations. Several thousand hours of material and ceramic component characterization tests (oxidation, modulus of rupture, heat treatments, etc) are not included in the 5540 hr total.

Table III shows the engine test hours for the ceramic development components. Ceramic components used in all of the AGT 100 test builds (572 hr) were the combustor body, pilot tube, and dilution band rings, the regenerator disk and bulkhead, and the gasifier and power turbine shims. Other ceramic components received less engine test time depending on the development required to qualify the parts for engine testing.

1.4 AGT 100 COMBUSTOR EMISSION AND MULTIFUEL CAPABILITY RESULTS

The challenge of meeting emission standards was addressed early in the AGT 100 program. A representative band of CO and NO_x emissions for diffusion-flame type combustion systems typical of aircraft and industrial engines, as applied to an AGT engine, is shown in Figure 6. The temperature of regenerated air entering the combustor in the AGT is far higher than typically found in simple cycle aircraft and industrial engines. This high CO and NO_x condition eliminated the diffusion flame combustor as a candidate for AGT 100. Many other fuel injection methods were considered, and the premixed (fuel + air) and prevaporized (gaseous fuel into the combustion chamber) combustor was selected as the most desirable configuration for the AGT. Prior combustor studies at Allison provided the data base for this selection.

In Figure 6, the legislated limits for CO and NO_x emissions are presented, and the unburned hydrocarbons are shown at a level of 0.41 g/mi. Testing of diesel fuel No. 2, JP-5 fuel, and methanol fuel was conducted in the combustor rig on the selected premixed-prevaporized combustor and results are shown in Figure 6. Steady-state NO_x values achieved are one order of magnitude less than Federal Emission Standards and two orders of magnitude less than diffusion flame combustors would produce. The CO production for methanol fuel is at least one order of magnitude less than the Federal Emission Standard, and the JP/diesel fuels fall within the operational envelope for CO. The unburned hydrocarbons are one-twentieth (JP/diesel) and one-

fiftieth (methanol) of the Federal Emission Standard. These data verify the premix-prevaporization combustor approach as a logical candidate for future AGT applications.

1.5 AGT 100 CERAMIC COMPONENT DEVELOPMENT

Ceramic components in AGTs offer the following substantial benefits:

- improved specific fuel consumption from higher TIT
- smaller engines and higher specific power from higher TIT
- lower weight
- lower inertia
- lower friction
- potentially lower cost in mature components
- no strategic elements

The major thrust in the ceramics development activity for AGT 100 has been to make ceramic components that have the required statistical strength using improved analysis/design tools, improved nondestructive evaluation (NDE) techniques, improved processing methods, and necessary component evaluation equipment (rigs, engines, materials characterization, etc). This has involved iteration with ceramic suppliers on real and perceived problems, assimilation of data from other programs, cooperation with technical and advisory groups, and continual project planning to incorporate ceramic state-of-the-art advances into the AGT 100 engine ceramic components.

Figure 7 shows some of the actual ceramic components fabricated in this program. These comprise 23 different parts with a total count of 60 pieces in each all-ceramic turbine engine build. Special recognition is deserved by the major suppliers of ceramic parts. The Standard Oil Engineered Materials Company was the largest single supplier of AGT 100 ceramic parts including rotors, scrolls, combustors, vanes, and backplates. The Corning Glass Company supplied the regenerators, ceramic bulkhead, and inner backplates, while the GTE Laboratories supplied vanes, turbine rotors, and backplates, and the Norton Company supplied gasifier scrolls. These four companies received development and parts buy funds from the project. All other suppliers sold parts to the AGT 100 project, including the Kyocera Company, which made scrolls and rotors. Table IV presents ceramic components which were successfully tested in engines and/or hot rigs, along with their suppliers and material systems. The

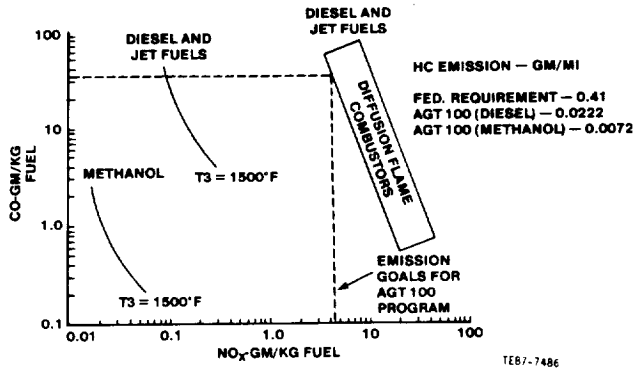

Figure 6. *AGT 100 combustor emissions.*

Societe Europeane de Propulsion (SEP) combustor body parts were successfully hot rig tested. Parts such as these successful components may well be currently suitable for gas turbine engines where design criteria include short life demands and temperatures to 2300°F. Such components may also be suitable for longer-life/higher temperature applications. The limits of such technologies are currently unknown.

1.6 CERAMIC COMPONENTS REQUIRING FURTHER STRUCTURAL DEVELOPMENT

Ceramic components identified in the AGT 100 program as requiring further development are as follows:

- SiC and Si_3N_4 turbine rotors, which failed in engine testing at times from 30 min to 100 hr.
- Scrolls made of alpha SiC and Si_3N_4, which failed at times from 3-60 hr of engine testing.
- Vanes, which failed when ceramic rotors failed in engine testing or before.
- Regenerator disks and seals, which require improved uniformity.

Problems identified with each component in this list were as follows:

- Rotors
  Apparent FOD damage to the inducer portion of the evaluated rotors suggests that improved material properties, including toughness, are desirable. Further, iteration between designs showing better blade stiffness from increased thickness and improved component processing requires immediate development (Figure 8).

Table IV.
AGT 100 components successfully tested in engines/hot rigs.

Supplier	Component	Material system	Trade name
Corning	Regenerator disk	Aluminum silicate (AS)	
Corning	Regenerator bulkhead	Lithium aluminum silicate (LAS)	
Standard Oil	Combustor assembly	Sintered alpha silicon carbide (SASC)	Hexoloy SA
GTE	Vane	Sintered silicon nitride (SSN)	AY6, PY6
Norton	Scroll	Siliconized silicon carbide (SiSiC)	NC-430
Kyocera	Rotor	SSN	SN220M, SN250
Standard Oil	Outer backplate	SASC	Hexoloy SA
Corning	Inner backplate	Glass ceramic matrix/SiC fiber	BMAS-III
Standard Oil	Rotor	SASC	Hexoloy SA
Societe Europeane de Propulsion	Combustor	SiC/SiC	Cerasep
Feldmuhle	Thermal barrier/shim	Partially stabilized zirconia (PSZ)	ZN-40
GTE	Inner backplate	SSN	SNW-1000, AY6
Standard Oil	Vane	SASC	Hexoloy SA
Pure Carbon	Coupling and piston rings	Reaction-bond silicon carbide (RB SiC)	Refel, PS-9242
Asahi Glass	Combustor body	SiC	C600
Coors Porcelain	Coupling	RB SiC	SC2
Kyocera	Backplates	SSN	SN250

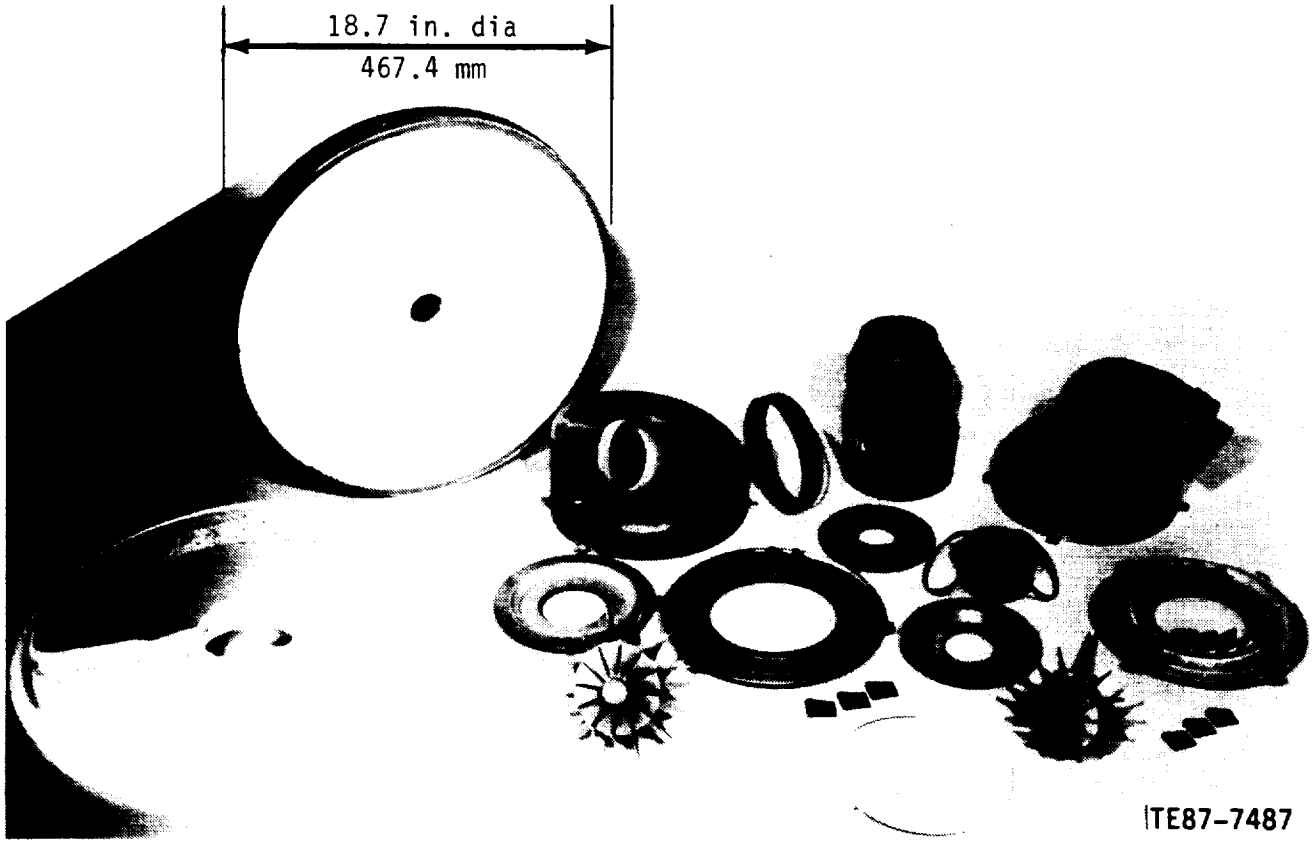

Figure 7. *AGT 100 engine ceramic components.*

Additional joining development between the ceramic rotor and metal shafts should explore both new designs and improved joining methods such as shrink fits, brazing, and mechanical joints. Also, improved combustor transient operating characteristics to minimize carbon agglomerate formation should be developed.

- Scrolls
  Failures with both alpha-SiC and Si_3N_4 scrolls occurred at joints in the scroll assembly. Improved design and joining (brazing and sintering) are areas requiring development.
- Vanes
  Failures in vanes were always secondary to primary rotor failures. However, sensitivity to FOD suggests improved impact capability as desirable in vanes. Therefore, improved design and tougher vane materials may be required.
- Regenerators
  Uniformity of the heat transfer matrix in disks and uniformity of seal surfaces on the disk and leaf sides of hot and cold seals require improvement to meet performance goals of the AGT. Extruded disks and new seal designs may be required to meet design criteria.

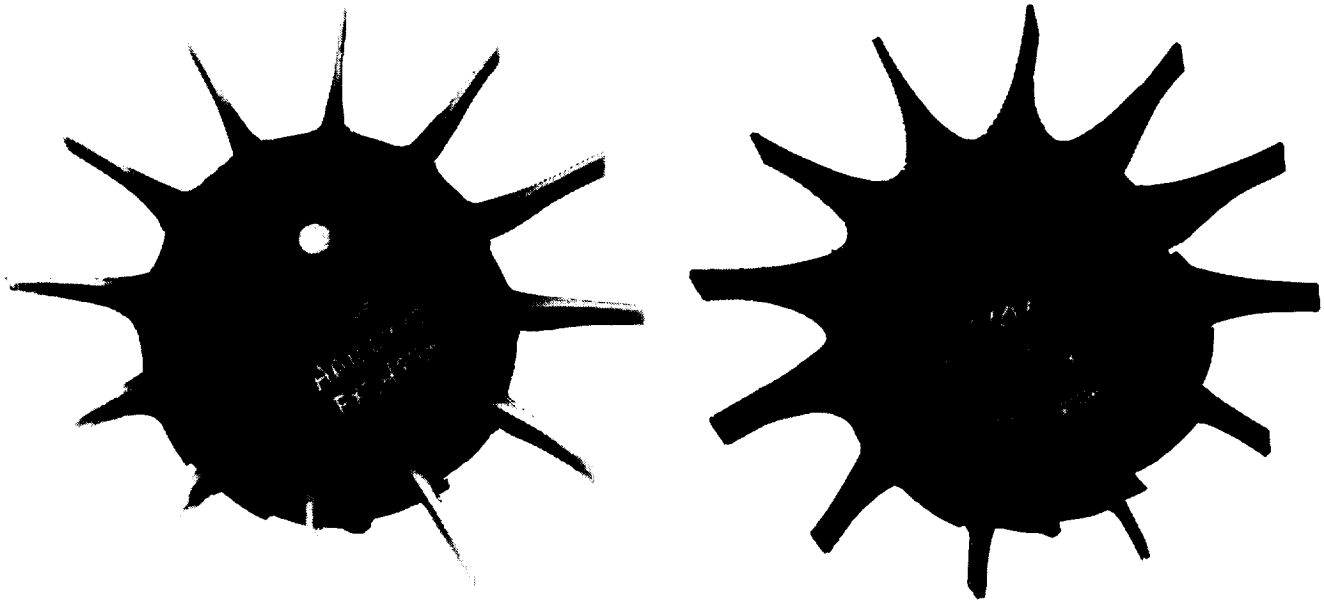

Figure 8. *Rotor change to address FOD problem.*

II. AGT 100 CERAMIC COMPONENTS— PROCESSING, MATERIALS, AND ANALYSIS METHODS

The ceramic development activity in the AGT 100 program consisted of three major tasks: ceramic component fabrication technology, the development of NDE techniques, and the failure analysis activities. The ceramic component fabrication technology subtask consisted of four major areas of material and processing development: monolithic ceramic rotor development, ceramic turbine scroll development, ceramic composite development, and thermal barrier development. The NDE development subtask covered the development and application of NDE methods for flaw detection and component inspection. These techniques included projection microfocus radiography, ultrasonic imaging, and X-ray computed tomography (CT). Finally, the failure analysis subtask detailed the results of fractographic analysis of both ceramic test specimens and engine-tested ceramic components. Each of these activities is summarized in following subsections.

2.1 SUMMARY

The ceramic component fabrication technology subsection summarizes the activities conducted on ceramic components for which either improved material characteristics and/or further development of fabrication methodology were required. The ceramic rotor development discussion covers the material and processing activities conducted at (1) Sohio on injection-molded SASC, (2) GTE Laboratories on injection-molded Si_3N_4, and (3) Kyocera for slip cast Si_3N_4. The development of ceramic turbine scroll assemblies includes activities with Sohio (SASC), Norton (SiSiC), and Kyocera (SSN). The ceramic composite development section reviews the efforts to develop toughened composite materials and components. Components were received and evaluated in this task from Corning (glass-ceramic composite inner backplates) and SEP (SiC/SiC combustor bodies). In addition, test bars from Sohio (SiC/TiB_2 particles) and Boride Products/Dow Chemical (Si_3N_4 with SiC whisker reinforcement) were characterized. The thermal barrier development section details the development of a zircon-based thermal insulator material at Allison used for the shaft attachment of SiC turbine rotors.

A two-path approach was used to develop near net-shape ceramic components that would meet both structural and reliability requirements. The first involved a series of iterative studies to translate state-of-the-art material properties into full-scale hardware. The second approach incorporated studies of material and processing variations to increase strength characteristics and processing yields. Component evaluations were conducted using both standard nondestructive inspection techniques (visual, fluorescent penetrant inspection [FPI], and radiography) and advanced NDE methods (microfocus X-ray, high frequency ultrasonics, and CT). In addition, the microstructural features of the components were characterized.

Qualification test bars processed with the components and material sectioned directly from the components were evaluated to determine the material strength characteristics and to determine the nature of the strength-controlling defects. These characteristics were used to generate appropriate material properties to support design and reliability assessments and subsequent rig and engine testing. Finally, this information was furnished to the ceramic suppliers for iterative component improvements.

2.2 MONOLITHIC CERAMIC TURBINE ROTOR DEVELOPMENT

Both the gasifier and power turbine stages of the AGT 100 engine are of a radial inflow design. This rotor configuration, which embodies a radical variation in section thickness, represents a difficult challenge from a ceramic manufacturing standpoint. In addition, stringent structural and geometric characteristics are required to meet the design reliability goals. The rotor development activities have focused on near net-shape processing, using both injection molding and slip casting of both SiC and Si_3N_4 material systems. Injection molding of SASC has been pursued with Sohio, while rotor fabrication efforts at GTE Laboratories have concentrated on injection-molded Si_3N_4 materials. Kyocera used a slip casting approach to fabricate Si_3N_4 turbine rotors. These efforts are summarized in the following subsections.

Sohio Sintered Alpha-Silicon Carbide Gasifier Turbine Rotor Development

Introduction

At Sohio, injection molding parameters were developed for fabrication of SASC gasifier turbine rotors. Molding and tool modifications, sintering optimization, and hot isostatic pressing (HIP) have been used to realize substantial improvements in process yield, microstructural homogeneity, strength, and spin speed. A successful design iteration, involving thickening the inducer blade tips to improve the impact resistance, was implemented. Spin tests of HIP-processed thick bladed rotors demonstrated an average burst speed of 98,200 rpm with a Weibull modulus of 19.

Discussion

Efforts at Sohio on the development of gasifier turbine rotors concentrated on the establishment of injection molding parameters for producing rotors with minimal defects using SASC material. Injection molding was selected as the procedure for forming the gasifier rotor because this process is capable of economically forming complex shapes having wide variations in cross sections. Initially, a prototype rotor configuration was selected for development. This configuration differed from the RPD rotor design in that the exducer blades were shortened to facilitate blade insert pulling in the injection molding tool.

The initial injection molding of prototype rotors used a polystyrene base binder system developed at Sohio for blade fabrication in the Ceramic Applications in Turbine Engines (CATE) program. This compound was relatively brittle and surface cracking and chipping of the blade tips were frequently encountered during demolding. In addition, further investigations of binder removal procedures with variations in the heat-up rates, temperatures, and atmosphere showed that it was difficult to remove the binder from the thick hub section without causing permanent damage to the rotor.

A new proprietary binder system was developed in late 1980 under a separate internally funded development program at Sohio. This binder system was significantly tougher and more flexible than the prior binder system. After the key process parameters were established, prototype rotors were molded without demolding problems and were processed through the binder removal stage without cracking.

Following the establishment of a suitable binder system, a limited processing matrix was conducted addressing variables such as binder level, molding conditions, binder removal procedures, presintering treatment, and sintering parameters including atmosphere, temperature, heat-up rates, and hold times. Density determination, visual appearance, microfocus X-ray, and FPI inspections were conducted to assess the rotors.

One hundred prototype rotors were molded by the optimized molding procedures established by the processing matrix, and 33 of these rotors were shipped to Allison. Fifteen of these rotors were of acceptable quality and were characterized by spin burst testing. Of the 15 rotors spin tested, 14 achieved burst speeds in excess of 100% design speed with an average burst speed of 97,100 rpm. The spin results are summarized in Figure 9. The application of Weibull statistics in conjunction with finite element analysis enabled equivalent four-point modulus of rupture (MOR) strengths to be inferred from the spin results. The equivalent MOR and Weibull modulus were calculated to be 339.92 MPa (49.3 ksi) and 7.3, respectively.

To further evaluate component strength characteristics, test bars were sectioned from three of

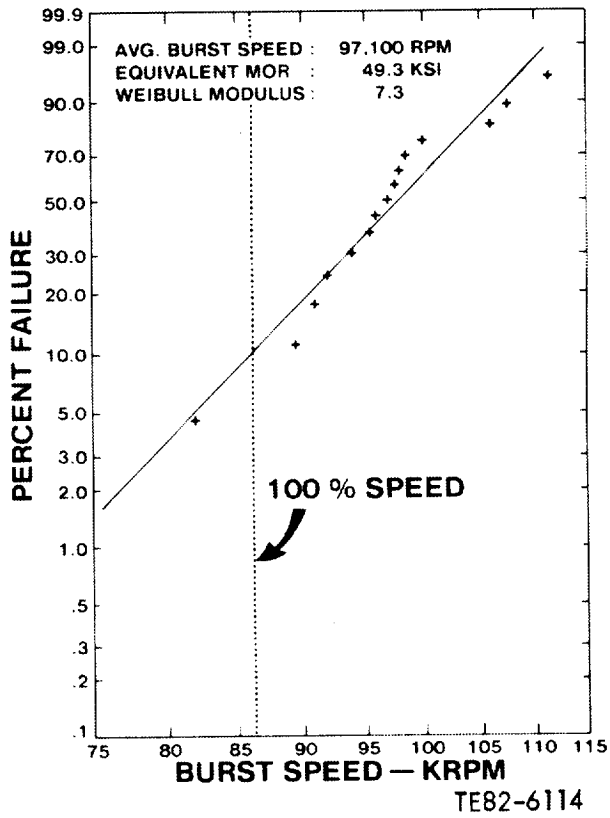

Figure 9. *Spin test results of Sohio injection-molded SASC prototype rotors.*

the rotors. The average MOR of 335.79 MPa (48.7 ksi) measured for bars cut in the radial direction from the highly stressed backface region of the rotors correlated well with the predicted bar strengths calculated from the spin test results. However, material from the central portion of the rotor hub (axial test bars) had an average strength of only 203.40 MPa (29.5 ksi). The defects identified in the axial test bars were typical of the strength-controlling flaws observed in failures of early prototype rotors, i.e. internal pores and agglomerations. The densities of the axial test bars were significantly lower (up to 0.08 g/cm^3) than the density measured for the overall rotor.

As a result of the initial processing study conducted on prototype rotors, a set of processing parameters was established for the fabrication of injection-molded SASC engine configuration rotors. The parameters selected were those that yielded the highest average burst speed in spin testing. The engine configuration rotor differed from the prototype rotor in the direction of rotation (blade camber) and the thickness of the rotor shaft. In addition, the exducer blade tips were lengthened for aerodynamic considerations. A new injection molding tool was designed to accommodate these modifications and was delivered in May 1982. Following preliminary molding activities, an extensive process and tool optimization study was conducted. The first phase of the study focused on the definition of injection molding parameters intended to produce rotors free of surface imperfections, particularly flow and knit lines associated with the injection and compaction of the injection molding strands. The major molding parameters investigated included injection temperature, pressure, rate, and microprocessor control. The second phase addressed modifications of the injection molding tool, including gating, venting, and thermal control.

At the conclusion of these studies, a large run of 242 rotors was fabricated under invariant conditions and evaluated. The total process yield was 11%, including a molding yield of 28% and a sintering yield of 85%. Inspection of the sintered rotors, which included visual, FPI, X-ray, and dimensional examinations, revealed that 45% met quality requirements.

Test bars were sectioned from three rotors to evaluate material strength characteristics. Bars cut from the rotors had an average strength of 406.12 MPa (58.9 ksi) for radial bars from the highly stressed rotor backface region and a strength of 286.83 MPa (41.6 ksi) for axial test bars from the central portion of the hub. The typical strength-controlling flaw observed in both sets of material was porosity, shown in Figure 10, although the pores observed in the axial test bars were typically larger and more numerous in extent.

Further strength characterization of the rotors was conducted by spin testing a sample of 10 rotors to failure. The spin test results are summarized in Figure 11. The average burst speed measured 99,300 rpm (115% design speed) with a Weibull modulus of 6.9. With one exception, all of the rotors failed at speeds between 95,000 and 105,000 rpm. Examination of the rotor fragments after spin testing of the single low-speed failure (82,000 rpm) revealed that the fracture initiated from a large internal pore, as shown in Figure 12. Fractographic analysis indicated a stress at failure of 87.57 MPa (12.7 ksi) (calculated from the radius of the fracture mirror), which was in good agreement with the stress of 81.36 MPa (11.8 ksi) predicted from finite element model (FEM) analysis. The remaining rotors failed from the backface region at or near the surface.

Additional studies were conducted at Sohio to address improvements in process yield and the elimination of the strength-limiting flaws at the backface region of the rotors. The major process modification was the injection of the molding compound into the die cavity through the shaft, as opposed to the pre-

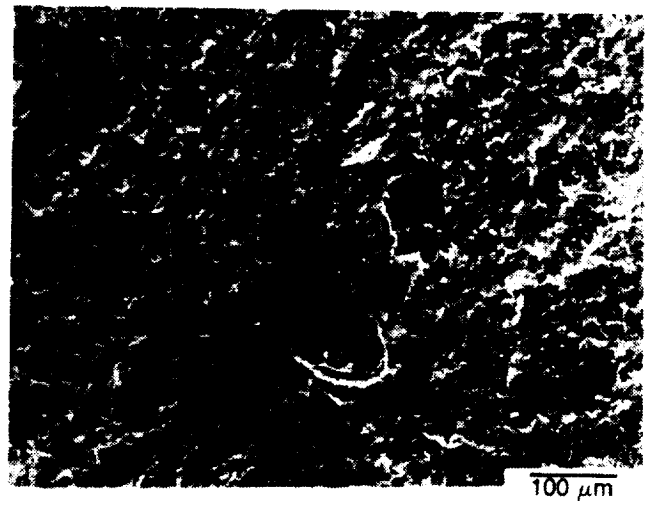

TE87-7430
430494

Figure 10. *Typical fracture origin (internal pore) observed in axial test bars cut from Sohio sintered SiC engine configuration rotor.*

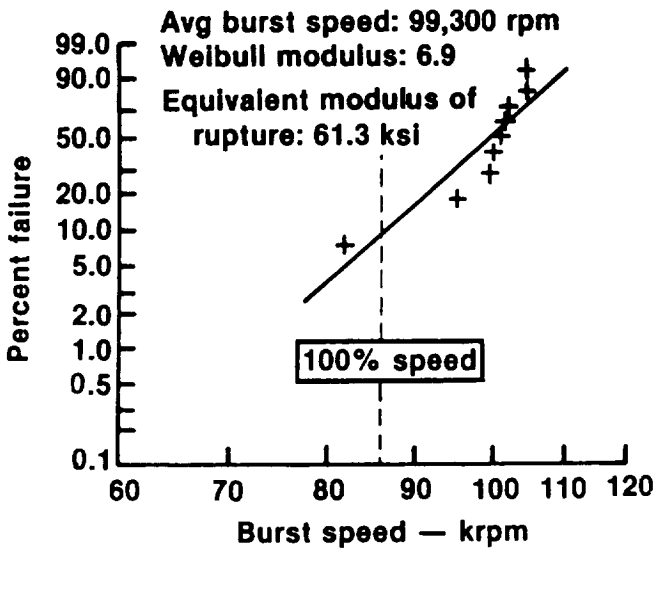

Figure 11. *Spin test results of initial Sohio engine configuration rotors.*

vious nose-end injection. The shaft-end injection allows the initial knitting of the injection strand to occur in the low-stress exducer (nose) region of the rotor. To access the yield and structural capability of the shaft-end injection rotors, a group of 302 rotors was evaluated. The overall process yield of acceptable quality rotors was 45%, a fourfold improvement over the yield of 11% observed in prior rotors. Both the as-molded quality and the dimensional control of sintered rotors increased. Test bars sectioned from the rotors demonstrated improvements in uniformity, with an average strength of 369.57 MPa (53.6 ksi) measured for radial bars (sectioned from near the rotor surface) and 324.75 MPa (47.1 ksi) measured for axial bars from the central portion of the rotor hub. Spin testing of 70 rotors resulted in an average burst speed of 99,800 rpm (116% design speed) with a Weibull modulus of 12.0.

As a result of engine testing of SiC gasifier turbine rotors, in which the inducer blade tips were damaged as a result of FOD, a redesign was initiated in 1985 to thicken the inducer blade tips (from

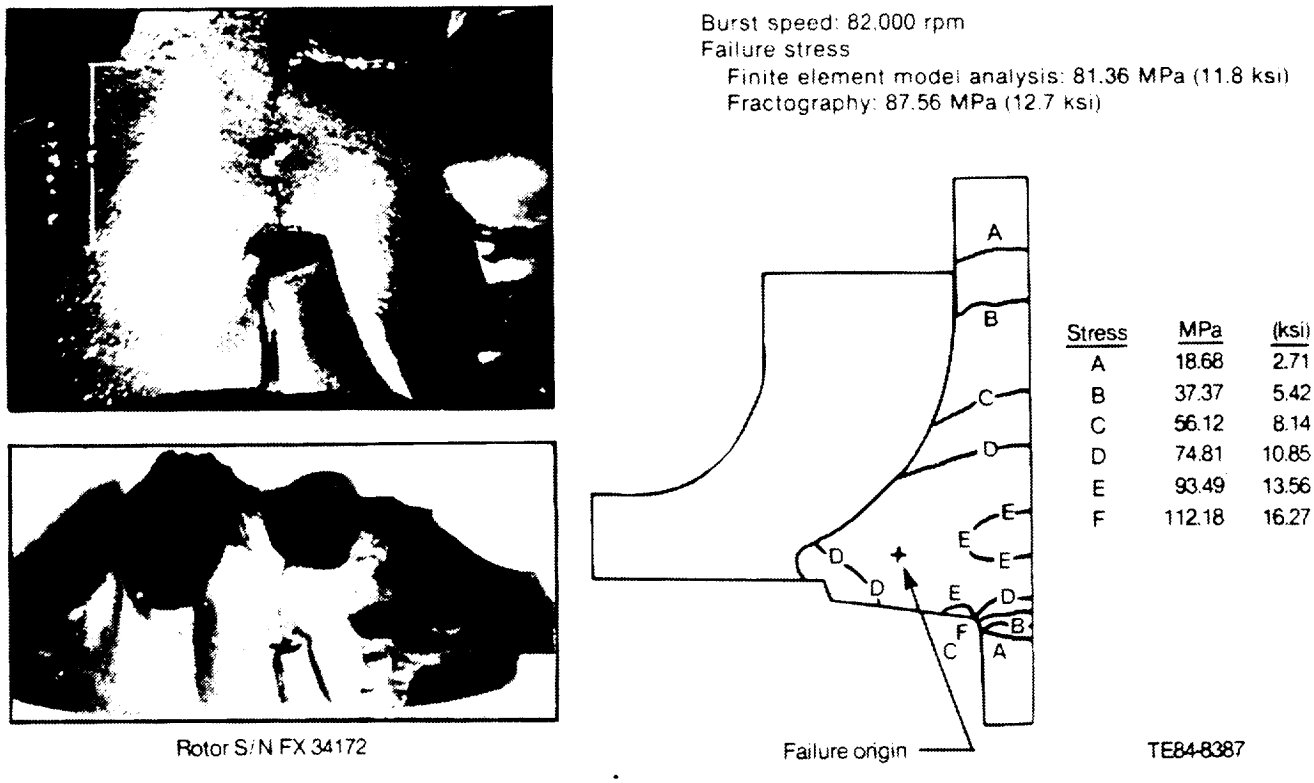

Figure 12. *Fractographic analysis of spin-tested Sohio SiC rotor. Fracture initiated from a large internal pore.*

0.76 mm [0.030 in.] to 1.91 mm [0.075 in.]) to improve the airfoil impact resistance. Both the thin-bladed and thick-bladed rotors are shown in Figure 13. Upon receipt of the modified injection molding tool, efforts focused on optimizing density and microstructure via sintering cycle modifications and compound homogeneity. In addition, the use of HIP processing was investigated as a means of improving microstructure and component strength. The sintering studies focused on reduced impurity levels in the furnace atmosphere and modifications in the sintering cycle. As a result of these efforts, 56 rotors were processed and delivered. The average density of these rotors increased to 3.14 g/cm^3, as compared with the average density of 3.10 g/cm^3 obtained for prior rotors. In addition, the average grain size (12 microns) and maximum grain sizes (18 microns) demonstrated improved uniformity. A total of 23 of the thick-bladed sintered SiC rotors were subjected to spin burst testing. The average burst speed measured 90,700 rpm with a Weibull modulus of 16.0. This observed component/material performance would demonstrate an average burst speed of 98,800 rpm for the reduced mass, thin airfoil rotor.

The use of HIP processing as a means of improving microstructural uniformity and increasing the rotor strength characteristics was also investigated. HIP processing trials were conducted at both the NASA-Lewis Research Center and the ASEA Pressure Systems facility in Ohio. A group of 12 sintered SiC rotors were HIP-processed at NASA at temperatures of 2050°–2150°C (3722°–3902°F) and a pressure of 137.9 MPa (20 ksi) for a period of 3 hr. The average density of the HIP-processed rotors increased from 3.100 g/cm^3 (96.6% theoretical density) to a value of 3.156 g/cm^3 (98.3% theoretical density). The strength of test bars sectioned from the HIP-processed rotors also exhibited a 10%–20% improvement over the strength of bars sectioned from sintered rotors, with a strength of 391.64 MPa (56.8 ksi) obtained for radial test bars (versus 369.57 MPa [53.6 ksi] for the non-HIP-processed rotors) and a strength of 413.01 MPa (59.9 ksi) measured for axial test bars (versus 324.75 MPa [47.1 ksi]). However, the average spin burst speeds of both sets of rotors were not significantly different, with a speed of 97,300 rpm for the HIP-processed rotors and 99,800 rpm for the sintered rotors.

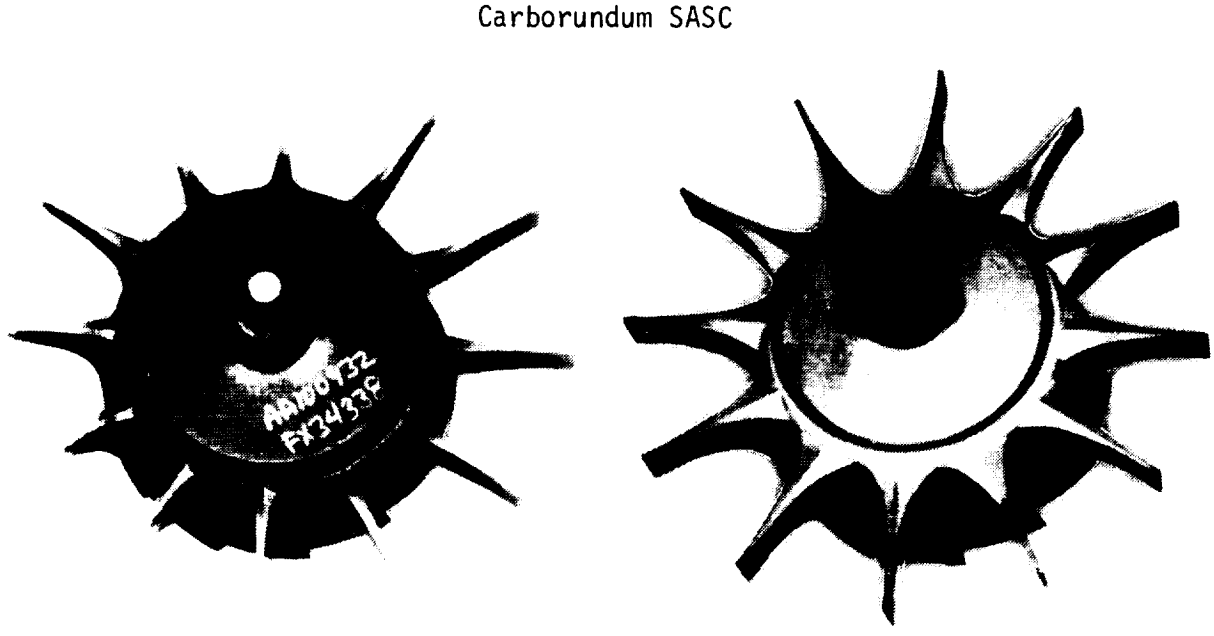

Figure 13. *Sohio injection-molded SiC gasifier turbine rotors.*

An additional sample of 30 thick-bladed SiC rotors were subjected to HIP processing trials using an ASEA HIP unit. These rotors were HIP-processed at a temperature of 2100°C (3812°F) and a pressure of 206.8 MPa (30 ksi) with a hold time of approximately 30 min at maximum temperature. The average density of the rotors measured 3.11 g/cm^3 prior to HIP processing, which increased to an average of 3.16 g/cm^3 after HIP processing.

Computed X-ray tomography at Sohio's Research Laboratory was used to analyze the density gradients present in both the sintered SiC and the HIP-processed SiC turbine rotors. Figure 14 shows the CT results for both a sintered rotor (3.12 g/cm^3 density) and a HIP-processed rotor (3.17 g/cm^3 density). The pressureless sintered rotor had a density gradient of approximately 0.25 g/cm^3, with a significantly reduced density in the rotor hub region, while the HIP-processed rotor exhibited little density variation. Spin test evaluation of the rotors HIP-processed at ASEA demonstrated substantially improved burst speeds, with an average burst speed of 98,200 rpm (equivalent to 107,100 rpm for the thin-bladed rotors) with an associated Weibull modulus of 19.3.

The present process for SiC rotor fabrication based on injection molding and HIP processing has demonstrated the capability for producing rotors that satisfy all dimensional requirements and exhibit significant improvements in microstructural homogeneity, fracture strength of bars sectioned from rotors, and spin test performance. These properties are sufficient to satisfy the design reliability requirements at RPD temperature and speed for steady-state operation. However, further improvements in strength and Weibull modulus are needed to achieve the RPD reliability level for maximum transient operation conditions. In addition, increases in process yield and impact resistance in the rotor airfoils are required.

GTE Laboratories Silicon Nitride Turbine Rotors

Introduction

At GTE Laboratories, a detailed process routing was established for the fabrication of injection-molded Si_3N_4 gasifier turbine rotors of both AY6 and PY6 material compositions. Spin test characterization of these rotors has demonstrated a maximum burst speed of 110,800 rpm for HIP-processed AY6 Si_3N_4 rotors and 120,600 rpm for HIP-processed PY6 Si_3N_4 turbine rotors.

Discussion

Efforts at GTE Laboratories have focused on the development of injection molding technology

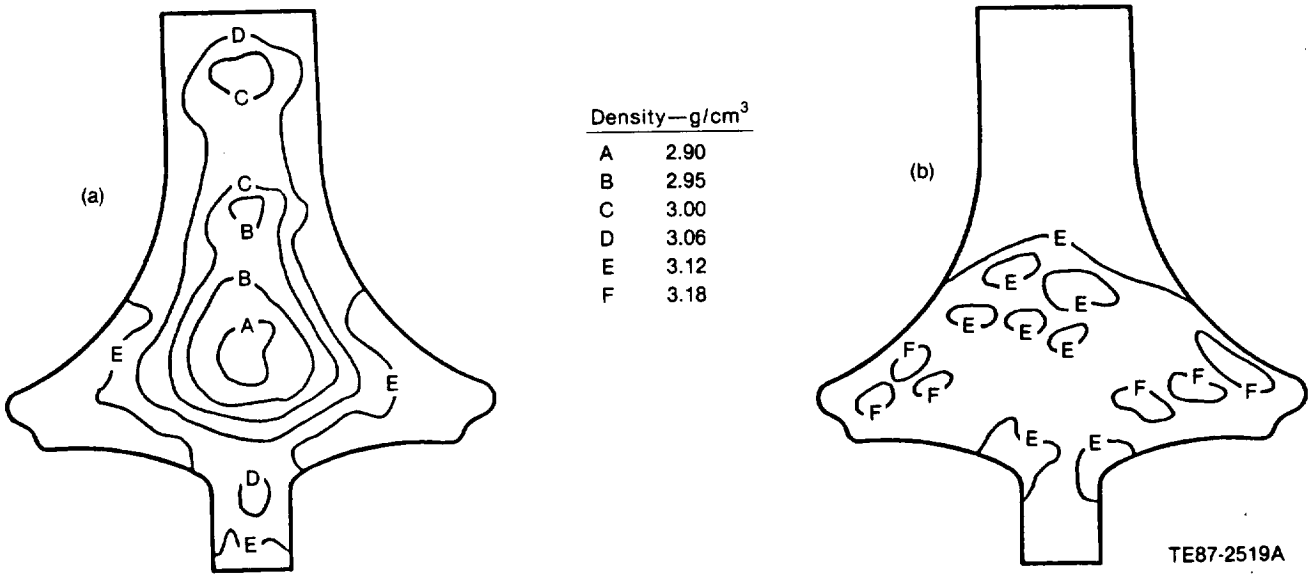

Figure 14. *CT results for SOHIO alpha-SiC rotor (a) sintered and (b) HIP-processed.*

required for fabrication of gasifier turbine rotors. The base material system selected for the initial rotor processing was AY6 Si_3N_4, which contains 6% yttria (Y_2O_3) and 2% alumina (Al_2O_3) as sintering additives. Subsequent rotor processing concentrated on PY6 Si_3N_4, a more refractory composition, which contains only 6% Y_2O_3 as a sintering additive.

The fabrication of Si_3N_4 components by injection molding involves five basic steps. In the first step, the ceramic powders are blended to a uniform composition, then processed to render them highly reactive for sintering and/or HIP processing to a high density. In the next step (compounding), the ceramic is mixed with an organic thermoplastic resin or combination of resins that serve as a binder system. The injection molding step involves heating the mix above its flow point and injecting it into a relatively cold metal die where the mix solidifies. The fourth process step involves thermal removal of the binders, leaving behind a nondisrupted ceramic structure. The final step is consolidation by sintering and/or HIP processing. The total process routing for rotor fabrication (designated AY6-100), along with NDE inspection points, is shown in Figure 15.

SN 502 Si_3N_4 powder, a commercially available Si_3N_4 powder produced by GTE, was used for all injection molding activities. This powder is a fine, highly reactive powder with crystalline and amorphous phases. Densification of Si_3N_4 currently requires the addition of minor phases that combine with the SiO_2 present in Si_3N_4 to form a liquid phase that, in turn, allows sintering to high densities. As mentioned previously, Y_2O_3 and Al_2O_3 were used as sintering additives for initial rotor fabrication.

Prior injection molding studies, which were conducted with internal funding, resulted in the establishment of a powder/binder system with an associated process routing that yielded visually and radiographically flaw-free green (as-molded) rotors. However, subsequent inspection after sintering revealed two distinct but related flaws present in the rotors: surface cracking at the blade/hub intersection and internal laminations, as shown in Figure 16. Both flaw types were found to result from particle rearrangement during the course of the binder removal process. Room temperature spin burst testing confirmed the gross defects present in the rotors, with a sample of seven rotors attaining an average burst speed of only 52,010 rpm (60% design speed). A basic study was then initiated at GTE to understand the cracking mechanisms observed in large cross section parts (12.7 mm [0.5 in.] thick). These investigations included modifications in the injection molding tool, binder development,

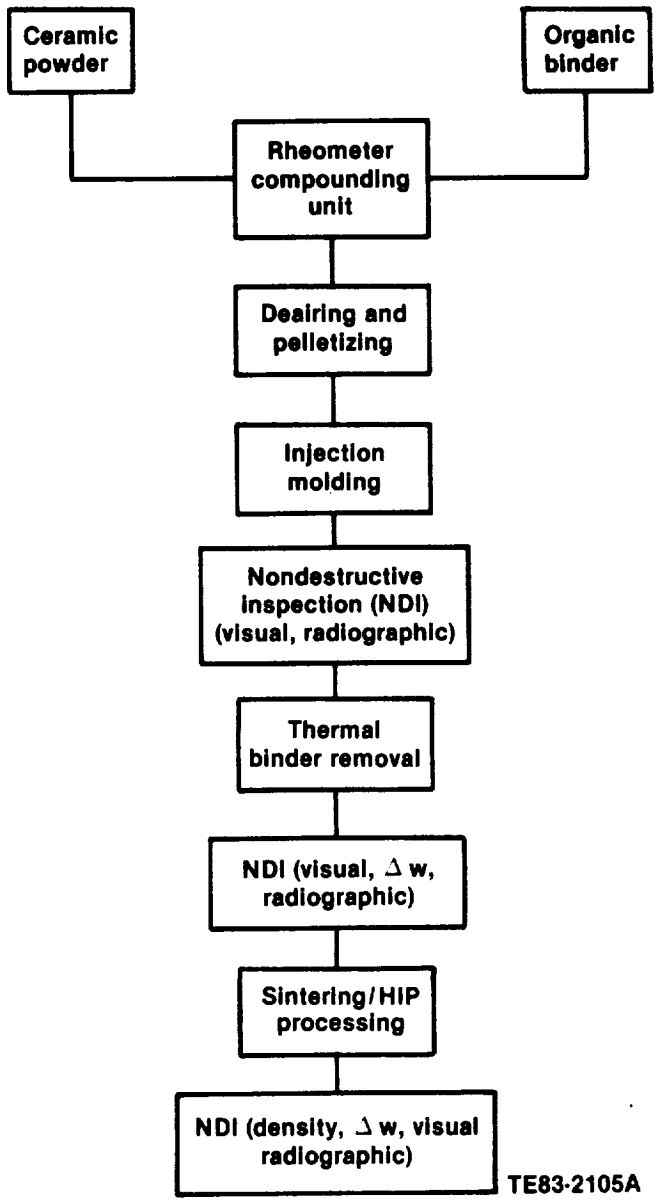

Figure 15. *Process routing for GTE Laboratories injection-molded Si_3N_4 turbine rotors.*

powder/binder system alterations, and improvements in both the binder removal and consolidation processes. As a result of this basic study, the cracking mechanisms were identified, and a new proprietary processing method was developed for fabrication of radial turbine rotors. In particular, the use of HIP processing proved useful as a means of improving the material strength characteristics and eliminating the internal and surface cracking previously observed in pressureless sintered AY6 Si_3N_4 rotors.

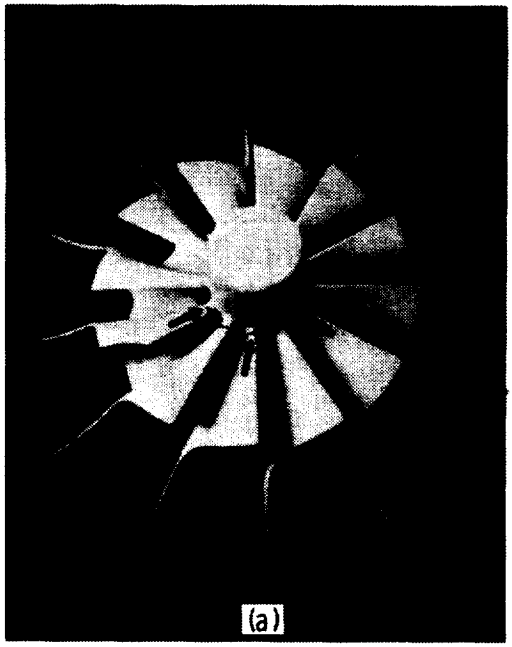

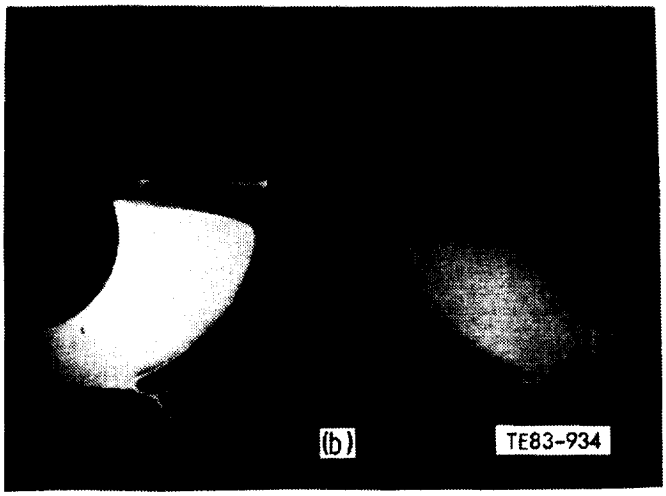

Figure 16. *Typical flaws observed in GTE AY6 SSN rotors (a) surface cracking and (b) internal laminations.*

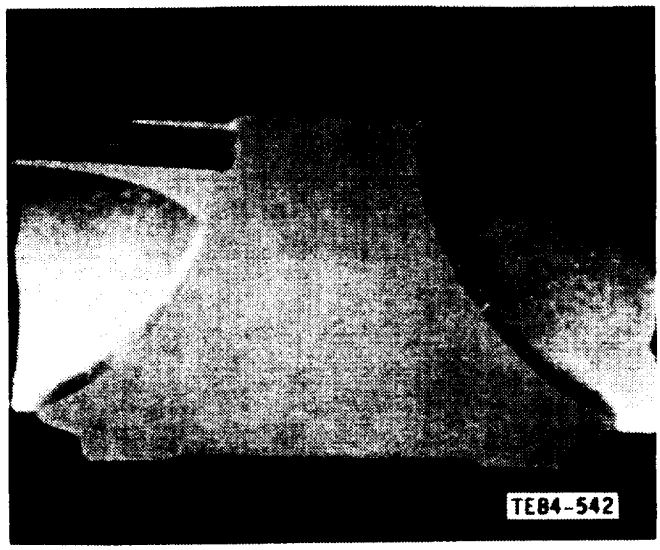

Figure 17. *Internal structure of GTE injection-molded and HIP-processed AY6 Si_3N_4 rotor.*

A quantity of AY6 Si_3N_4 rotors were injection-molded at GTE Laboratories, subjected to binder removal, partially sintered to approximately 75% density to provide structural integrity, and shipped to ASEA, Sweden, for HIP processing using their proprietary glass particle encapsulation process. A total of ten rotors were then received at Allison for evaluation. The average density of the rotors measured 3.21 g/cm^3 (98% theoretical density). The internal structure of sectioned HIP-processed rotors exhibited no evidence of macroscopic laminations or flaws, as shown in Figure 17. Visual and FPI examinations of the rotors revealed numerous shallow surface indications; however, these indications were much less severe than those previously observed in the sintered rotors.

Injection-molded test bars were evaluated to provide an estimate of material strength and to determine the nature of the strength-controlling defects associated with the AY6 Si_3N_4 material. The average density of the test bars measured 3.22 g/cm^3 (98.7% theoretical density). The typical microstructure, shown in Figure 18, was very fine grained, with an average grain size of 0.9 microns.

The results of the strength testing of the AY6 Si_3N_4 material are summarized in Table V. The average room temperature strength of test material with a machined tensile surface condition measured 632.69 MPa (91.76 ksi). The corresponding Weibull modulus was 9.92. Bars with an as-fired surface had an average room temperature strength of 486.24 MPa (70.52 ksi) with a Weibull modulus of 7.19. The primary strength-controlling flaw observed in these specimens was surface and internal porosity, as shown in Figure 19. Bars with a machined tensile surface condition tested at elevated temperature had an average strength of 496.65 MPa (72.03 ksi) at 800°C (1472°F), 517.75 MPa (75.09 ksi) at 1000°C (1832°F), and 388.81 MPa (56.39 ksi) at a temperature of 1200°C (2192°F). The average strength of bars with an as-fired surface tested at 1000°C (1832°F) was 381.29 MPa (55.30 ksi). The

Figure 18. Typical microstructure of GTE AY6 SSN material.

Figure 19. Typical fracture origin (internal pore) observed in GTE AY6 Si_3N_4 bars tested at room temperature.

Table V.
Strength characteristics of GTE AY6 SSN.

Temperature—°C (°F)	Strength—MPa (ksi)	
	Machined	As fired
Room	632.69 (91.76)	486.24 (70.52)
800 (1472)	496.65 (72.03)	—
1000 (1832)	517.75 (75.09)	381.29 (55.30)
1200 (2192)	388.81 (56.39)	

typical fracture origins were observed to be surface and internal pores, as shown in Figure 20. The fracture toughness (K_{IC}) value for the GTE AY6 Si_3N_4 material measured 5.2 MPa$\sqrt{m}$ (4.7 ksi$\sqrt{in.}$) determined using the single-edged notch beam (SENB) test method.

The material strength characteristics of the HIP-processed AY6 Si_3N_4 rotors were determined at GTE by cutting test bars measuring 25.4 mm × 2.54 mm × 1.27 mm (1.0 in. × 0.10 in. × 0.05 in.) from HIP-processed rotors in both radial (near the rotor backface) and axial (near the exducer) directions. The average room temperature four-point bend strength (outer span = 22.86 mm [0.90 in.], inner span = 10.16 mm [0.40 in.]) of the radial test bars was 761.07 MPa (110.38 ksi), with a strength of 687.09 MPa (99.65 ksi) measured for the axial test bars. Five of the HIP-processed AY6 rotors were also

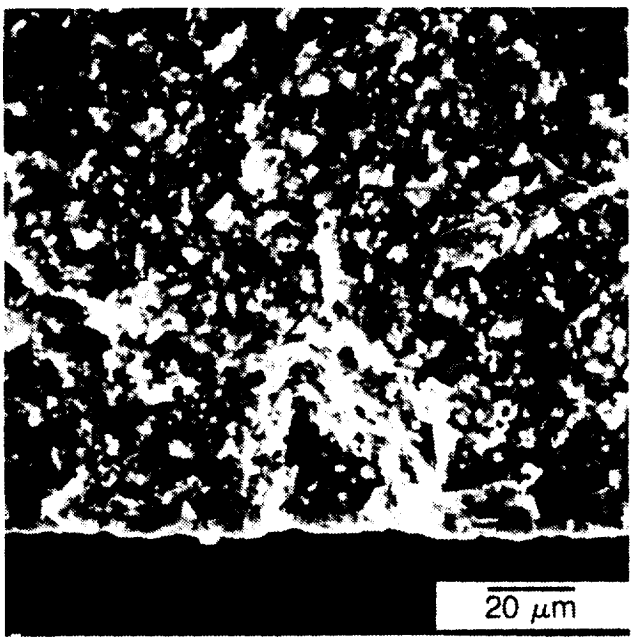

Figure 20. *Typical strength-controlling flaw (surface pore) observed in GTE AY6 Si_3N_4 tested at 1200°C.*

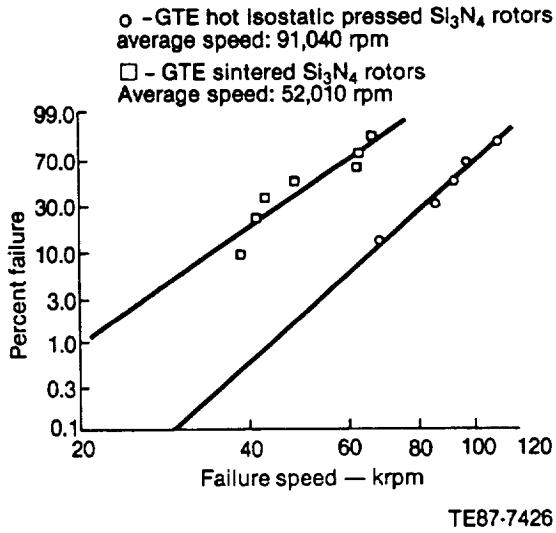

Figure 21. *Spin test results of GTE sintered and HIP-processed AY6 Si_3N_4 rotors.*

spin-tested to failure in a vacuum spin pit. The average burst speed of these rotors was 91,040 rpm (106% design speed), with one of the rotors attaining a speed of 110,800 rpm. The spin test results of both the sintered and the HIP-processed AY6 Si_3N_4 rotors are summarized in Figure 21.

Beginning in 1985, efforts were conducted with GTE Labs on the development and fabrication of injection-molded and HIP-processed PY6 Si_3N_4 turbine rotors. The PY6 material composition features improved elevated temperature strength and time-dependent properties relative to the AY6 Si_3N_4 material. A new injection molding tool, featuring a revised engine configuration rotor design with radially pullable exducer tooling inserts, was obtained in 1986 by GTE. Approximately 75 rotors were molded, subjected to binder burnout, and prepared for subsequent processing. Densification of these rotors required HIP processing by glass encapsulation technique in the ASEA facility in Sweden. To ensure that the parts were strong enough for handling during transportation, they were prefired to approximately 75% density after binder removal. Attempts to HIP process the first set of 10 rotors revealed blade cracks and shallow surface cracks present in the rotors. This phenomenon was not observed in the prior HIP processing at ASEA of the AY6 Si_3N_4 rotors.

To resolve the cracking issue, a systematic series of experiments were performed at GTE. The results indicated that the cracking was caused by a compositional change that occurs in the part surface during the prefiring step prior to HIP processing. The PY6 composition was observed to be particularly susceptible to such changes during densification. This was resolved by modifying/eliminating the prefiring step and using a newly acquired HIP furnace in conjunction with the ASEA process at GTE Laboratories.

Five injection-molded and HIP-processed PY6 rotors were received and evaluated at Allison. The rotors met all dimensional requirements and passed FPI. Microfocus radiography did not reveal any indications of internal defects. Two of the rotors were proof spin-tested for engine qualification. The rotors attained speeds of 88,000 and 90,000 rpm, respectively, without failure. Further spin test characterization was conducted by spin testing seven additional GTE HIP-processed PY6 Si_3N_4 rotors to failure at room temperature. The results of this testing are summarized in Table VI. The average burst speed measured 95,040 rpm, with a maximum spin speed of 120,600 rpm attained.

Test bars of the GTE PY6 Si_3N_4 material were evaluated to determine the material strength characteristics. The test bars were injection-molded and HIP-processed using identical parameters to those established for rotor fabrication. The average density of this material measured 3.250 g/cm^3. The results of the strength testing are summarized in Table VII. The average room temperature strength

Table VI.
Spin test results for GTE Laboratories injection-molded and HIP-processed PY6 Si_3N_4 GT rotors.

Rotor serial No.	Spin speed—krpm
ALL1	100.9 (burst)
ALL2	119.5 (burst)
106	101 (burst)
107	88 (proof)
109	90 (proof)
129	120.6 (burst)
130	58.6 (burst)
152	74 (burst)
156	90.7 (burst)

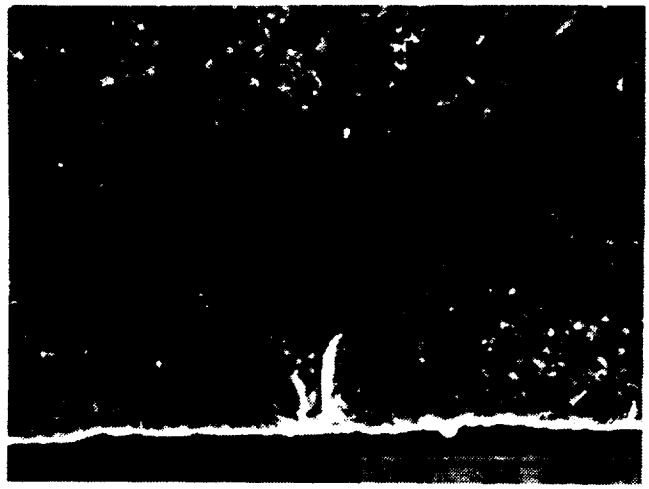

TE87-7429

Figure 22. *Typical fracture origin (surface crack) observed in GTE PY6 Si_3N_4 machined bars tested at room temperature.*

Table VII.
Fracture strength of GTE injection-molded and HIP-processed PY6 Si_3N_4.

Temperature—°C (°F)	Strength—MPa (ksi)	
	Machined	As fired
Room	551.05 (79.92)	456.52 (66.21)
1000 (1832)	517.81 (75.10)	376.33 (54.58)
1150 (2102)	519.88 (75.40)	321.72 (46.66)
1250 (2282)	420.53 (60.99)	355.58 (51.57)
1370 (2498)	396.60 (57.52)*	

*Bars tested at NASA-Lewis Research Center

of material with a machined tensile surface condition was 551.05 MPa (79.92 ksi). The typical strength-controlling flaws in these specimens were observed to be surface cracks, shown in Figure 22.

The elevated temperature strength measured 517.81 MPa (75.10 ksi) at 1000°C (1832°F), 519.88 MPa (75.40 ksi) at 1150°C (2102°F), and 420.53 MPa (60.99 ksi) at a temperature of 1250°C (2282°F). The typical fracture origins observed for the machined bars tested at elevated temperature were surface and internal porosity, shown in Figure 23. PY6 bars with a machined surface tested at NASA had an average strength of 396.60 MPa (57.52 ksi) at a test temperature of 1370°C (2500°F). Test bars with an as-fired surface condition had an average strength of 456.52 MPa (66.21 ksi) at room temperature, 376.33 MPa (54.58 ksi) at 1000°C (1832°F), 321.72 MPa (46.66 ksi) at 1150°C (2102°F), and 355.58 MPa (51.57 ksi) at a temperature of 1250°C (2282°F). The typical strength-controlling defects observed in the bars with an as-fired surface were surface flaws and cracks, as shown in Figure 24. The fracture toughness of the injection-molded and HIP-processed PY6 Si_3N_4 material mea-

TE87-7427

Figure 23. *Typical fracture origin (internal pore) observed in GTE PY6 Si_3N_4 machined bars tested at elevated temperature.*

TE87-7428

Figure 24. *Typical strength-controlling defect (surface flaw) observed in GTE PY6 Si_3N_4 test bars with an as-fired surface.*

sured 4.1 MPa$\sqrt{m}$ (3.7 ksi$\sqrt{in.}$) determined using the SENB test method.

To evaluate the component strength characteristics, test bars were sectioned from a GTE HIP-processed PY6 Si_3N_4 gasifier rotor (S/N ALL3). The density of the test bars was 3.248 g/cm^3. All of the rotor bars were evaluated with a machined surface condition. The average room temperature strength of the bars measured 644.82 MPa (93.52 ksi). The typical fracture origins were surface flaws and small internal pores. The average strength of the rotor bars tested at a temperature of 1000°C (1832°F) was 449.21 MPa (65.15 ksi), with a strength of 350.06 MPa (50.77 ksi) measured at a temperature of 1150°C (2102°F). All fractures of the bars tested at elevated temperature originated from surface flaws.

The current process developed by GTE for fabrication of injection-molded and HIP-processed PY6 Si_3N_4 turbine rotors has resulted in the delivery of flaw-free rotors with a density of over 99% theoretical and a maximum spin burst speed of 120,600 rpm. Characterization of the injection-molded and HIP-processed PY6 Si_3N_4 material in test bar form indicate excellent strength characteristics and oxidation resistance to temperatures in excess of 1250°C (2282°F). Significant further development activities are required to achieve these test bar characteristics in full scale rotors. In addition, improvements in process yield, dimensional control, and consistency in the properties of the injection-molded rotors are required to satisfy the RPD reliability and cost requirements.

Kyocera Silicon Nitride Gasifier Turbine Rotors

Introduction

The activity with Kyocera on gasifier turbine rotors focused on the fabrication and characterization of slip cast SSN rotors. Initially, efforts were focused on SN220M Si_3N_4, a well-developed material system used extensively for lower temperature radial turbocharger rotors. Rotors of the SN220M material were received and evaluated both with and without shaft attachments. Subsequent efforts with Kyocera were directed toward the fabrication of rotors using SN250M Si_3N_4, a material that exhibited improved elevated temperature strength and time-dependent characteristics. Test bars were also evaluated of SN270M Si_3N_4, a developmental material currently available only in test bar form.

Discussion

SN220M Silicon Nitride Rotors—An internally funded Allison ceramic technology program resulted in the delivery of SN220M Si_3N_4 gasifier

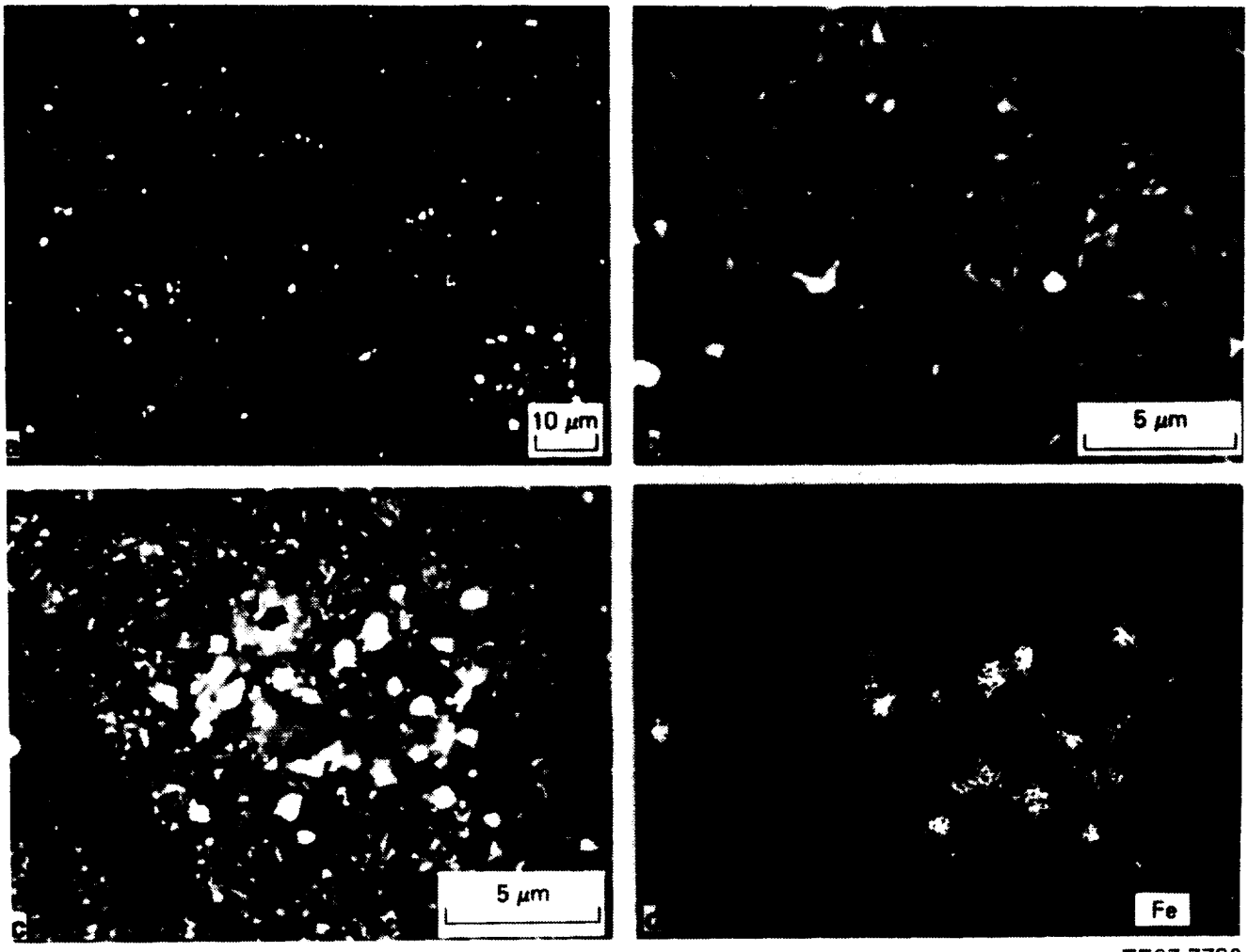

Figure 25. *Backscattered electron images of a metallographically polished Kyocera SN220M qualification bar and an iron characteristic X-ray raster (d).*

turbine rotors from Kyocera. Inspection, evaluation, attachment development, and engine testing of these rotors were accomplished in the AGT 100 program. The SN220M Si_3N_4 material had been extensively developed by Kyocera for production of slip cast radial turbine rotors and was used for initial rotor fabrication efforts to support intermediate temperature engine test activities. The SN220M material is comprised of beta-Si_3N_4 grains surrounded by a secondary silicate phase containing alumina and yttria. The microstructure, shown in Figure 25, includes variable-sized rod-shaped grains of Si_3N_4 surrounded by an intergranular phase that appears as a brighter, lacy network around the grains of Si_3N_4. The contrast between the two phases is due to the presence of the heavier element (yttria) in the grain boundary phase. Iron-rich impurity particles were visible as light-colored discrete spots. Transmission electron microscopy (TEM) evaluation showed the grain boundary phase to be entirely amorphous.

The characteristics of Kyocera slip cast SN220M SSN were evaluated on standard-size MOR test bars cut from slip cast billets. The average density of the test bars measured 3.203 g/cm^3. The results of the material strength evaluation are summarized in Table VIII. The room temperature fracture strength of material tested with an as-fired tensile surface condition averaged 459.83 MPa (66.69 ksi). A Weibull modulus of 9.84 was measured for this material. The strength-controlling flaws were pores

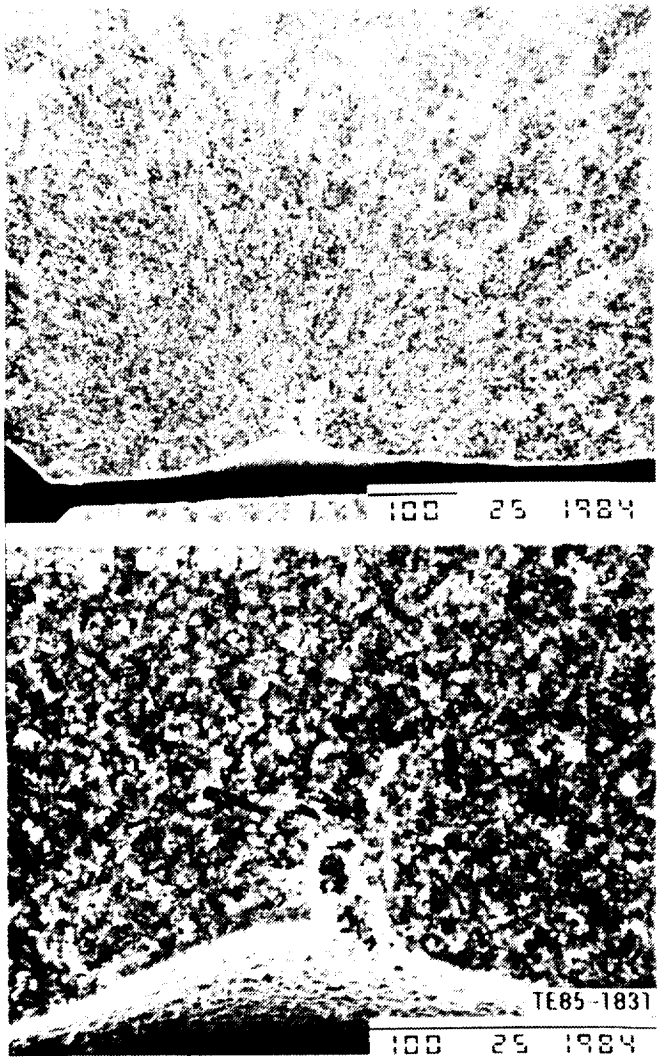

Figure 26. *Typical fracture origin (surface pore) in as-fired Kyocera SN220M Si_3N_4 tested at room temperature.*

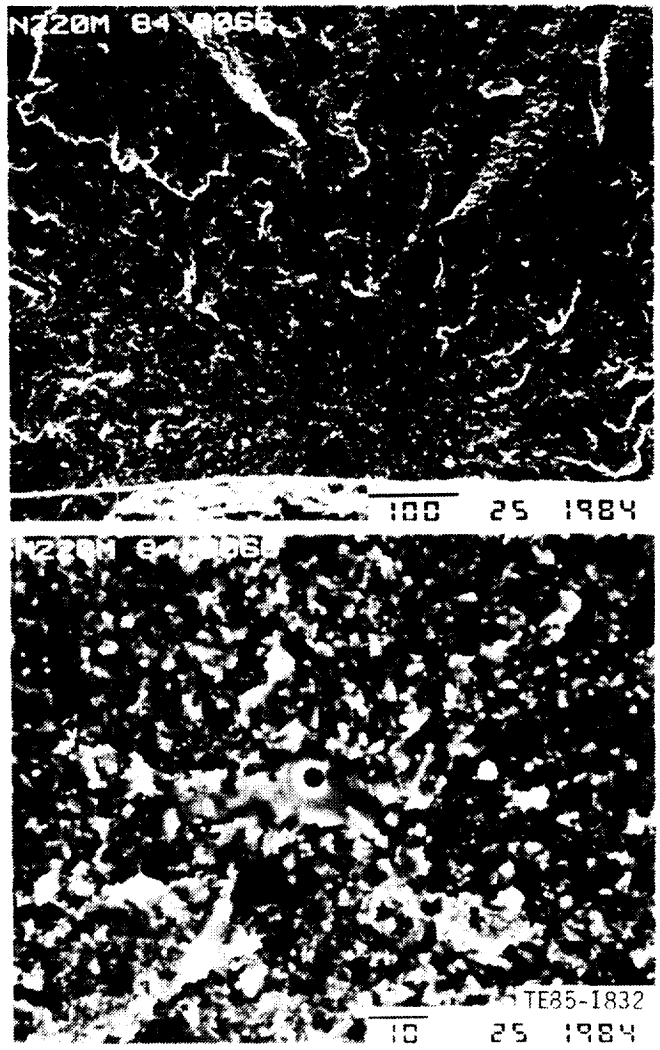

Figure 27. *Typical fracture origin (glassy phase inclusion) in machined Kyocera SN220M tested at room temperature.*

Table VIII.
Fracture strength of Kyocera slip cast SN220M Si_3N_4.

Temperature—°C (°F)	Strength—MPa (ksi)	
	Machined	As fired
Room	699.08 (101.39)	459.83 (66.69)
1000 (1832)	603.45 (87.52)	413.49 (59.97)
1150 (2102)	333.72 (48.40)	282.28 (40.94)

located either on the tensile surface or at the base of surface depressions, as shown in Figure 26. Bars tested at room temperature with a machined surface had an average fracture strength of 699.08 MPa (101.39 ksi). The Weibull modulus was 9.70. The typical fracture origins were internal inclusions, composed either of a glassy phase rich in aluminum, calcium, yttrium, and silicon (see Figure 27) or clusters of large grains rich in iron, chromium, titanium, and silicon (Figure 28).

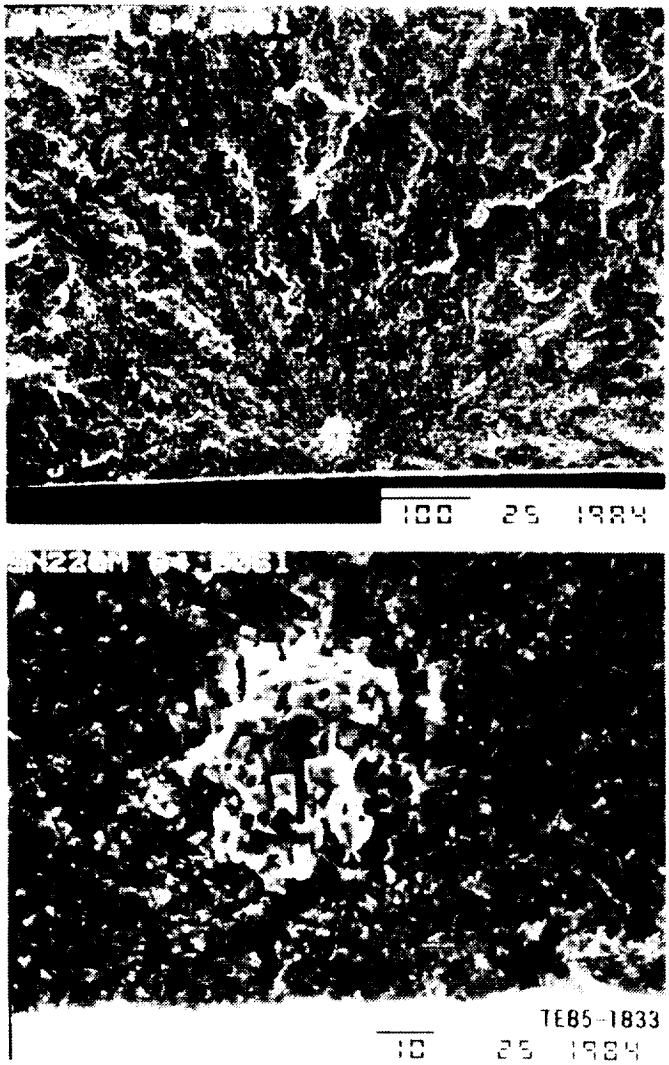

Figure 28. *Typical fracture origin (internal inclusion) in machined Kyocera SN220M tested at room temperature.*

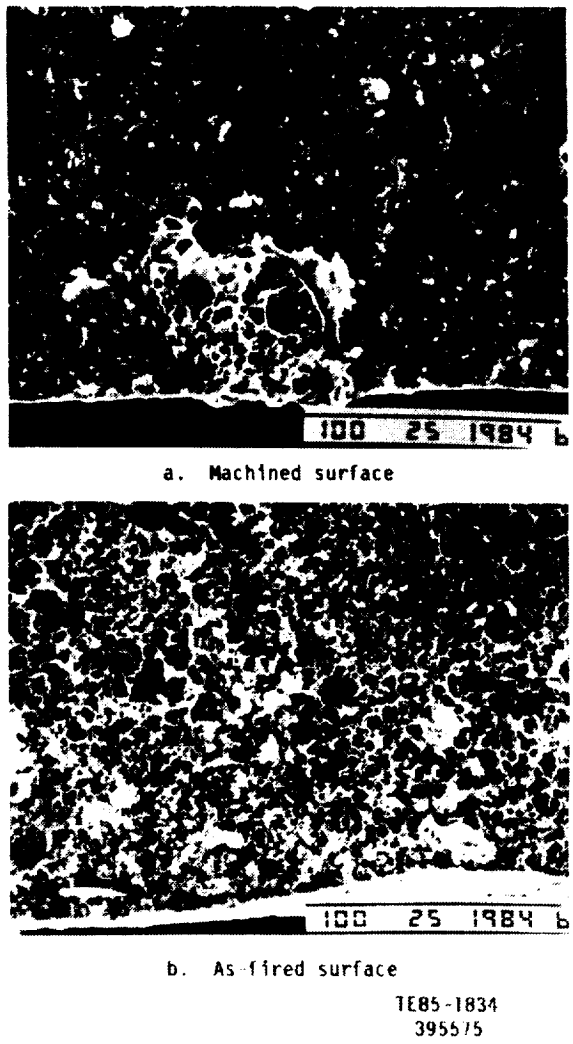

Figure 29. *Typical fracture origin (glassy bubbles) observed in Kyocera SN220M Si_3N_4 tested at 1150°C.*

The average strength of bars tested at 1000°C (1832°F) with an as-fired surface measured 413.49 MPa (59.97 ksi). Bars tested with a machined surface at 1000°C (1832°F) had an average strength of 603.45 MPa (87.52 ksi). For both the as-fired and machined test bars, evidence of light oxidation was observed with fractures initiating from small surface pores. At a test temperature of 1150°C (2102°F), the average strength of bars with an as-fired surface condition decreased to 282.28 MPa (40.94 ksi), while the machined bars had an average strength of 333.72 MPa (48.40 ksi). All bars tested at 1150°C (2102°F) were heavily oxidized, with the as-fired surfaces oxidized more than the machined surface. The strength-controlling flaws were observed to be glassy bubbles near the tensile surface, as shown in Figure 29. The average room temperature fracture toughness (K_{IC}) of the SN220M material measured 5.7 MPa$\sqrt{m}$ (5.2 ksi$\sqrt{in.}$), determined using the SENB test method.

A total of 18 SN220M Si_3N_4 gasifier turbine rotors were provided by Kyocera for analysis and testing. These rotors, shown in Figure 30, were fabricated by slip casting and configured for an interference fit shaft attachment. NDE (visual, fluorescent penetrant, and X-ray) of these rotors revealed no objectionable indications. Dimensional evaluation indicated that all dimensions were within print tolerance with the exception of a minor closing of the exducer throat spacing observed in the first two rotors received (S/N K-1 and K-2). This was corrected in subsequent rotors by the use of appropriate fixturing during the sintering process, and the remainder of the rotors met all structural and dimensional requirements. Kyocera indicated that

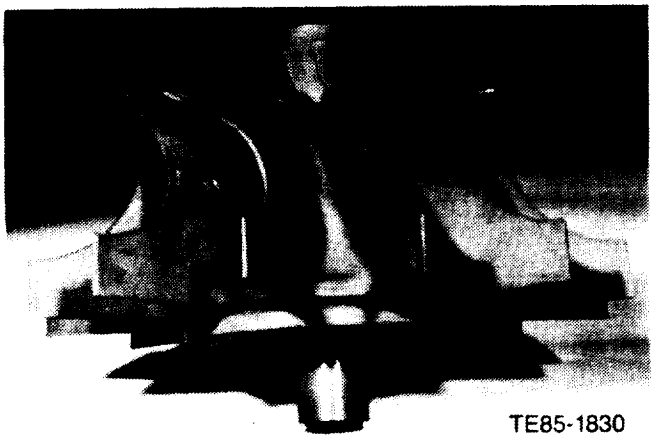

Figure 30. *Kyocera slip cast SN220M sintered SSN gasifier turbine rotor.*

Table IX.
Spin test results for Kyocera slip cast SN220M Si_3N_4 gasifier turbine rotors.

Rotor serial No.	Spin speed—rpm
0001-1	137,800
0002-2	140,700
0002-3	142,800*
0002-4	139,500
0002-5	126,800
0003-1	138,000*
0003-2	134,000*

*Rotor intact, test terminated at this speed due to facility limitations

the overall process yield of acceptable quality rotors was 42%. Each of the rotors was proof spin-tested by Kyocera to 100,000 rpm (116% design speed) prior to receipt. Additional characterization of the material strength characteristics of the slip cast SN220M Si_3N_4 rotors were conducted by spin burst testing seven of the rotors. The results of this spin test evaluation are summarized in Table IX. The average burst speed of these rotors (calculated by suspended item analysis) measured 141,000 rpm (163% design speed).

Further characterization of the material strength characteristics of Kyocera slip cast SN220M Si_3N_4 gasifier turbine rotors was conducted by sectioning standard size (50.8 mm × 6.35 mm × 3.18 mm [2 in. × 0.25 in. × 0.125 in.]) test bars from a rotor (P/N AA101029, S/N 0006-3) that had been previously proof spin-tested by Kyocera to 100,000 rpm (116% design speed). The strength characteristics of the rotor test bars are summarized

Table X.
Flexural strength of test bars cut from Kyocera slip cast SN220M Si_3N_4 rotor.

Temperature—°C (°F)	Strength—MPa (ksi)
Room	754.52 (109.43)
1000 (1832)	476.10 (69.05)
1150 (2102)	369.30 (53.56)

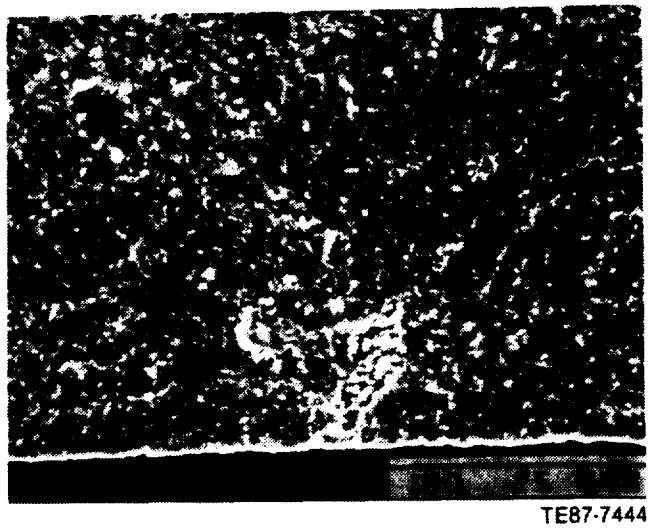

Figure 31. *Fracture origin (surface pore) observed in Kyocera rotor bars tested at room temperature.*

in Table X. All bars were tested with a machined tensile surface condition. The average density of the test material measured 3.162 g/cm^3. The average room temperature strength measured 754.52 MPa (109.43 ksi). The typical fracture origins were observed to be scattered porosity and surface flaws, as shown in Figure 31. The strength of the bars tested at 1000°C (1832°F) was 476.10 MPa (69.05 ksi). Surface porosity was again observed as the primary strength-controlling defect, Figure 32. The average strength of the bars tested at a temperature of 1150°C (2102°F) was 369.30 MPa (53.56 ksi). Typical fracture origins were small surface and internal pores, shown in Figure 33, with some evidence of light local oxidation observed.

Ten additional semi-finished gasifier turbine rotor assemblies were received from Kyocera. The assemblies consisted of a slip cast SN220M SSN turbine rotor attached to an Incoloy 907 metal compressor shaft by a Kyocera developed and applied braze operation, using a silver/copper braze alloy that had been developed by Kyocera for attachment of ceramic turbocharger rotors to metal shafts. The rotors were proof spin-tested to 112,000 rpm (130%

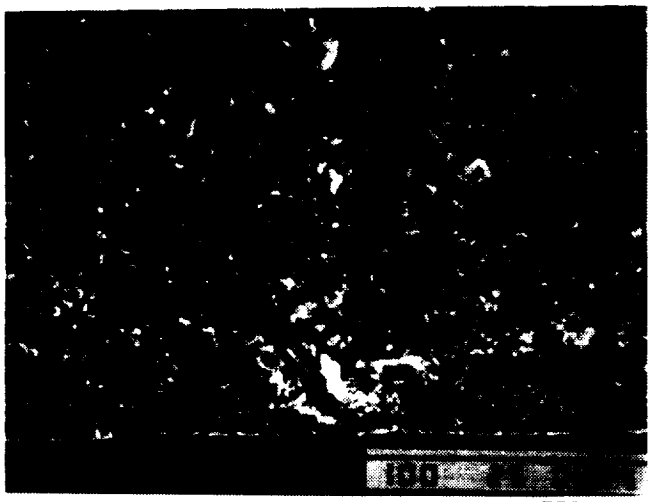

TE87-7445

430487

Figure 32. *Typical fracture origin (pore) in Kyocera rotor bars tested at 1000°C.*

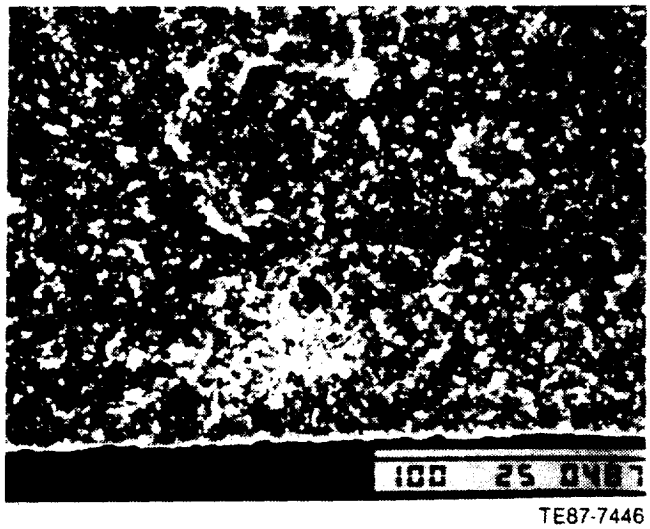

TE87-7446

430486

Figure 33. *Fracture origin (internal pore) observed in Kyocera SN220M rotor bars tested at 1150°C.*

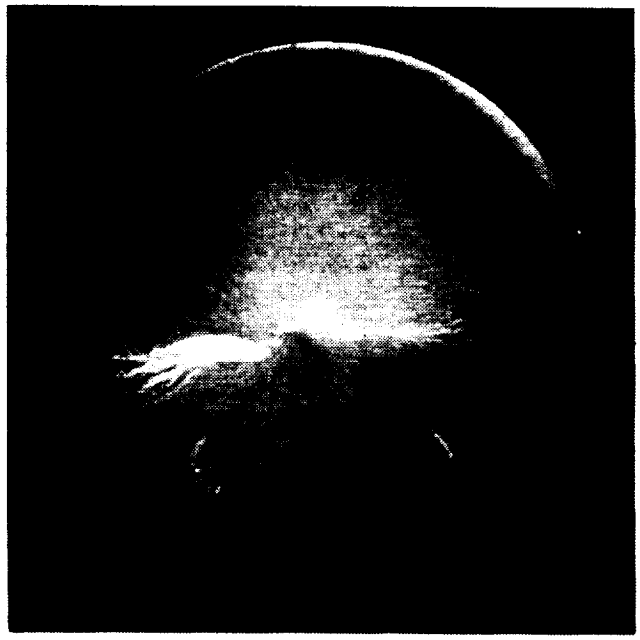

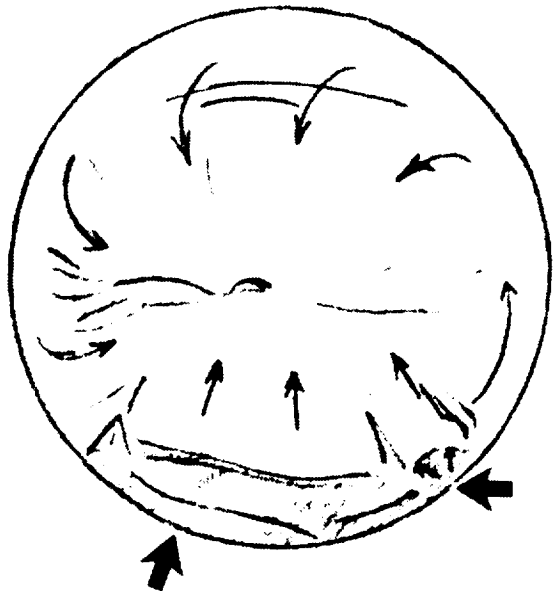

TE86-2800

Figure 34. *Fracture surface of Kyocera Si_3N_4 rotor brazed to Inco 907 shaft (0004-8). Origins are located at large black arrows.*

design speed) at room temperature by Kyocera prior to shaft attachment.

One of the rotor/shaft assemblies (S/N 0004-8) fractured during an airfoil machining operation. The rotor separated from the Inco 907 shaft at the front surface of the braze joint. Fractographic analysis of the Si_3N_4 rotor shaft revealed that the fracture initiated from two pre-existing cracks, identified in Figure 34 by the large black arrows. The two surface cracks were interpreted as having been present in the rotor shaft prior to the finish machining operation because both crack surfaces were observed to have a thin layer of an iron-nickel alloy present. Further analysis revealed a nonuniform braze layer in the attachment, depicted in Figure 35, with no braze alloy present at the failure origins (direct ceramic/metal contact). An approximately 120 micron thick layer of braze was located opposite the fracture origins.

The Kyocera brazed rotor shaft attachment underwent additional evaluation by selecting a second rotor assembly (S/N 0004-3) for flexural load

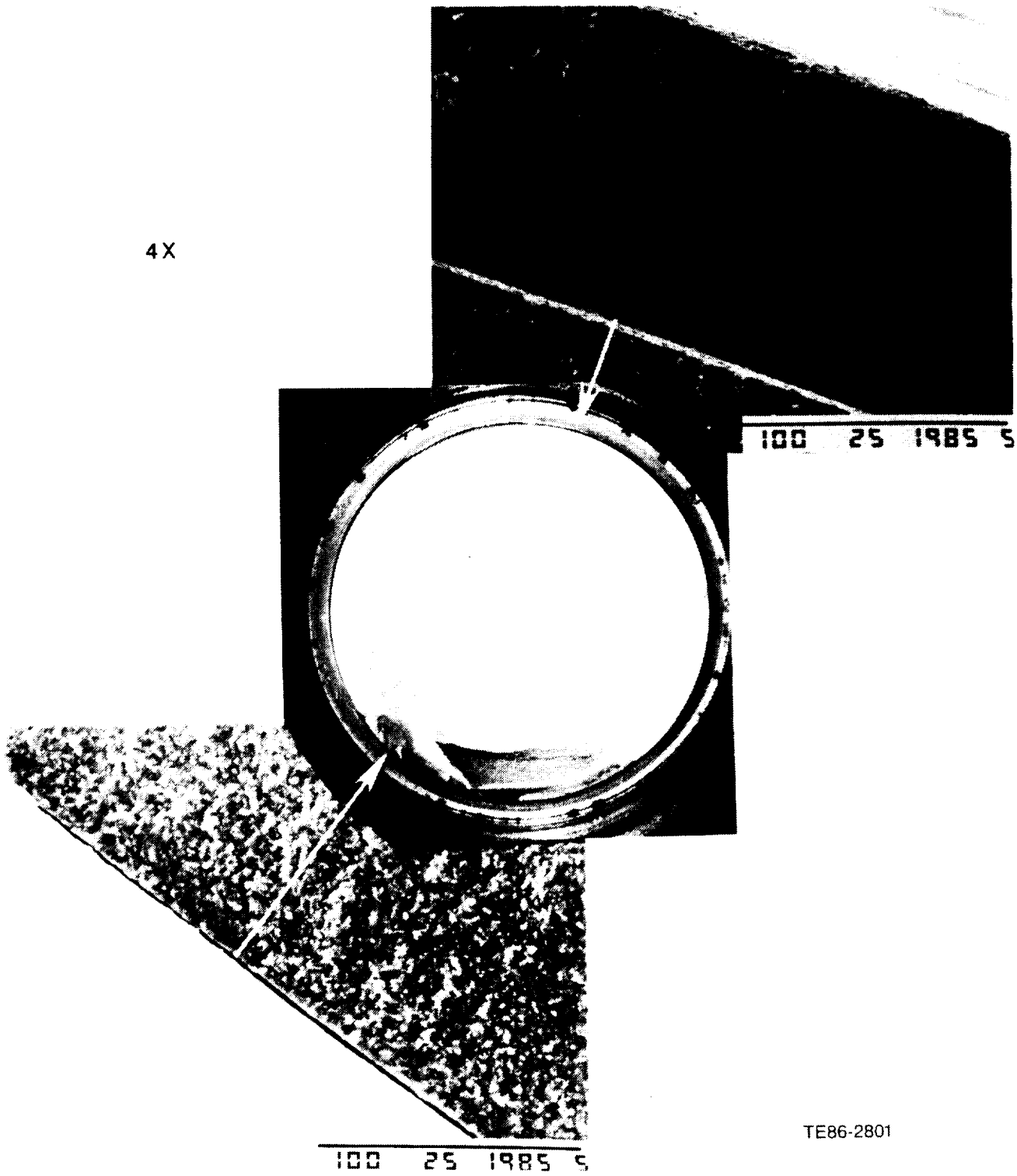

Figure 35. *Cross section of Kyocera Si_3N_4 rotor 0004-8 showing nonuniform braze thickness. Note direct contact at fracture origin (bottom picture).*

testing, which subjects the rotor shaft/metal shaft joint to bending stresses. The rotor was rotated through 720° after application of the load, which was applied in increments of 1.1 N-m (10 in.-lb), to stress the attachment uniformly. This rotor assembly failed at a bending moment of 25.4 N-m (225 in.-lb), corre-

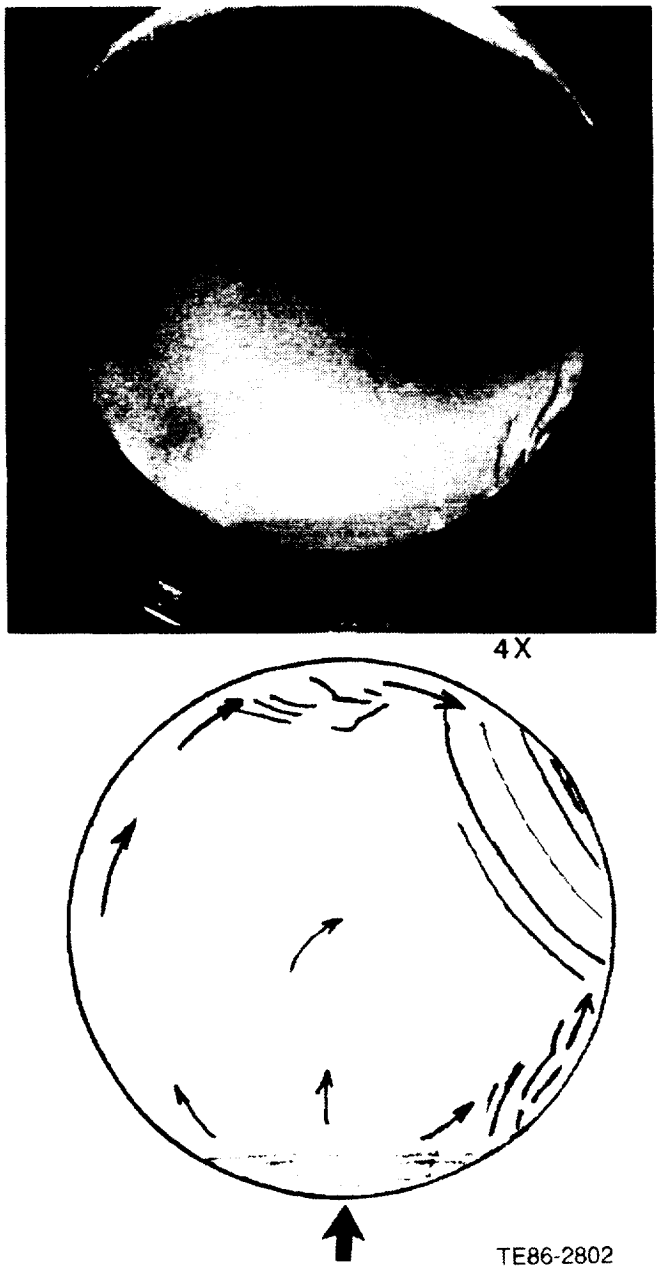

Figure 36. *Fracture surface of Kyocera Si_3N_4 rotor 0004-3 broken in load test (5.3 ksi stress). Origin is located at large black arrow.*

sponding to a stress level of 40.68 MPa (5.9 ksi). The fracture initiated from a large crescent-shaped surface flaw in the Si_3N_4 shaft, shown in Figure 36. This rotor assembly also had a nonuniform braze layer thickness, shown in Figure 37, with no evidence of braze alloy adjacent to the fracture origin. Following this failure, the remainder of the brazed Kyocera rotor assemblies were flexural load tested to ensure the integrity of the braze joint. The goal of this testing was to apply a bending moment at twice the level encountered during engine operating conditions, corresponding to a bending moment of 27.1 N-m (240 in.-lb) (44.13 MPa [6.4 ksi]) stress. With one exception, the rotors fractured in the Si_3N_4 shaft at stress levels between 24.13 – 35.86 MPa (3.5 – 5.2 ksi), with the fracture origins again resulting from nonuniform braze coverage.

As a result of this evaluation, Kyocera supplied an additional five SN220M Si_3N_4 rotors configured for an interference fit shaft attachment and five SN250M rotors with a brazed shaft attachment. The brazed rotors had an improved braze joint, with special emphasis placed on modified fixturing during the brazing process to ensure uniform braze coverage. Flexural load testing of the brazed SN250M Si_3N_4 rotors resulted in each of the five rotor assemblies achieving a bending moment of 27.1 N-m (240 in.-lb) (44.13 MPa [6.4 ksi] stress) without failure. Nondestructive inspection and sectioning of the rotor shaft attachments revealed that the braze joints were more uniform both circumferentially and radially than the previous brazed SN220M rotors.

SN250M Silicon Nitride Rotors—Ten slip cast SN250M Si_3N_4 gasifier turbine rotors were received from Kyocera and evaluated. These rotors were configured for an interference fit shaft attachment. Each of the SN250M rotors was proof spin-tested at room temperature by Kyocera to 112,000 rpm (130% design speed) prior to delivery. Kyocera indicated an overall process yield of acceptable quality rotors of 30%. The average density of the rotors measured 3.298 g/cm^3.

Evaluation of the material characteristics of Kyocera slip cast SN250M SSN were conducted on qualification test bars. The microstructure of this material, shown in Figure 38, consists of relatively uniform Si_3N_4 grains with a few large grains of beta-Si_3N_4 observed. X-ray elemental analysis in the SEM revealed yttrium and strontium in the grain boundary material. The grain boundary phase in the SN250M material is partially recrystallized, consisting of large scale crystal networks interconnected around the beta-Si_3N_4 grains in conjunction with areas exhibiting glassy grain boundary regions. The average density of this material measured 3.268 g/cm^3.

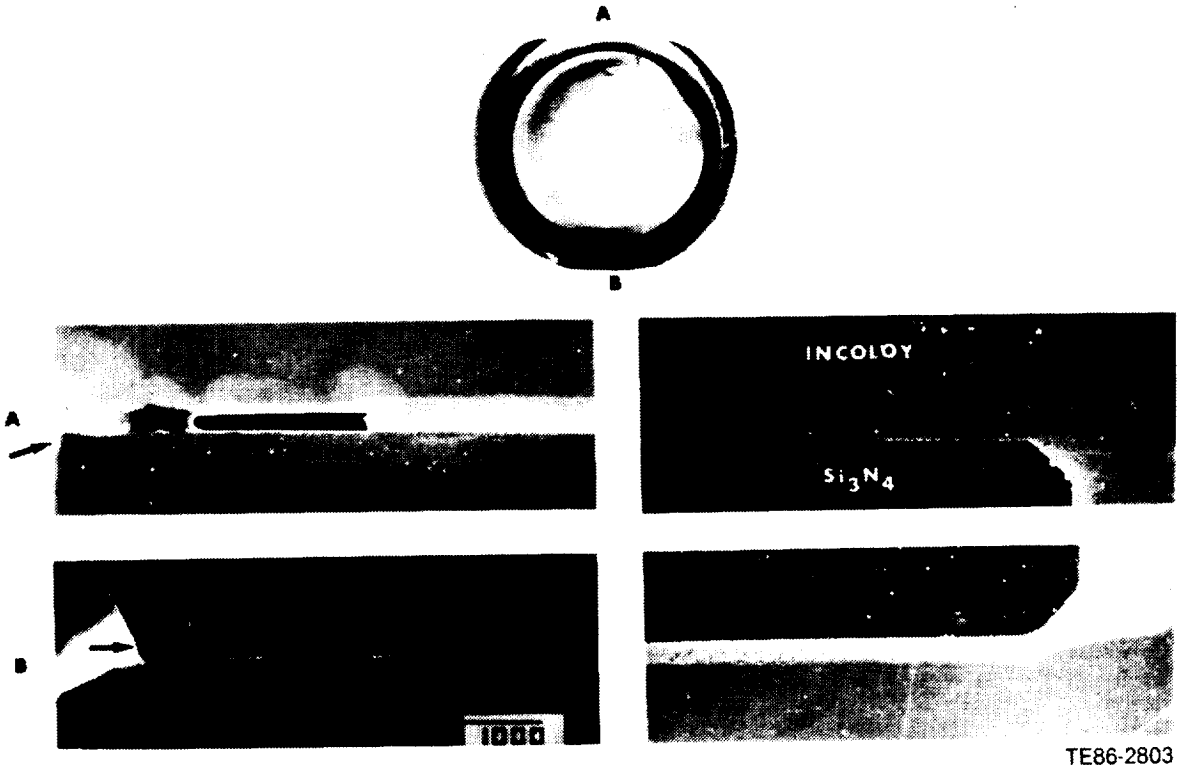

Figure 37. *Cross section Kyocera Si_3N_4 rotor 0004-3 showing nonuniform braze thickness. Note direct contact at fracture origin (B).*

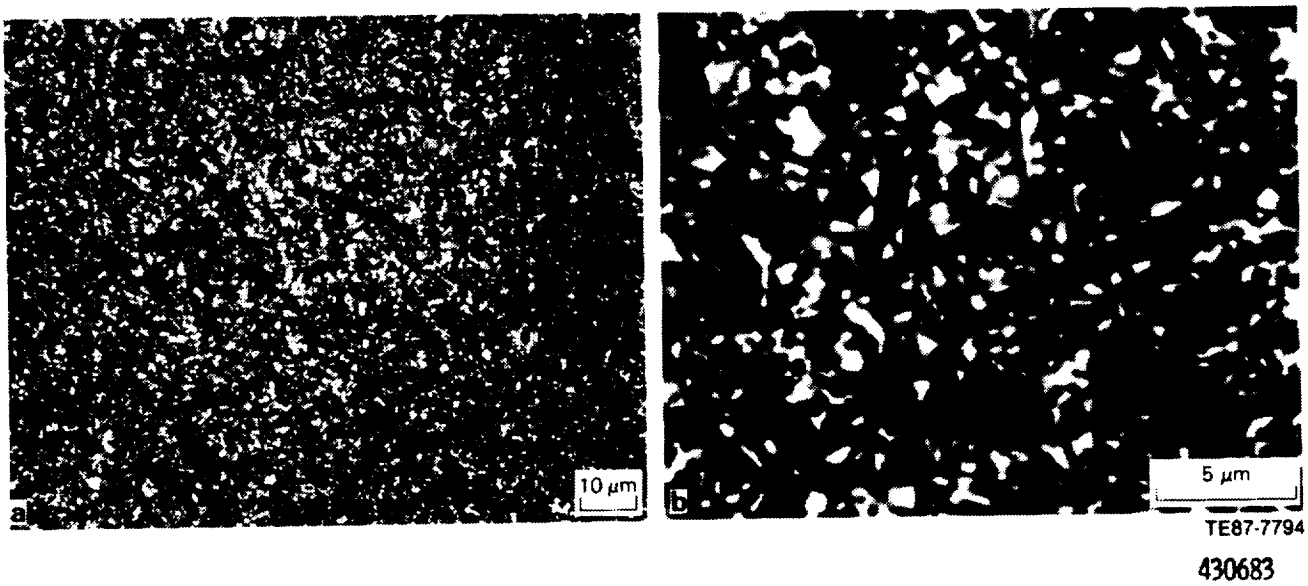

Figure 38. *Backscattered electron images of a metallographically polished Kyocera SN250M qualification.*

The strength characteristics of the slip cast SN250M test bars are summarized in Table XI. The average room temperature bend strength of bars with a machined tensile surface condition measured 618.76 MPa (89.74 ksi). The primary strength-controlling defects were surface and internal pores

in darkish regions that fractured transgranularly, as shown in Figures 39 and 40. Bars with a machined tensile surface tested at 1000°C (1832°F) had an average estrength of 603.04 MPa (87.46 ksi), while material tested at a temperature of 1150°C (2102°F) demonstrated an average strength of 597.80 MPa (86.70 ksi). Surface pores were identified as the primary fracture origins in both instances. Test material with an as-fired tensile surface condition had an average room temperature strength of 446.18 MPa

Table XI.
Fracture strength of Kyocera slip cast SN250M Si_3N_4.

Temperature—°C (°F)	Strength—MPa (ksi)	
	Machined	As fired
Room	618.76 (89.74)	446.18 (64.71)
1000 (1832)	603.04 (87.46)	452.38 (65.61)
1150 (2102)	597.80 (86.70)	462.65 (67.10)

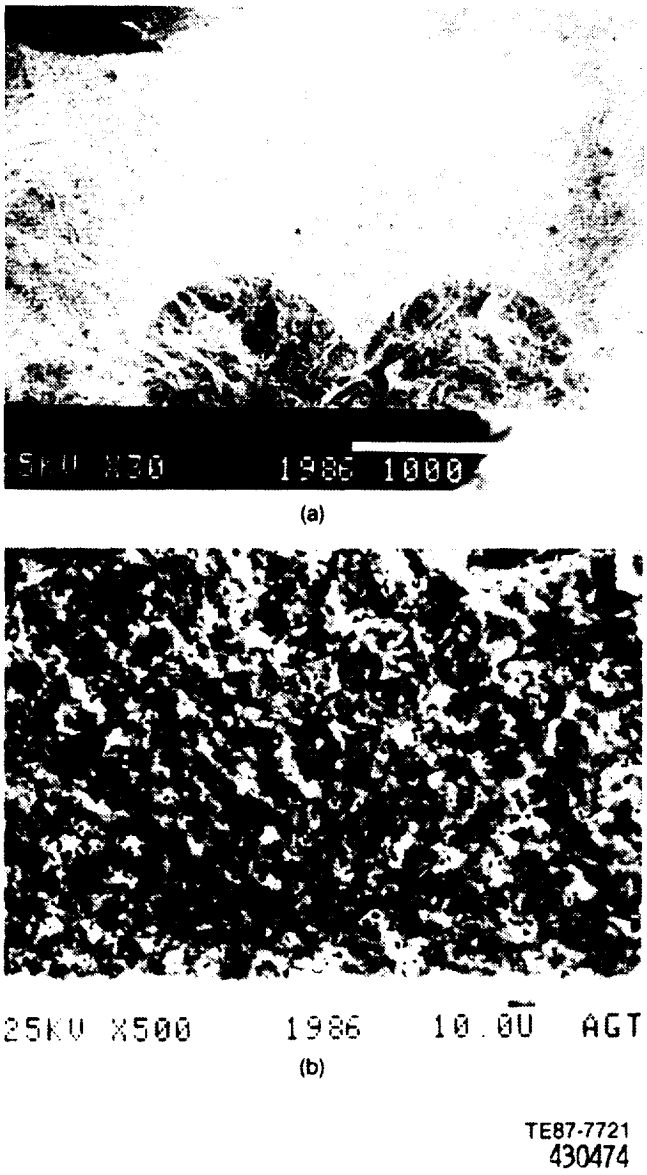

Figure 39. *Typical strength-controlling defect (surface pore) observed in Kyocera SN250M Si_3N_4 machined bars tested at room temperature.*

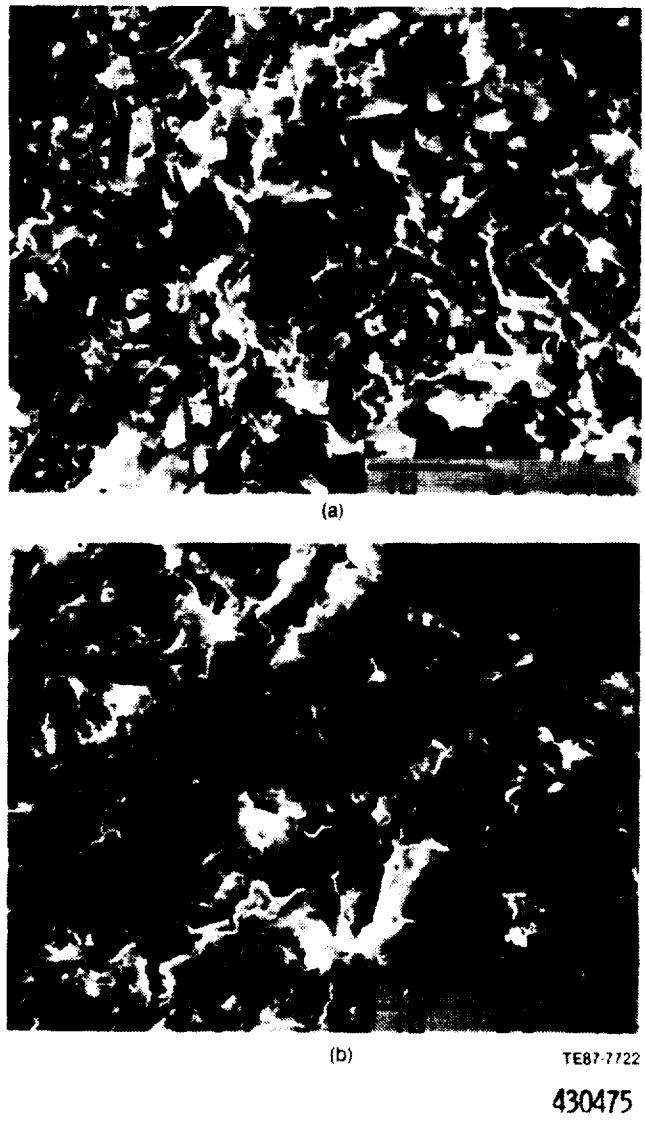

Figure 40. *Light region of intergranular fracture (a) and darker region of transgranular fracture (b) observed in Kyocera SN250M Si_3N_4.*

(64.71 ksi). The primary strength-controlling flaws were surface pores in regions with long crystals, as shown in Figure 41. The average strength of bars with an as-fired surface tested at 1000°C (1832°F) was 452.38 MPa (65.61 ksi), while bars tested at a temperature of 1150°C (2102°F) had an average strength of 462.65 MPa (67.10 ksi). The primary fracture origins observed in the as-fired bars tested at elevated temperature were similar to those found in the room temperature tests (surface pores with long crystals). The fracture toughness (SENB) of the Kyocera SN250M Si_3N_4 material measured 5.2 MPa$\sqrt{m}$ (4.7 ksi$\sqrt{in.}$).

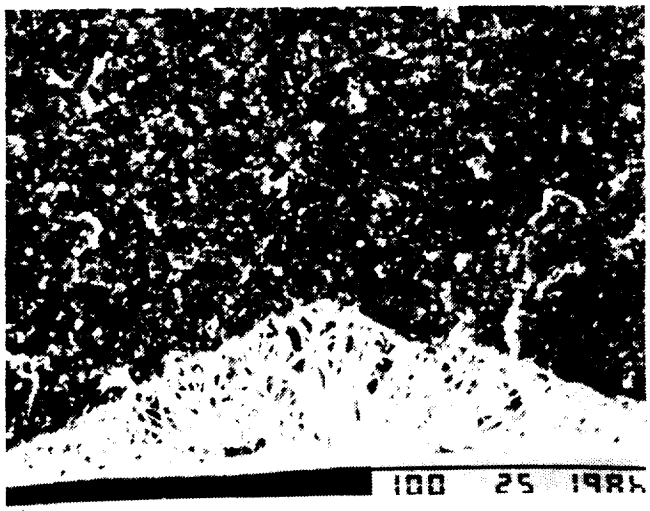

TE87-7723

430482

Figure 41. *Typical fracture origin (surface pore) observed in Kyocera SN250M Si_3N_4 with as-fired tensile surface.*

Additional evaluations of the component strength characteristics were conducted by sectioning test bars from a SN250M Si_3N_4 gasifier turbine rotor (P/N AA101327, S/N 0004-1). This rotor was proof spin-tested at room temperature by Kyocera to 112,000 rpm (130% design speed). The strength characteristics of the rotor test bars is summarized in Table XII. All bars were tested with a machined tensile surface condition. The average room temperature strength of this material was 622.07 MPa (90.22 ksi). Bars tested at a temperature of 1000°C (1832°F) had an average strength of 388.26 MPa (56.31 ksi). A strength of 377.16 MPa (54.70 ksi) was measured for bars tested at 1150°C (2102°F). The typical fracture origins observed in the SN250M Si_3N_4 rotor bars were clusters of small surface and internal pores. Examples of the strength-controlling flaws found in bars tested at room temperature, 1000°C (1832°F), and 1150°C (2102°F) are shown in Figures 42, 43, and 44, respectively. The primary reason for the strength decrease observed at elevated temperature for the test material sectioned from the SN250M rotor versus the qualification test bars was related to microstructural variations. The bars from the rotor exhibited increased porosity, with little or no grain boundary phase present in the rotor hub region.

The slip casting process used by Kyocera for rotor fabrication has resulted in the receipt of SN250M Si_3N_4 turbine rotors that exhibit excellent

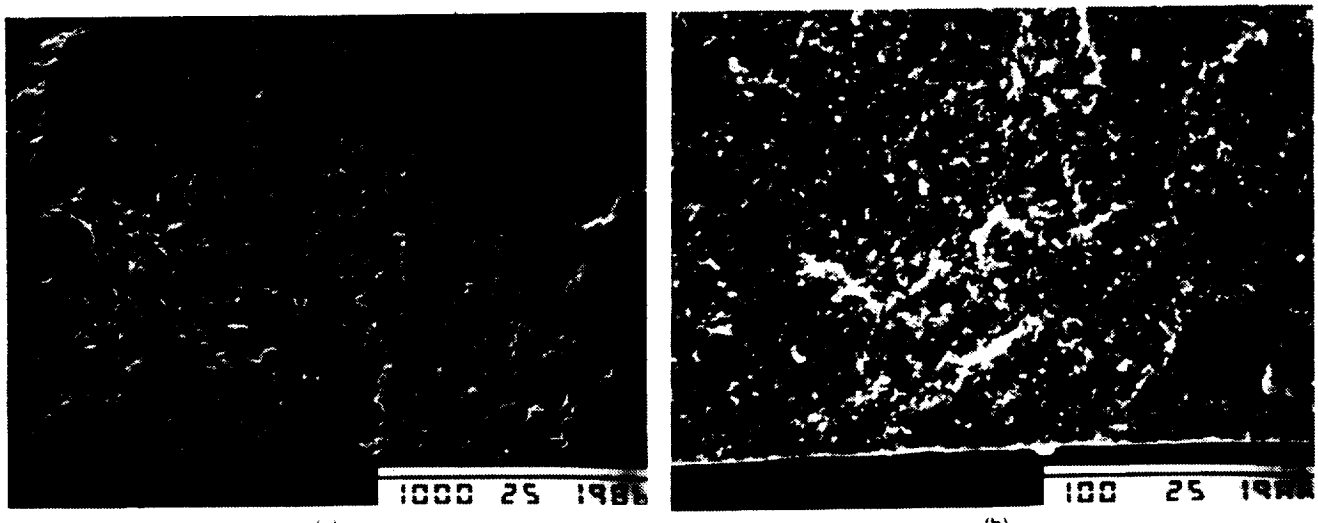

(a) (b)

TE87-7447

430481

Figure 42. *Typical fracture origin (pore cluster) observed in Kyocera SN250M Si_3N_4 rotor bars tested at room temperature.*

room temperature spin test results and dimensional conformance. The strength characteristics of the SN250M material are sufficient to meet the short term reliability requirements for the AGT 100 engine; however, improvements in the time-dependent properties are required to achieve the 3500 hr life goal. Further process development activities are necessary to achieve the test bar characteristics in full-scale rotors. In addition, increases in process yields and impact resistance/fracture toughness are also needed.

Table XII.
Flexural strength of test bars cut from Kyocera slip cast SN250M Si_3N_4 rotor.

Temperature—°C (°F)	Strength—MPa (ksi)
Room	622.07 (90.22)
1000 (1832)	388.26 (56.31)
1150 (2102)	377.16 (54.70)

SN270M Silicon Nitride—Evaluation of the material strength characteristics of Kyocera slip cast SN270M SSN was conducted. This material system is a developmental composition, currently available only in test bar form, that features improved elevated temperature strength and time-dependent properties relative to other versions of Kyocera

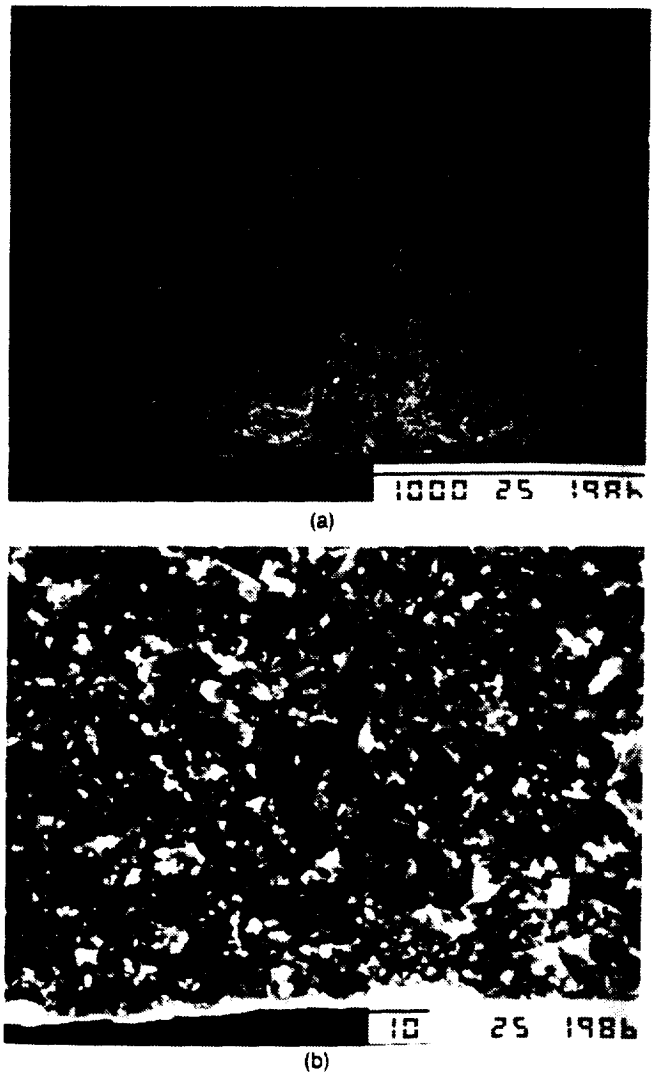

TE87-7448
430480

Figure 43. *Typical fracture origin (pore cluster) observed in Kyocera SN250M Si_3N_4 rotor bars tested at 1000°C.*

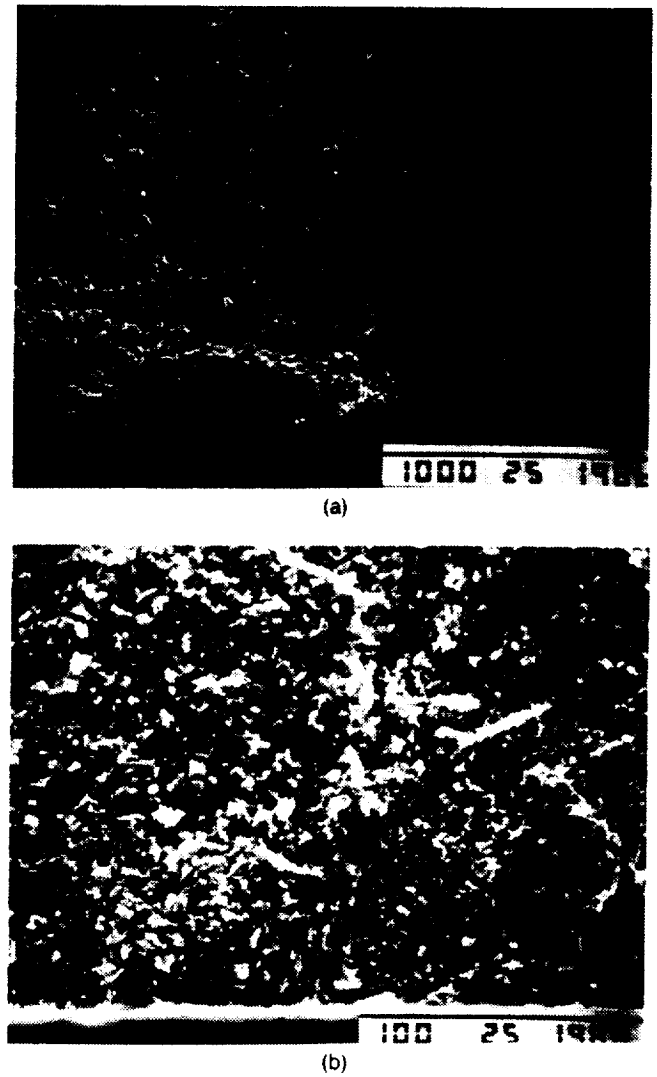

TE87-7449
430479

Figure 44. *Typical fracture origin (pore cluster) observed in Kyocera SN250M Si_3N_4 rotor bars tested at 1150°C.*

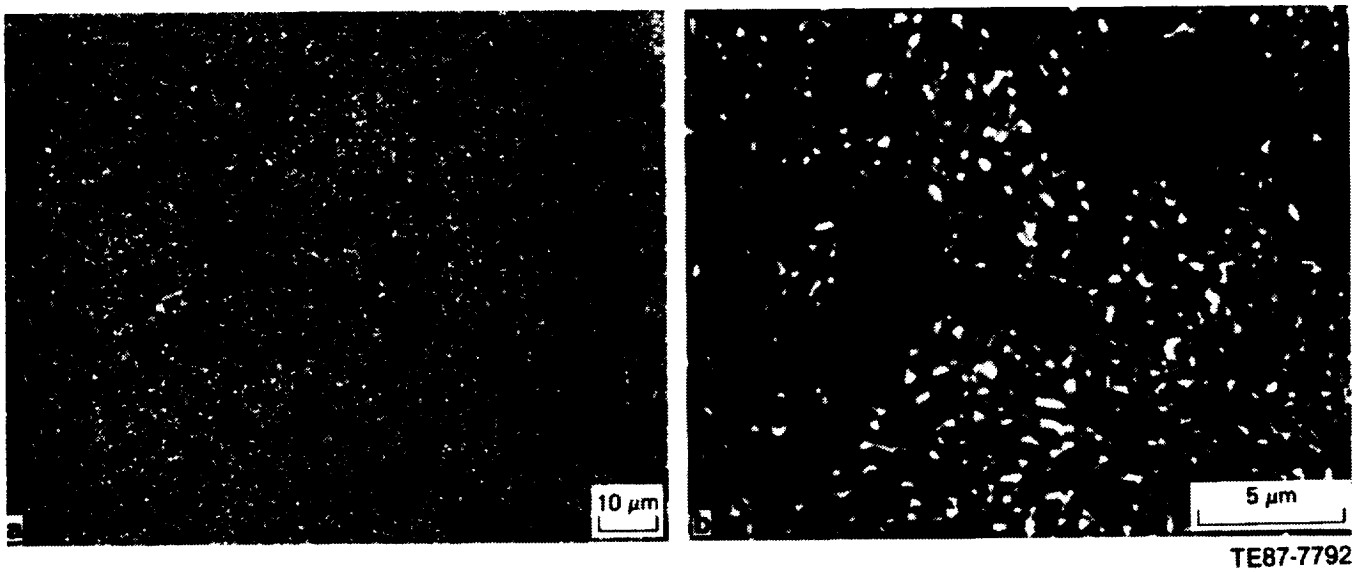

Figure 45. *Backscattered electron images of a metallographically polished Kyocera SN270M qualification bar.*

Table XIII.
Fracture strength of Kyocera slip cast SN270M Si_3N_4.

Temperature—°C (°F)	Strength—MPa (ksi)	
	Machined	As fired
Room	691.84 (100.34)	555.81 (80.61)
1000 (1832)	502.99 (72.95)	452.38 (65.61)
1150 (2102)	481.82 (69.88)	413.49 (59.97)
1370 (2498)	476.93 (69.17)*	

*Bars tested at NASA-Lewis Research Center

Si_3N_4. The average density of the specimens measured 3.256 g/cm^3. The microstructure of the SN270M material, shown in Figure 45, consists of small, relatively equiaxed Si_3N_4 grains with occasional long grains of beta-Si_3N_4 with aspect ratios of greater than 20 to 1. X-ray elemental analysis in the SEM revealed only yttrium in the grain boundary material. The grain boundary phase was found to be partially crystallized in this material.

The strength characteristics of the Kyocera SN270M Si_3N_4 test bars are summarized in Table XIII. The average room temperature strength of specimens with a machined tensile surface condition measured 691.84 MPa (100.34 ksi). The fractures were observed to originate at the tensile surface from the needle-shaped Si_3N_4 grains, shown in Figure 46. The room temperature strength of bars with an as-fired surface averaged 555.81 MPa (80.61 ksi). The primary strength-controlling flaws were surface depressions/pores, occasionally associated with the long crystals (Figure 47). A strength of 502.99 MPa (72.95 ksi) was measured for machined specimens tested at a temperature of 1000°C (1832°F), with a strength of 481.82 MPa (69.88 ksi) obtained at 1150°C (2102°F). Machined bars tested at NASA-Lewis at a temperature of 1370°C (2500°F) had an average strength of 476.93 MPa (69.17 ksi). The fracture origins were similar to those observed for the specimens tested at room temperature, i.e., surface crystals. Bars with an as-fired surface condition tested at a temperature of 1000°C (1832°F) had an average strength of 452.38 MPa (65.61 ksi), and a strength of 413.49 MPa (59.97 ksi) at a temperature of 1150°C (2102°F). The fracture origins were again identified to be surface porosity. The fracture toughness (K_{IC}) of the SN270M Si_3N_4 material, determined by the SENB method, measured 5.8 MPa$\sqrt{m}$ (5.3 ksi$\sqrt{in.}$).

2.3 CERAMIC TURBINE SCROLL DEVELOPMENT

The AGT 100 turbine scroll assemblies are complex duct structures consisting of three major individual ceramic components (a scroll body, turbine shroud, and connecting duct) joined together to form a single structure. In addition to structural and stringent geometric constraints required for the scroll assemblies, the ceramic-to-ceramic joints must be uniform with adequate strength and temperature capabilities. The development of fabrication, processing, and joining methodologies for the scroll assemblies was undertaken at Sohio and Norton, while scrolls were obtained on a parts-buy basis from Kyocera. The effort at Sohio has focused on the use of SASC for scroll fabrication, with activities at Norton using NC-430 SiSiC, and Kyocera producing scrolls from SN250 SSN. Each of the suppliers used a high temperature braze process for joining the individual components into a final assembly. An overview of the scroll development activities is reviewed in the following subsections.

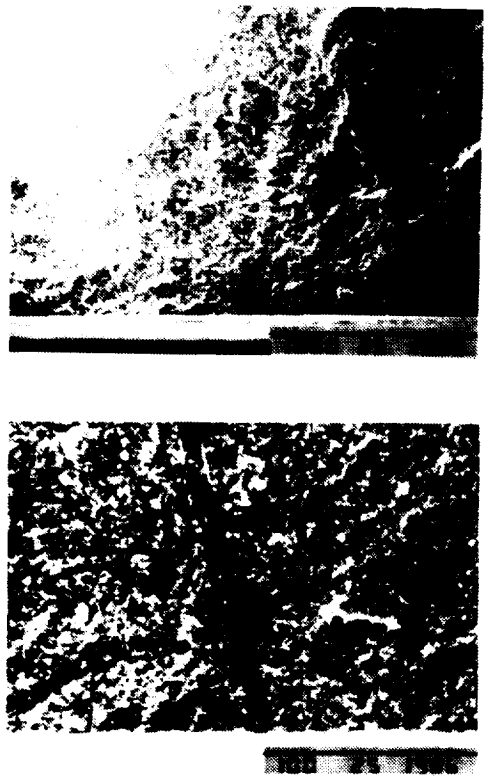

TE87-7420
429818

Figure 46. *Typical fracture originating from needle-shaped Si_3N_4 grains observed in machined Kyocera SN270M Si_3N_4 test bars.*

Standard Oil Gasifier Turbine Scroll Development

The development activities at Sohio on the gasifier turbine scroll assembly have used SASC as a material system. The scroll assembly, shown in Figure 48, consists of five individual ceramic components. The scroll body and connecting duct were formed by slip casting, with the shroud and two adapter sleeves fabricated by isostatic pressing and green machining. Two methods were used for joining the separate components into the final scroll assembly: sintering-joining and a high temperature braze.

The scroll body was formed by drain casting, using a water-based slurry with a bimodal mixture of SiC particles. The slurry was poured into a plaster of Paris mold that consisted of several sections to facilitate demolding. The cast component was demolded in stages to reduce the probability of slumping and sticking if demolded too early, or cracking if demolded too late. Initial cast scroll bodies exhibited extensive surface cracking, primarily in the inside diameter of the scroll body. These casting and demolding difficulties resulted in an in-depth study of the starting powder, the slurry composition, and the mold design to determine the cause of the cracking. Mold-related problems were investigated first because other less complicated slip cast parts did not exhibit the same behavior. Because of the geometric complexity of the scroll body, the mold is made up of 11 separate pieces. Five of these pieces form the inside core and must be removed at a precise point in time to prevent shrinkage cracks. In addition, the freshly cast scroll must release uniformly from all surfaces because of

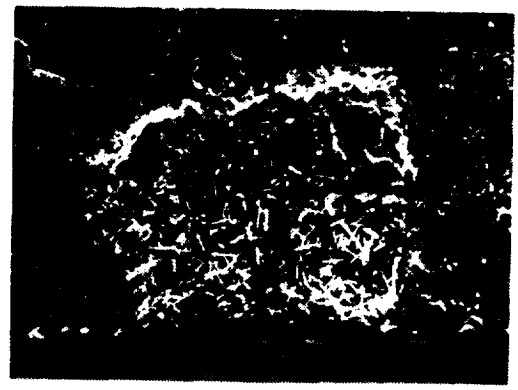

TE87-7421
429819

Figure 47. *Typical strength-controlling flaw (surface pore) observed in Kyocera SN270M Si_3N_4 test bars with an as-fired surface.*

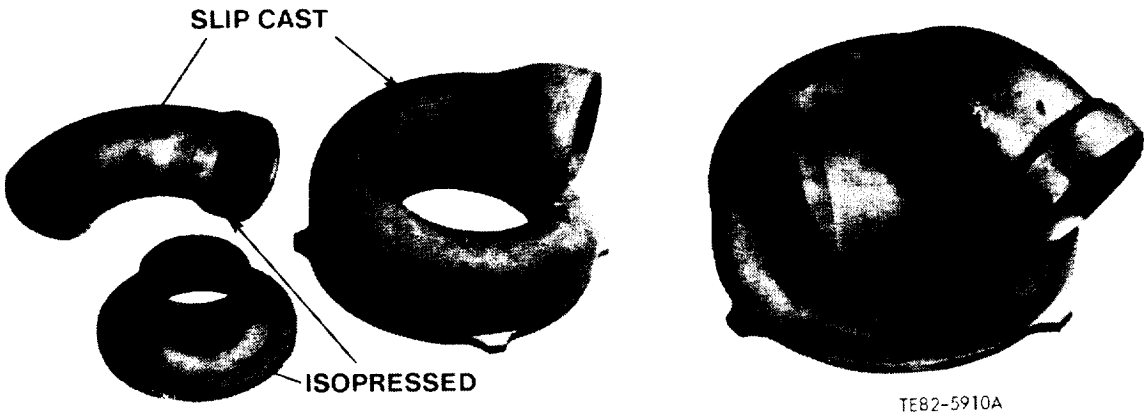

Figure 48. *Sohio sintered SiC gasifier turbine scroll assembly.*

the delicate nature of the casting. Changes with respect to the mold and its core design did not improve the casting yield. A similar result was found for modifications of the slurry. However, the use of a new powder lot virtually eliminated all demolding difficulties, and no sticking or slumping was observed in subsequent castings.

Initial efforts at assembly of the individual scroll components concentrated on the use of sequential sinter joining steps, shown in Figure 49. First, the fully sintered connecting duct and the green adapter sleeve were shrunk-fit together to form Subassembly I. A partially sintered shroud was then shrunk-fit onto this assembly to form Subassembly II, and a presintered scroll body and sleeve were shrunk-fit to Subassembly II to form the final scroll assembly. Due to shrinkage variations between the cast (11.0% shrinkage) and the isopressed components (17.5% shrinkage), the individual components could not be sintered as a green assembly. To accommodate this situation, the scroll bodies were partially sintered to approximately 75% of full density. A similar procedure was applied to the connecting duct/sleeve/shroud subassembly. In each case, the cast part was fully sintered before the respective isopressed components were shrunk-fit in a subsequent sintering operation.

The shrunk-fit scroll assemblies appeared visually to have an acceptable bond, but subsequent inspection revealed a deficiency in joint integrity. As a result, shrink-fitting the three-piece shroud/connecting duct assembly to the scroll body by itself was unsatisfactory, and a subsequent braze joint application was performed. The braze used a molybdenum disilicide ($MoSi_2$) braze material that had previously been observed to wet SiC material systems. The $MoSi_2$ braze powder was mixed with a wax to form a slurry that was applied to the joints of the shrunk-fit scroll assembly.

Because of the nonuniform fit between the scroll body and shroud after the shrink-fitting procedure, it was found necessary to fully sinter the

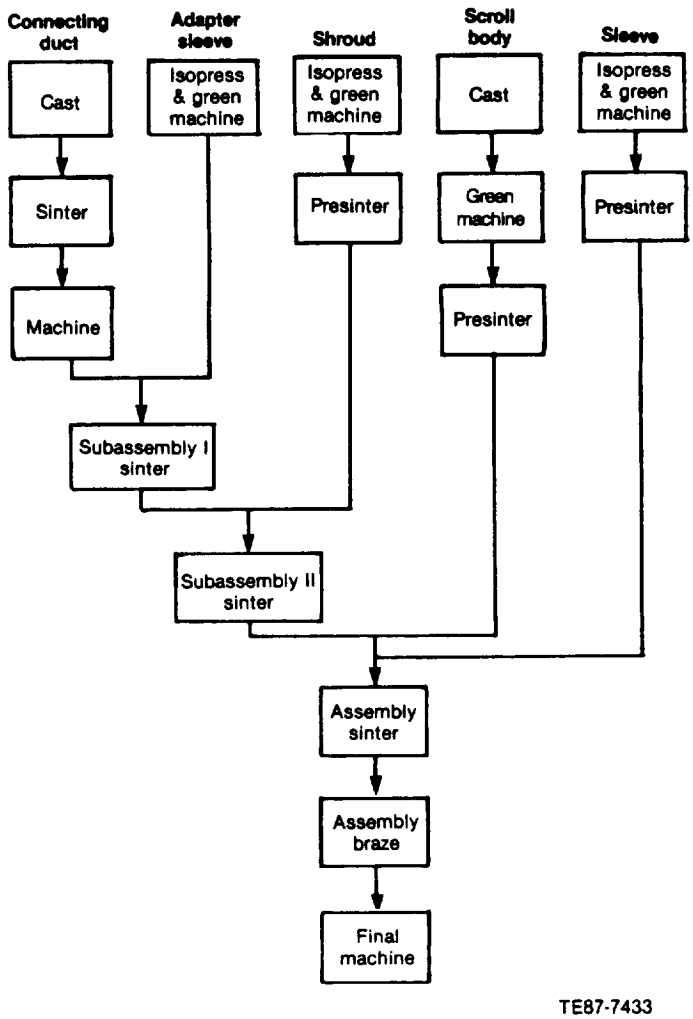

Figure 49. *Sohio sintered SiC gasifier scroll assembly flow chart.*

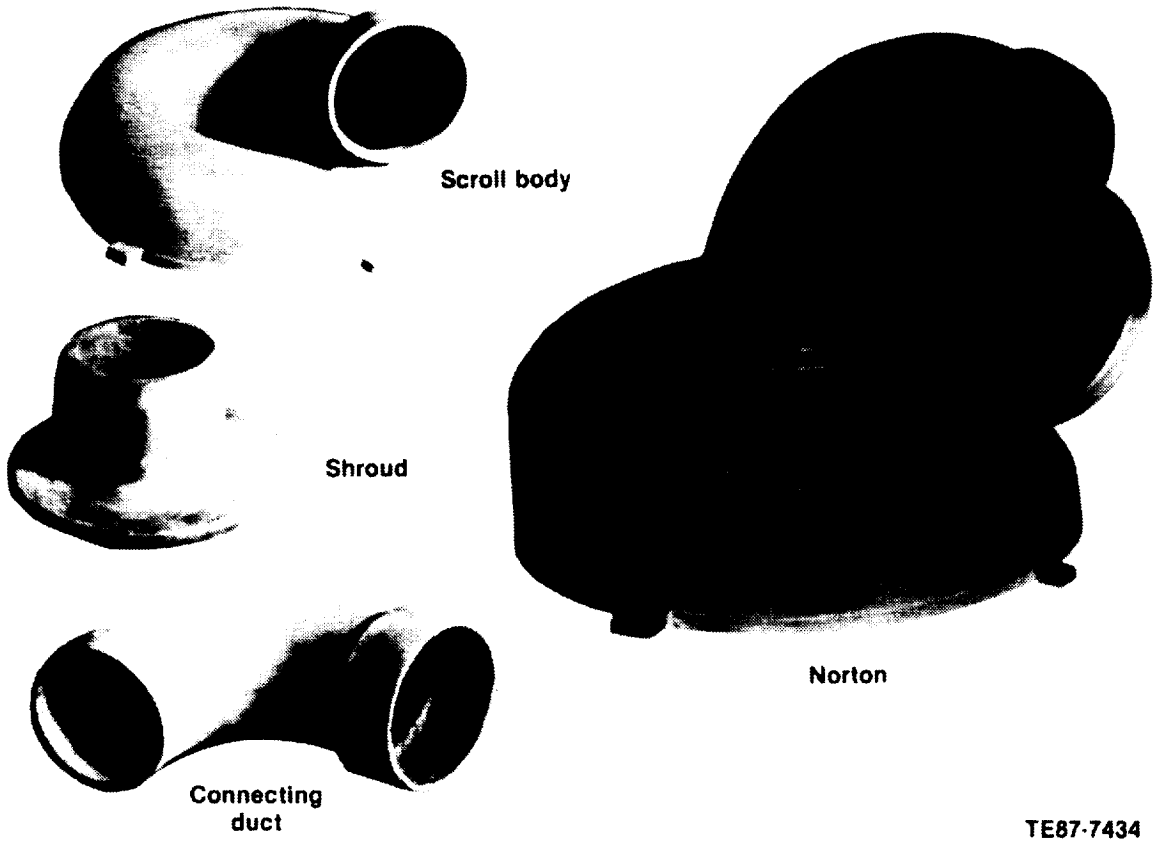

Figure 50. *Norton NC-430 SiC gasifier scroll assembly.*

scroll body and to machine both the scroll body and shroud mating surfaces prior to joining using only a braze process. Additional optimization of the brazing process resulted in improved ceramic/ceramic joints, with radiographic examination indicating approximately 75% braze coverage of the interface. Alternate braze materials, including a CrVTi braze developed at ORNL, were applied to the scroll joints and demonstrated improvements in wettability, uniformity of coverage, and oxidation resistance.

The gasifier turbine scroll assemblies fabricated by Sohio from SASC have demonstrated the capability of producing dimensionally sound components with strength and temperature characteristics to satisfy the RPD reliability requirements. However, significant improvements in the process yields of the individual components, particularly the slip cast scroll body, and improved dimensional control of the final assembly are required. Further development of suitable braze materials and joining methodology is also necessary.

Norton SiC Gasifier Turbine Scroll Assemblies

Ten gasifier turbine scroll assemblies were received from Norton and evaluated at Allison. These components, shown in Figure 50, were fabricated from NC-430, a SiSiC material system. The microstructure consists of a bimodal mixture of large (50–200 micron) and small (25 micron) SiC grains surrounded by a network of free silicon, as shown in Figure 51. The scroll assemblies consist of three separate slip cast components: a scroll body, shroud, and connecting duct. The individual parts are siliconized, machined to rough dimensions, and then joined together in a final siliconization procedure. The average density of the scroll assemblies measured 3.11 g/cm^3.

The qualification test bars accompanying these assemblies were evaluated to provide an estimate of the component strength characteristics and to determine the nature of the strength-controlling defects observed in this material. The average room temperature fracture strength of test bars with a machined surface condition measured 262.84 MPa (38.12 ksi). Machined bars tested at a temperature of 1250°C (2282°F) had an average strength of 212.99 MPa (30.89 ksi). Due to the coarse nature of the grain structure, establishing failure origins in this material with certainty is extremely difficult. The fractures, however, appeared to originate from the surface, presumably from the large SiC grains

that form during firing. The average strength of test bars with an as-fired surface condition was 223.60 MPa (32.43 ksi). Bars with an as-fired surface tested at a temperature of 1250°C (2282°F) had an average strength of 212.99 MPa (30.89 ksi). All fractures of these specimens again initiated from surface flaws. The fracture toughness (K_{IC}) of the Norton NC-430 SiC material measured 3.6 MPa$\sqrt{m}$ (3.3 ksi$\sqrt{in.}$) using SENB testing.

The slip cast NC-430 scroll assemblies received from Norton met all dimensional requirements with structurally sound joints. The material strength characteristics are sufficient to meet the design reliability requirements for steady-state operation. However, improvements in the strength properties are needed to satisfy the life requirements for transient engine operation.

Kyocera Silicon Nitride Turbine Scroll Assemblies

A total of 12 turbine scroll assemblies (six gasifier turbine and six power turbine) were received from Kyocera and evaluated at Allison. These components, shown in Figure 52, were fabricated of SN250 SSN. The gasifier turbine scroll assemblies consist of four individual components: a slip cast scroll body, connecting duct (slip cast), combustor inlet (slip cast), and a shroud (isostatic pressed and green machined). The power turbine scroll assembly is comprised of three separate pieces: a slip cast scroll body, an isostatic pressed shroud, and an isostatic pressed sleeve. Each of the individual components were sintered to full density, machined, and then joined into the assembly by a brazing operation. The braze material used by Kyocera was a silicon-based material. Tests were conducted by Kyocera to evaluate the strength of the braze joints using flexural test bars with a brazed butt joint. The average room temperature joint strength was 183.41 MPa (26.6 ksi), with a strength of 171.00 MPa (24.8 ksi) measured at a temperature of 1300°C (2372°F). The room temperature strength of the brazed joint after exposure at 1370°C (2500°F) for 100 hr was 171.00 MPa (24.8 ksi).

The material strength characteristics of the isopressed SN250 Si_3N_4 material were evaluated. These results are summarized in Table XIV. The microstructure, shown in Figure 53, is comprised of relatively uniform beta-Si_3N_4 grains on the order of 0.5 microns in diameter, with a few larger beta-Si_3N_4 grains. The intergranular phase was determined to be primarily a glass; however, some isolated pockets were observed to contain a fine-grained polycrystalline structure with grains 20–40 nm in diameter. The average density of this material measured 3.38 g/cm^3. The average room temperature strength of test bars with a machined surface condition was 748.66 MPa (108.58 ksi). Machined bars tested at a temperature of 1000°C (1832°F) had an average strength of 493.20 MPa (71.53 ksi) and a strength of 559.18 MPa (81.10 ksi) at a temperature of 1150°C (2102°F). The typical strength-controlling

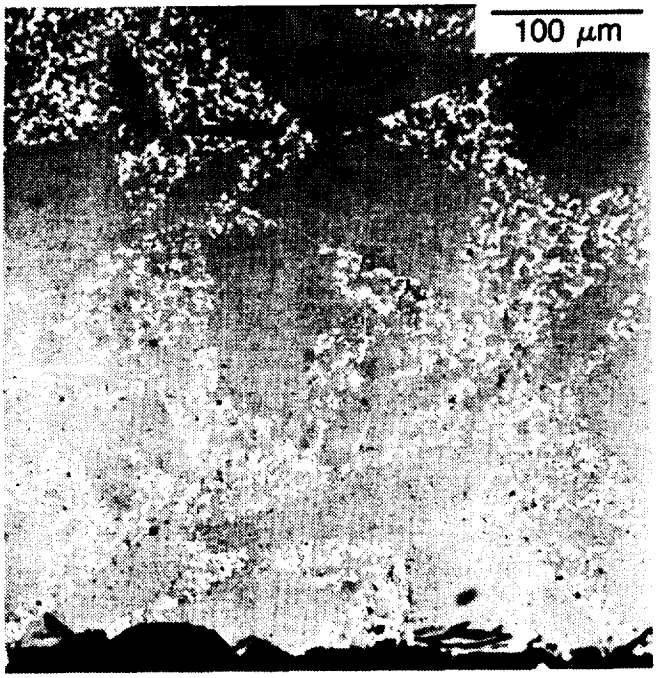

Figure 51. *Microstructure of Norton NC-430 SiSiC.*

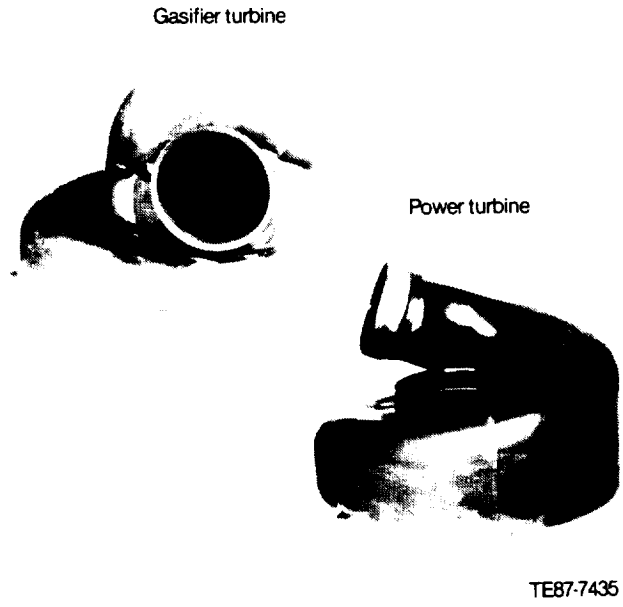

Figure 52. *Kyocera SN250 Si_3N_4 turbine scroll assemblies.*

Table XIV.
Strength characteristics of isostatic pressed Kyocera SN250 Si_3N_4.

Temperature—°C (°F)	Strength—MPa (ksi)	
	Machined	As fired
Room	748.66 (108.58)	475.27 (68.93)
1000 (1832)	493.20 (71.53)	477.89 (69.31)
1150 (2102)	559.18 (81.10)	478.31 (69.37)

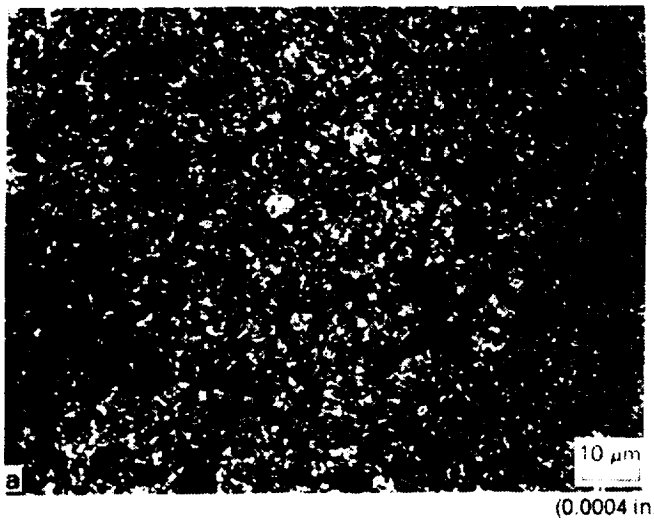

TE87-7438
430489

Figure 53. *Microstructure of isopressed Kyocera SN250 Si_3N_4.*

flaws observed in the machined test bars were small pores, shown in Figure 54. The average room temperature fracture strength of test bars with an as-fired surface condition was 475.27 MPa (68.93 ksi). The strength of the as-fired bars tested at a temperature of 1000°C (1832°F) was 477.89 MPa (69.31 ksi), with an average strength of 478.31 MPa (69.37 ksi) measured at 1150°C (2102°F). The typical fracture origins observed in the as-fired test bars were surface depressions and pores, as shown in Figure 55.

The gasifier and power turbine scroll assemblies made by Kyocera of the SN250 Si_3N_4 material met all structural and dimensional requirements. Based on the strength characteristics generated for qualification test bars, both scroll assemblies would satisfy the RPD reliability goals. However, engine testing of a Kyocera gasifier turbine scroll assembly resulted in the failure of the scroll from a pre-existing flaw in the braze joint, indicating a need for improvements in the braze joining material and processing. In addition, significant increases in process yields are required for production of cost-effective components.

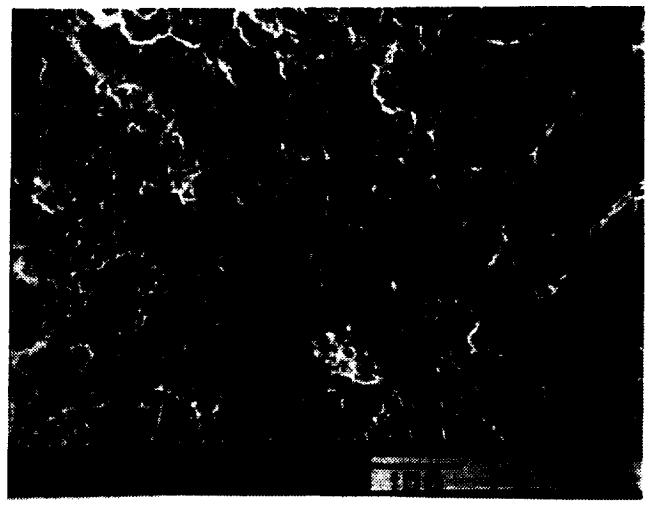

TE87-7436
430493

Figure 54. *Typical fracture origin (internal pore) observed in Kyocera SN250 Si_3N_4 test bars with a machined surface.*

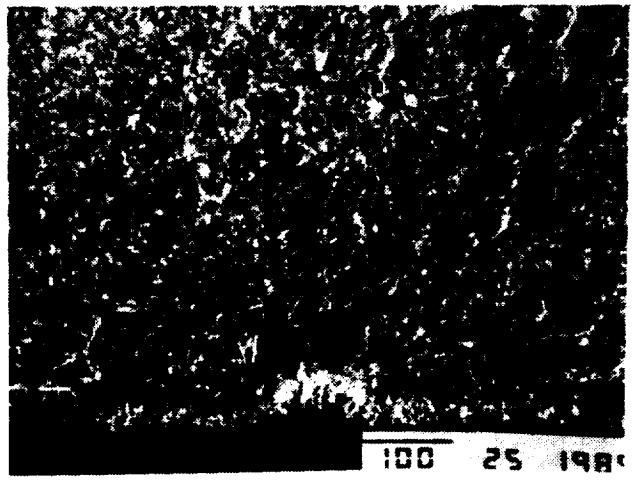

TE87-7437
430490

Figure 55. *Typical fracture origin (surface depression/pore) observed in as-fired Kyocera SN250 Si_3N_4.*

2.4 CERAMIC COMPOSITE DEVELOPMENT

Structural ceramic materials offer numerous potential benefits for use in AGT engines. These properties include excellent high temperature strength, oxidation/corrosion resistance, thermal shock capability, and low density and thermal expansion characteristics. However, current monolithic ceramics have major limitations, particularly for rotating components, due to their inherent brittleness and low fracture toughness. The development of ceramic composite material systems, using a variety of ceramic reinforcement media (particles, whiskers, and continuous fibers) in conjunction with a ceramic matrix, have demonstrated the potential for substantial improvements in fracture toughness, strength, and strain tolerance. The key processing issue with these composites is to create weak but stable interfacial regions between the reinforcement and matrix, so that high toughness is attained through crack deflection, debonding, and fiber pullout mechanisms.

Ceramic composite material systems evaluated in the AGT 100 program have used reinforcement with SiC whiskers, SiC fibers, and TiB_2 particulates in glass-ceramic, SiC, and Si_3N_4 matrices. The activity at Corning has focused on the development and fabrication of ceramic composite inner backplates. A variety of glass-ceramic matrices have been used in conjunction with both SiC whisker and SiC fiber reinforcements. Efforts at SEP have concentrated on continuous SiC fiber reinforcement in a chemical vapor infiltration (CVI)-applied matrix of SiC. Both combustor bodies and flexural test specimens, fabricated of the CERASEP SiC/SiC material, were received and evaluated. Injection-molded test specimens were received from Sohio fabricated of SASC reinforced with TiB_2 particles. In addition, hot pressed Si_3N_4 specimens reinforced with SiC whiskers were fabricated by Boride Products/Dow Chemical and characterized. These efforts are summarized in the following subsections.

Corning Glass—Reinforced Glass Composites

Component development activities at Corning have continued to address the development and fabrication of advanced ceramic composite material systems for the gasifier turbine inner backplate. Both SiC fibers (Nicalon) and SiC whiskers (Arco and Avco) have been used as reinforcements in a variety of glass-ceramic matrices.

To evaluate material strength characteristics, standard-size (50.8 mm × 6.35 mm × 3.18 mm [2 in. × 0.25 in. × 0.125 in.]) test bars were sectioned from two SiC whisker reinforced inner backplates: one with a magnesium aluminosilicate (MAS-I) glass-ceramic matrix (P/N AA101356, S/N KX19318) and one CAS-II (calcium aluminosilicate) matrix backplate (P/N AA101453, S/N 12.3). The typical microstructure of these material systems is shown in Figure 56. Both inner backplates, shown in Figure 57, were fabricated by hot pressing and contain approximately 30 weight percent SiC whiskers, with the MAS-I using Arco Silar SC-9 whiskers and the CAS-II using Avco/Tokai Tokomak whiskers. The Arco whiskers are primarily alpha-SiC while the Avco/Tokai whiskers consist primarily of beta-SiC. Typical properties of these whiskers are summarized in Table XV.

The average density of the SiC whisker reinforced MAS-I material measured 2.794 g/cm^3. All bars were tested with a machined tensile surface condition. The average room temperature flexural strength was 295.24 MPa (42.82 ksi). The typical strength-controlling defects were surface pores, Figure 58. The strength of bars tested at a temperature of 1000°C (1832°F) averaged 218.16 MPa (31.64 ksi). Surface pores were again observed as the primary

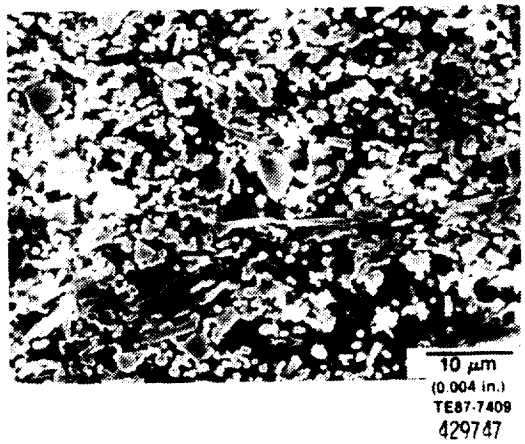

Figure 56. *Typical microstructure of Corning MAS-I and CAS-II glass-ceramic composite inner backplates with SiC whiskers.*

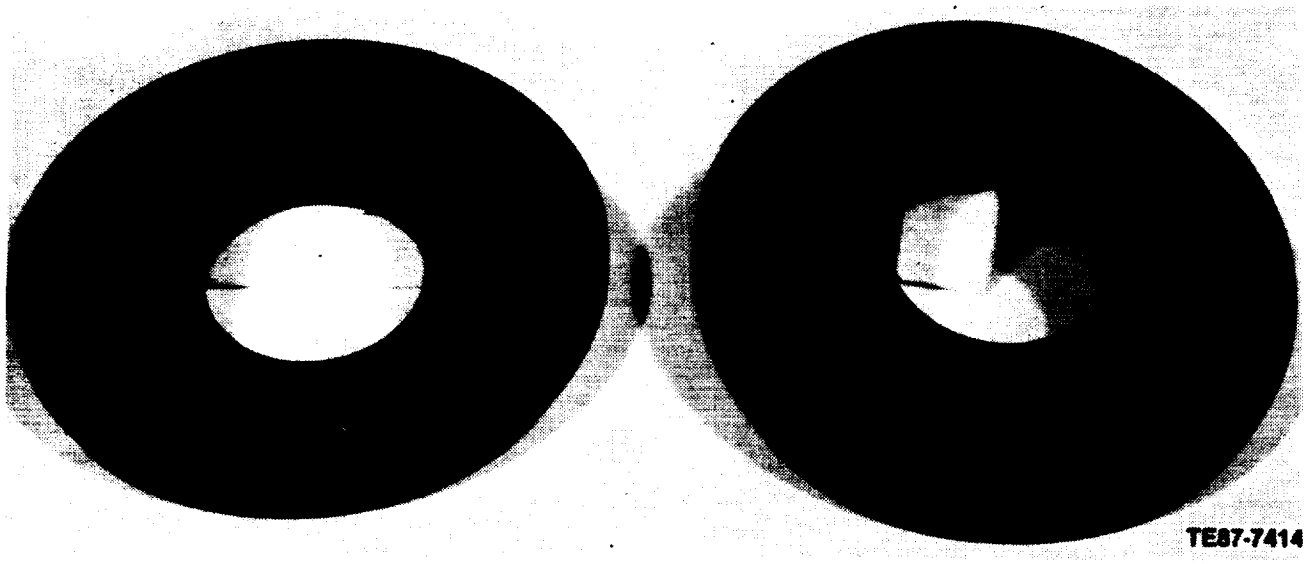

Figure 57. *Corning glass-ceramic/SiC whisker-reinforced composite inner backplates.*

Table XV.
Typical properties of SiC whiskers used in Corning ceramic composite inner backplates.

	Arco	Avco/Tokai
Diameter—microns	0.6	0.1–0.5
Length—microns	10–80	50–200
Tensile strength—MPa (ksi)	7000–12000 (1000–1800)	3500–1400 (500–2000)
Tensile modulus—GPa (msi)	700 (100)	420–700 (60–100)

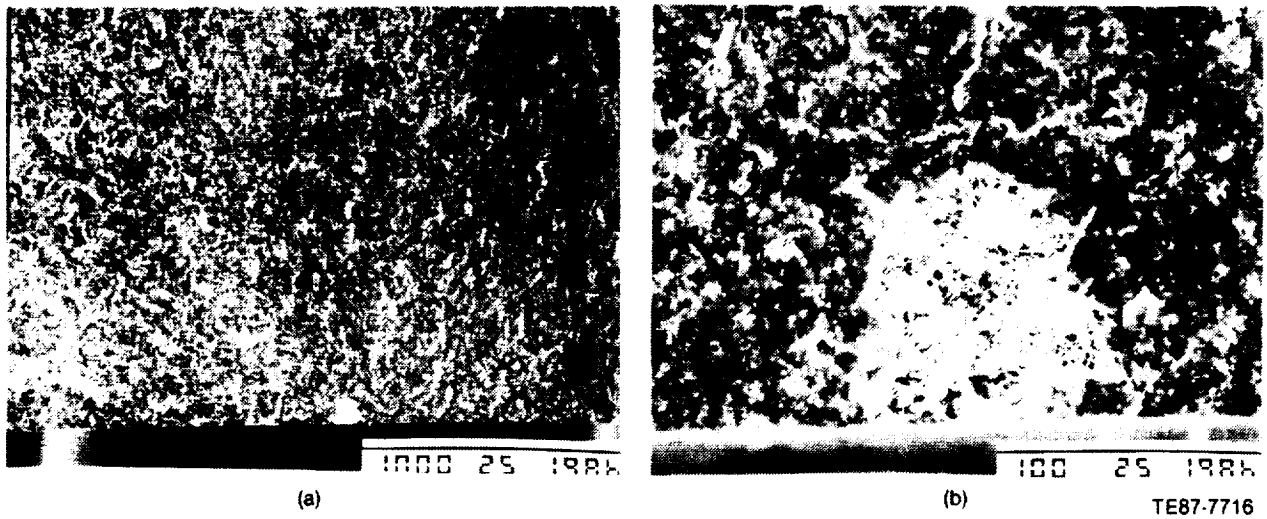

Figure 58. *Typical strength-controlling defect (surface pore) observed in bars cut from Corning MAS-I SiC whisker-reinforced inner backplate tested at room temperature.*

fracture origins, Figure 59. The average strength of material tested at 1150°C (2102°F) was 159.96 MPa (23.20 ksi). The strength-controlling defects observed for material tested at this temperature were surface pores that exhibited significant levels of oxidation, shown in Figure 60.

The test bars cut from the SiC whisker reinforced CAS-II inner backplate had an average density of 2.910 g/cm^3. The average room temperature flexural strength measured 398.05 MPa (57.73 ksi).

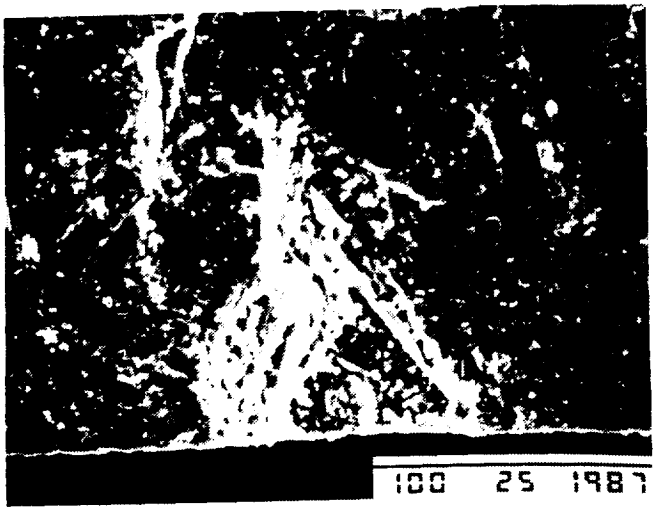

Figure 59. *Surface pore found to be primary fracture origin in Corning MAS-I material tested at 1000°C.*

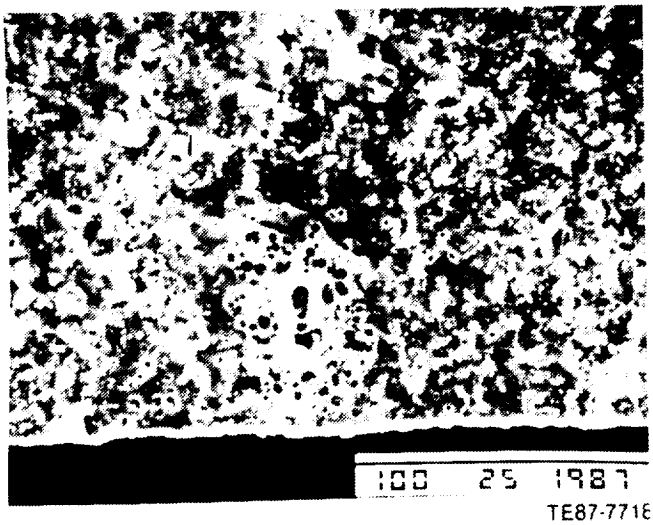

Figure 60. *Typical strength-controlling defect (oxidized surface pore) observed in Corning MAS-I material tested at 1150°C.*

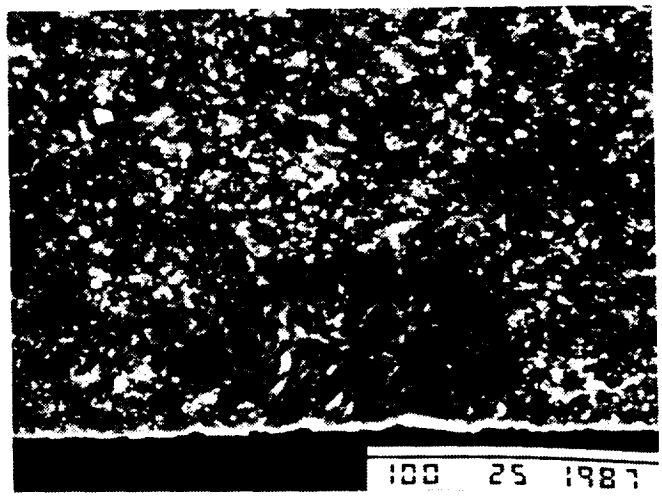

Figure 61. *Typical fracture origin (inclusion composed of calcium, aluminum, and silicon) observed in test bars cut from Corning CAS-II SiC whisker-reinforced inner backplate.*

Bars tested at a temperature of 1000°C (1832°F) had an average strength of 319.31 MPa (46.31 ksi). The average strength of bars tested at 1150°C (2102°F) was 254.22 MPa (36.87 ksi). The typical strength-controlling fracture origins were observed to be surface and internal inclusions, composed primarily of agglomerates of calcium, aluminum, and silicon (Figure 61). The fracture toughness of this material measured 4.1 MPa$\sqrt{m}$ (3.7 ksi$\sqrt{in.}$) using the SENB method.

Corning has also been actively pursuing the development of glass-ceramic inner backplates using fiber reinforcement. Three glass-ceramic matrices have been utilized for the fibrous composite backplates: LAS (lithium aluminosilicate), BMAS (barium magnesium aluminosilicate), and CAS (calcium aluminosilicate). These composite backplates, shown in Figure 62, contain approximately 30–40 volume percent Ceramic Grade Nicalon 102 SiC fibers from Nippon Carbon. The Nicalon fiber is manufactured through pyrolysis of polycarbosilane. It is not comprised of stoichiometric SiC, but has a composition which is more accurately described as Si_3C_4O, i.e., it contains excess carbon and oxygen. The fibers are essentially amorphous with homogeneously distributed ultrafine (25 angstrom) beta-SiC crystals. The low density of the fibers relative to that of pure beta-SiC (2.6 g/cm^3 versus 3.2 g/cm^3) is consistent with a chemical composition of approximately 60% SiC,

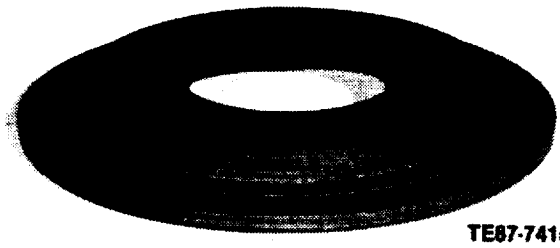

TE87-7415

Figure 62. *Corning glass-ceramic/SiC fiber-reinforced composite inner backplate.*

Table XVI.
Typical properties of Nicalon SiC fiber.

Average filament diameter	15 microns
Filaments/tow	500
Density	2.6 g/cm
Tensile strength—MPa (ksi)	2100–3150 (300–450)
Tensile modulus—GPa (msi)	170–210 (25–30)
Average strain to failure	1.5%
Thermal expansion coefficient	3.1 × 10^{-6} in./in./°C

30% amorphous SiO_2, and 10% amorphous carbon, by weight. Typical properties of the Nicalon fibers are summarized in Table XVI.

The fabrication of the fiber reinforced glass-ceramic composite backplates consists of three stages. In the first stage, called prepregging, the fibers are passed through a slurry of powdered glass suspended in water, wound on a faceted drum, and allowed to dry in sheets. The second stage, layup, consists of cutting the prepreg sheets into the desired geometry and stacking them to obtain the desired fiber orientation (42 layers of 0°/±45°/90° or 0°/90° for the inner backplates). Consolidation is the final stage of composite fabrication, involving hot pressing the prepreg and machining to required dimensions. The microstructure of the SiC fiber reinforced composite inner backplates is shown in Figure 63.

To evaluate material strength characteristics, test bars measuring 69.85 mm × 3.18 mm × 2.54 mm (2.75 in. × 0.125 in. × 0.10 in.) were machined from two BMAS-II composite billets, one with fibers oriented unidirectionally (0°) and the other with a 0°/90° fiber orientation. Bars from each billet were tested in three-point bending with a test span of 50.8 mm (2.0 in.), corresponding to a test span to specimen depth ratio of 20:1. The results of the flexural testing are summarized in Table XVII.

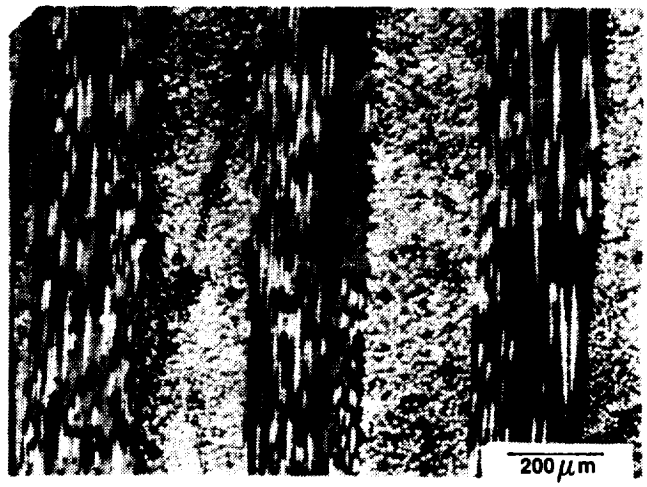

TE87-7422

Figure 63. *Microstructure of Corning glass-ceramic composite inner backplates reinforced with SiC fibers.*

Table XVII.
Flexural strength of Corning BMAS-II SiC fiber reinforced composite material.

Temperature—°C (°F)	Fracture strength—MPa (ksi) Unidirectional	0/90° orientation
Room	802.10 (116.33)	369.37 (53.57)
900 (1652)	546.50 (79.26)	202.16 (29.32)
1000 (1832)	—	221.40 (32.11)
1100 (2012)	473.76 (68.71)	200.44 (29.07)
1200 (2192)	—	238.29 (34.56)

The average room temperature strength of the unidirectional test bars measured 802.10 MPa (116.33 ksi). The typical fracture mode observed was pullout of the SiC fibers from the BMAS matrix, shown in Figure 64. Test bars with a 0°/90° fiber orientation exhibited an average room temperature strength of 369.37 MPa (53.57 ksi). The fracture mode of the 0°/90° test bars was observed to be both brittle and fibrous. Scanning electron microscope (SEM) fractographs, shown in Figure 65, indicated that brittle fractures developed in the matrix phase, along with fibers of 0° orientation pulling out of the BMAS matrix. The average strength of the unidirectional fiber test bars decreased from the room temperature value of 802.10 MPa (116.33 ksi) to 546.50 MPa (79.26 ksi) at a temperature of 900°C (1652°F) and 473.76 MPa (68.71 ksi) at 1100°C (2012°F). Test material with a 0°/90° fiber architecture had an average strength of 202.16 MPa (29.32 ksi) at a temperature of 900°C (1652°F), 221.40 MPa (32.11 ksi) at 1000°C (1832°F), 200.44 MPa (29.07 ksi) at 1100°C (2012°F), and 238.29 MPa (34.56 ksi) at 1200°C (2192°F). The dominant failure mechanism in the specimens tested at elevated temperature was observed to be brittle fracture along the tensile surface with fiber pullout at the center of the specimens, shown in Figure 66.

The glass/ceramic composite material systems and hot pressed processing methods developed by Corning have resulted in the fabrication of reinforced turbine inner backplates which have demonstrated substantial improvements in strength and fracture toughness. Additional improvements in the temperature capability and time-dependent characteristics of both the ceramic reinforcement and matrix material systems are required to meet the RPD life and reliability goals. Improvements in the fabrication processing are also needed for more cost-effective, near net-shape component fabrication.

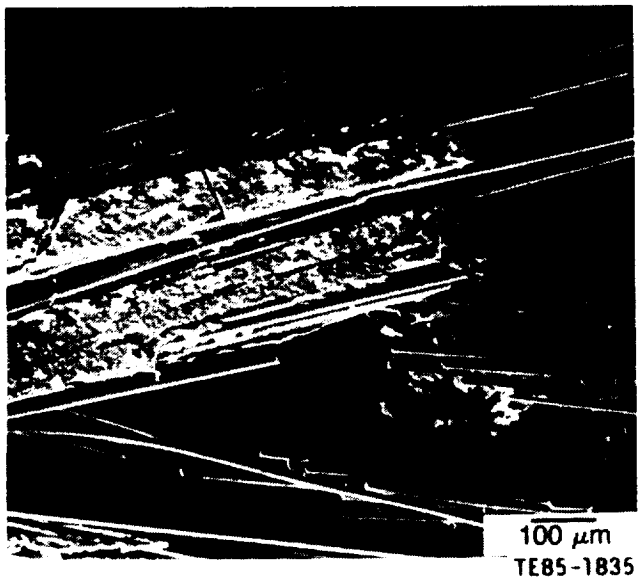

Figure 64. *Fracture surface of Corning BMAS-II SiC fiber-reinforced glass-ceramic composite test bars with unidirectional fiber orientation; fracture mode is fiber pull-out from BMAS matrix.*

Société Européene de Propulsion SiC/SiC

Flexural test specimens were received from SEP, fabricated of CERASEP SiC/SiC ceramic composite material. This material consists of Nicalon 102 SiC fibers in a CVI applied matrix of beta-SiC. The material is toughened by developing a weak interfacial bond between the SiC fiber and the first CVI SiC layer. The test specimens were rectangular beams measuring 69.85 mm × 3.18 mm × 2.54 mm (2.75 in. × 0.125 in. × 0.1 in.) and consisted of a 2-D laminate structure using an eight-ply balanced plain weave with a 0°/90° fiber architecture. The approximate fiber percentage was 40% by volume. The microstructure of this material is shown in Figure 67. The average density of the specimens measured 2.5 g/cm^3.

Evaluation of the mechanical strength characteristics of this material were conducted in three-point MOR testing with a 50.8 mm (2 in.) outer span and a load rate of 15.2 mm/min (0.6 in./min). All testing was conducted in an air atmosphere. The average room temperature flexural strength was 516.09 MPa (74.85 ksi). The typical fracture origins,

Figure 65. *Fracture surface of Corning BMAS-II fiber-reinforced glass ceramic composite test bars with SiC fibers in 0/90°orientation; fracture mode consists of both brittle fracture and fiber pull-out.*

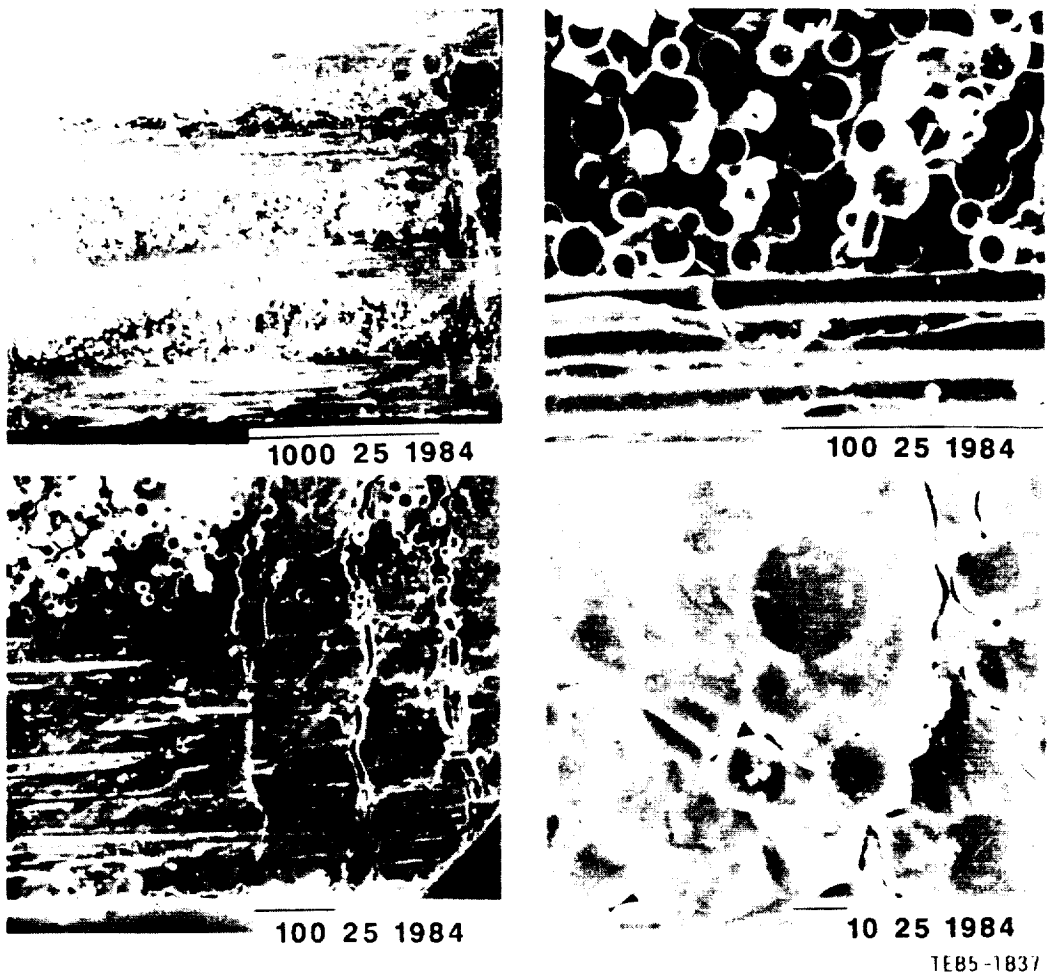

Figure 66. *Typical fracture surfaces observed in Corning BMAS-II/SiC composite bars with 0/90° orientation tested at 900°C (1652°F).*

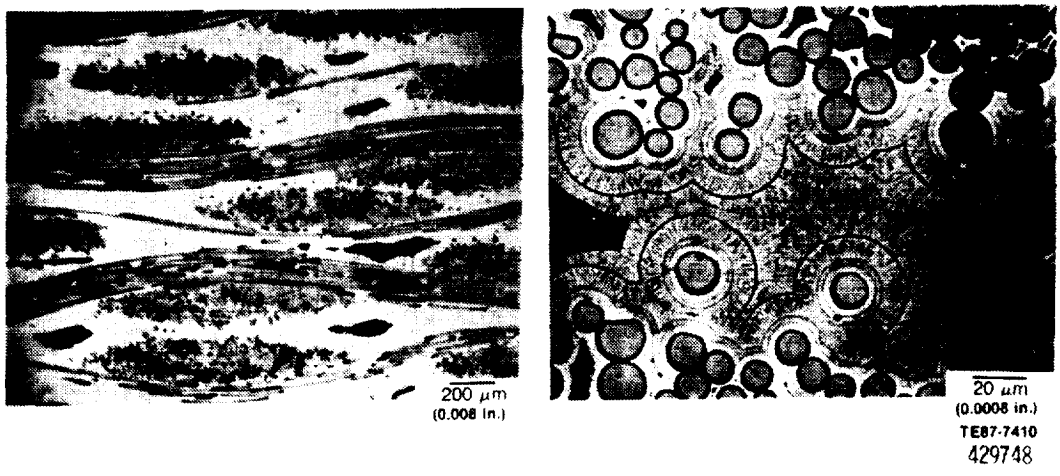

Figure 67. *Microstructure of SEP SiC/SiC fiber-reinforced ceramic composite material.*

shown in Figure 68, were fibrous in nature with fiber pull-out observed as the primary fracture mechanism. The strength at a temperature of 1000°C (1832°F) averaged 420.18 MPa (60.94 ksi). The fracture origins were again fibrous in nature, Figure 69. Specimens tested at 1150°C (2102°F) had an average strength of 283.73 MPa (41.15 ksi). Fiber pull-out was the dominant fracture mechanism, shown in Figure 70, although the length of the fractured fibers was shorter in the elevated temperature tests, which indicates some degree of fiber or fiber/matrix interface oxidation and embrittlement.

Allison also received two SiC/SiC ceramic composite combustor bodies from SEP, sized for the AGT 100 engine, which were purchased and evaluated through an internally funded program. The combustor bodies, shown in Figure 71, were fabricated of CERASEP SiC/SiC and consisted of Nicalon 102 SiC fibers which are filament-wound into the preform shape and processed with a CVI-applied matrix of SiC. The dilution holes were ultrasonically machined into the component after processing. One of the SEP combustor bodies underwent extensive testing and evaluation in the Allison AGT 100 combustor rig test facility. Initially, two thermal cycles on the combustor start nozzle were run, consisting of lighting-off at a BOT of 900°C (1652°F), with a total burn time of 25 min. Nondestructive inspection revealed no apparent distress to the component. Following this testing, a total of three thermal cycles on the combustor main nozzle system were run to average BOT levels of 1080°C (1976°F), 1204°C

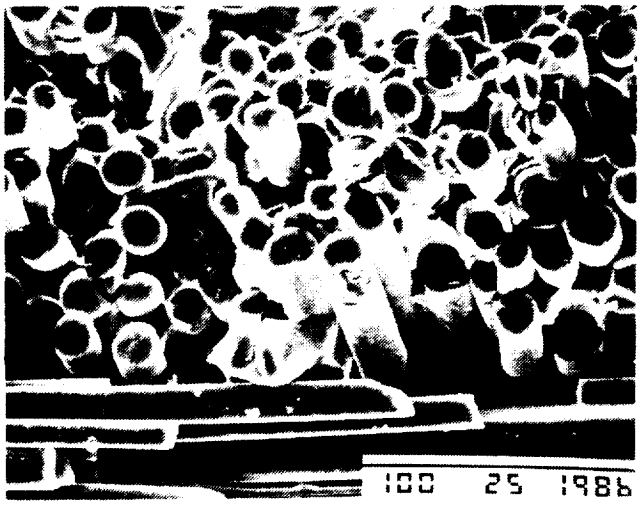

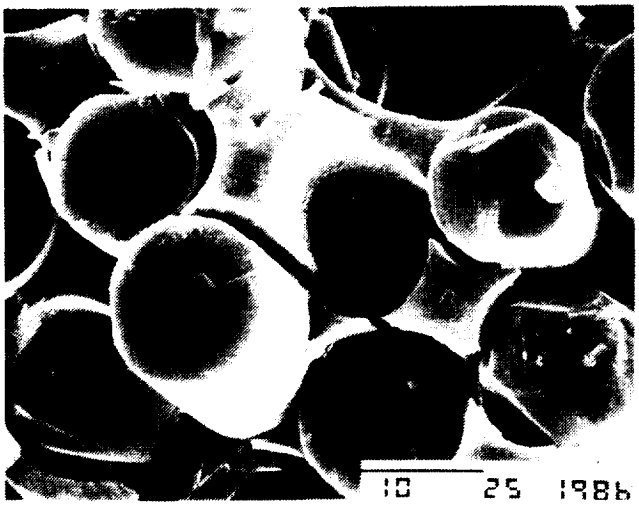

Figure 68. *Fracture surface of SEP SiC/SiC ceramic composite material broken at room temperature. Fiber pull-out was the primary fracture mechanism.*

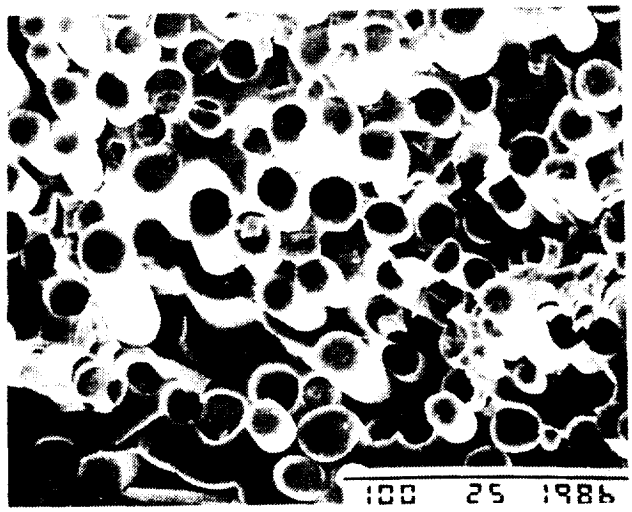

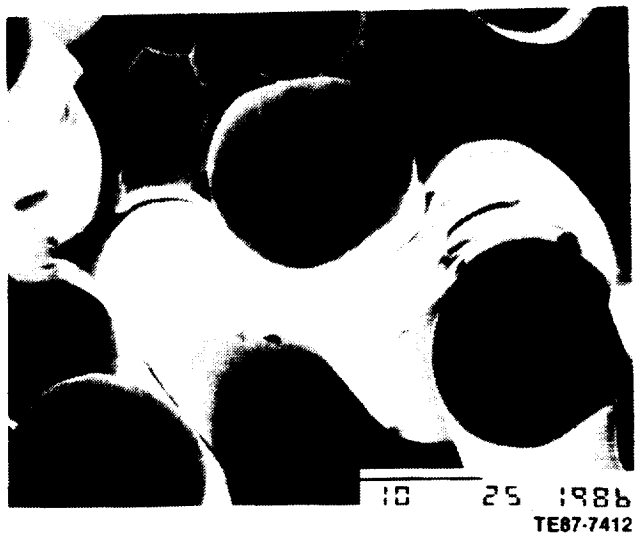

Figure 69. *Fracture surface of SEP SiC/SiC tested at 1000°C.*

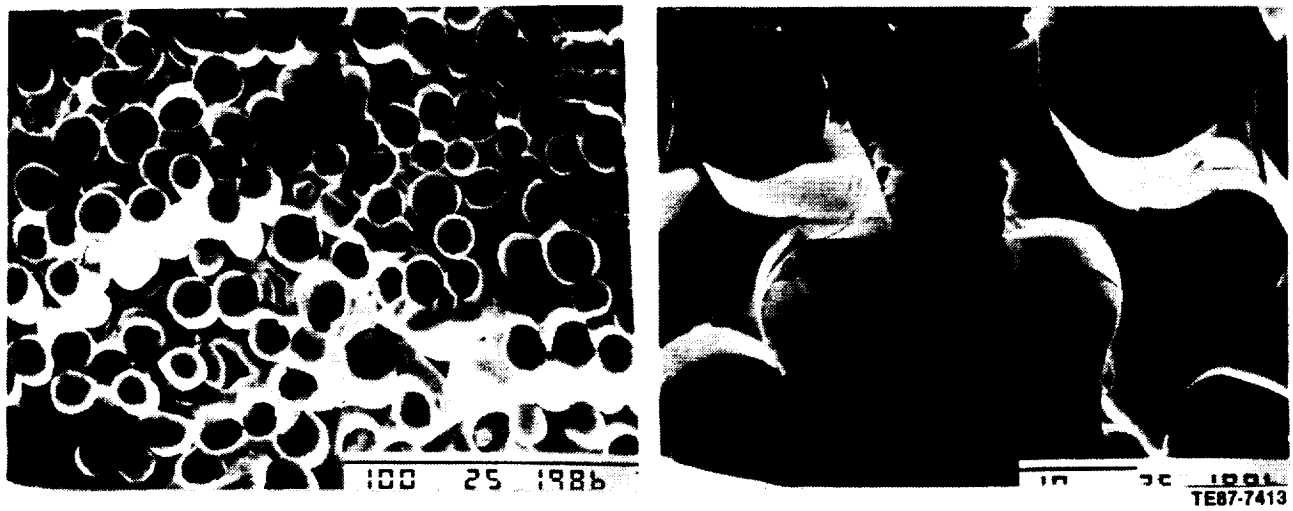

Figure 70. *Fracture surface of SEP SiC/SiC material tested at a temperature of 1150°C.*

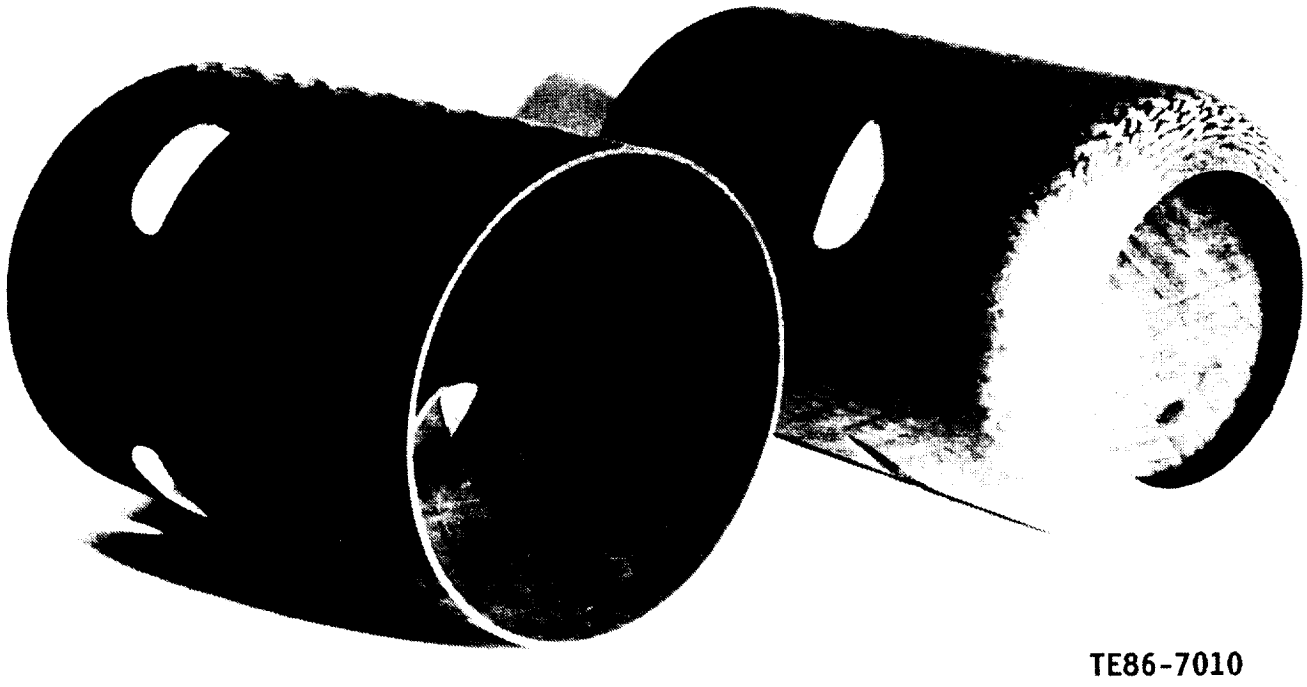

Figure 71. *SEP SiC/SiC ceramic composite combustor bodies.*

(2200°F), and 1288°C (2350°F), respectively, with a 1-hr hold time at each of the maximum temperatures. Inspection of the combustor at the conclusion of this testing again revealed no indication of flaws or material degradation. Following this testing, a total of 20 hr were successfully accumulated using the main nozzle at an average BOT of 1204°C (2200°F). At the conclusion of this testing, inspection of the combustor revealed evidence of local oxidation and minor deposits (primarily silica) at the inside diameter of the component, in addition to minimal spalling of material at these locations (see Figure 72). However, the combustor body was judged to be in satisfactory condition and suitable for continued testing.

Sohio SiC/Titanium Diboride

Sohio has been actively pursuing the development of toughened SiC-based material systems. The prime approach has been the addition of titanium diboride (TiB_2) particles as a means of reinforcing

SASC. The SiC/TiB_2 composite is obtained by pressureless sintering a mixture of fine SiC and TiB_2 powders which are compacted and shaped by conventional forming methods, including injection molding and isostatic pressing. The resulting microstructure contains discrete TiB_2 particles distributed uniformly throughout the SiC matrix. Little chemical interaction with some microcracking is observed at the SiC/TiB_2 interface, resulting in crack deflection as the dominant toughening mechanism. Analysis of the fracture surfaces and microstructure by Sohio clearly show the deflection of the cracks by the second phase TiB_2 particles in the SiC matrix, Figure 73. The development of residual stresses around the particulate inclusions (due to thermal expansion mismatch between the matrix and the particles) also contributes to the improved fracture toughness.

Figure 72. *Deposits on SEP SiC/SiC combustor body after rig testing at 1204°C BOT for 20 hr.*

Evaluation of injection-molded SASC test bars reinforced with approximately 15 weight percent TiB_2 particles was conducted at Allison. The average density of this material measured 3.34 g/cm^3. The room temperature fracture strength of bars with a machined tensile surface condition averaged 350.89 MPa (50.89 ksi). The primary strength-controlling flaws were observed to be surface and internal porosity, shown in Figure 74. The average room temperature strength of material with an as-fired surface condition measured 377.57 MPa (54.76 ksi). The primary fracture origins were surface cracks, Figure 75. The average fracture strength of machined bars tested at a temperature of 1250°C (2282°F) was 284.49 MPa (41.26 ksi). Bars with an as-fired surface had an average strength of 336.41 MPa (48.79 ksi) at a temperature of 1250°C (2282°F). Both sets of bars tested at elevated temperature were observed to have extensive oxidation on the fracture surfaces, Figure 76. A strength increase was observed for bars thermally exposed in air at 1250°C (2282°F) for 24 hr and tested at room temperature. The average strength of material with a machined surface increased to 395.36 MPa (57.34 ksi), with a strength of 402.25 MPa (58.34 ksi) measured for bars with an as-fired surface. Fracture origins for the bars were observed to be surface and internal porosity, Figure 77. The fracture toughness (SENB) of the SiC/TiB_2 material was 4.2 MPa$\sqrt{m}$ (3.8 ksi$\sqrt{in.}$), a 30% increase over the toughness of 3.1 MPa$\sqrt{m}$ (2.8 ksi$\sqrt{in.}$) measured for unreinforced SASC.

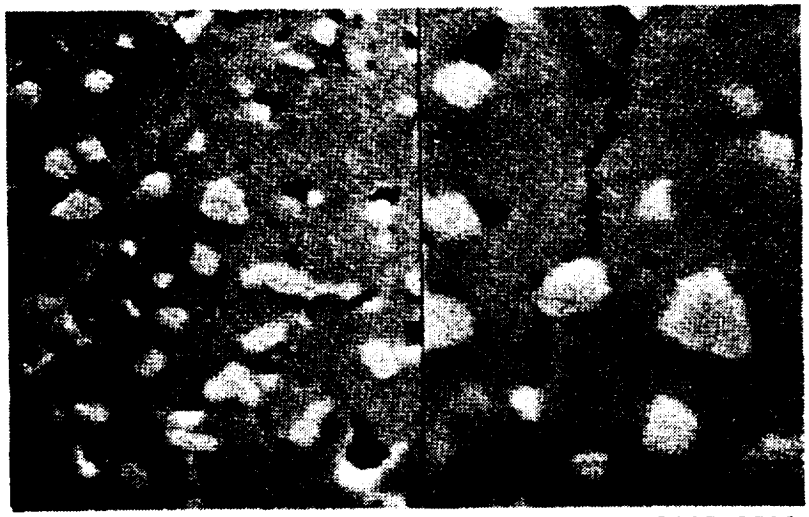

Figure 73. *Fracture surface of Sohio SiC/TiB_2 material showing toughening mechanism (crack deflection).*

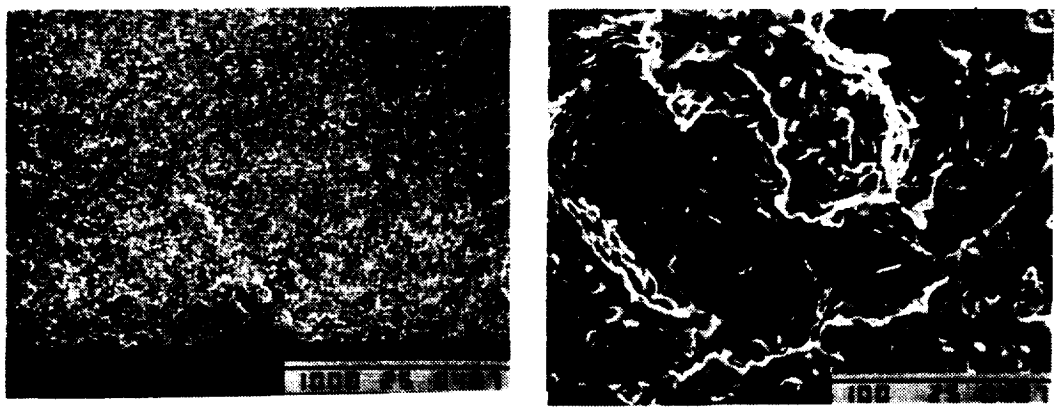

TE87-7416

Figure 74. *Typical strength-controlling defect (internal pore) observed in machined Sohio SiC/TiB_2 test bars.*

TE87-7417

Figure 75. *Primary fracture origin (surface crack) observed in Sohio SiC/TiB_2 tested with an as-fired surface.*

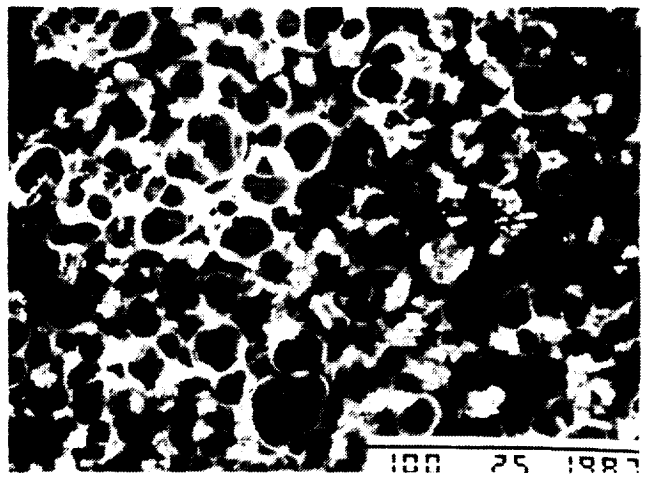

TE87-7418

Figure 76. *Oxidation of Sohio SiC/TiB_2 after flexural test at 1250°C.*

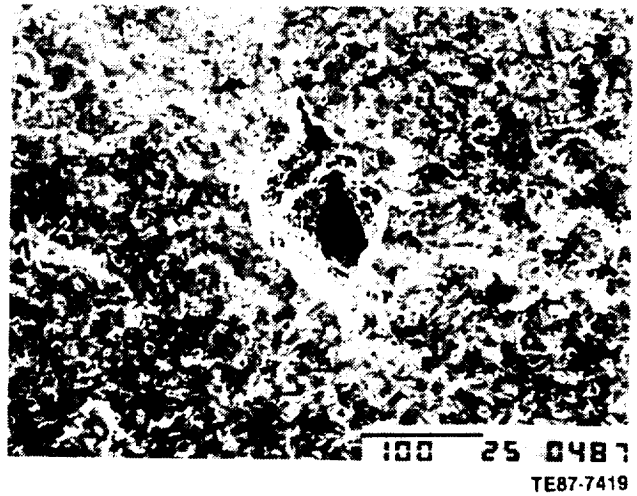

TE87-7419

Figure 77. *Typical fracture origin (internal pore) observed in Sohio SiC/TiB_2 exposed at 1250°C for 24 hr in air.*

Boride Products/Dow Chemical Silicon Nitride/SiC Whiskers

Test material was received and evaluated from Boride Products, a wholly-owned manufacturing subsidiary of the Dow Chemical Company. The material consisted of a Si_3N_4 matrix, originally developed for cutting tool applications, reinforced with 34 weight percent Tateho SiC whiskers. The test material was fabricated by hot pressing at a temperature of 1750°C (3182°F) and a pressure of 27.6 MPa (4 ksi). The microstructure of this material

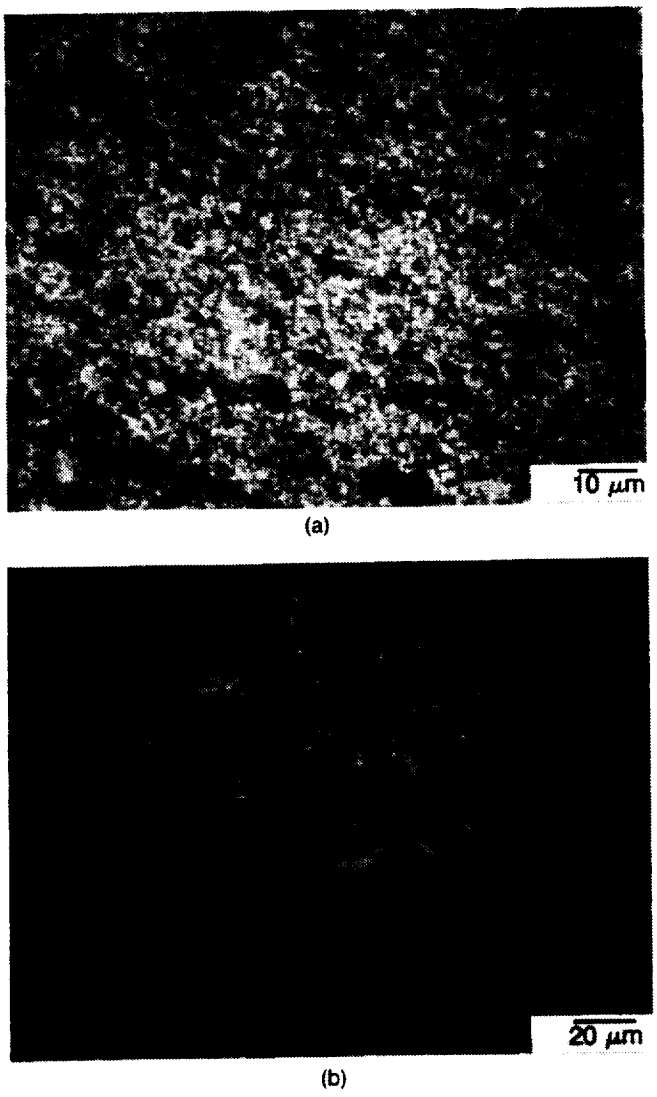

Figure 78. *Microstructure of Boride Products Si_3N_4 material with 34% SiC whiskers.*

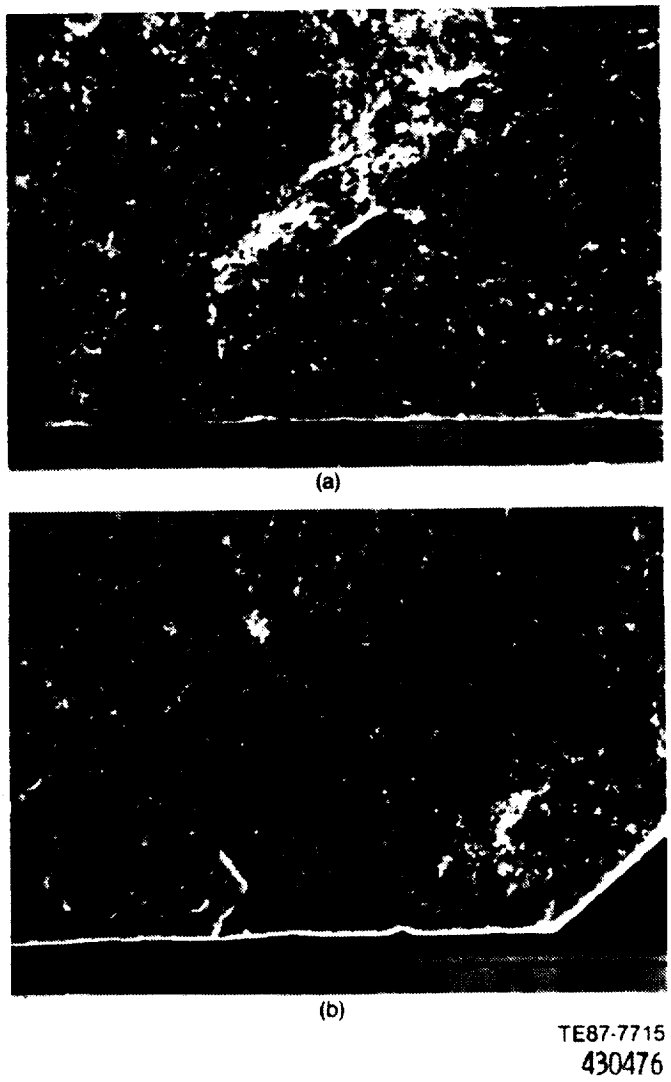

Figure 79. *Typical fracture origins observed in Boride Products Si_3N_4/SiC material (a) internal porosity and (b) internal inclusion.*

is shown in Figure 78. The dark region is composed of the Si_3N_4 matrix with the light region containing the SiC whiskers. The whiskers were observed to have a preferential orientation perpendicular to the hot pressing direction. The average density of this material measured 3.214 g/cm^3.

The material strength characteristics were determined in four-point bending with a load rate of 0.508 mm/min (0.020 in./min). All test bars were evaluated with a machined tensile surface condition. The average room temperature strength was 703.84 MPa (102.08 ksi). The strength at a temperature of 1000°C (1832°F) averaged 560.15 MPa (81.24 ksi). An average strength of 510.30 MPa (74.01 ksi) was observed at a temperature of 1150°C (2102°F), and a strength of 397.57 MPa (57.66 ksi) was measured at a temperature of 1250°C (2282°F). The primary strength-controlling flaws were observed to be surface and internal inclusions/porosity, shown in Figure 79. The fracture mode was primarily brittle in nature, with little or no evidence of crack deflection and/or whisker pull-out. Determination of the fracture toughness (K_{IC}) of this material system was conducted using the SENB method. The K_{IC} value averaged 6.4 MPa$\sqrt{m}$ (5.8 ksi$\sqrt{in.}$) for this material.

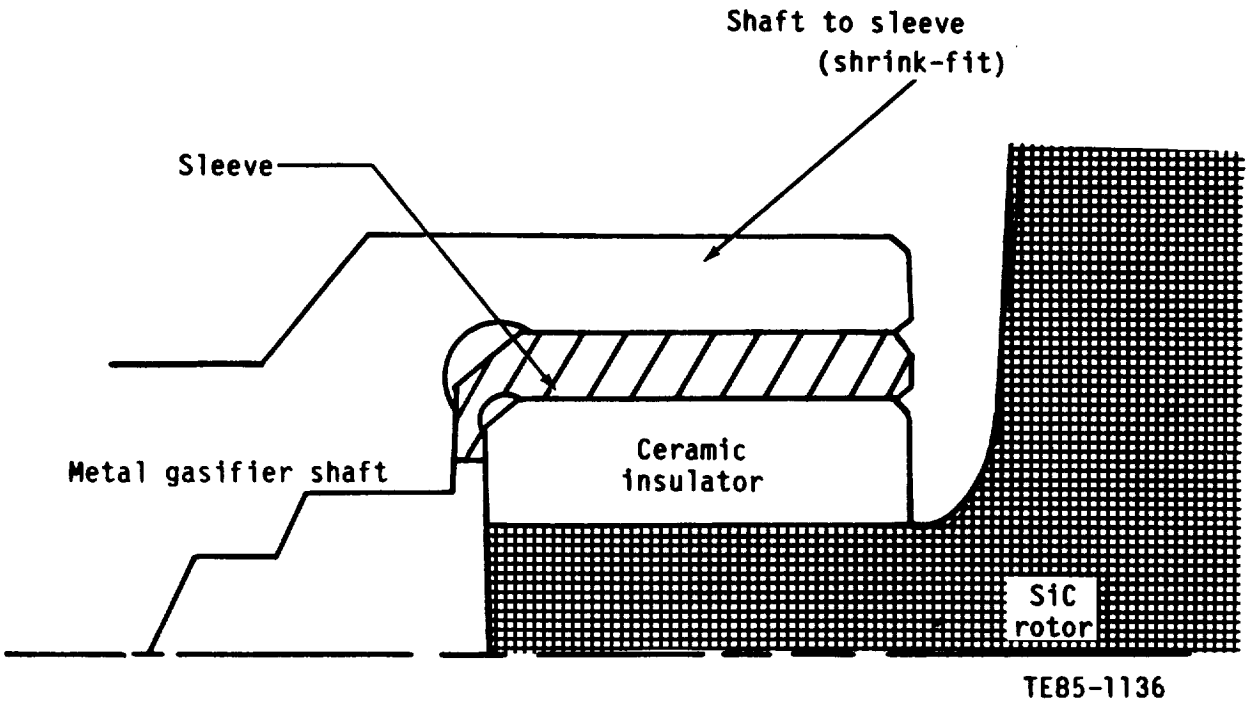

Figure 80. *Schematic of ceramic rotor-to-metal shaft attachment system.*

2.5 THERMAL BARRIER DEVELOPMENT

Introduction

The development of a shaft attachment method for SiC turbine rotors required a thermal barrier material to insulate the metal structures from the high turbine temperatures. A zircon-based ceramic material system with associated process routing was developed at Allison and successfully utilized for rotor shaft attachment. The zircon material has low thermal conductivity, adequate strength, and a good thermal expansion match with SASC.

Discussion

Silicon carbide exhibits physical and mechanical properties which have made it a prime candidate material for high temperature applications in the AGT 100 engine. However, because SiC has a relatively high thermal conductivity, steps must be taken to reduce the heat transfer to the surrounding metallic support structures. It is necessary, therefore, to introduce thermal barrier materials in strategic locations to prevent excess heat loss from the engine and to maintain structure temperatures within acceptable operating ranges. Candidate thermal barrier materials need to have low thermal conductivity, compatible thermal expansion coefficients, and the capability of being fabricated in proper shapes and sizes.

The SiC rotor/shaft attachment incorporates a thermal barrier between the rotor and shafting to control heat flux to the bearing support structure. The development of the thermal barrier material and processes for joining to both the SiC rotor shaft and the metal compressor shaft have been the subject of extensive development activities. Efforts in this area concentrated on two material systems: a zircon-based material developed at Allison, and a mullite/cordierite material developed at Sohio. These material systems were selected because they possess good insulating characteristics and have similar thermal expansion coefficients to SASC.

A zircon-based material system (ZrO_2-SiO_2) was developed at Allison for use as a thermal barrier for the SiC rotor/shaft attachment, shown in Figure 80. A detailed process routing was established for this material, including powder preparation and processing, binder system and removal procedures, fabrication, and consolidation parameters. In addition, the critical thermal and mechanical characteristics of this material were evaluated.

The ceramic raw materials used for the fabrication of the thermal barriers consists of zircon, alumina, and titania powders which are mixed with an organic binder system. The resulting slurry is then processed by ball milling, spray drying, and particle separation processes to provide a uniform homogeneous powder. The zircon thermal barrier ring is then formed by die pressing followed by isostatic

pressing to 206.85 MPa (30 ksi). The zircon ring is then joined to the SiC rotor shaft by direct pressureless sintering and is diamond-machined to finish dimensions. A tight interlocking fit of the thermal dam onto the rotor shaft is achieved while maintaining the integrity of the thermal insulator. Because the zircon has a slightly greater thermal expansion coefficient than the SiC rotor, good contact is maintained throughout the full operating temperature range of the attachment. A Kennametal tungsten carbide (WC) ring is then brazed to the zircon insulating ring with a silver/copper based braze material. Subsequently, the IN 907 metal compressor shaft is interference fit onto the WC support ring, and the entire rotor/shaft assembly is machined to final dimensions.

The material strength characteristics of the zircon material were evaluated by cutting standard size (50.8 mm × 6.35 mm × 3.18 mm (2 in. × 0.25 in. × 0.125 in.)) test bars from a billet which had been processed using the same parameters as the zircon thermal barrier rings used for rotor shaft attachment. The average room temperature fracture strength of the zircon material was 263.39 MPa (38.20 ksi). The Weibull modulus of this material measured 13.36. The typical strength-controlling flaws were observed to be surface and internal porosity, shown in Figure 81. The average strength of the zircon material tested at a temperature of 1000°C (1832°F) measured 216.30 MPa (31.37 ksi). Surface and internal porosity were again observed as the primary fracture origins.

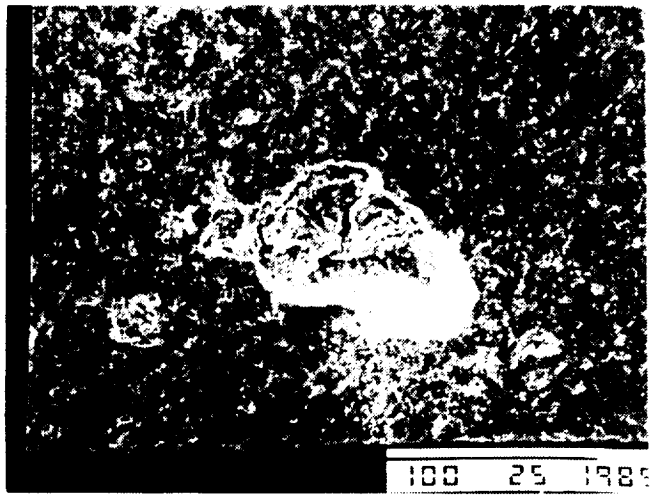

Figure 81. *Typical fracture origin (internal pore) observed in zircon thermal insulating material.*

2.6 DEVELOPMENT OF NONDESTRUCTIVE EVALUATION TECHNIQUES

Summary

NDE techniques were developed to detect 25–200 micron failure controlling surface and subsurface flaws in structural ceramic materials and components. Microfocus radiography detected process-induced and simulated flaws in ceramic turbine rotors and backplates. Simulated 20–50 micron pores were detected in thin cross sections of silicon based ceramics. The X-ray thickness and equivalent penetrometer sensitivity for detecting holes and voids in SiC and Si_3N_4 varied between 0.5% to 1.1%. Natural flaws were detected in a gasifier rotor with a thickness sensitivity of 1.8%. Ultrasonic imaging has been shown to detect 40 to 60 μm surface flaws, and 250 μm size bulk flaws 3.81 cm (1.5 in.) below the interrogating surface. CT detects process-induced defects in an injection-molded alpha-SiC rotor, and disbonds at the ceramic/ceramic interface simulating rotor shaft attachment.

Objective

The successful use of these brittle ceramics can only be achieved with the advent of reliable failure and life prediction schemes, both of which require detection and characterization of minute strength-controlling surface and sub-surface flaws (e.g., voids, cracks, and inclusions) of 10–250 micron size. These inherent flaws, which are normally introduced during the various stages of the fabrication process, are generally responsible for the wide variability in flexural strength. Nondestructive detection of these flaws can screen out defective parts and substantially reduce variability, offering the potential for increased operating stresses. In addressing this problem, projection microradiography, ultrasonic imaging, and X-ray CT NDE techniques were experimentally examined and evaluated.

Discussion

Projection Microfocus Radiography

Detectability and spatial resolution of flaws in radiography is a function of X-ray tube characteristics, imaging medium (film, intensifier, solid state devices), host material, and flaw characteristics (type, size, shape, orientation, location). Resolution in x-radiography is dependent on the focal spot

diameter of the tube that controls the geometric unsharpness (U_g) by the equation

$$U_g = F_s * \frac{a}{d} \quad (1)$$

where F_s is the focal spot diameter of the X-ray tube, "d" the source-to-object distance, and "a" the object-to-film distance. A conventional system with large focal spot diameter has excessive geometric unsharpness, Figure 82, resulting in poor spatial resolution. Microfocus X-ray tubes with small focal spot diameters (1–100 micron) have negligible U_g and are essential to resolve critical flaws in ceramic materials. Resolution is also affected by the grain size of the imaging medium that governs the ultimate signal-to-noise ratio and fuzziness of the detected flaws.

Optimum flaw detection requires both good spatial resolution and high image contrast. The difference in the absorption coefficients of the defect and matrix at a given wavelength and the dynamic range of the imaging medium determine the final image contrast (C) which is given by:

$$C = \frac{[K\ \Delta\mu\ \ x]}{1 + \frac{I_s}{I_d}} \quad (2)$$

$\Delta\mu$ = Difference in the X-ray absorption of the defect and matrix at a given K_v or wavelength

x = Defect size in the direction of the X-ray beam

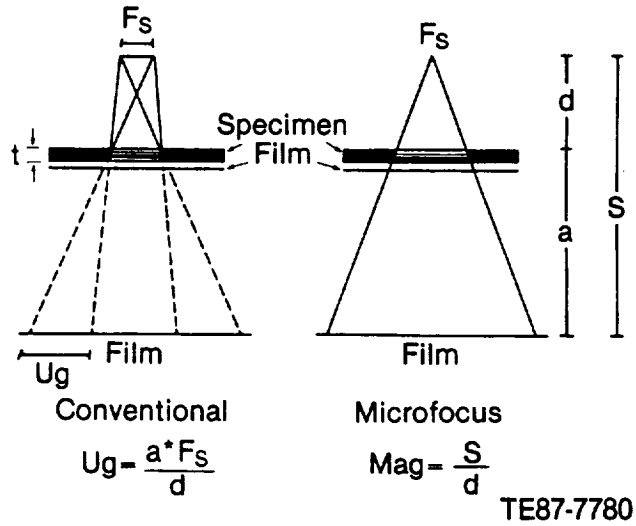

Figure 82. *Schematic showing two radiographic techniques.*

K = Image medium constant

I_s = Intensity of scattered radiation

I_d = Intensity of the imaging radiation

In the microfocus X-ray system,

$$\frac{I_s}{I_d} \rightarrow 0,$$

equation (2) simplifies to

$$C = K\ \Delta\mu\ x \quad (3)$$

The composition of structural ceramic materials is made up of low atomic number elements (Si, C, N). The failure-controlling defects range from voids of very low density to tungsten carbide (WC) of very high density relative to the host matrix material. The linear absorption coefficient (μ) is dependent on the mass absorption coefficient (μ/ρ) of the element or compound and is given by:

$$(\mu/\rho)_m = \Sigma_i\ w_i\ \ (\mu/\rho)_i \quad (4)$$

where

$(\mu/\rho)_m$ = mass absorption coefficient of material

w_i = mass fraction of element i

$(\mu/\rho)_i$ = mass absorption coefficient of element i

By multiplying $(\mu/\rho)_m$ by the density of the material, the linear absorption coefficient is determined. At higher K_eV, which is required to penetrate thick components, $\Delta\mu$ decreases rapidly resulting in poor image contrast. At lower K_eV, $\Delta\mu$ is much higher providing excellent image contrast but with poor X-ray penetration of components. Experimental parameters of a microfocus X-ray system must be optimized to maximize flaw detectability and resolution.

Detection of flaws in X-ray is generally quantified by percent thickness sensitivity (TS) and equivalent penetrameter sensitivity (EPS), which are defined as follows:

$$\text{Thickness sensitivity (\%)} = \frac{x}{t} * 100 \quad (5)$$

$$\text{Equivalent penetrometer sensitivity (\%)} = (100/t)\sqrt{(xd/2)} \quad (6)$$

where

x = defect size in the direction of the X-ray beam

d = flaw diameter

t = part thickness to be radiographed

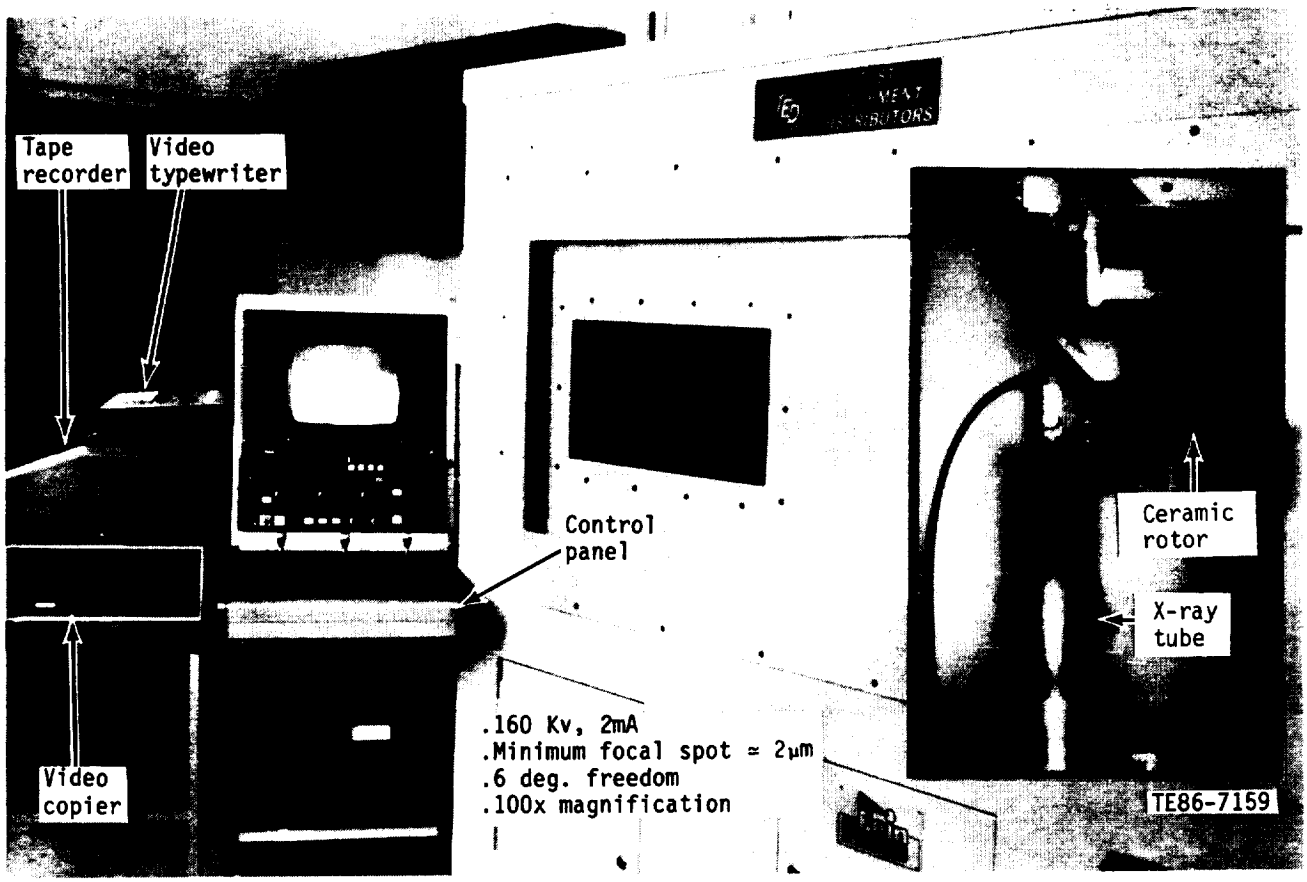

Figure 83. *Real-time FeinFocus microfocus X-ray system.*

Equipment—The real-time FeinFocus microfocus X-ray system that was used is shown in Figure 83. The system consists of a microfocus X-ray tube, a parts handling system, dual field (101.6 mm/152.4 mm [4 in./6 in.]) intensifier, video camera (Vidicon or plumbicon), control panel, 19 mm (3/4 in.) tape recorder, video typewriter, and a video copier. This system is capable of operating up to 160 K_eV voltage and 2 mA current with maximum incident photon energy of 320 watts. The focal spot of the X-ray beam can be varied from 1 to 100 mm providing an extremely sharp image of the detected flaws. The X-ray tube, parts handling system, and the X-ray recording medium (film or intensifier/cameras assembly) are enclosed in a leaded radiation proof cabinet, Figure 84. The system has 6 degrees of freedom that can be controlled by joysticks. The parts handling system has 5 degrees of freedom for optimum component orientation and flaw detection. Intensifier/camera assembly can also be moved along the X-ray beam axis. Control of the distance of the X-ray source from the part and intensifier/camera assembly, respectively, along the beam axis enables both optimum flaw detection and magnification which is very critical for small flaw detection in ceramic materials.

Specimens—SASC and SSN image quality indicator (IQI), commonly known as penetrometers, were fabricated by drilling top-drilled holes in MOR bars. A rectangular specimen with seeded voids was manufactured by placing organic beads of 20 to 50 micron diameter to create surface and internal defects, Figure 85. Ceramic gas turbine components such as gasifier rotors were made by injection molding alpha-SiC and alpha-SiC/TiB_2 particulate composite. Backplates were fabricated by hot-pressing SiC whiskers with MAS (magnesium aluminosilicate) matrix material.

Experimental—The penetrometers were examined by microradiography at 45 K_eV and 0.21 mA with 5X magnification. Projection radiographs with 20X magnification of the seeded void specimen were obtained at 45 K_eV and 0.20 mA. Ceramic gasifier rotors contain naturally occurring process-induced (injection-molded or slip-casted) flaws which are generally created either because of abnormal rheological behavior of the slip or the molding process. Detection of these type of flaws was conducted both in real-time and on the film at about 120 K_eV voltage and 0.24 mA using projection microradiography for an alpha-SiC and alpha-SiC/

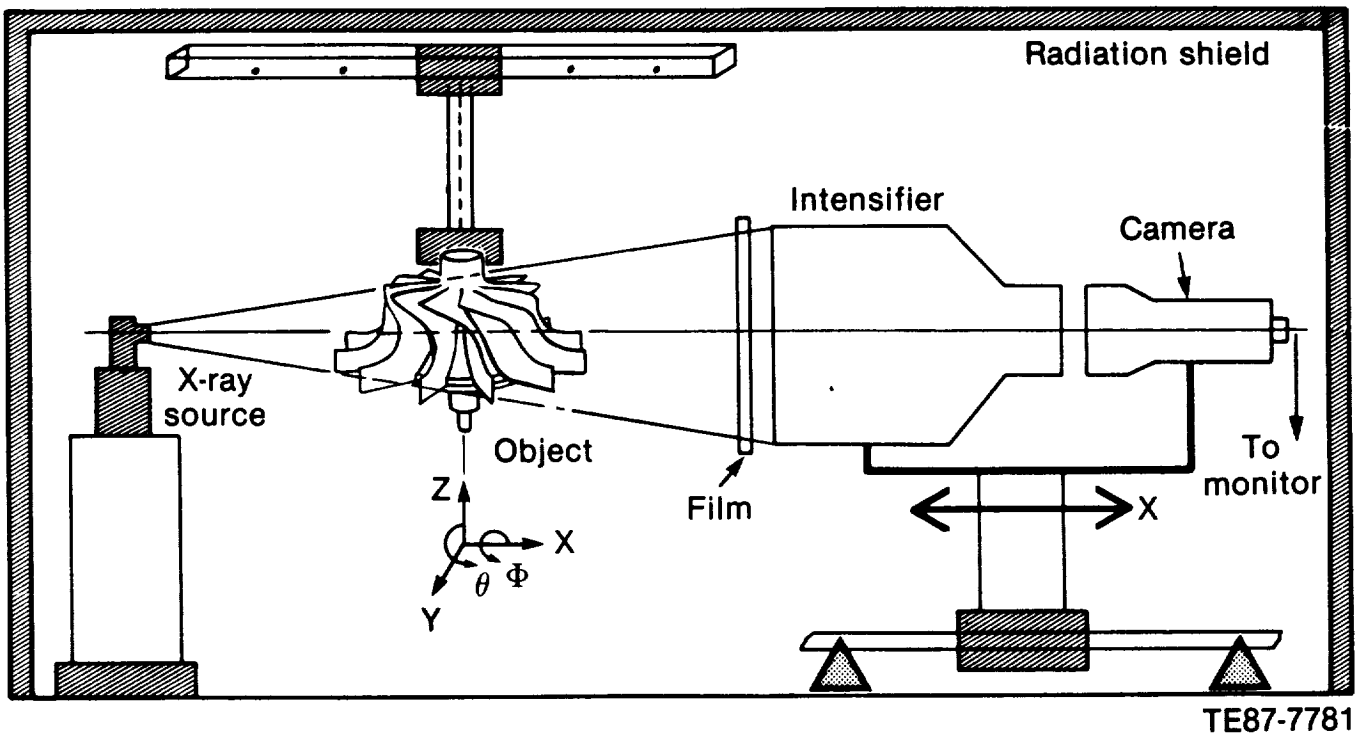

Figure 84. *Schematic of ceramic component inspection technique by projection microradiography using FeinFocus X-ray system.*

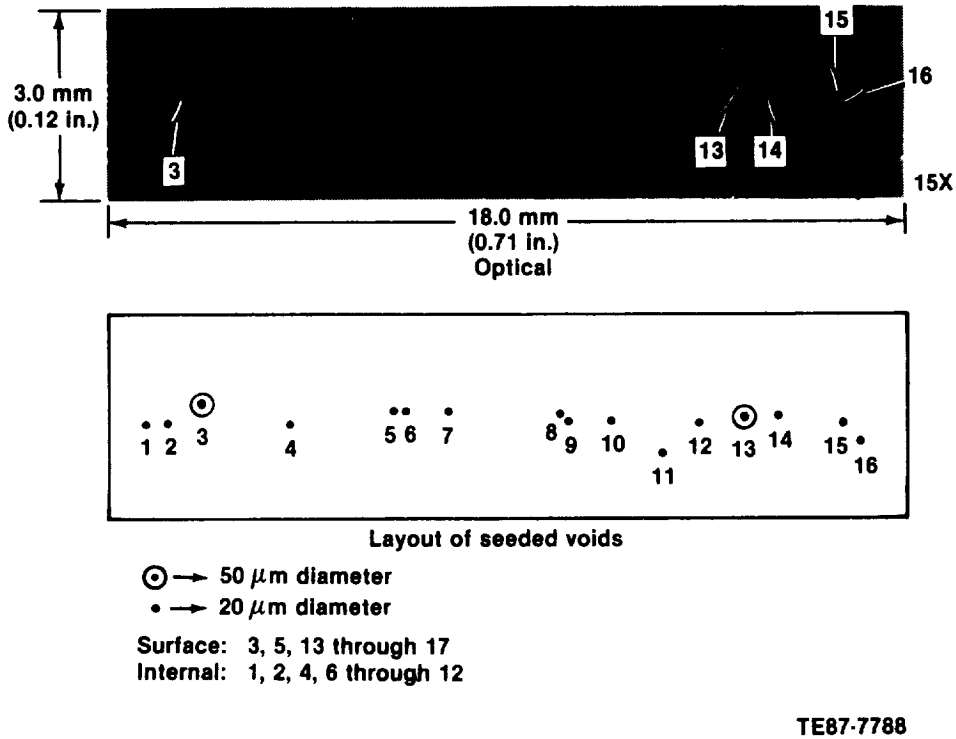

Figure 85. *Layout of seeded voids in SSN specimen fabricated by NASA-Lewis Research Center.*

TiB_2 rotors. The backplate was characterized at 53 K_eV and 0.26 mA.

Measurement of Resolution and Sensitivity—Results in Figure 86 show that tungsten wires of 8 micron diameter were readily detected and resolved from a 12 micron diameter wire. Examination of the images reveals that it is sharper in the vertical direction compared to the horizontal direction, indicating a non-spherical focal spot. Other measurements on a gold mask pattern have shown that 2 micron wide grating lines 2 microns apart can be resolved in one direction whereas 5 micron wide grating lines 10 microns apart can be resolved in the other direction. It is therefore concluded that the system has very good resolution in both directions even at the high magnification generally required for ceramic components.

Results summarized in Tables XVIII and XIX show that both the minimum thickness and equivalent penetrometer sensitivity for surface hole detection in SiC and Si_3N_4 varies between 0.5% to 1.1%. The majority of the holes have a depth-to-diameter ratio of less than 0.5 in Tables XVIII and XIX. Examination of the data indicates that the TS is always less than EPS for such holes. This can also be deduced by combining equations (5) and (6), which results in:

$$TS = \left(2\frac{x}{d}\right)^{1/2} * EPS \qquad (7)$$

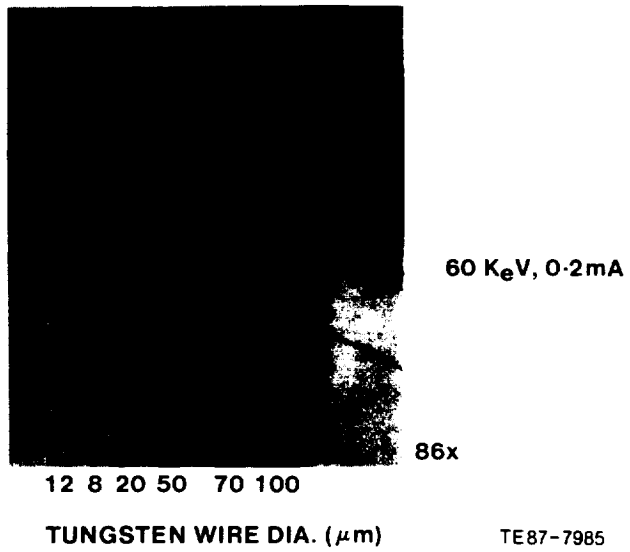

Figure 86. *Resolution measurement by projection microradiography.*

Table XVIII.
Detection of holes in alpha-SiC by microradiography.

Specimen thickness—mm (in.)	Hole			Sensitivity—%	
	Diameter—microns	Depth—microns	X-ray detection	Thickness	Equivalent penetrometer
	117	38	D	3.0	3.7
1.27	221	89	D	7.0	7.8
(0.05)	457	113	D	8.9	12.7
	229	52	D	2.0	3.1
2.54	254	212	D	8.3	6.5
(0.1)	584	233	D	9.2	10.3
	229	52	D	2.0	3.1
5.08	483	186	D	8.3	6.5
(0.2)	483	37	D	9.2	10.3
	229	387	D	4.1	2.2
9.525	457	186	D	1.9	2.2
(0.375)	483	375	D	3.9	3.2
	229	162	D	1.3	1.1
12.70	229	222	D	1.8	1.3
(0.5)	559	249	D	2.0	2.1

D—detected

for x/d < 0.5, TS < EPS; and for x/d > 0.5, TS > EPS. Results in Tables XVIII and XIX clearly show that large diameter shallow holes can be readily detected by microradiography because sufficient X-ray photons are absorbed by the volume of the flaw to discern it from the background material microstructure and noise. The detectability of such holes is controlled by the depth and diameter of the holes. For example, Table XIX shows that 75 × 23 micron and 125 × 10 micron size shallow holes are easily detected. Therefore, thickness sensitivity alone is not a true measure of radiographic sensitivity. For small flaws of 10 to 50 micron in size, both types of sensitivity should be calculated and reported wherever possible. This will provide a realistic measure of flaw detectability from the background noise by X-rays. Table XX shows that surface and near subsurface seeded voids of 25 to 30 micron

Table XIX.
Detection of holes in SSN by microradiography.

Hole			Sensitivity—%	
Diameter—microns	Depth—microns	X-ray detection	Thickness	Equivalent penetrometer
75	23	D	0.9	1.2
75	38	D	1.5	1.5
100	30	D	1.2	1.5
100	70	D	2.8	2.4
125	10	D	0.5	1.0
125	20	D	0.8	1.4
125	35	D	1.4	1.9
250	13	D	0.5	1.6
250	20	D	0.8	2.0
250	43	D	1.7	2.9

Specimen thickness = 2.5 mm (0.1 in.)
D — detected

Table XX.
Detection of seeded voids by microradiography in SSN.

		Flaw size—microns		Sensitivity—%	
Flaw No.	Flaw location	Optical	X-ray detection	Thickness	Equivalent penetrometer
1	I	—	ND	—	—
2	I	—	ND	—	—
3	S	92	100	3.8	2.7
4	S	30	40	1.5	1.1
5	I	—	100	3.8	2.7
6	I	—	ND	—	—
7	I	—	30	1.2	0.8
8	I	—	80	3.1	2.2
9	I	—	40	1.5	1.1
10	I	—	40	1.5	1.1
11	I	—	60	1.6	1.6
12	I	—	25	1.1	0.8
13	S	100	119	4.6	3.3
14	S	40	28	1.1	0.8
15	S	53	119	4.6	3.3
16	S	40	28	1.1	0.8

Specimen thickness = 2.578 mm (0.101 in.)
I — internal
S — surface
ND — not detected

size were detected with about 1% thickness and EPS. The size and location of these flaws was well characterized by NASA-Lewis Research Center.

Ceramic Gasifier Rotor—Process-induced defects were detected in an injection-molded alpha-SiC gasifier turbine rotor. Figure 87 shows two positives of the film radiographs taken 180° apart. At $\Theta = 0°$, three flaws were detected, and at $\Theta = 180°$, only one flaw was detected, which clearly indicated the significant advantage of real-time part manipulation for optimum orientation and defect detection. By rotating the part, the airfoils can be moved to avoid their overlap with the areas of interest and effective rotor inspection can be conducted. Part motion in z, y, Θ, and ϕ axes provided the capability to optimally orient the rotor. The smallest flaw detected was 1000 × 208 micron.

An alpha-SiC/TiB_2 injection-molded rotor was examined in two orthogonal orientations by microfocus X-ray. X-ray detected nine individual flaws which could not be resolved by ultrasonic imaging because of large beam divergence and proximity of the flaws to each other (Figure 88). A flat 25 MHz transducer was used for ultrasonic characterization. The size of the flaws was measured from the X-rays and the thickness sensitivity calculated. The smallest detected flaw was 1390 × 794 × 2183 micron in size with a thickness sensitivity of 2.9% and 1.8% in 0° and 90° orientations, respectively. The thickness of the part in the region of flaw No. 8 is about 7.62 cm (3 in.).

Ceramic Composite Backplate—Figure 89 shows the positive of the microradiograph of a SiC whisker-reinforced MAS backplate. Both low and high density flaws were detected. The exact nature of the flaws have not yet been identified. The smallest detected flaw had a 794 micron diameter.

Ultrasonic Imaging

Ultrasonics is a sensitive technique to detect fracture controlling flaws of 25 to 200 microns in structural ceramic materials. The sensitivity for flaw detection is, of course, determined by the wavelength (λ), and thus the frequency of the incident ultrasonic beam and microstructure (grain size, porosity, second phase, etc) of the materials. Because of the necessity for the detection of small flaws, frequencies much higher than those in conventional use have to be employed.

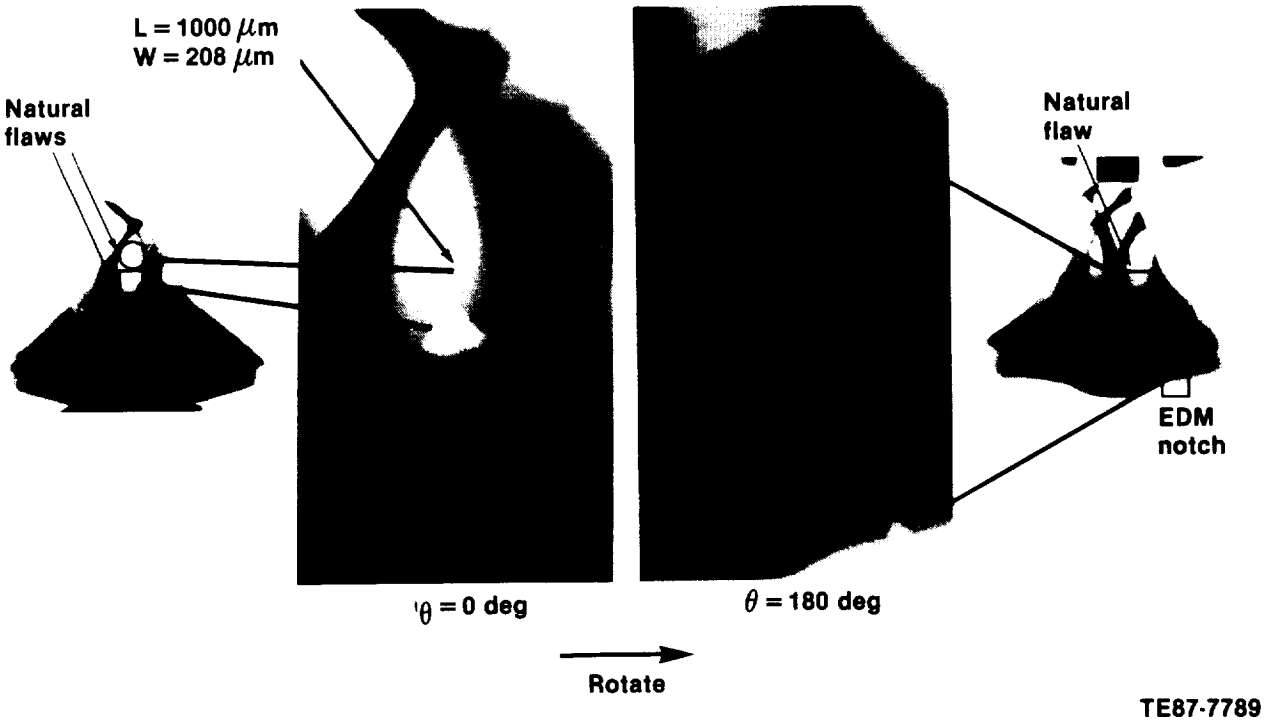

Figure 87. Detection of process-induced natural flaws in injection-molded alpha-SiC gasifier rotor.

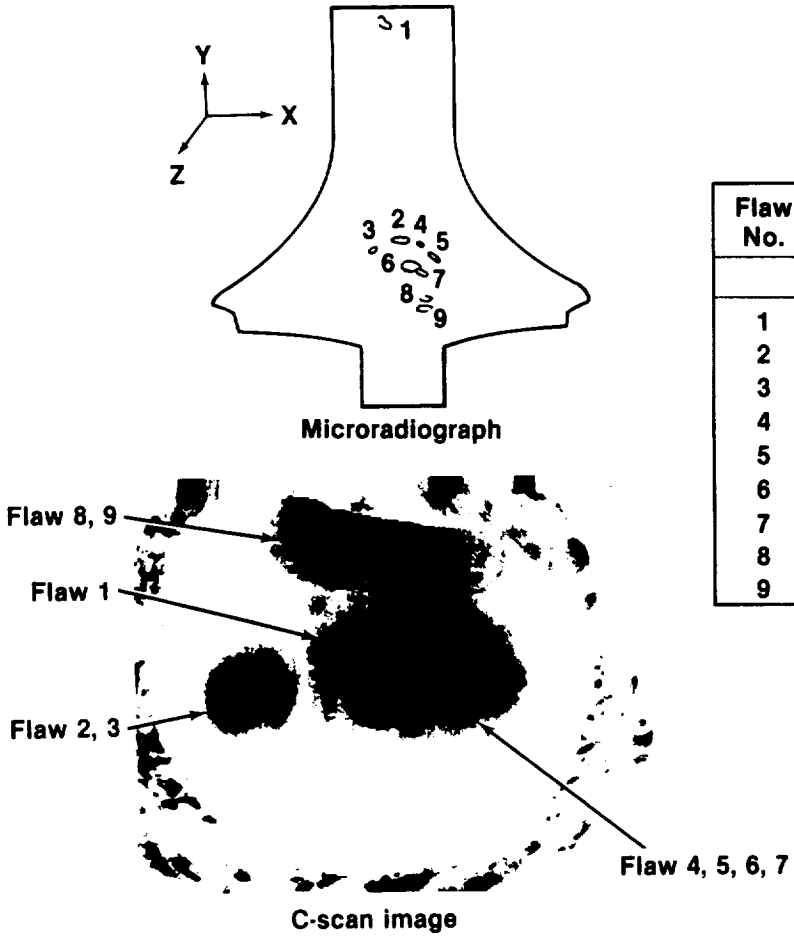

Flaw No.	Flaw size—μm				% Thickness sensitivity	
	0 deg		90 deg			
	X	Y	X	Y	0 deg	90 deg
1	1984	2282	2381	1984	11.8	9.8
2	2580	1091	2778	1091	5.6	5.1
3	1785	794	1290	694	2.4	3.3
4	1588	794	1785	794	3.3	3.3
5	2381	794	2381	1191	4.0	4.1
6	3175	1389	3968	1191	6.1	5.0
7	2381	1191	2580	992	3.7	4.2
8	1390	794	2183	794	2.9	1.8
9	1984	1191	1984	1191	2.6	2.6

TE87-7790

Figure 88. *Detection of process-induced natural flaws in injection-molded alpha-SiC/TiB_2 gasifier rotor.*

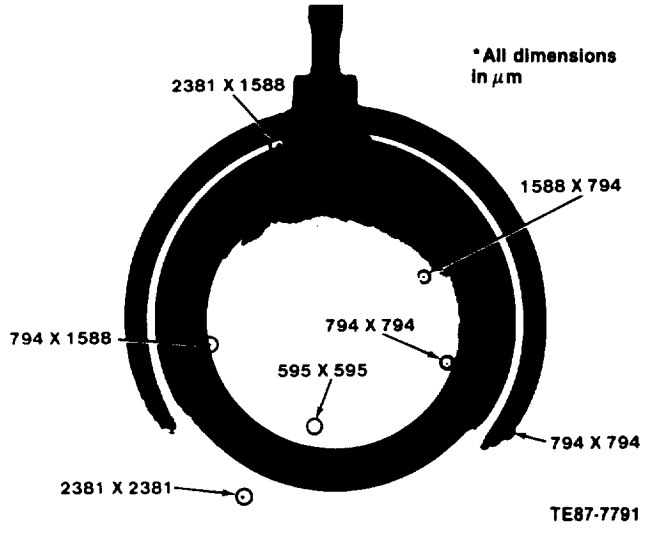

Figure 89. *Detection of high and low density natural flaws in SiC whisker/MAS composite backplate.*

A 50.0 MHz computer-aided ultrasonic imaging system, shown in Figure 90, was used to evaluate the machined surface of the MOR specimens. This system consists of a programmable x-y scanner, a 75 MHz broadband pulser/receiver, a gated peak detector, a 16-grey scale image recorder, and a 50 MHz nominal frequency 1.27 cm (0.5 in.) focal length focused transducer. The reflected radio frequency (r.f.) signal is gated, peak-detected, and converted into a dc signal. This signal is displayed on a 16-grey scale recorder. The images can be magnified easily to 20X or more. A 25 MHz broadband flat transducer was used to examine the gasifier rotors.

Detection of Surface Flaws—The sensitivity of longitudinal wave ultrasonic imaging to detect surface flaws was determined by characterizing a U.S. penny using a 50 MHz 1.27 cm (0.5 in.) focal length transducer focused at the back surface of the coin. The back surface echo was time-gated and modulations in the signal were imaged. Figure 91 is a magnified sharp C-scan image (7.5 X) of the penny indicating that minute variations and surface flaws can be readily detected by ultrasonics.

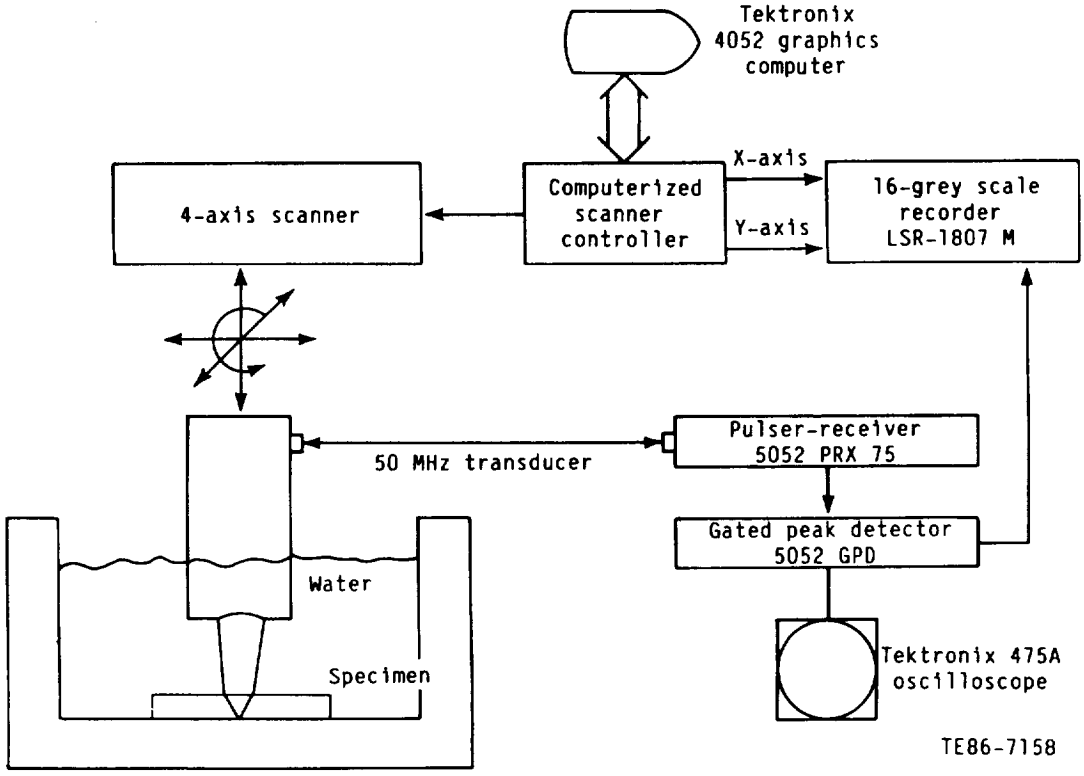

Figure 90. *Schematic of computer-aided ultrasonic C-scan imaging system.*

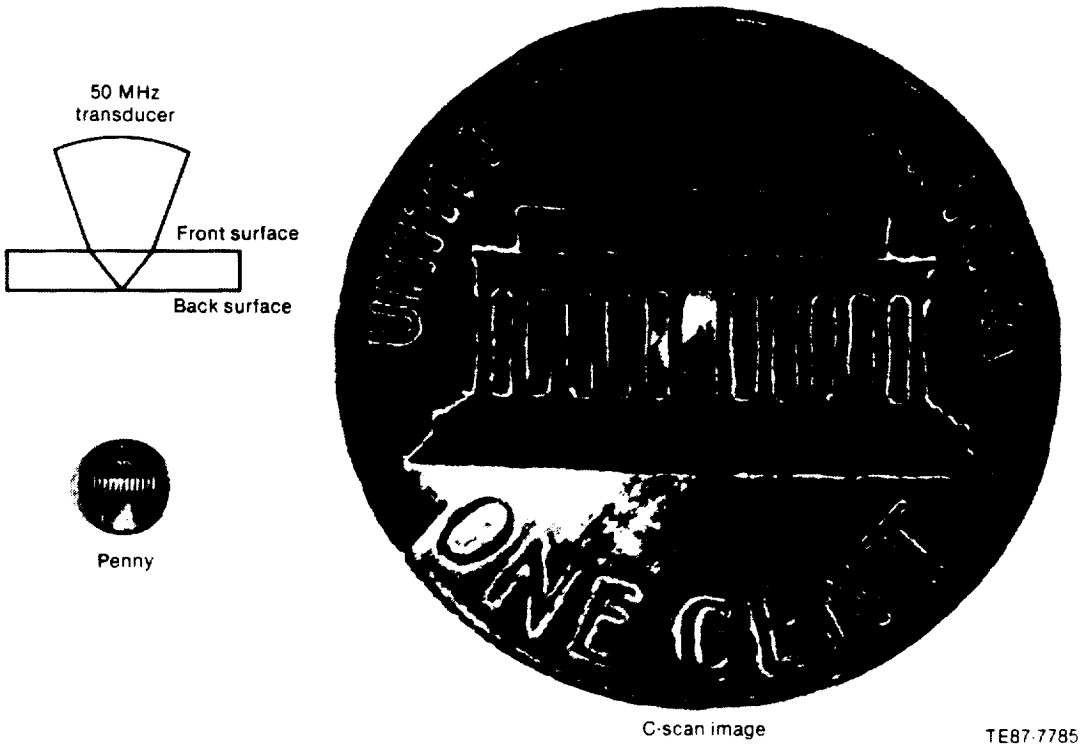

Figure 91. *Ultrasonic C-scan imaging of a U.S. penny.*

An alpha-SiC X-ray penetrometer with simulated surface holes was examined by focusing the above transducer on the front surface of the specimen. Figure 92 shows that seven natural and simulated surface voids were detected by ultrasonic C-scan imaging. Table XXI shows the measured flaw sizes by optical micrography and acoustic grey scale images. The smallest simulated hole was 38 micron deep and clearly shows that shallow flaws can be resolved from the surface topographical variations. The smallest detected natural surface pore was 40 μm × 64 μm in size. Grey scale modulations in the ultrasonic image were observed across the surface of the specimen, indicating that much smaller microstructural changes and flaws compared to the aforementioned defect are being detected. Optical examination showed random distribution of a large number of very small pores on the surface but no correlation with the C-scan image was possible. The large flaw size from the acoustic images, as shown in Table XXI, compared to the optical images is predominantly affected by the transducer focal spot diameter that is about 144 μm. Both the examples show that small 40 to 60 micron size fracture controlling defects can be detected by ultrasonics.

Characterization of Gasifier Rotor—The gasifier rotor is a critical component of the AGT 100 program. Injection-molded and sintered rotors are generally flawed in the thick center cross section of

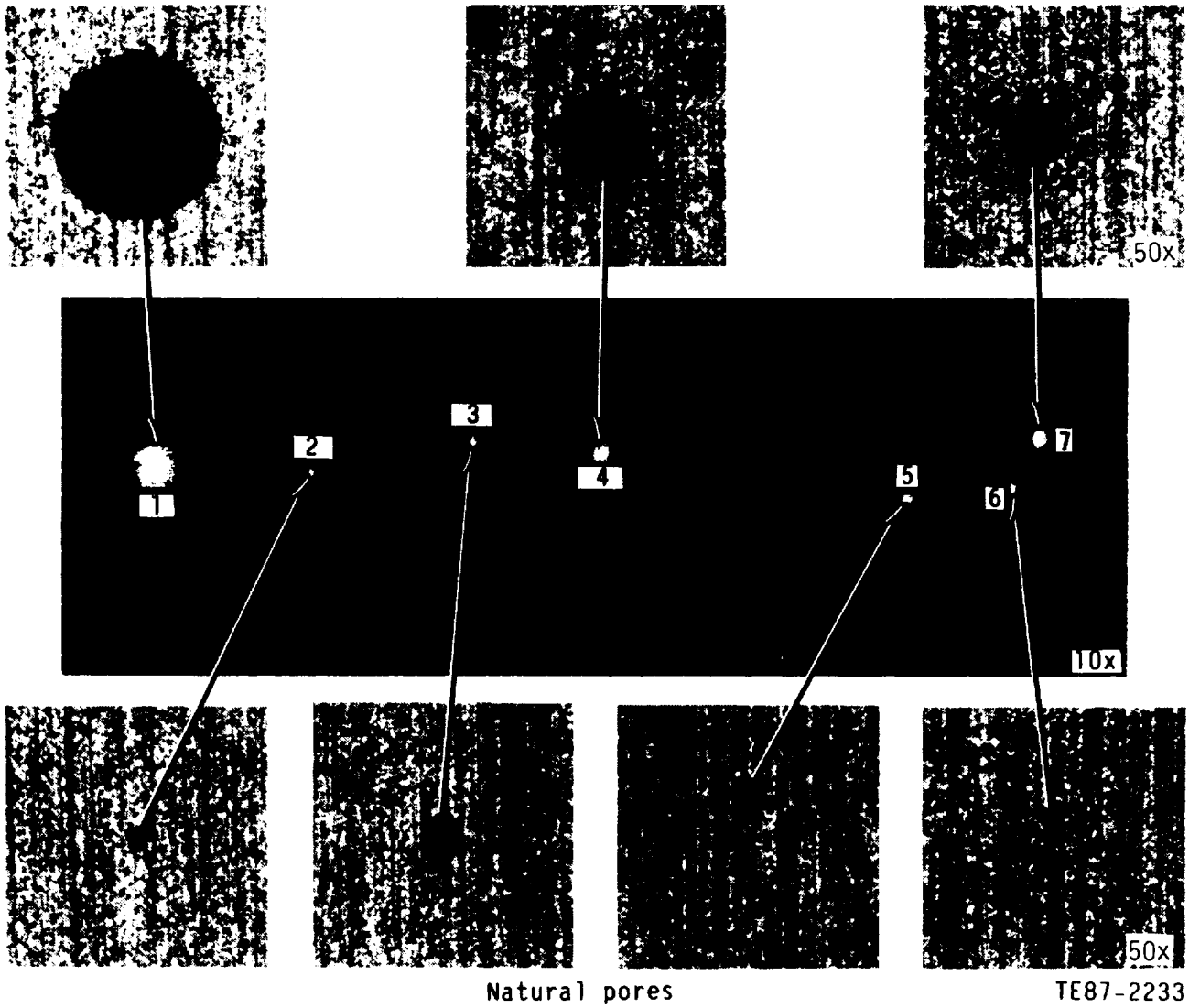

Figure 92. *Ultrasonic surface flaw detection in alpha-SiC.*

Table XXI.
Comparison of optical and ultrasonic measured surface pore size.

Flaw No.	Type of pore	Optical flaw size—mm			Ultrasonic flaw size—mm	
		Direction x	Direction y	Depth	Direction x	Direction y
1	Simulated	468	468	113	505	577
2	Natural	40	64	—	108	144
3	Natural	103	120	—	144	180
4	Simulated	238	238	89	253	289
5	Natural	40	95	—	108	144
6	Natural	71	95	—	144	144
7	Simulated	159	159	38	216	216

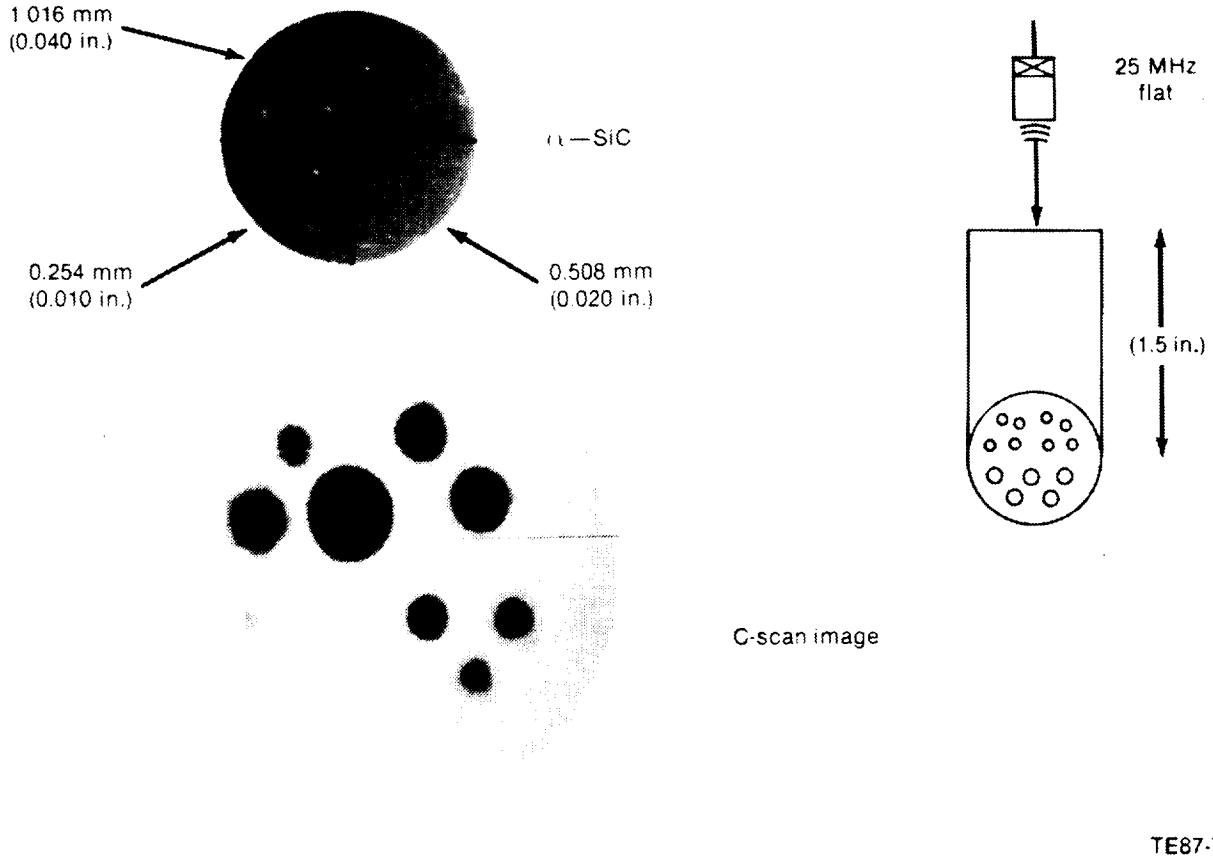

Figure 93. *Ultrasonic detection of bulk flaws in alpha-SiC.*

the hub. The flaw detection sensitivity of the ultrasonic imaging technique used to characterize the center hub section of the rotors was optimized using a 2.54 cm (1 in.) diameter × 3.81 cm (1.5 in.) long alpha-SiC cylinder with a total of 13 holes of 250 μm, 500 μm, 1000 μm diameters, and various depths ranging from 250 to 3100 microns. The holes were fabricated by ultrasonic machining in the back surface of the specimen. A 25 MHz flat transducer was used. The back surface reflection was time-gated and the r.f. signal amplitude variation imaged using a peak detector. Eleven holes were detected as shown in Figure 93. All the undetected holes were 250 μm (0.010 in.) in depth from the back surface and could not be discerned from background microstructure signal. It is believed, however, that 250 micron size or smaller flaws can be detected in the bulk of the rotor when they are encapsulated in the matrix.

Figure 94 shows the results of microradiography and ultrasonic imaging of an alpha-SiC rotor with naturally occurring pores. These flaws were

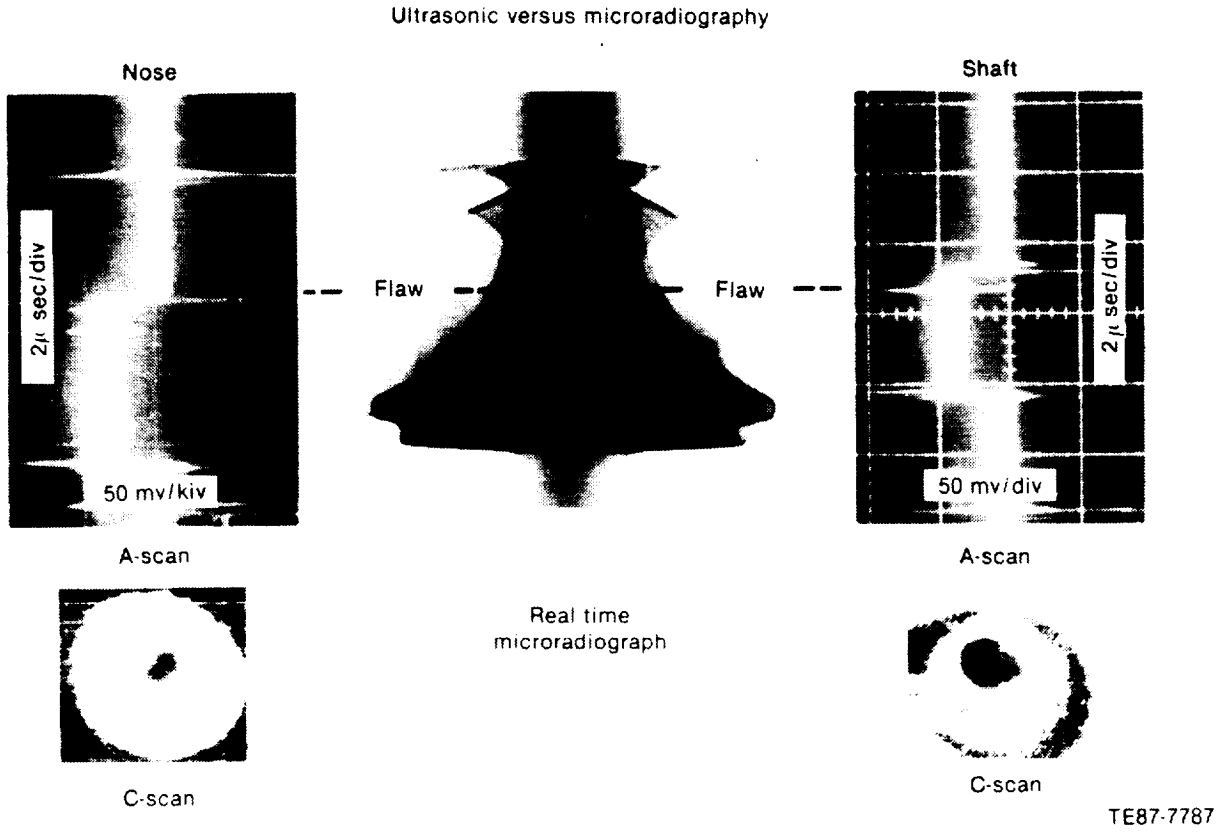

Figure 94. *Flaw detection in alpha-SiC gasifier rotor by micro-radiography and ultrasonic.*

detected both from the exducer (nose) and the inducer (shaft) side of the rotor both by ultrasonic A-scan and C-scan images. The axial location of the flaws was found to be identical both from the A-scans and the microradiograph. This suggests that both techniques can detect such natural flaws for component process development and improved reliability.

X-Ray Computed Tomography

CT is a sensitive X-ray imaging technique to detect minute microstructural density variations and discrete flaw detection in structural ceramic materials. In tomographic imaging, projection data is used to construct cross-sectional images of a given object. The object under examination is irradiated by a beam of X-rays from various angular positions. For each beam position the intensity of emerging radiation is measured electronically using scintillation detectors. The sum total of all projections is computer analyzed to reconstruct a cross-sectional image of the object. The CT images can be used for materials improvement, process control, and component characterization.

A feasibility study was conducted at Chalk River Nuclear Laboratories, Canada, to ascertain the sensitivity of the tomographic technique to characterize the injection-molded alpha-SiC gasifier rotors and SiC-zircon joint, respectively. The CT scans were performed using the first generation (translate-rotate, single detector) scanner as shown in Figure 95. The in-slice thickness was 1.6 mm (0.063 in.) in all cases. All the images were corrected for beam hardening effects.

Gasifier Rotor—The CT images of the rotor were obtained using a Ir-192 X-ray source in a plane crossing the center axially. The spatial resolution was 0.72 mm (0.028 in.), the density resolution (noise) was below 1%, and the image was reconstructed in a 256 × 256 grid with a pixel size of 0.36 mm (0.014 in.). Figure 96 shows the CT image and density profiles as a function of the position across the lines superimposed on the image. Two pores, a large one and a small one, were detected. In addition, the rotor has a nonuniform material density distribution in the thick hub cross section. The density in the center is 7% lower compared to that

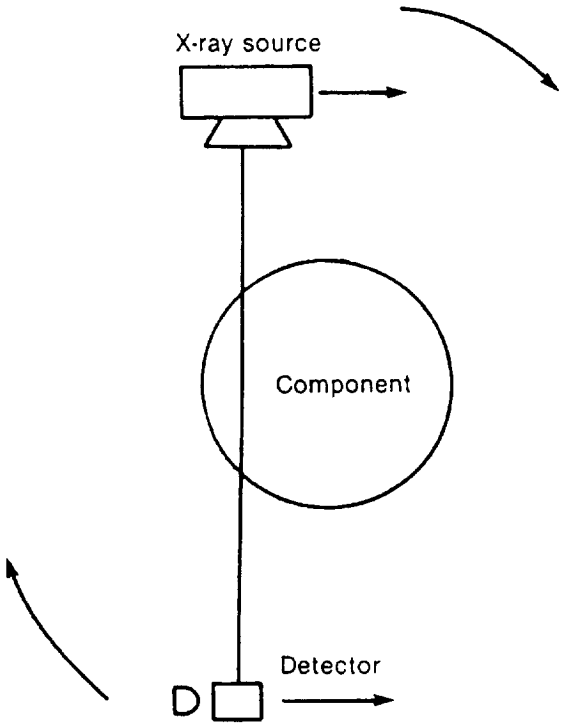

Figure 95. *Schematic of a first generation CT system.*

at the edges. The presence of flaws and density gradient is attributed primarily to the inadequate control of the injection molding process. These results indicate that CT can be successfully utilized to optimize component processes to ascertain uniform material microstructure and discrete flaw detection.

Ceramic/Ceramic Joint—The sensitivity of CT to detect tight disbonds was conducted using an alpha-SiC cylindrical rod, which had a natural linear flaw on the periphery, on which a zircon donut was shrunk fit as shown in Figure 97. The specimen was irradiated by a Co-60 X-ray source in a plane perpendicular to the symmetry axis of the assembly. The spatial resolution was 0.5 mm (0.02 in.), the density resolution was 1%–2%, and the image was reconstructed on a grid of 128 × 128 pixels, with a pixel size of 2.5 mm (0.1 in.). Figure 97 shows that a disbond is detected at the interface on the outer surface of the alpha-SiC cylinder which causes a dip in the density profile. The linear vertical flaw is 0.33 mm (0.013 in.) deep in the direction of the X-ray propagation yielding CT thickness detection sensitivity of 1.35%. Clearly, tight defects at the

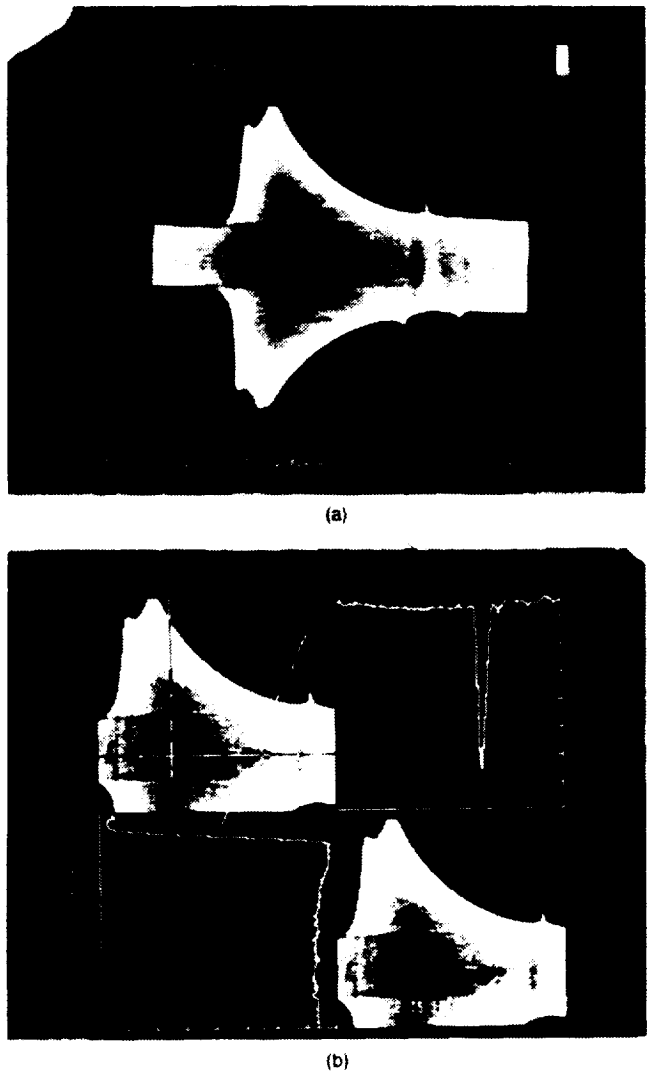

Figure 96. *CT found (a) detection of pores and (b) density variation in injection-molded alpha-SiC rotor.*

dissimilar ceramic material interfaces can be detected by CT.

2.7 FRACTOGRAPHIC ANALYSIS

Introduction

During the course of the AGT 100 program, fractographic analysis has proved to be a useful tool in evaluating advanced ceramics. Fractographic analysis was first applied to new laboratory test materials. The fracture mode, type of strength controlling defects, and fracture features were obtained

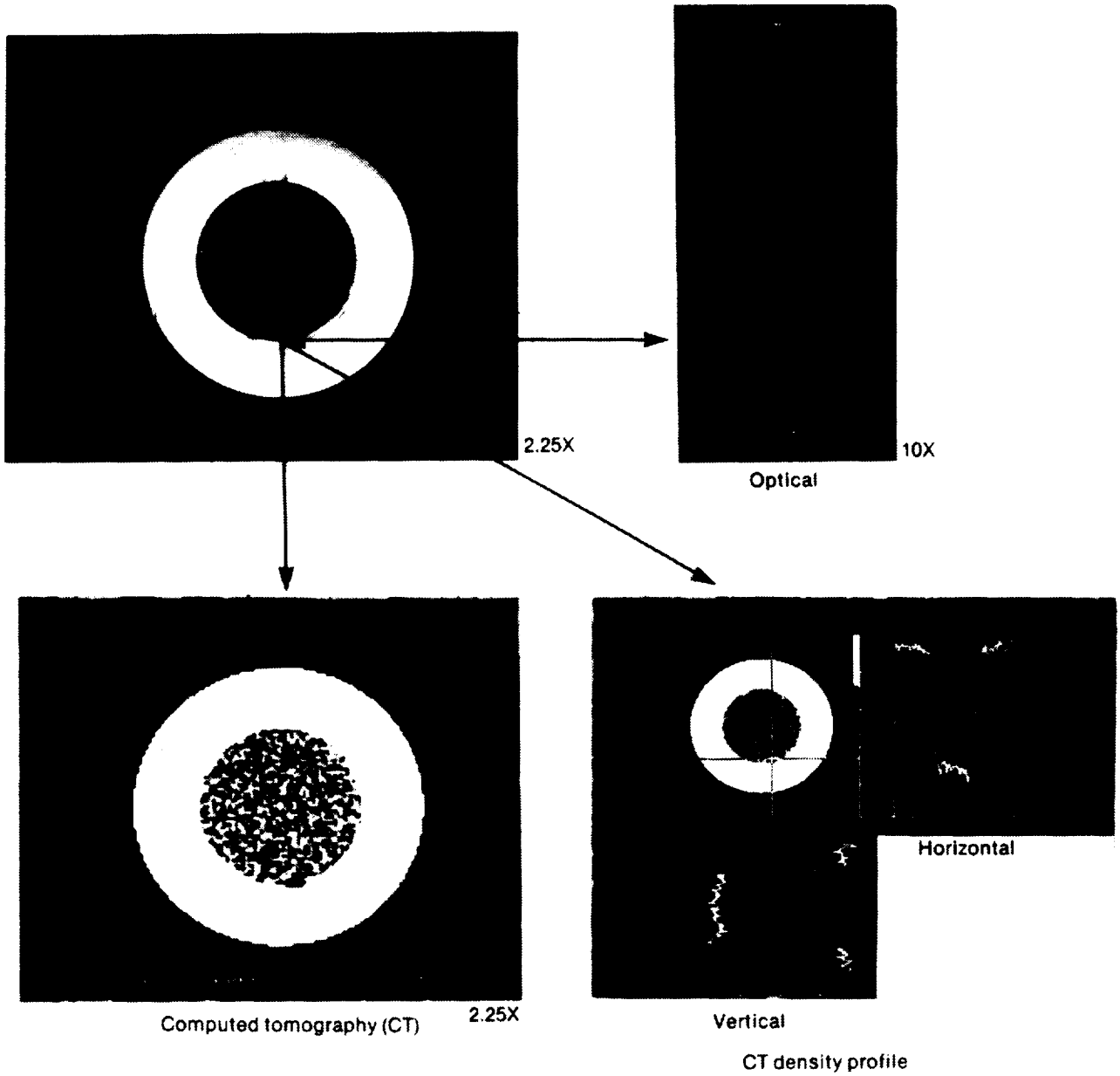

Figure 97. *Detection of a linear flaw at the alpha-SiC/zircon joint interface by computed tomography.*

to set up a baseline data. The information obtained was then used to identify ways in which processing, chemistry, and microstructure could be altered to yield enhanced properties. In other words, fractographic analysis served as a screening process to select the best materials for engine components. Furthermore, the specific fracture features could be used as fingerprints to identify the primary fracture origin in complicated multiple component failure events. This allowed the separation of design limitations from material insufficiencies, defects, or improper fabrication procedures, and has allowed identification of the appropriate corrective measures.

Fundamental Fractography of Ceramics

Fracture is the process of crack initiation and growth, and fractography is the study of fracture surface topography. Under typical tensile or flexural loading, fracture of the ceramic is the result of the propagation of a single crack. The fracture topography changes as the crack front accelerates along the path of crack development. Starting at the fracture origin, the fracture features of a fine polycrystalline ceramic include mirror, mist, hackle, and crack branching along the path of crack development. The number of fracture feature types present in a specific specimen depends on the size and the strength of the specimen. Figure 98 shows the representative fractograph of a SiC rotor that failed in spin testing. Features of mirror, mist, and hackle are present.

Fracture origin — A crack has to start somewhere. Usually the origin represents the weakness in the material, such as a large pore, a foreign inclusion, a local peaking of effective stress, or some combination of these. The weakness could be on the surface or in the volume.

Mirror — The mirror is a flat, highly reflecting region surrounding the fracture origin and is approximately perpendicular to the tensile axis around the fracture origin. Previous studies have shown that the radius of the mirror varied with the fracture stress, σ_f,

$$\sigma_f (r_m)^{1/2} = A = \text{a material constant}$$

This relationship provides a powerful tool in the determination of the fracture stress of a component once the material constant is known.

Mist, hackle, and crack branching - The mirror is typically bounded by mist, small ridges oriented in the crack propagation direction. Mist merges into the similar larger ridges called hackle because of the resemblance to a feather. Hackle merges into crack branching if the specimen is large enough. These features resemble a river pattern and are very useful in tracing the fracture back to the fracture origin.

The fracture features are observed in the specimen which failed under tensile stress. Different fracture features are frequently associated with other failure modes, e.g., contact damage, impact, and vibration. The contact damage generally shows a shell-type fracture topography resulting from Hertzian fracture (Figure 99), while impact usually ruins the contact point. Both are easily identified. However, when the tensile stress combines with vibration, the specimen usually fails in a lower stress, and the fracture topography has less features. This will be discussed in Section 2.8.

Fractographic Analysis of Test Specimens

Thousands of flexural test specimens of various ceramic materials have been evaluated in fast fracture at room and elevated temperatures to establish a material data base. Test bars in the size of 1/4 in. × 1/8 in. × 2 in. were tested in a quarter-point-loading, four-point bending fixture. The fracture origins of each specimen were evaluated using optical and scanning electron microscopy techniques to identify the location and nature of the strength-controlling flaws. These fracture origins were categorized into the various flaw types (surface and internal pores, inclusions, machining damage) and compiled into an extensive fractographic data base for use in the engine design/failure analysis iterative process. Examples of the flaw types for

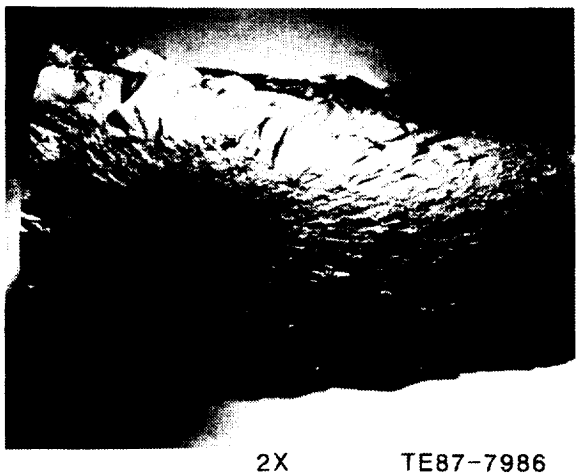

Figure 98. *An example of typical fracture features (mirror, mist, and hackle) observed in spin tested SiC rotor. The primary fracture origin is a pore.*

Figure 99. *Example of contact fracture feature.*

each material have been shown in the materials component section in this report. In addition, the empirical relationship between the fracture mirror size and the fracture strength was established for each ceramic material. This data proved extremely valuable in the determination of the stress at fracture of the ceramic components which failed during engine testing and evaluation.

Test specimens of several silicon nitrides and one silicon carbide have also been evaluated in a variety of time-dependent tests at elevated temperatures. Fractographic analysis revealed that slow crack growth (SCG) occurred at 1000°C for GTE AY6 and Kyocera SN220M silicon nitrides at certain test conditions. Figure 100 shows a representative SEM fractograph of an AY6 specimen that failed after 0.475 hr under a constant load of 60 ksi at 1000°C. The SCG zone is a bright semi-circular area. Details of the SCG zone and the fast fracture zone are shown in Figure 101. While the fast fracture zone consists of intergranular and transgranular fractures, the SCG zone fractured intergranularly with ductile grain boundary phase separation. Transmission electron microscopy examination of the SCG zone revealed degradation of the glassy grain boundary phase by the formation of spherical microvoids. The SCG zone also existed in the SN220M specimen as illustrated in Figure 102. The SCG zone consists of intergranular fracture as in the case of AY6, however, TEM examination revealed that grain boundary microcracking was the fracture mechanism.

TE87-7988

Figure 100. *SEM fractograph of an AY6 specimen failed after 0.476 hr under a constant load of 60 ksi at 1000°C. The SCG zone is the bright semi-circular area.*

2.8 FAILURE ANALYSES

Failure Analysis After Rig/Engine Testing of Single Ceramic Components

The rig or engine testing of a single ceramic component was used extensively in the AGT 100 program as a proof test of the component prior to engine testing of a ceramic assembly. This testing provided good opportunities to study the cause of failures in ceramic components, since in the event of a failure, the fracture origin and mechanism could typically be easily identified. Failure mechanisms of components could be summarized into cases of FOD, inferior part, overstress due to improper design, and sometimes due to improper handling. Some examples are shown in the following sections.

In Engine S/N 1, BU20, a Si_3N_4 gasifier turbine rotor failed after 99:54 hr of engine testing. Failure was due to FOD as the carbon deposits on the ID

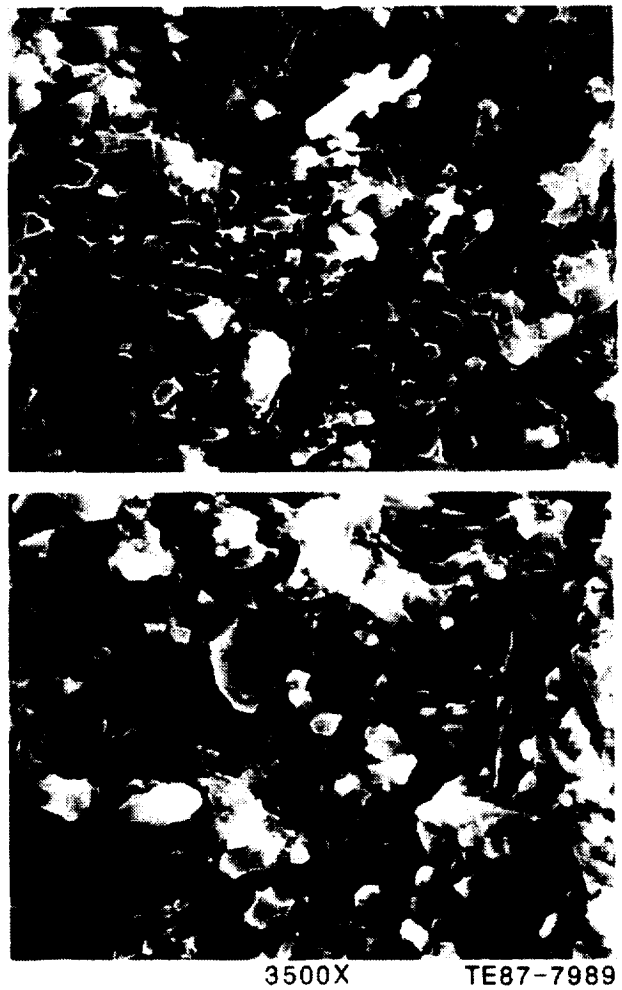

3500X TE87-7989

Figure 101. *Details of fast fracture zone (top) and SCG zone (bottom) of the AY6 specimen.*

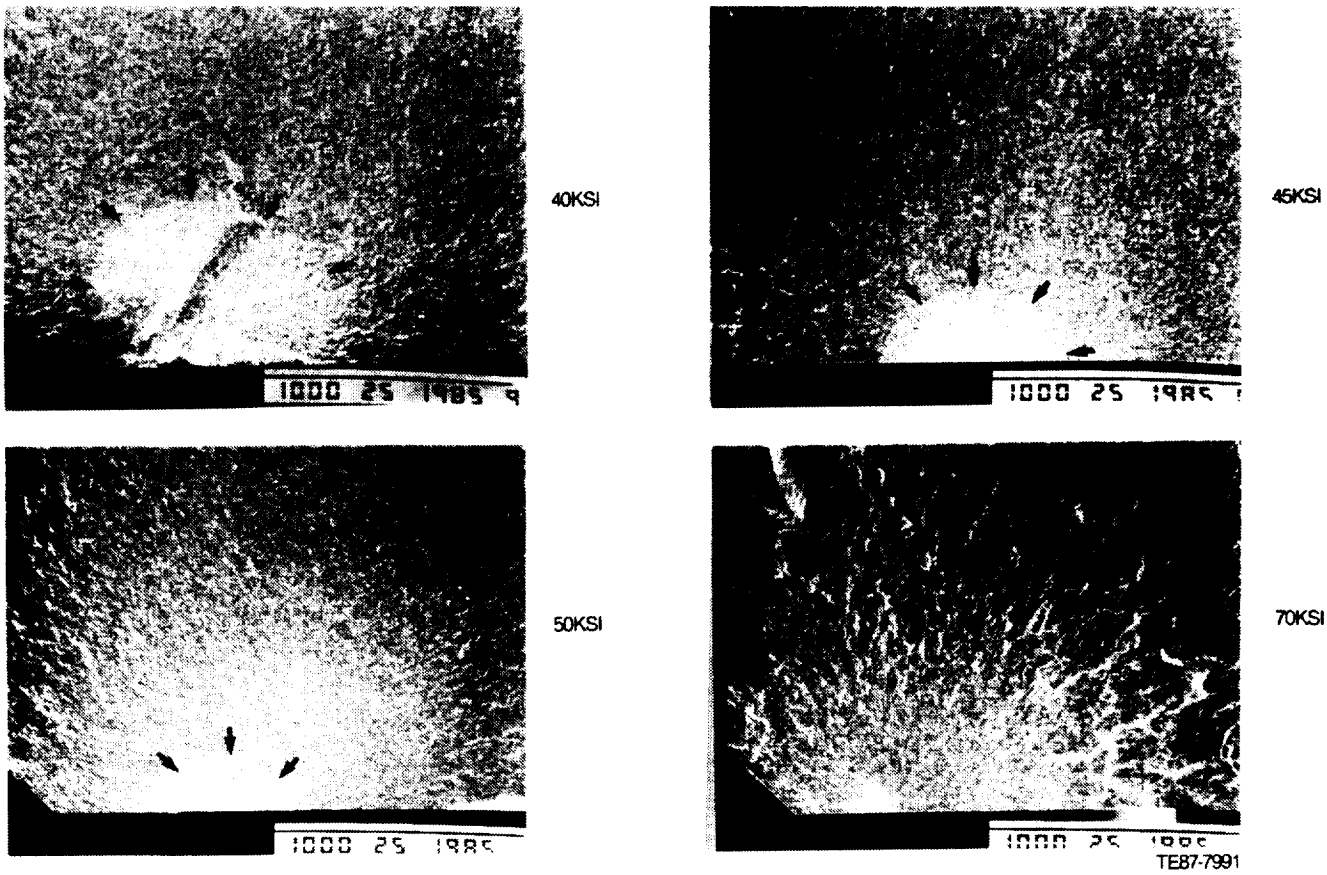

Figure 102. *Representative fractographs of SN220M static fatigue tested at 40, 45, 50, and 70 ksi. SCG was observed in the specimen under 50 ksi. SCG zone was outlined by black arrows.*

wall of the combustor fell off and struck the rotor. The rotor lost all inducer tips (Figure 103).

In Engine S/N 2, BU14, a SiC gasifier scroll failed after a total test time of 35 hr in several engine tests. The failure was due to an incomplete brazing joint between the scroll and shroud. The brazing compound formed glasses with machining media and leaked out of the joint during engine tests. Figure 104 shows the fractured gasifier scroll assembly and the fracture origin A.

In Engine S/N 1, BU21, the gasifier turbine failed after 6 hr of engine test time. The gasifier rotor fractured at the stub shaft by high tensile stress, and the inner backplate failed by multiple fractures at the back side near the ID, Figure 105. Failure of both components was caused by excessive pressure at the gasifier turbine backplate cavity, which in turn lifted the inner backplate.

The rotor stub shaft that fractured from tensile stress had an apparent fracture mirror around the failure origin. This distinct fractographic feature differentiated itself from similar rotor shaft failures caused by the complex tensile and vibration stresses

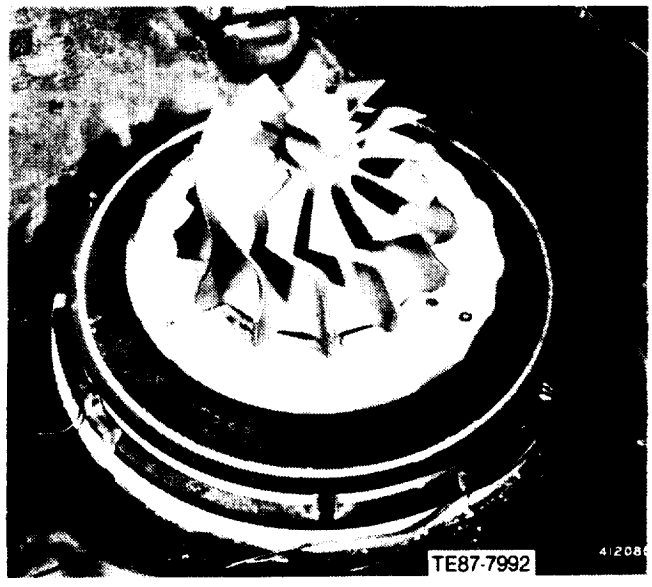

Figure 103. *A Si_3N_4 gasifier turbine rotor lost all inducer tips after engine testing for 99:54 hr in engine S/N 1, BU20.*

resulting from machining or handling damages. Figure 106 shows the fracture surfaces of two rotor stub shafts. The shaft shown on the left, which fractured due to vibratory stress, reveals a lack of a clearly defined fracture mirror.

Failure Analysis After Engine Testing of Multiple Ceramic Components in AGT 100 Engine S/N 1, BU26

Inspection at teardown revealed that all of the ceramic components except the combustor assembly and the interturbine coupling were broken, as

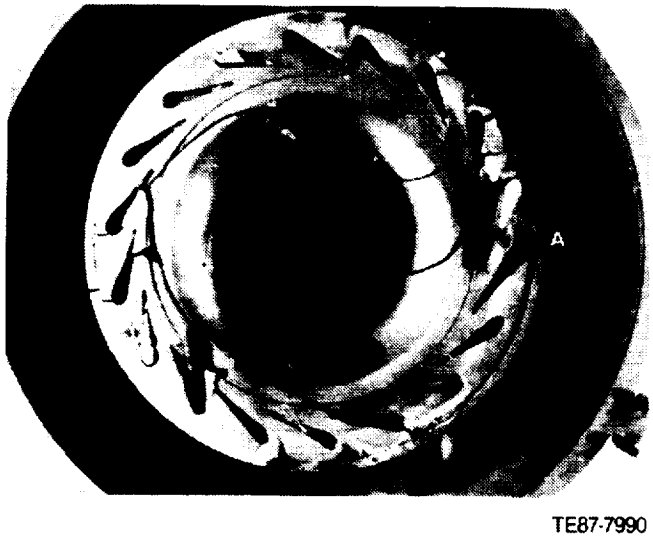

Figure 104. *The gasifier scroll assembly failed in engine S/N 2, BU14. The fracture origin A is located at the bad brazing joint between the scroll and shroud.*

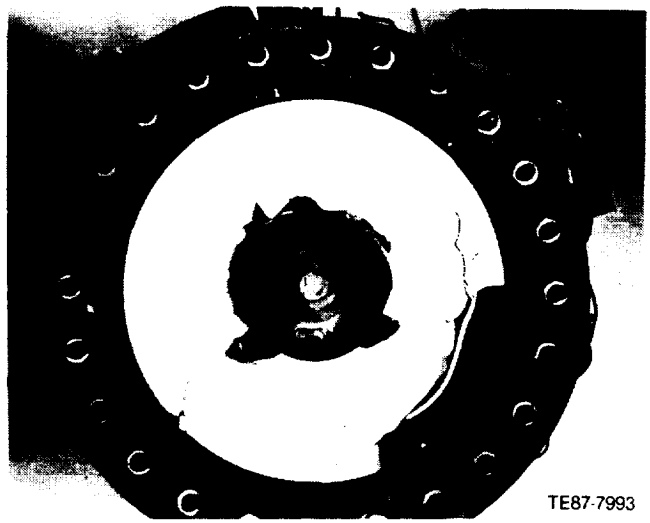

Figure 105. *As-torn-down condition of the gasifier turbine in Engine S/N 1, BU21. The Si_3N_4 rotor snapped at the stub shaft and stuck in the elbow.*

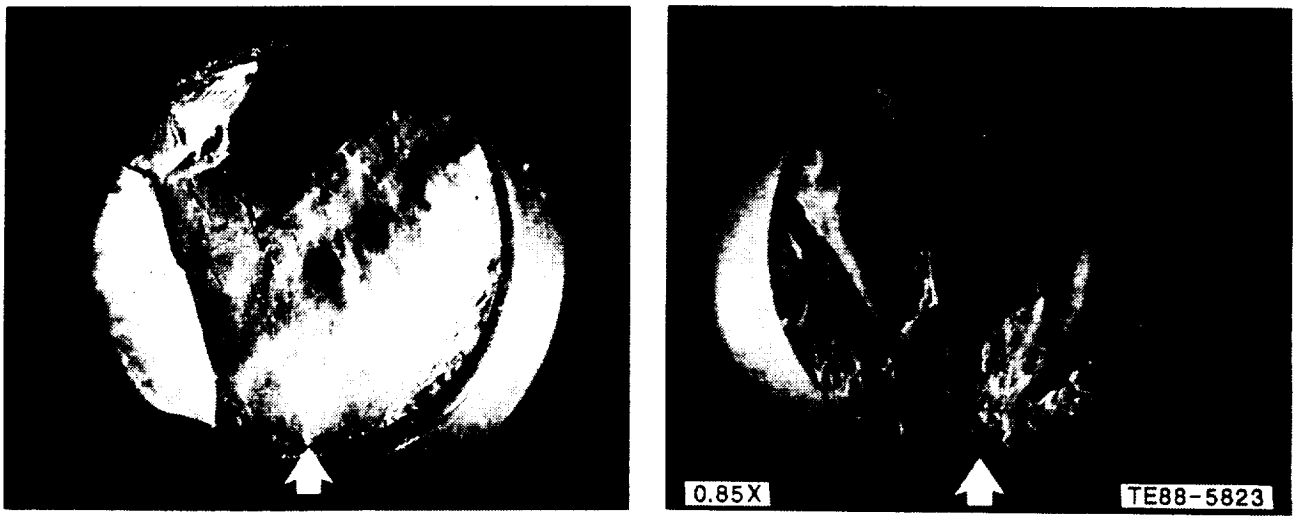

Figure 106. *Examples of Si_3N_4 rotor shafts fractured by vibration (left) and tensile stress (right).*

White arrows point at failure origins.

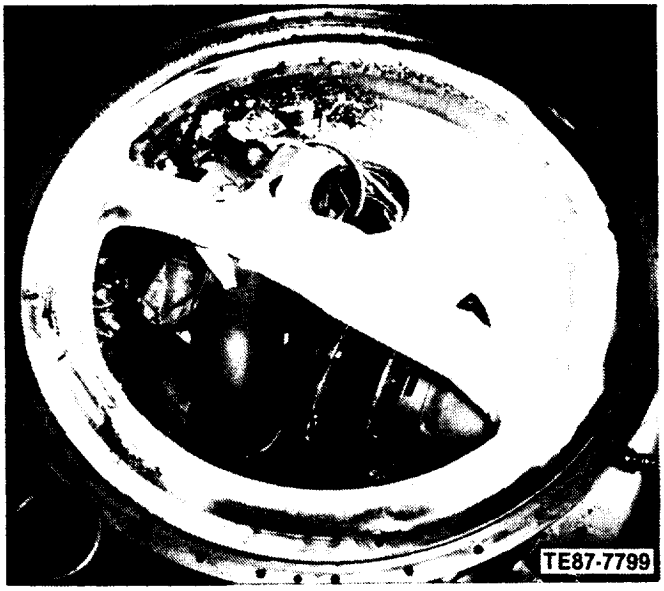

Figure 107. *As-torn-down condition of AGT 100 S/N 1 engine in BU26 revealed by removing the engine cover and the regenerator disk.*

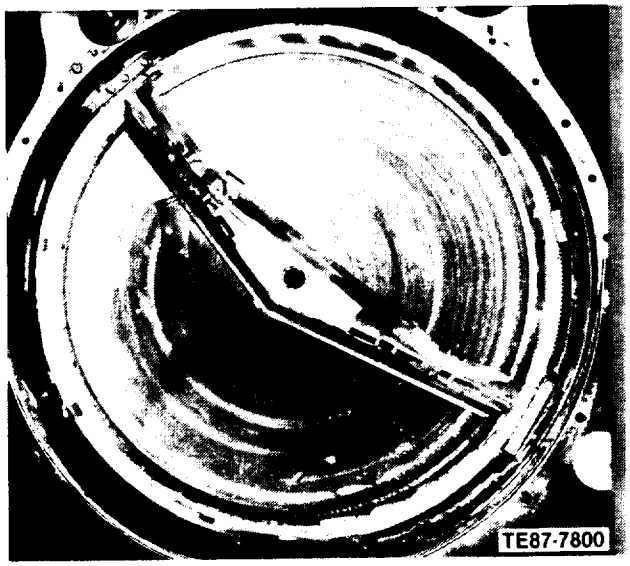

Figure 108. *As-torn-down condition of the regenerator disk. A piece of the power turbine exhaust coupling was wedged between the disk and the seal and cut deep in the disk.*

shown in Figures 107 and 108. After recovering all broken ceramic parts, each component was reconstructed for subsequent fractographic analysis. The failure origin for each component was then

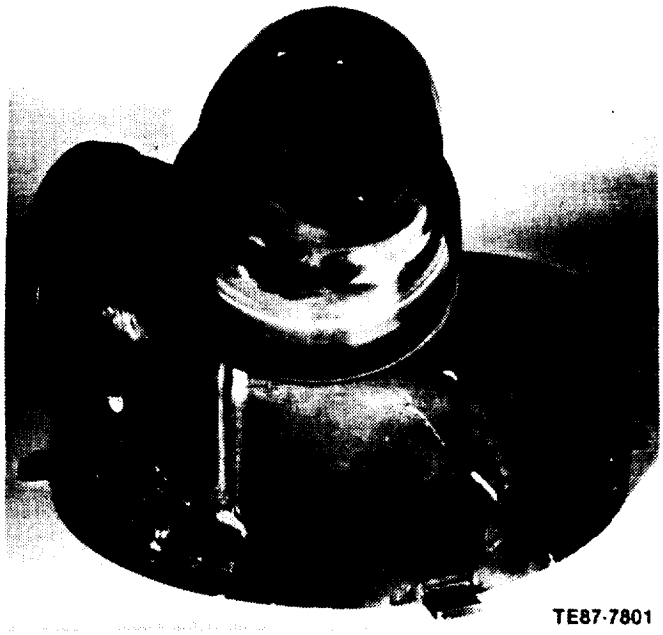

Figure 109. *Reconstructed gasifier turbine scroll assembly. The combustor inlet adapter broke loose along the braze joint.*

analyzed and the information scrutinized in an effort to determine the initial/primary component failure.

Gasifier Turbine Section

Gasifier turbine scroll — The GT scroll assembly broke into rather large pieces. Figure 109 shows the reconstructed scroll. The combustor inlet adaptor broke free from the scroll body immediately along the braze joint. The fracture surface was very smooth. A portion of the braze joint at the fracture surface was discolored (Figure 110) indicating that the crack had been exposed to high temperatures for some time prior to the engine failure. The scroll body was fractured by three cracks as shown in Figure 111. Cracks 1 and 2 originated at the sharp corners of the mating area of the adaptor. The scroll body failed by the mechanical loading of the combustor and by thermal stress.

Gasifier inner backplate — Fracture of this part occurred at the back side of the inner edge and radiated outward. All origins were damaged. On the front face, there was a half ring rub mark and

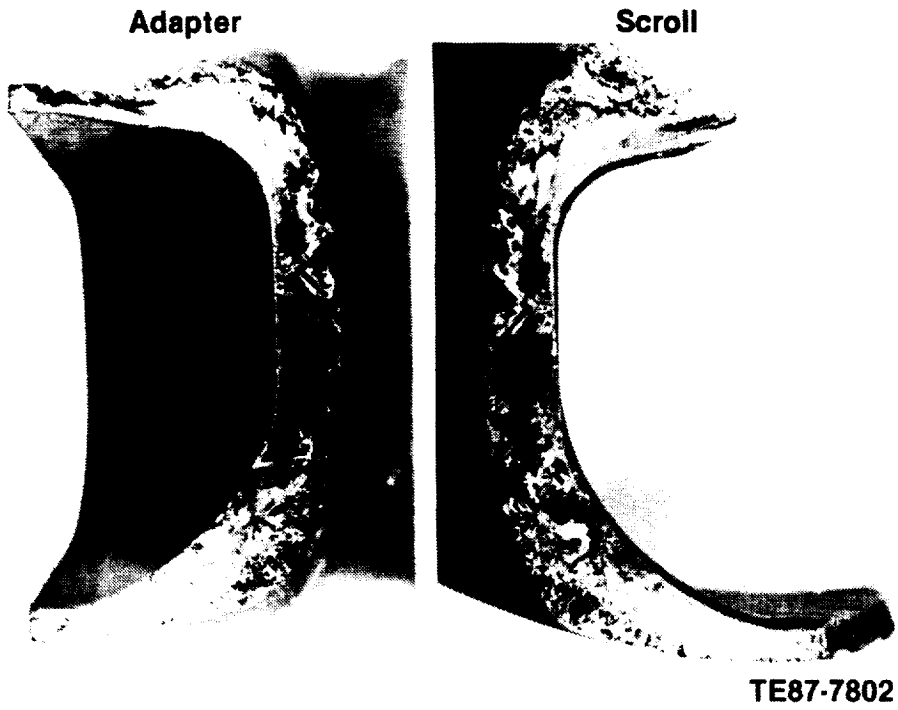

Figure 110. *Braze joint fracture of the scroll combustor inlet adapter.*

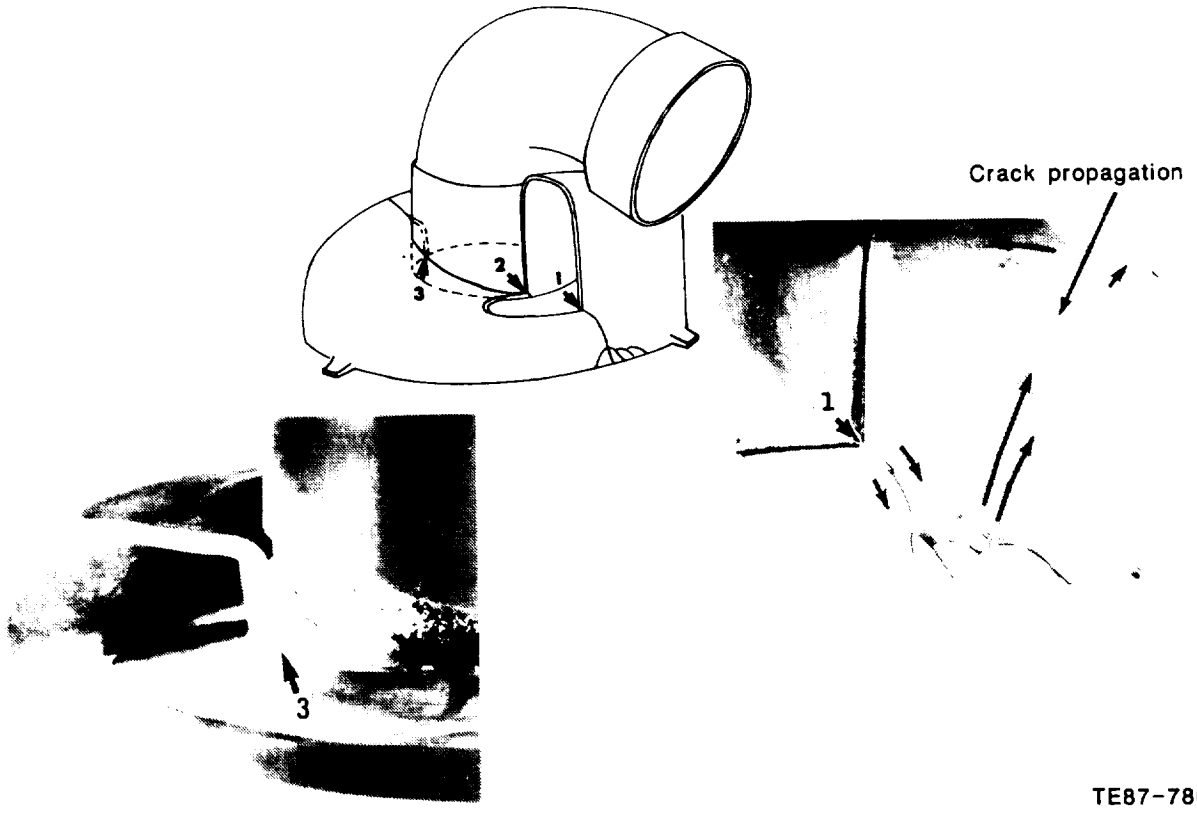

Figure 111. *Fractured gasifier turbine scroll assembly. Black arrows point to three fracture origins at the braze joints.*

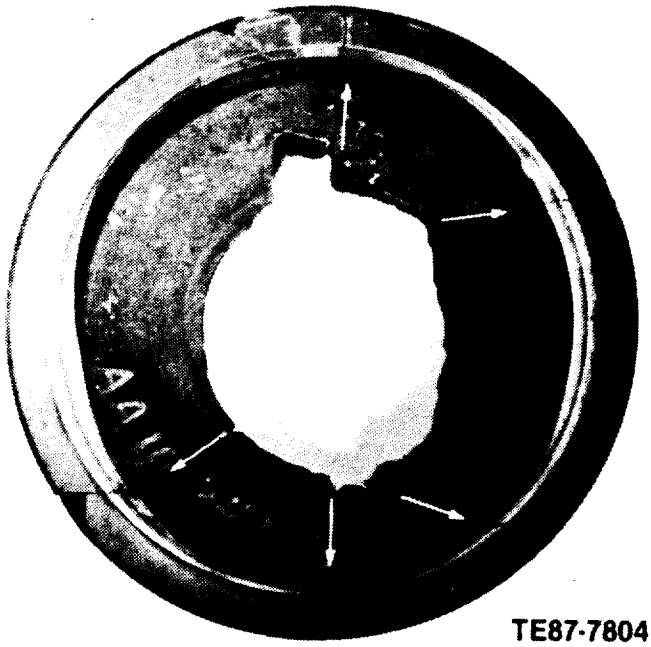

Figure 112. *Reconstructed gasifier turbine inner backplate. White arrows indicate the crack propagation directions.*

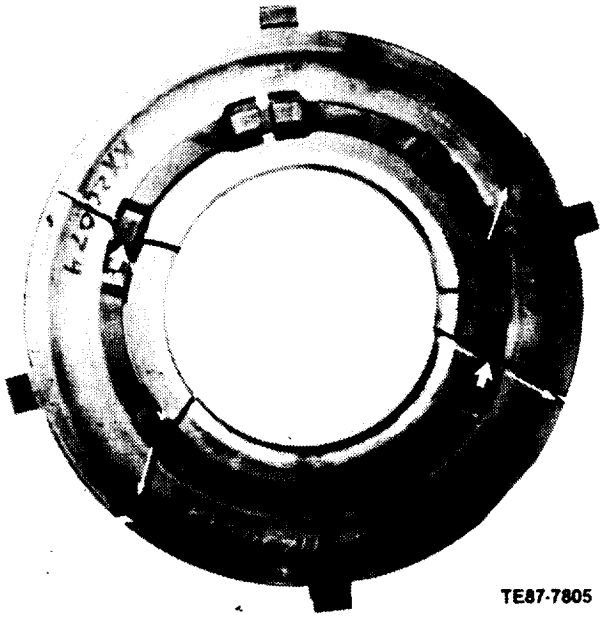

Figure 113. *Reconstructed gasifier turbine outer backplate. The wide arrows indicate the fracture origins at the key slots, and the slim arrows point out crack propagation directions.*

several radial rub marks (Figure112). The location of the ring rub mark matched very well to the edge of the rotor backface. These indications showed that the inner backplate lifted and rubbed the rotor.

Gasifier outer backplate — This part fractured into four major pieces. Two cracks originated at two key slots 180° apart (Figure 113). The other two cracks had origins at the vane pockets on the front side. Since one vane pocket crack was arrested at the key slot crack, it indicated that the plate broke into halves with the key slot fractures first.

Gasifier turbine rotor — The rotor snapped at the stub shaft just above the metal compressor shaft, lost all airfoils, and was wedged inside the scroll shroud (Figure 114). Figure 115 shows the failure origin on the stub shaft from a surface elliptical flaw. The radius of the fracture mirror was 0.56 mm (0.022 in.) and the fracture stress calculated from the radius was 463.3 MPa (67.2 ksi).

Vanes, gasifier turbine and power turbine — There were 18 GT vanes and 20 PT vanes in the engine. Figure 116 shows the as-retrieved condition of the vanes. The trailing edges of the vanes were severely damaged, and the leading edges were still in large pieces. Fourteen (14) of the large chunks of the leading edges belonged to GT vanes. All fracture origins were damaged.

Power Turbine Section

Power turbine inner backplate — This part suffered extensive damage, as shown in Figure 117. Two fracture origins were found at the outside step, almost 180° apart, and ran axially on the flange only. This indicated that the plate was held against the outer backplate. Only radial rub marks were found at the front face of the inner backplate, indicating that the plate was struck by the shattered rotor.

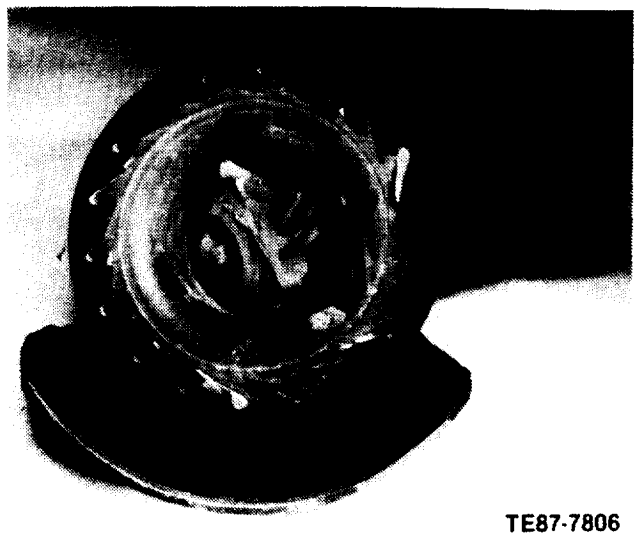

Figure 114. *As-torn-down condition of the gasifier turbine rotor, which was wedged in the scroll shroud.*

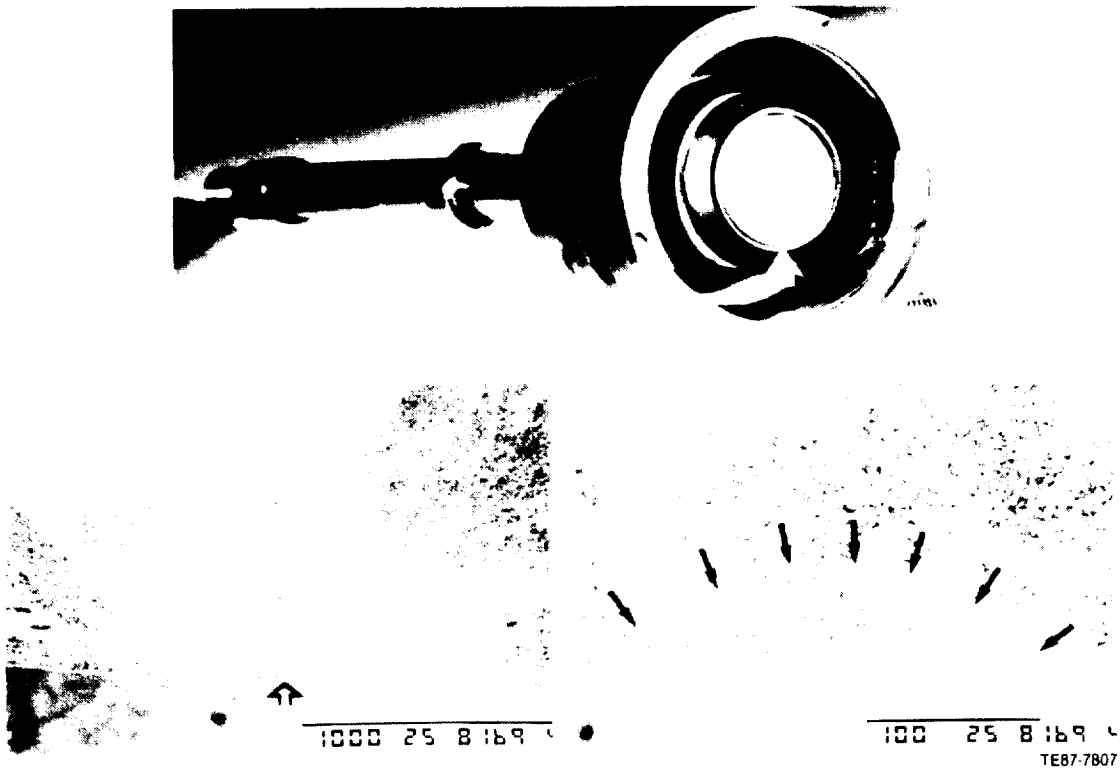

Figure 115. *Fractographs of the stub shaft of the gasifier turbine rotor. The failure origin is outlined by the narrow arrows.*

Figure 116. *As-retrieved condition of gasifier turbine vanes and power turbine vanes.*

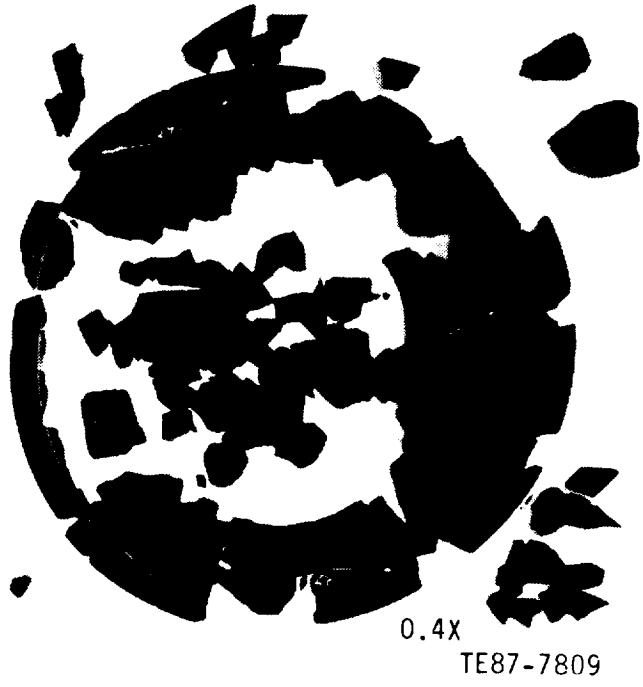

Figure 117. *Reconstructed power turbine inner backplate. The hollow arrows point the failure origins and the slim arrows represent crack propagation directions.*

Power turbine outer backplate — This part fractured in a similar pattern to the GT outer backplate. Fractures were initiated at the key slots and vane pockets. A greater number of fracture origins were observed for the PT outer backplate, as shown in Figure 118.

Power turbine rotor — The rotor broke into many small pieces. Rub marks on the inner backplate indicated that the rotor was broken before it contacted the plate. However, a failure origin was also located at the stub shaft right above the compressor shaft, Figure 119. The origin had numerous small subsurface pores. The fracture mirror radius was 0.28 mm (0.011 in.) and the fracture stress calculated was 636.4 MPa (92.3 ksi).

Power turbine scroll — The scroll assembly broke into many pieces (Figure 120). The reconstructed scroll showed that the major cracks originated at the outside edge. They were long, running parallel to the flow path in the scroll. Three cracks originated at the inside edge of the scroll at the braze joint. These cracks followed curved paths and terminated at the braze joint. All fracture origins in the shroud were located around the braze joint to

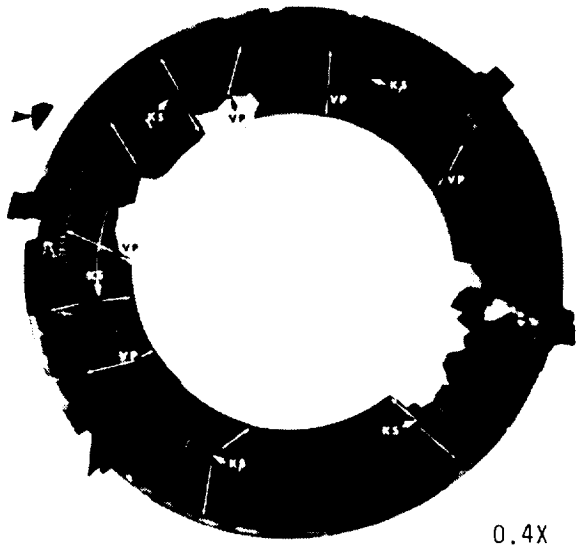

Figure 118. *Reconstructed power turbine outer backplate. Multiple fractures occurred at key slots (KS) and vane pockets (VP) on the other side of the plate. Slim arrows represent the crack propagation directions.*

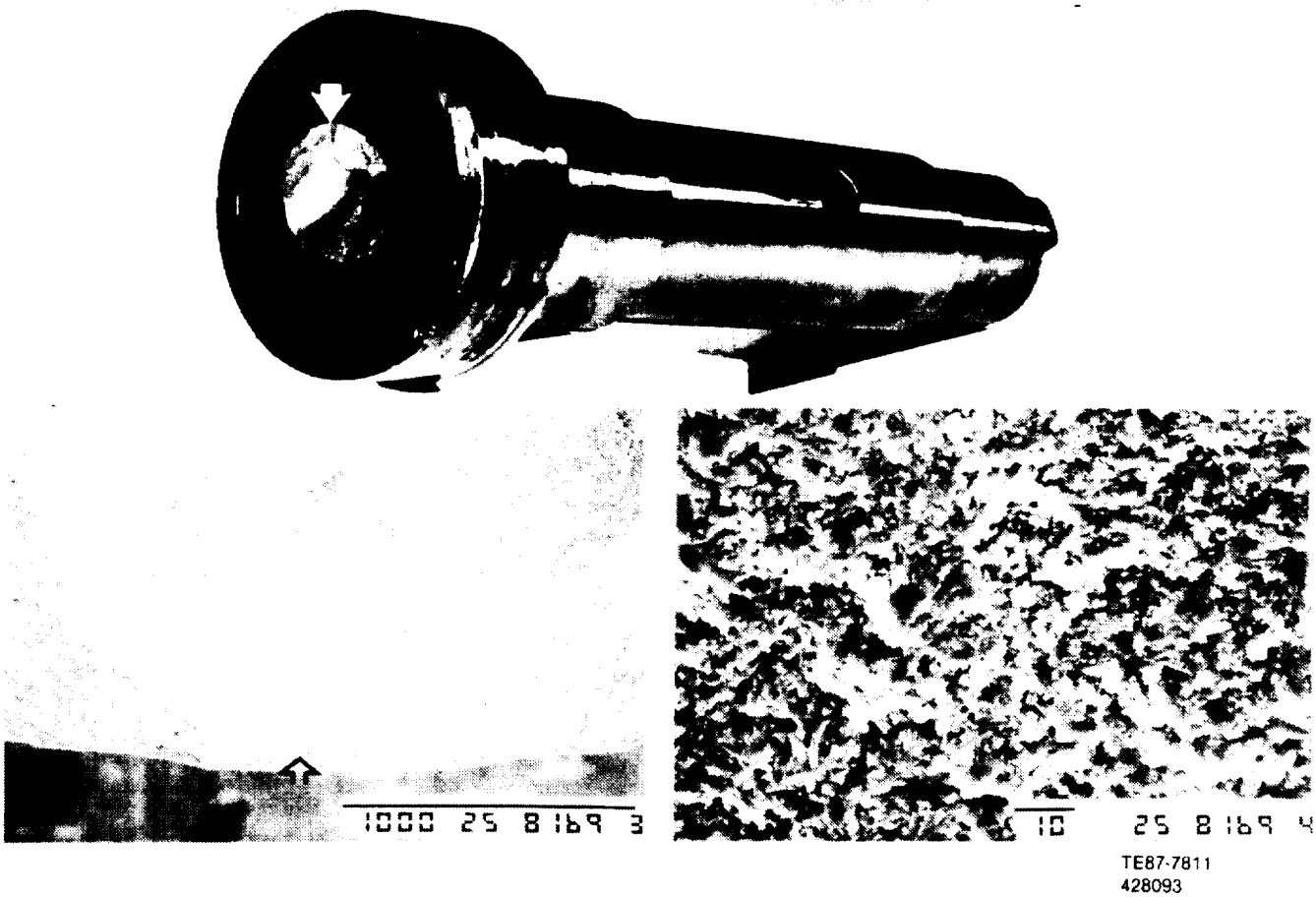

Figure 119. *Fractographs of the stub shaft of the power turbine rotor and the failure origin.*

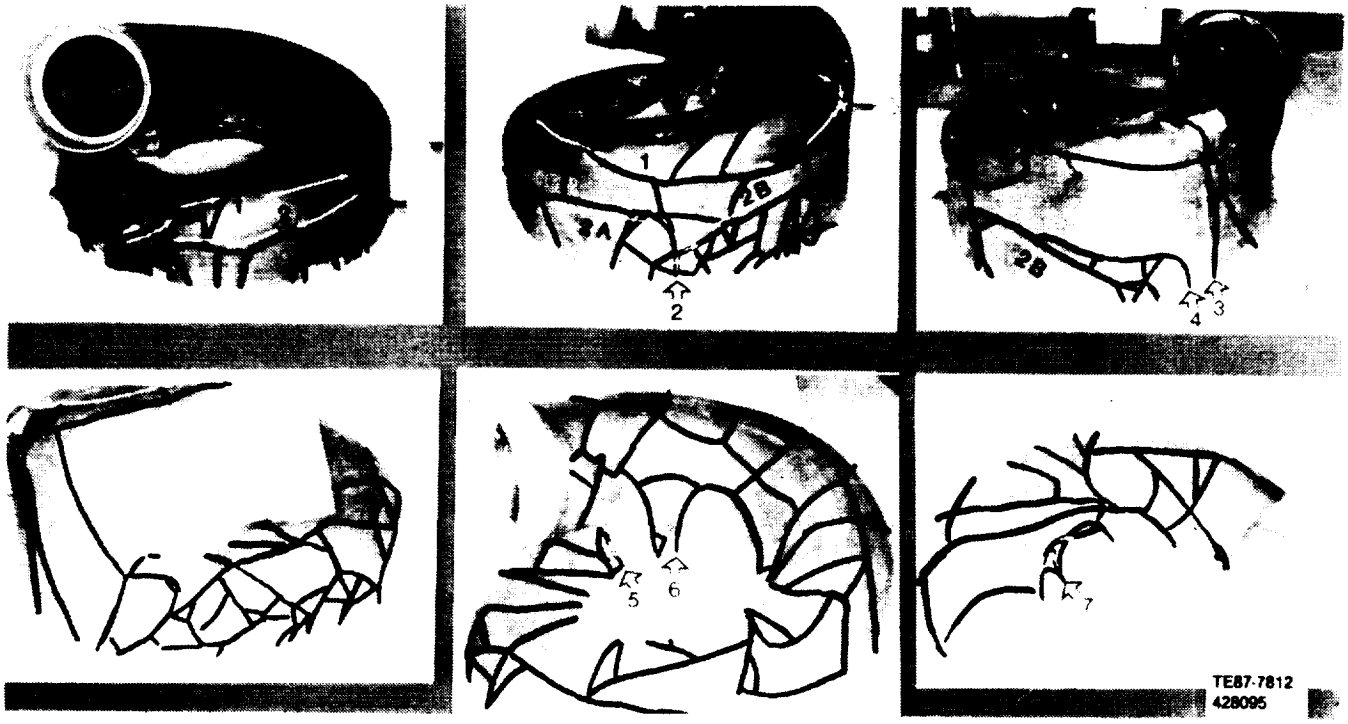

Figure 120. *Reconstructed power turbine scroll assembly at different angles. The cracks are enhanced by heavy dark lines.*

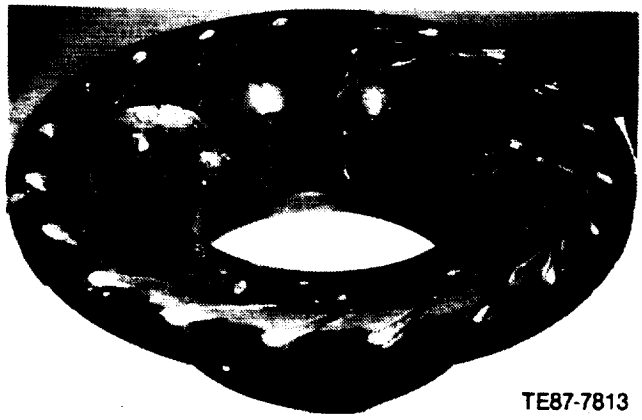

Figure 121. *Reconstructed power turbine scroll shroud.*

the scroll. Two heavy abrade marks were on the shroud surface and probably were caused by an incursion with the PT rotor (Figure 121).

Power turbine exhaust coupling — As shown in Figure 122, all cracks were initiated from the side of the PT scroll outlet. One of two probe holes was intersected by one crack. The hole was not the primary failure origin of the coupling. One piece of the coupling was wedged between the regenerator disk and the metal spring seal.

Exhaust duct/bulkhead — Figure 123 shows the locations of the fracture origins and direction of cracks in the bulkhead. Crack 1, which originated at the reduced wall thickness of the inlet, preceded over other cracks and was the primary failure origin of the bulkhead. Crack 4 was the result of contact damage with the connecting duct of the GT scroll assembly.

Conclusions Drawn from Failure Analyses

Damage to the power turbine section was much more severe than to the gasifier section. Analyses showed that the power turbine section failed in a complex mode involving impact (rotor airfoils and vanes), lifting of backplates, rubbing of the rotor

Figure 122. *Fracture pattern of the power turbine exhaust coupling. Dark arrows represent crack propagation directions. The lower photo shows that the instrumentation hole was not a failure origin.*

Figure 123. *Reconstructed exhaust duct/bulkhead. The heavy arrows and numbers point to the failure origins. The slim arrows represent the crack propagation directions.*

with the backplate, and the fracture of the braze joint of the scroll. Failure analyses do not clearly vindicate the power turbine as the primary cause for engine failure. Power turbine failure was probably a consequence of impact damage from gasifier turbine failure debris.

Gasifier turbine analyses do not clearly indicate which component failed first. The braze joint at the combustor inlet adapter of the scroll showed cracking and oxidation prior to engine failure, as well as very small chipping at the exposed edges. The scroll body/shroud braze joint also showed evidence of small chipping indicating that the braze joints were in distress. For a complete discussion on the failure scenario, see subsection 3.6, Gasifier Turbine Static Structure.

III. CERAMIC COMPONENT DESIGN, ANALYSIS, EVALUATION, AND DEVELOPMENT

3.1 SUMMARY

During the course of the AGT project, ceramic components were designed and fabricated for the entire hot section of the AGT 100 engine. A cross-sectional view of the engine is shown in Figure 124. The components made of ceramic are the following:

- combustor system
  - combustor body
  - dome
  - pilot tube
  - dilution band
- gasifier turbine rotor
- gasifier turbine static structure
  - scroll/shroud assembly
  - outer backplate
  - inner backplate
  - vanes (18)
  - shim insulator ring
  - interturbine coupling
  - coupling seal rings (2)
- power turbine rotor
- power turbine static structure
  - scroll/shroud assembly
  - outer backplate
  - inner backplate
  - vanes (20)
  - shim insulator ring
  - exhaust coupling
  - coupling seal rings (2)
- regenerator system
  - regenerator disk
  - bulkhead/seal platform

The following are the AGT 100 ceramic component suppliers:

- Standard Oil (Carborundum)
- Corning Glass
- GTE Laboratories
- Kyocera
- Norton
- Pure Carbon
- Coors Porcelain
- Feldmuhle
- Asahi Glass
- AC Sparkplug
- Societe Europeane de Propulsion
- c-cat
- Amercom/3M
- NGK

Table IV shows the various material systems that have been successfully tested in engine or test rigs. Figure 125 shows a representative sample of the ceramic components in the AGT 100 engine.

During the development process, these components were subjected to numerous rig tests and proof tests prior to being put into an engine test. Several components were fabricated of ceramic from the onset of the program and were part of every engine test. Others were introduced to engine test in a systematic manner as ceramic parts replaced their metal counterparts one by one. A total of 572 hr of total engine test time was accumulated during this program. Of that total, 415 hr were under hot running conditions. Table XXII shows engine test times, by component. For each component listed, the maximum time accumulated by an individual part is shown as well as the total time for all like parts. For example, one of the ceramic combustor domes accumulated 135:06 hr of engine test time, while the summation of all ceramic combustor dome engine testing was 400:41 hr. Because this value is less than the 572 total hours of engine testing accomplished in this program, it indicates that some engine testing was done with a metal combustor dome.

The following subsections describe the design and development of the major ceramic components of the AGT 100 engine. Each subsection first summarizes the accomplishments and objectives of the design, and then discusses the development process. In addition, one subsection details the probabilistic design techniques used to design and evaluate the ceramic components. However, this is all preceded by a subsection that lists the major conclusions that have been drawn as a result of designing and developing ceramic components during the AGT program.

3.2 OBSERVATIONS FROM WORK ACCOMPLISHED IN AGT 100 PROGRAM

The following observations have been made as a result of designing and developing ceramic components during the AGT project:

1. The Advanced Gas Turbine project has successfully demonstrated concept feasibility and the performance potential of using structural ceramics in an automative gas turbine. Design methodology has evolved, and initial ceramic data bases

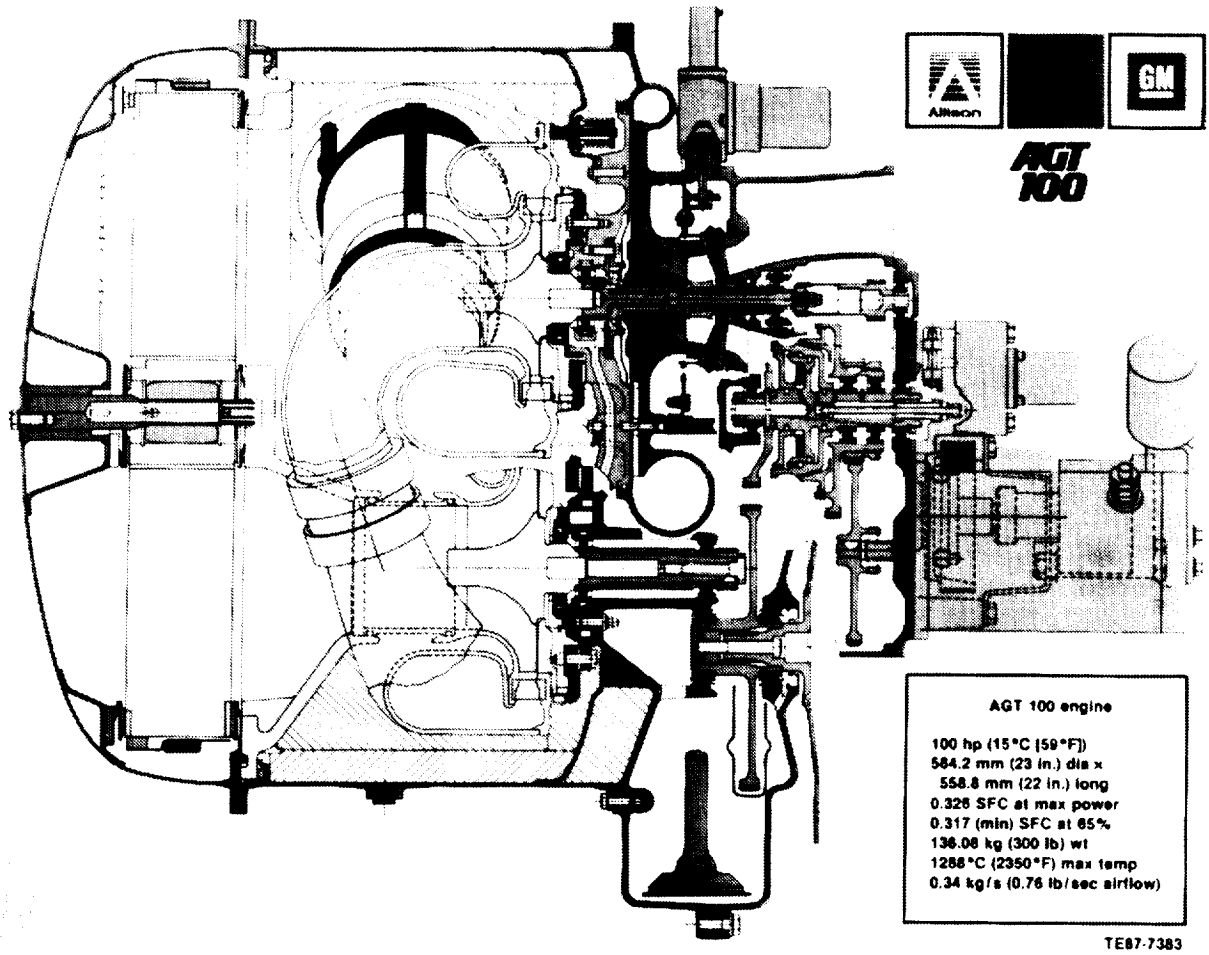

Figure 124. *Cross section of AGT 100 engine.*

have been generated in an engine environment for various materials and component designs. Ceramic component evaluation tools have been established including test rigs and test procedures.

2. FOD to rotor blades and vanes is a major concern. Current designs/materials are very vulnerable to FOD, as shown by the rotor in Figure 126. Additional development is needed to create improved designs using better materials having increased toughness to make the rotors and vanes more resistant to impact damage. Design modifications to reduce or eliminate the foreign objects from the gas stream are also required.
3. Although considerable progress has been made during the AGT project, additional development is needed in ceramic component processing. Current techniques have low yields and result in a wide scatter in material properties (i.e., the processes are not sufficiently repeatable). There has been difficulty in obtaining test bar strength in actual components. The thick cross section of the radial rotors contributes to these difficulties.
4. Current materials/designs have inadequate strength and/or undesirable thermal properties to tolerate high thermal stresses generated by the rapid transients required of an automotive powerplant. AGT engine testing had to be conducted in a manner to minimize transient effects to at least assess steady state capability of the ceramic components.
5. The current fabrication process used to make regenerator disks results in inconsistent quality, as shown in Figure 127, and nonuniform strength within the disk. In addition, the process is labor intensive and not conducive to low-cost mass production. A new technique, such as an extruded fabrication process, is needed for the disk

Table XXII.
Total engine test times (including motoring) and total hot engine test times of AGT 100 ceramic components, in hours: minutes (through AGT 100 S/N 1 BU26 and AGT 100 S/N 2 BU19).

	Engine time		Hot time	
Ceramic component	High time part	Total time	High time part	Total time
Combustor				
Dome	135:06	400:41	97:26	291:10
Body	213:54	572:21	167:58	415:29
Pilot tube	119:25	572:21	94:33	415:29
Dilution band	246:46	572:21	167:19	415:29
Gasifier turbine				
Vane	71:22	192:24	66:08	157:54
Rotor	100:17	142:12	82:54	117:41
Scroll	29:49	77:31	23:26	61:30
Inner backplate	52:57	152:10	38:32	118:34
Outer backplate	22:25	77:31	19:06	61:30
Power turbine				
Vane	71:22	99:50	66:08	87:32
Rotor	6:01	6:01	4:21	4:21
Scroll	22:42	22:42	18:53	18:53
Inner backplate	17:41	22:42	14:32	18:53
Outer backplate	22:42	22:42	18:53	18:53
Regenerator				
Disk	267:10	572:21	212:38	415:29
Bulkhead	160:58	572:21	127:35	415:29
Miscellaneous				
Shim, gasifier turbine	126:21	572:21	119:11	415:29
Shim, power turbine	126:21	572:21	119:11	415:29
Coupling, interturbine	37:22	69:10	29:02	54:39
Coupling, power turbine	17:41	23:42	14:32	18:53

that will lead to improved quality, uniform strength, and the potential for less expensive manufacture. In addition there is a need for regenerator seal development. Current seal design is incapable of the maximum steady state temperature required for the RPD.

6. Ceramic inspection methodology has been established and developed including photoacoustic microscopy, ultrasonic, and microradiography. Additional development is required, however, since current technology cannot quantitatively identify, a priori, the potentially fatal flaws in the ceramic components.
7. Certain ceramic composite components have been successfully demonstrated with initial test experience.
8. Durability of the AGT 100 ceramic combustor assembly has been demonstrated in over 415 hr of hot engine testing and 161 hr of hot testing in static test rigs. Minor chipping of ceramic components has occurred but recent incidents were caused by misfit interference with other engine components that have been corrected. Additional development and testing is required to perfect long term combustor fuel system performance and to minimize soot accumulation in the combustor.

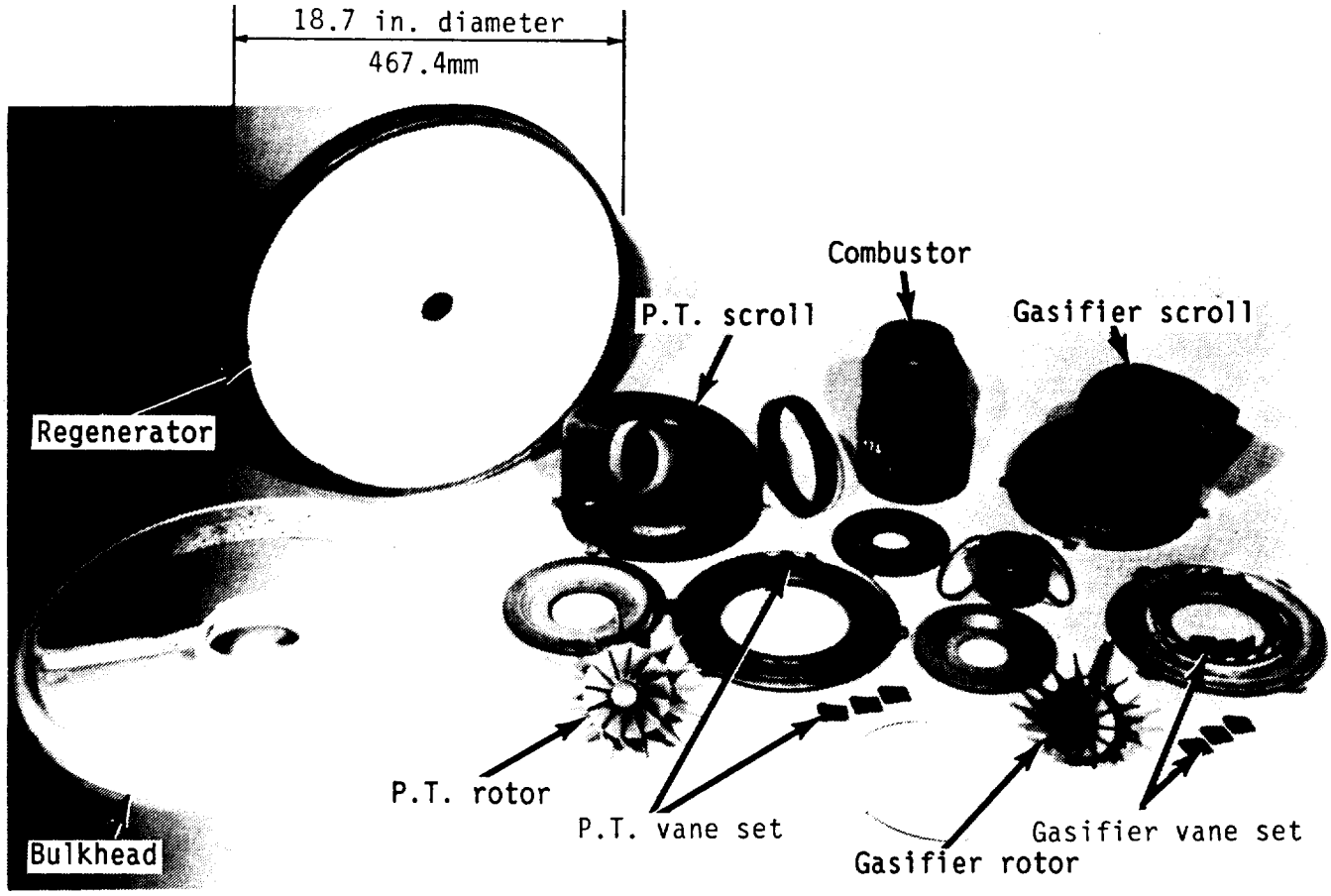

Figure 125. *Ceramic hot section components used in AGT 100 engine.*

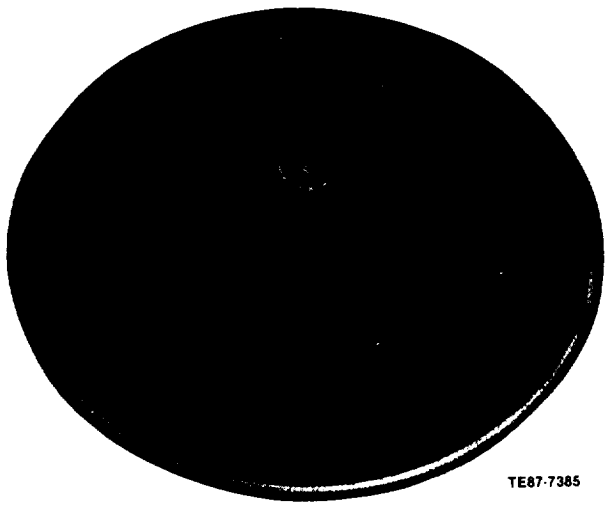

Figure 126. *Ceramic gasifier turbine after chip ingestion.*

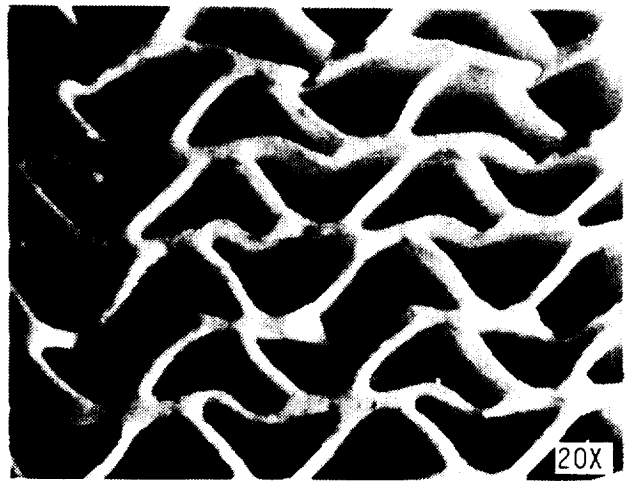

Figure 127. *Regenerator disk showing inconsistent structural uniformity.*

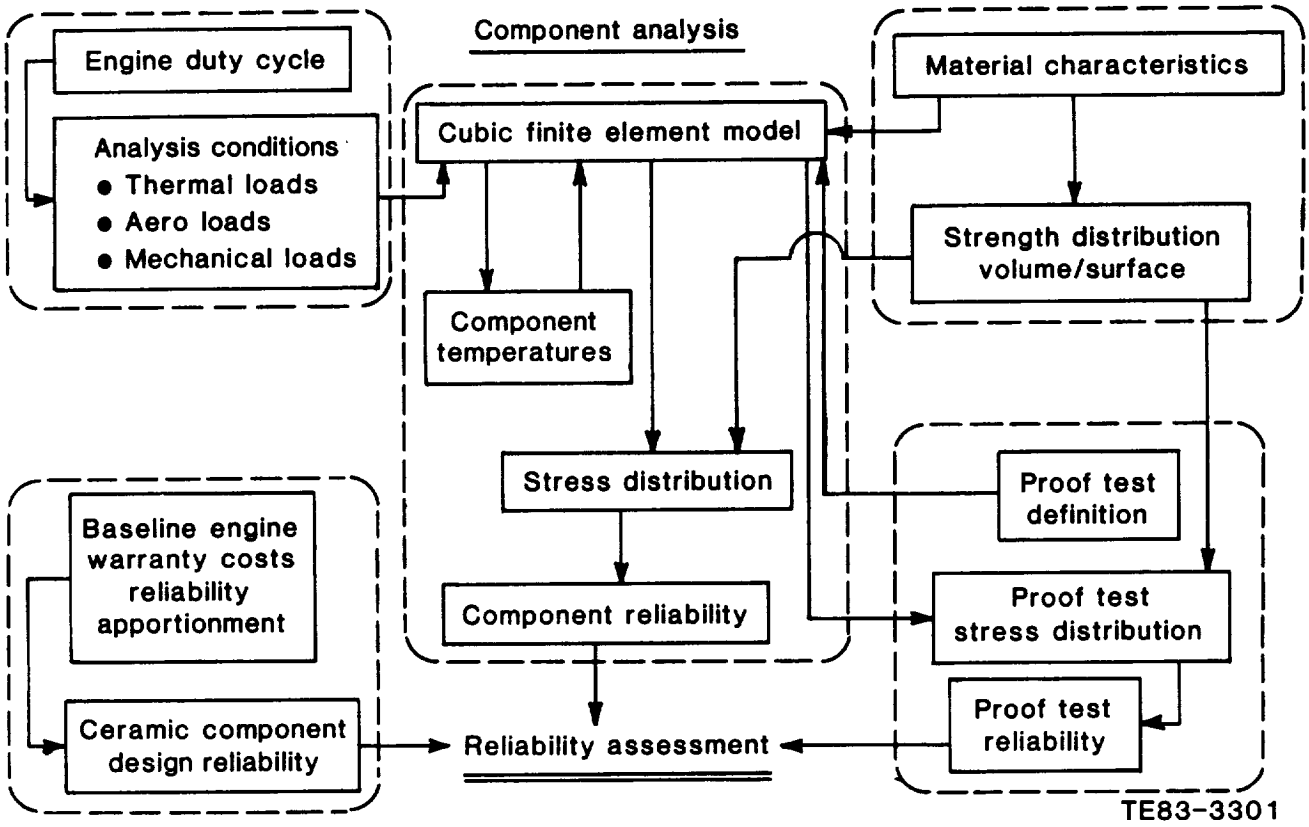

Figure 128. *Ceramic component probabilistic design methodology.*

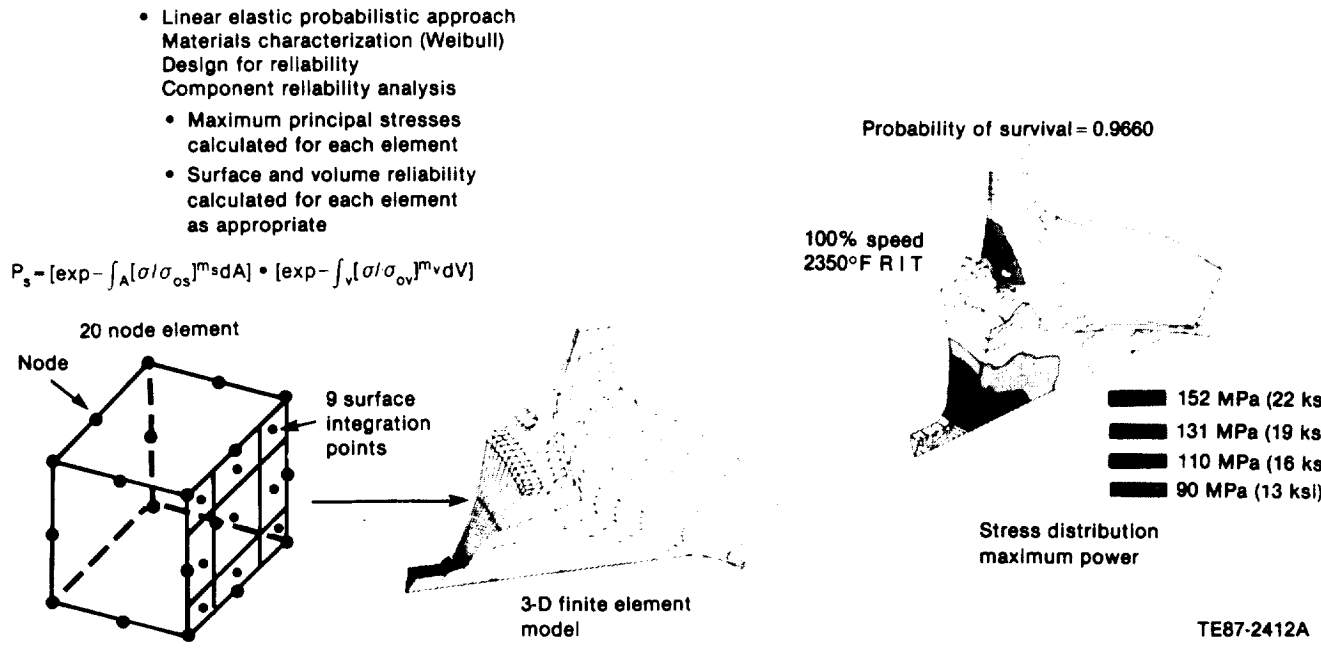

Figure 129. *Ceramic component design methodology.*

3.3 DESIGN METHODOLOGY

Introduction

Ceramic components for the AGT 100 program were designed using methodology developed especially for brittle materials. Linear elastic, fast fracture probabilistic analysis techniques, using two- and three-dimensional finite element models, were used to design and evaluate each component. Extensive heat transfer analyses of critical operating conditions, which typically occur during engine transients, were conducted to select the most severe cases for stress analysis. Dynamic analyses were conducted for the rotating airfoils. Component reliability was assessed by application of Weibull characterization of the material strength and compared with reliability goals. Methods of interfacing proof tests have also been developed and incorporated into the reliability analysis routines. These methodologies have been substantiated by the successful demonstration of ceramic components in the test engine.

Discussion

The brittle nature and low fracture toughness of current ceramic materials have required the development of new design methodologies relative to traditional schemes for ductile (metal) structures. These methodologies allow the successful design of structural ceramic components for turbine engine applications. This, in conjunction with the unique, high temperature capabilities of ceramics, allows for realization of the significant improvements in energy use associated with high temperature engine operation.

A probabilistic design methodology has been developed that addresses the statistical nature of a ceramic's strength function and the reliability requirement for the component in service. This methodology is schematically represented in Figure 128. The reliability requirements for the AGT 100 engine were based on failure rates of production automobile engines. A similar failure rate was established for the design of the AGT 100 engine for reasons of comparable warranty cost exposure. The ceramic components reliability service life goal was apportioned for this engine reliability. Table XXIII lists the design reliability goals for the ceramic components.

The material surface and volume unit strengths are characterized by two parameter Weibull functions derived from four point bend tests MOR bars. The engine operating environment is input to sophisticated two- and three-dimensional finite element models of the components to analytically assess the fast fracture reliability. An example of the analysis of the gasifier rotor is shown in Figure 129.

Another key element in this methodology is the proof test. This test, which is structured to expose the ceramic component to service-like stress gradients prior to service, is an integral part of the methodology. The proof test can be configured for static, dynamic, thermal, or combined loads. The test can be physically interpreted as a technique for culling the lower strength components from a population and thus enhancing operational reliability of the remaining population. This is shown in Figure 130. In the absence of a proof test, higher strength material is required to achieve the goal reliability.

An essential partner to the linear, fast fracture probabilistic design methodology is the ceramic component development cycle.

The cycle, schematically shown in Figure 131, identifies the consideration of ceramic component fabricability and engine test as the closed loop assessment of the design process. Various NDE schemes have been developed for measuring the quality of ceramic fabrications: photoacoustic emissions, ultrasonic scanning, microfocus radiographic along with conventional FPI and visual examination. These techniques are fully discussed in Section II. Engine test provides the final verification of the design methodology in the design/development cycle.

The probabilistic, fast fracture design methodology was developed under the CATE and AGT 100 programs and has resulted in the successful test demonstration of multiple ceramic components.

3.4 COMBUSTOR ASSEMBLY

Introduction

The AGT 100 combustor assembly is a premix, prevaporization configuration similar to other Allison low-emission combustors. Variable geometry is used to maintain low emissions throughout the operating range of the engine. Ceramic materials are used in four combustor assembly components to allow operation without air cooling. The ceramic combustor components have been used in all AGT 100 test engine assemblies, except for the dome, and also in static combustor test rigs and the turbine static structure thermal shock test fixture. Operating temperatures as high as 1168°C (2130°F) have been experienced in the engines while temperatures up to 1288°C (2350°F) have been

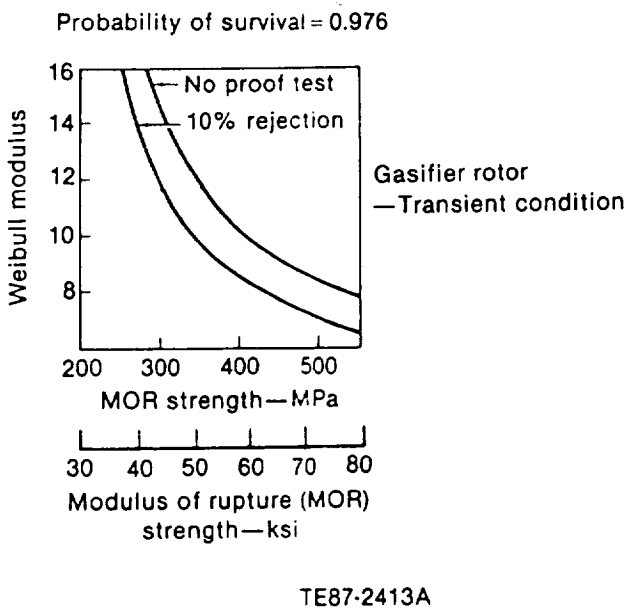

Figure 130. *Influence of proof test on required SiC material strength for gasifier rotor.*

achieved in the combustor test rig. Pollutant formulation in the AGT 100 combustion system is negligible with NOx emissions an order of magnitude below program goals. The combustion system has demonstrated multifuel capability using three fuels of widely varying physical properties.

Sintered SiC has been the primary material used in the combustor dome, body, dilution band, and pilot burner tube. SiC/SiC composite ceramic combustor bodies were tested in the combustor test rig to 1288°C (2350°F). Siliconized SiC combustor bodies were procured but not tested.

Objective

The requirements of the combustor assembly design are the following:

- to provide means to deliver to the gasifier turbine a uniformly mixed carbon-free combustion gas at a temperature up to 1288°C (2350°F)
- to provide low emission exhaust gas products:
  - hydrocarbon—0.26 g/km (0.41 g/m)
  - carbon monoxide—2.11 g/km (3.40 g/m)
  - oxides of nitrogen—0.25 g/km (0.40 g/m)
- to be constructed of materials that permit operation to 1288°C (2350°F) without cooling
- to maintain a constant percent pressure drop (2 1/2%) over a wide flow factor range
- to provide multifuel operation capability

Table XXIII.
Design reliability goals, AGT 100 engine ceramic components.

Failure rate of 0.25 major failures per engine per 100,000 miles.

Ceramic components	Probability of survival
Gasifier section	
Combustor	0.99250
Scroll	0.99439
Vane (each)	0.99875
Rotor	0.97625
Power turbine	
Scroll	0.99439
Vane (each)	0.99875
Rotor	0.97625
Exhaust duct	0.999375
Regenerator	0.99813

- to have a probability of survival of 0.999375 at each failure site for an operational life of 3500 hr

Discussion

The combustor concept used in the AGT 100 engine is a variable geometry prechamber configuration. The design features a swirl prechamber followed by a sudden expansion to a reaction zone that is closely coupled to a dilution zone. Features necessary for successful low emissions operation include prevaporized-premixed fuel and air, low reaction zone temperatures, and variable geometry, which provides control of both primary zone and dilution zone air admission.

A low fuel flow pilot burner is used to facilitate initial main fuel ignition with a negligible emission spike. Flameout protection is also provided with the pilot. A combustor assembly that uses an increased capacity electric ignition system that takes the place of the pilot burner has also been fabricated and tested.

Ceramic materials have been used in four combustor assembly detail components to provide design goal durability at the high AGT 100 operating temperature 1288°C (2350°F) without cooling and to avoid the use of high cost strategic materials. The four ceramic components are the following:

- combustor body
- combustor dome
- dilution band
- pilot tube

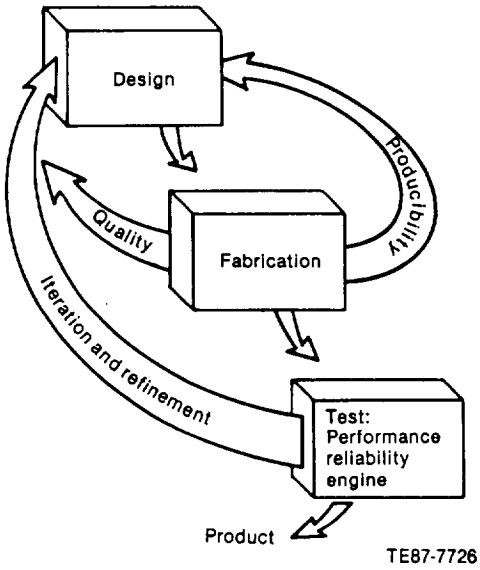

Figure 131. *Design/development cycle emphasizing ceramic component fabricability and test.*

These components and associated metal combustor components are shown in Figure 132. The combustor body assembly (including dilution band, dome, preswirler, and variable geometry) is held against the gasifier turbine scroll by three spring loaded rods as shown in Figure 133. The center body assembly, pilot flame holder, and ignitor plug attach to mounting flanges on the outer surface of the outer combustion case. The primary material used in the ceramic combustor components is SASC. A heat transfer analysis was performed on the combustor at the conditions corresponding to a vehicle speed of 96 km/h (60 mph). The COSMIC (computation of swirl/mixing in combustors) computer program was used to generate the internal flow field and to define the velocities and temperatures used as the boundary conditions for this analysis.

The combustor temperatures predicted by the heat transfer analysis were relatively low and quite uniform. The maximum temperature on the cover plate (dome) was 1041°C (1906°F) and was located near the outer diameter. The minimum temperature of 1037°C (1888°F) was located near the prechamber exit. The maximum temperature in the cylindrical portion of the combustor was 1170°C (2138°F) and was located at the exit; the minimum was 1020°C (1886°F) located about 1.3 mm (0.05 in.) below the front edge of the cylinder.

These temperatures were then used as boundary conditions for a stress analysis of the steady state, 96 km/h (60 mph) condition. An analysis of the cover plate (dome) was not made because the thermal gradients were too low to produce any significant stresses. In the cylindrical portion of the combustor, the computer analysis predicted low stresses with the maximum stress being approximately 10 MPa (1.45 ksi). This level would yield a probability of failure of about 10^{-12}.

The stresses that result from the calculated thermal gradients have been analyzed. The maximum thermal gradients occur 8 sec after the start of the transient cycle; therefore, this condition was chosen for analysis. The second largest thermal gradient occurs 6 sec after the start of the transient cycle, and the resulting stresses were determined for this condition as well.

A summary of the thermally induced stresses is given in Figure 134. Note that the maximum stress during the transient cycle is more than four times the stress at steady state. However, the stress is still very low and leads to a probability of failure of 1.7×10^{-8} (1 failure in 59 million). The stress at the 6-sec condition was considerably less than that at 8 sec.

The heat transfer and stress analysis of the combustor assembly are reported in greater detail in NASA Report CR-165346, July 1981.

Analysis of Thermal Growth of Combustor Assembly

During several tests involving ceramic gasifier turbine static structure assemblies, fractures occurred on the cross-key slots located on the ceramic turbine outer backplate. Subsequent to revisions made to the turbine hardware to increase clearances in the cross-key slots and to increase the flexibility of the interturbine coupling, another cross-key slot failure occurred.

Attention was then focused on the thermal expansion of the combustor assembly, which, if greater than allowed for by the combustor mounting system, would cause an unintended load to be imposed on the gasifier turbine static structure and ultimately the cross-key slots on the gasifier turbine outer backplate. These cross-key slots position the turbine static structure in the engine.

The combustor assembly is loaded against the gasifier turbine scroll by three spring-loaded rods as shown in Figure 135. An analysis of the thermal growth of the combustor showed that the combustor and turbine scroll grow 2.46 mm (0.097 in.) in length at RPD operating conditions. If this growth occurs rapidly (start-up transient) before the outer engine structure heats up, the 2.46 mm (0.097 in.) expansion must be accommodated by the springs located at the outer end of the rods. (After engine

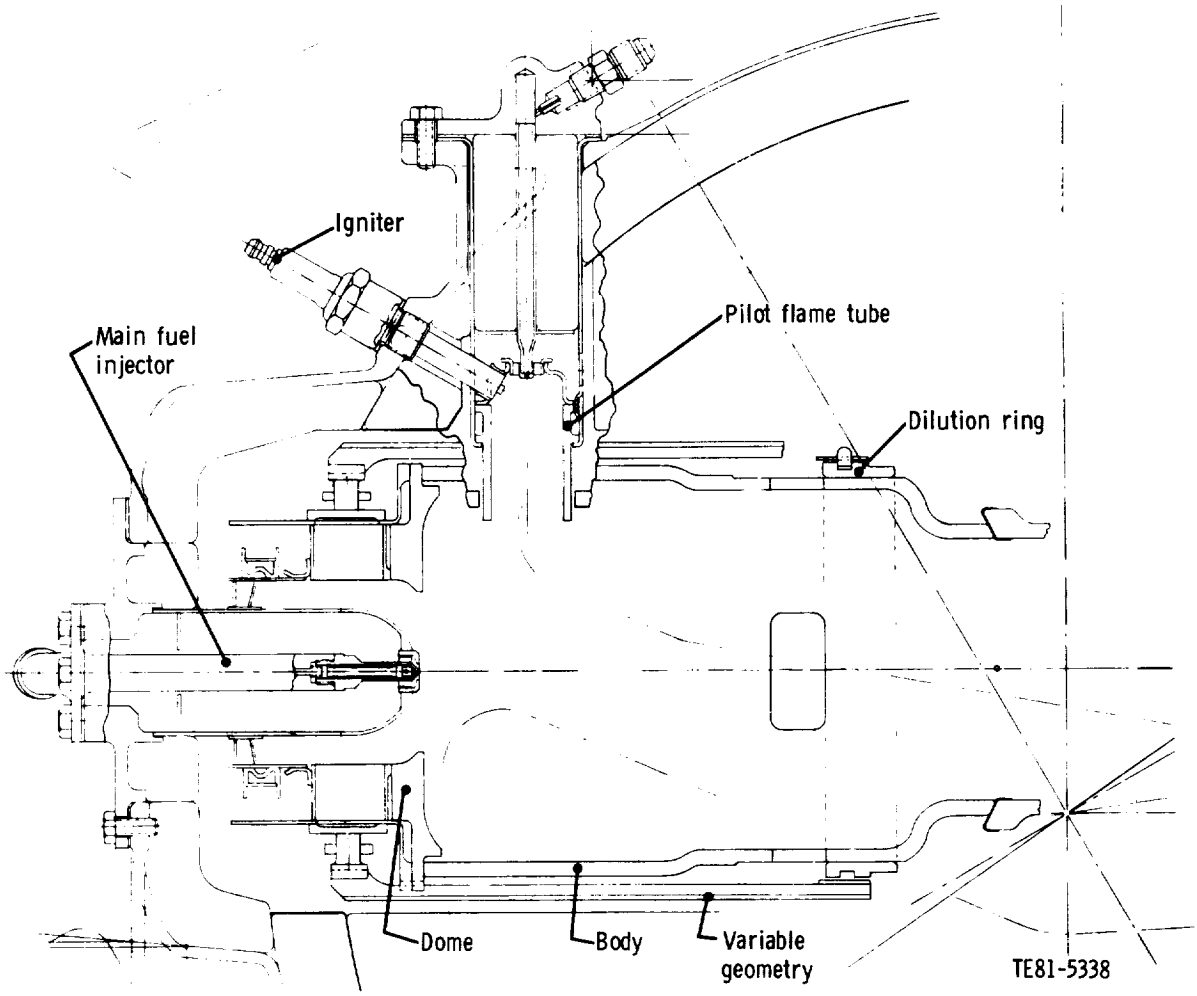

Figure 132. *Cross section of AGT 100 combustor assembly.*

operating temperatures stabilize, the relative thermal growth of the combustor is about 1.5 mm [0.059 in.].) Analysis showed the engine assembly specifications in use when the cross-key slots were fractured would not accommodate 2.46 mm (0.097 in.) thermal expansion before spring coil bind would occur. Hence, the assembly specifications have been revised to eliminate the possibility of coil bind and no contact load type of failures have occurred in the cross-key slots since the revised specification was issued.

Another similar situation existed at an interface between the combustor center body and the swirler assembly. In this case the center body (attached to the outer engine structure) moves toward the swirler as the engine warms to operating temperature. The worst case relative displacement between the center body and the swirler was about 2.46 mm (0.097 in.) in a fast transient start-up. If this displacement is not accommodated, an unintended load would be exerted on the turbine assembly. The centerbody was modified to accommodate this clearance requirement while still allowing for adjustment of the axial clearance between the centerbody and the combustor dome. Five engine tests have been conducted since the burner assembly specifications were revised, and no evidence of interference between the swirler and the center body has been observed.

Combustor Component Experimental Testing—Engine Testing

Ceramic combustor bodies, dilution rings, and pilot burner tubes have been incorporated in every engine assembly tested during the AGT 100 program. Total hot test time of these components in engines is about 415 hr. The design configuration of

C-2

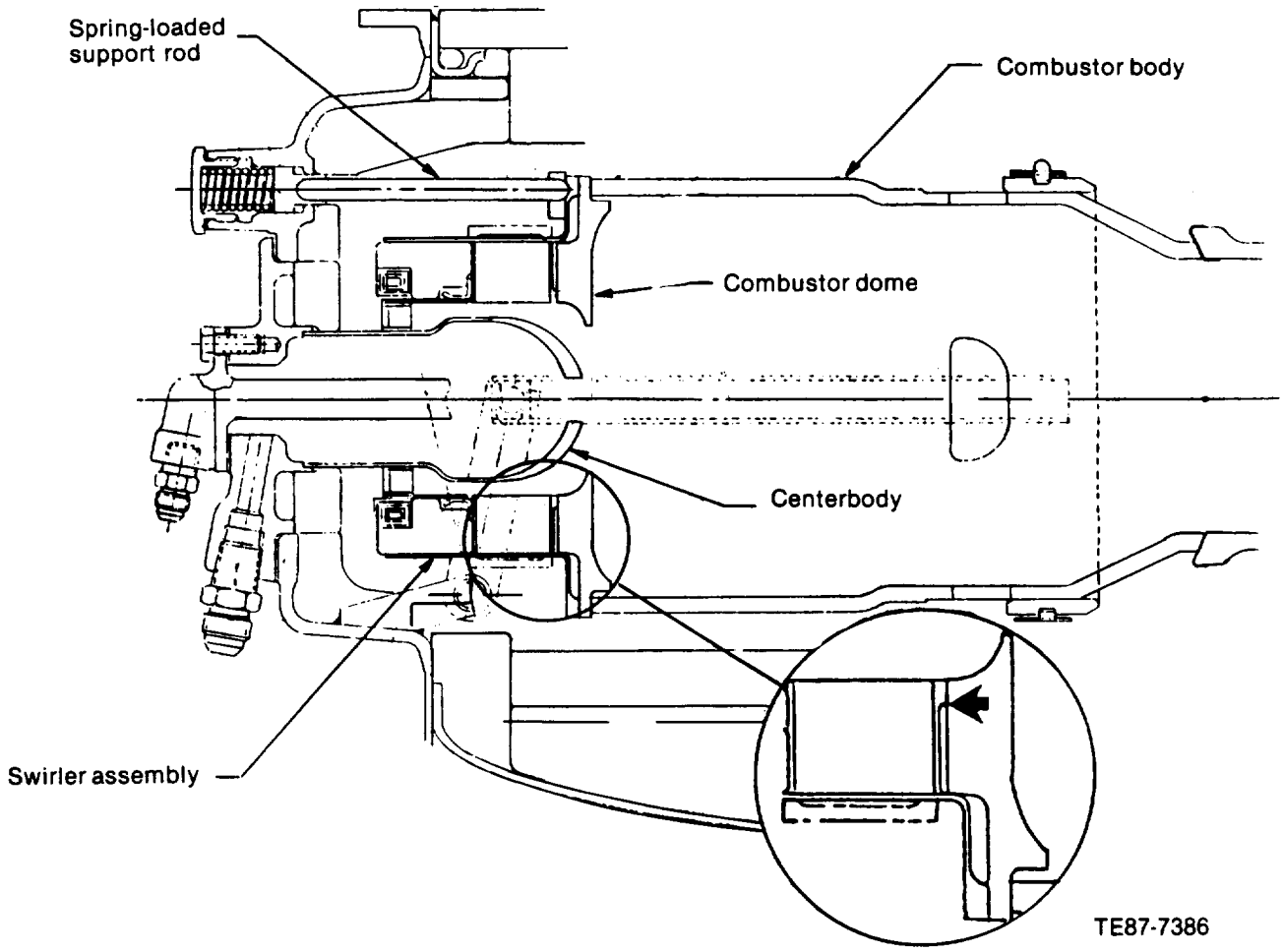

Figure 133. *Combustor assembly.*

these components has remained essentially unchanged since engine testing began. One exception is the relocation of the dilution holes in the combustor body to eliminate interference between the burner variable geometry mechanism and ceramic gasifier turbine scrolls. This change did not affect the structural performance of the body component.

Ceramic combustor domes have been installed in 26 engine builds during the program and have accumulated 290 hr of hot engine testing. Combustor domes fabricated of metal were used in 19 engine builds during two phases of the program when the design of the ceramic dome was being revised and new parts fabricated. The first revision to the dome was the addition of radial slots from the swirler holes to the inside diameter of the dome to eliminate hoop stresses in the inner part of the dome.

Following additional failures of the dome in combustor rig testing, a second design revision, which decreased the outside diameter of the dome to eliminate the portion of dome that extended beyond the outside diameter of the combustor body, was implemented. This extended portion of the dome included features that served to position the dome circumferentially so that the swirler holes in the dome were aligned with corresponding holes in the metal swirler assembly.

The environment of the portion of dome extending beyond the combustor body was relatively cool compared to that of the portion just inside the combustor body. This caused tensile hoop stresses to develop in the outer portion of the dome resulting in fractures. These stresses were decreased when the outside diameter of the dome was reduced, which placed that portion of the dome in a more uniform temperature environment. Features (pins and slots) were added to the metal swirler and the revised dome to control the circumferential position of the dome in the combustor assembly. Recent fractures of combustor domes in engine tests have

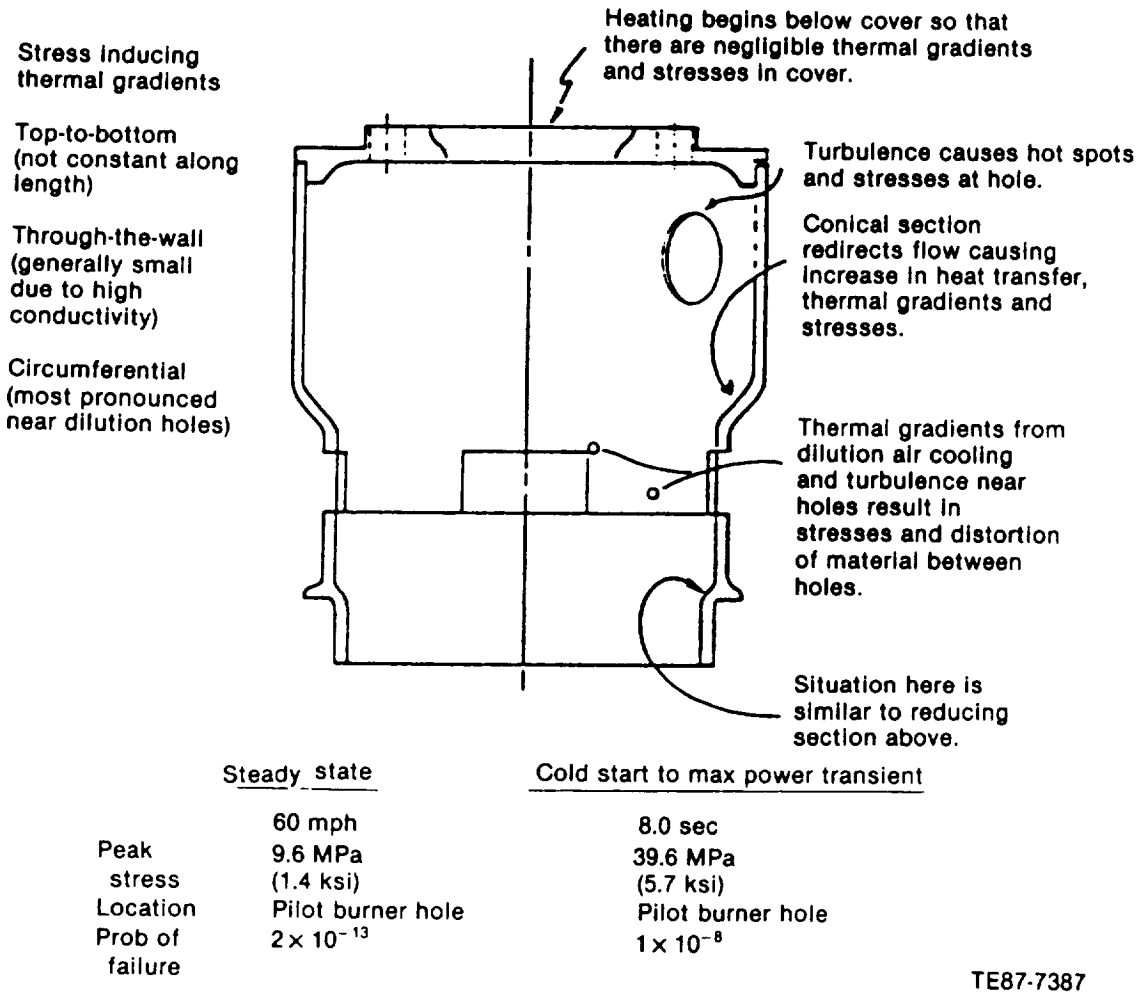

Figure 134. *Summary of the thermally-induced stresses.*

been caused by contact stresses resulting from misfitting associated metal parts. These incidents are summarized in the following paragraphs. A summary of hot test time accumulated on the ceramic combustor components is shown in Table XXIV.

Combustor Dome Failure in Engine S/N 1, BU24

Investigation of the ceramic component failures in engine S/N 1, BU24 concluded that chips breaking from the combustor dome was the primary failure and subsequent damage to the turbines was secondary. Two large chips separated from the combustor dome and passed through the turbines. One chip was adjacent to a locating notch in the dome, and the other was from a region between a swirler hole and the inside diameter of the dome at one of the thermal expansion slots. The chip at the notch may have been fractured at assembly. The other chip resulted from an unintended load on the face of the dome from the adjacent metal swirler at the dome's inside diameter. This contact was the result of both the dome and swirler being slightly out of print, and about 0.076 mm (0.003 in.) interference existed at the location of the chip.

Combustor Dome Failure in Engine S/N 2, BU17

Two large segments of combustor dome fractured from the dome during testing of engine S/N 2, BU17. The separated pieces remained in place and were discovered during a routine inspection of the engine on the test stand after shutdown. Analysis showed a misfit between the dome and adjacent metal swirler that allowed the swirler to shrink tightly around the outside of the dome during cooldown. No contact was intended between the parts at this location. The swirlers being used in engine and

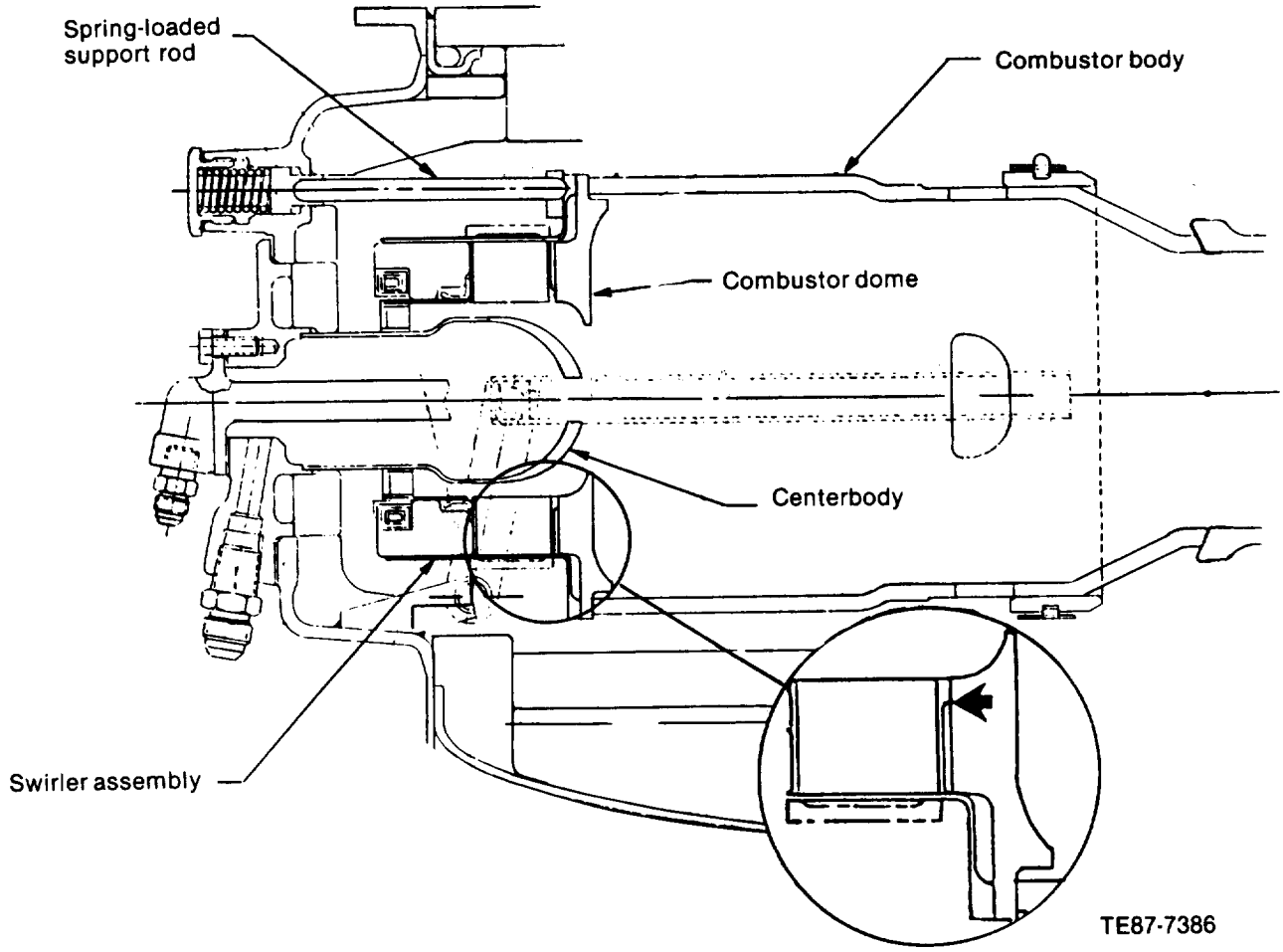

Figure 135. *Combustor assembly.*

Table XXIV.

Summary of ceramic combustor component experimental testing.

Component	Number of engine tests	Number of static rig/ proof test	Total hot test hr in engine	Total hot test hr in rig
Combustor body	45	32	415.5	161.0
Combustor dome	26	23	290.1	130.3
Dilution band	45	32	415.5	161.0
Pilot nozzle tube	45	31	415.5	121.1

rig testing were examined for this interference and modified as required to prevent recurrence of this failure. Design revision of the dome was not considered necessary.

Combustor Component Experimental Testing—Combustor Test Rig

A static combustor test rig has been used throughout the AGT 100 program to: (1) proof test ceramic combustor assembly components to qualify them for engine test, (2) evaluate combustor performance including exhaust emissions, (3) study the use of alternate fuels, and (4) evaluate advanced (composite) ceramic material systems for combustor components. A total of 23 combustor test rig builds incorporating ceramic components were tested during the program accumulating 122.3 hr of hot testing.

Three tests were conducted in the combustor test rig since the last annual report. The SEP SiC/SiC composite ceramic combustor body was evaluated in two of the three test rig assemblies. In the third test rig assembly a conventional monolithic ceramic combustor assembly was proof-tested and the performance of an Excello airblast fuel nozzle was evaluated.

The first test of the composite ceramic combustor body was the standard experience based proof test—two start nozzle ignition sequences to about 871°C (1600°F) and one main nozzle ignition sequence to about 1038°C (1900°F). In the second test, the SEP combustor body was exposed to increased temperatures: 1204°C (2200°F) for 1 hr, 1288°C (2350°F) for 1 hr, and 1204°C (2200°F) for 20 hr, in that sequence, to further evaluate the material's performance. Following completion of the test, the combustor body was removed and thoroughly inspected. Its condition was rated good with little or no evidence of material oxidation.

The Excello airblast nozzle was installed in a monolithic ceramic combustor assembly for evaluation. The Excello nozzle fits in the centerbody cavity in place of the Rochester Products (RP) start nozzle, which is used to sustain the engine while the regenerator warms up. The Excello nozzle was, however, intended to also serve as the main fuel nozzle during engine operation. The ignition performance of the Excello nozzle was superior to the RP nozzle. The threshold fuel flow at light off for the Excello nozzle was about half the fuel flow required for the RP nozzle. Test data showed that for the Excello nozzle combustion efficiency decreased significantly as burner variable geometry closed off the dilution holes and that an unacceptably hot core region developed in the central part of the combustor under that condition.

The Excello nozzle produces a diffusion flame flow field in contrast to the low temperature reaction zone produced by the premixed/prevaporized main nozzle. Consequently, the emission levels of NOx and CO for the Excello nozzle are roughly an order of magnitude larger. Smoke measurements and particulate counts were not taken for the Excello nozzle.

Combustor Tests in Thermal Shock Test Rig

A standard engine configuration combustor assembly is used in the thermal shock test rig. This rig was used to proof test ceramic static turbine structure components in an environment as similar to the engine environment as possible. During the AGT 100 program nine assemblies of this rig were tested with a total hot test time of 38.7 hr. Since the last annual report, one assembly of the thermal shock rig was tested for a total of 29.9 hr. Combustor assemblies are interchanged between the thermal shock rig and both test engines on an as-available basis.

3.5 GASIFIER TURBINE ROTOR

Introduction

Allison has designed and tested ceramic gasifier turbine rotors for the AGT 100 engine. Detailed finite element heat transfer, stress, vibration, rotor dynamics, and probability of survival analyses have been performed. A unique thermal barrier scheme was designed, developed, and successfully demonstrated for joining the SiC rotor to the metal compressor shaft. Braze and interference fit attachments were used for the Si_3N_4 rotor. A flexural load proof test was developed that subjected the attachment to twice the maximum engine loads. A dynamic proof stress test of the inducer airfoil, which vibrated the airfoil at its natural frequency for a controlled amplitude, was developed.

Over 140 hr of total engine test time has been accumulated on eight different rotors. Three of the tested rotors were SiC material, while the other five were Si_3N_4. Two grades of Si_3N_4 were tested: SN220M and SN250M.

One of the Si_3N_4 rotors experienced nearly 100 hr of testing. Maximum temperature achieved during engine testing was 1166°C (2130°F) TIT and

maximum speed was 73,300 rpm. Results of these efforts clearly identified FOD as a critical issue in ceramic rotor development. Initial designs/materials are vulnerable to FOD. The airfoil was redesigned by thickening the inducer area by a maximum factor of 2.5 and linearly tapering this increase to a factor of 1.0 (original) thickness in the flow controlling exducer throat region. A SiC material rotor fabricated to this configuration was successfully engine demonstrated.

Additional development is needed to create improved designs using better materials with improved toughness, making the rotors even more resistant to impact damage.

Objective

The objective of the AGT 100 gasifier rotor task was to design, develop, and successfully engine demonstrate a structurally sound, cost-competitive ceramic material, radial inflow turbine, which provides high efficiency over the broad operating range of an automobile engine. The objective includes addressing the specific goals of 1288°C (2350°F) TIT, 508 m/s (1668 ft/sec) tip speed, potential 3500 hr service life, the stress, temperature, and vibration environment, and the interface with metal companion components.

Discussion

The discussion of the design of the ceramic gasifier rotor is organized into the following three headings:

Design and Analysis
Component Development
Component Engine Test

These are the steps of the ceramic development process previously described and thus offer a functional outline for discussion.

Design and Analysis

Design Parameters—The RPD engine cycle requirements for the gasifier turbine at the maximum power, sea level static, condition are listed in Table XXV.

Although the turbine operates at the maximum power point only a small fraction of the time, this point does represent the most severe steady-state structural design condition. The maximum power condition, therefore, was selected as the design point to ensure a systematic integration of fabrication, aerodynamic, heat transfer, stress, and vibration design disciplines. The design process commenced with aerodynamic definition of flow path, vane and blade contours, and thickness distribution.

Several factors were involved in the selection of "optimum" flow path parameters. First is the realization that part power is emphasized at the expense of full power performance. Caution was used, however, to avoid any severe efficiency reduction at maximum power, which would result in unacceptable vehicle response. A second major factor was the selection of aerodynamic and geometric parameters consistent with structural design for fabricability, long life, and low cost. This second factor became particularly important with respect to achieving adequate life of the ceramic wheel. A third important consideration related to selection of flow path parameters conducive to low inertia. The gasifier turbine flow path selected to satisfy the

Table XXV.

RPD engine cycle requirements for the gasifier turbine at maximum power, SLS.

Inlet temperature—°C (°F)	1288 (2350)
Inlet pressure—kPa (psia)	438.4 (63.58)
Fuel/air ratio	0.0129
Equivalent flow, $W\sqrt{\theta cr}\epsilon/\delta$—kg/s (lbm/sec)	0.178(0.391)
Equivalent work, $\Delta h/\theta cr$—kJ/kg (Btu/lbm)	42.07 (18.09)
Equivalent speed, $N/\sqrt{\theta cr}$—rpm	37,630
Expansion ratio (total-total)	1.8726
Efficiency with inlet scroll (total-total)	84.7

AGT 100 turbine design criteria is illustrated in Figure 136. This turbine features a symmetrical vane with endwall contouring and a low-inertia rotor. Salient features of the turbine design are listed in Table XXVI.

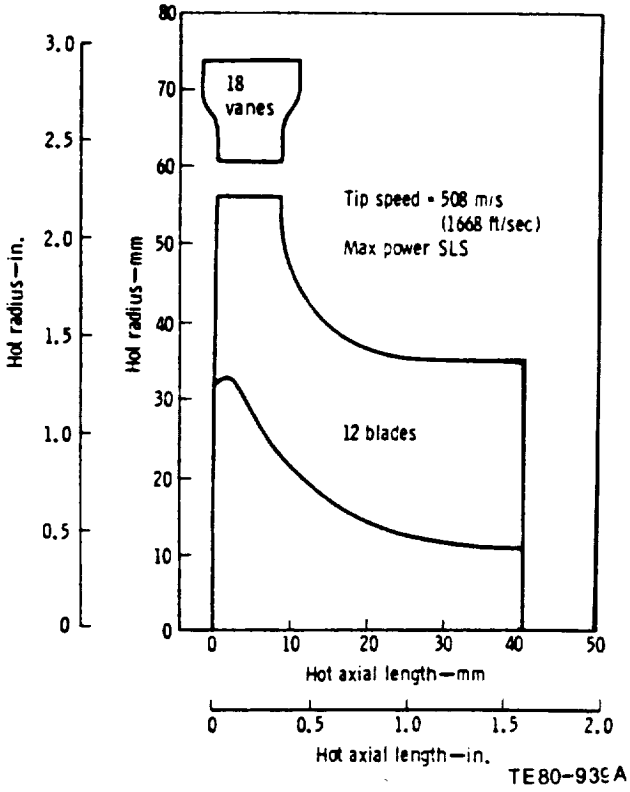

Figure 136. *RPD gasifier turbine flow path.*

Operating at the sea level static (SLS) maximum power condition, the turbine exhibits a tip speed of 508 m/s (1668 ft/sec) and an aerodynamic loading parameter of 0.7 which is an optimum value for radial in-flow turbines. The specific speed, 75, a dimensionless shape parameter independent of rotor size that expresses geometric and velocity-diagram compatability is also optimum.

The power transfer engine concept allows cycle temperatures to remain high over a wide operating range. This is accomplished by extracting additional work from the gasifier turbine and applying it to the power turbine shaft. Figure 137 illustrates the ratio of gasifier turbine power to compressor power over the engine road-load operating range.

The flow path selection has been verified through a sensitivity study of critical design parameters. This study included specific speed, tip diameter, vane exit angle, exducer hub/tip radius ratio, and exducer area (Ref 1).

The rotor has been designed with emphasis on low cost through use of radial blading, low inertia through use of fully scalloped backplate and deeply cut hub, low exit Mach number to minimize transition duct loss, and relatively high maximum power reaction to achieve a broad efficiency band. Consistent with ceramic construction, the minimum blade thickness is 0.762 mm (0.030 in.). The blade thickness distribution is that of an optimum "dog leg." At each axial location, the blade thickness is constant from the tip inward to a specified radius and then follows a logarithmic profile toward the hub. The hub contour was selected to provide balance between blade and hub stress levels.

Table XXVI.
Salient features of the turbine design.

Vane inlet diameter—mm (in.)	147.38 (5.802)
Rotor tip diameter—mm (in.)	112.52 (4.43)
Vaneless space diameter ratio	1.078
Rotor tip width—mm (in.)	8.38 (0.330)
Exducer hub/tip radius ratio	0.30
Rotor tip diameter/exducer tip diameter ratio	1.600
Rotor tip width/rotor tip diameter ratio	0.0745

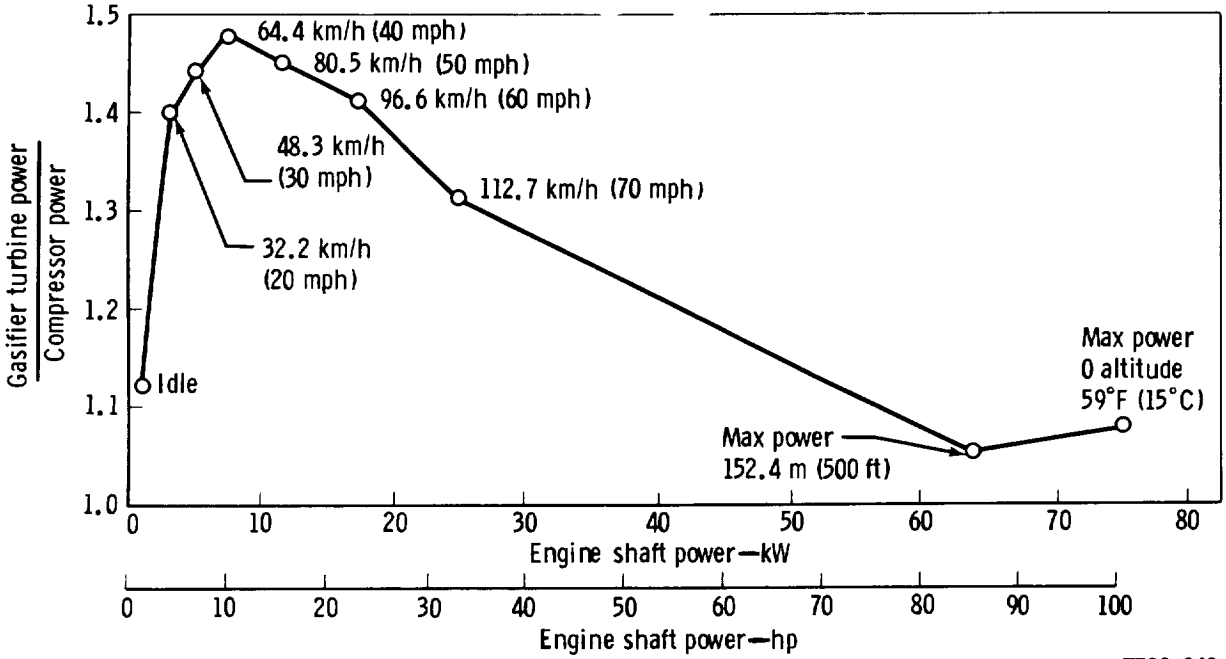

Figure 137. *Ratio of RPD gasifier turbine power to compressor power.*

The blade shape is illustrated by radial section cuts in Figure 138.

Additional aerodynamic data, such as blade-to-blade velocity distributions for hub, mean, and shroud under SLS maximum power operation, rotor exit swirl, Mach number, and efficiency, are presented in Reference 1.

Structural Analysis—

1. Alpha-SiC Material, 0.75 mm (0.030 in.) Thick Inducer Airfoil (Original Configuration)

Alpha-SiC was selected as the primary material system for development of the ceramic gasifier rotor. This selection, based on the demonstrated strength, stability at time and temperature, fabricability, and other factors, is fully discussed in section II.

The requirement to limit the heat flux from the SiC gasifier rotor into the turbine bearing area was identified, and the design to satisfy this is shown in Figure 139. This rotor/shaft system was fully analyzed for rotor dynamics, airfoil frequencies, temperature and stress gradients, probability of survival, and the benefit of proof test. Rotor system dynamic analyses indicated the reduced mass of the ceramic turbine rotor (versus the metal) was of little influence on the system natural modes. Thus, the design of the rotor suspension system is identical for both turbine rotor materials; a mass isolator spring rate of 10.5×10^6 N-m (60,000 lb/in.) at the turbine end, 7×10^6 N-m (40,000 lb/in.) at the compressor end, combined with a squeeze film damper. These rates shift all rotor modes outside of the engine operating range. A complete discussion of the analyses is presented in Section V including the response to balance limits.

The airfoil natural frequencies were calculated utilizing a finite element simulation of the airfoil. The calculated frequencies and corresponding modes are shown in Figure 140. Interference (potential airfoil response) with 18th engine order (18 nozzle vanes) is calculated for the first exducer and inducer modes outside the engine operating range and above fourth order interference. (Fourth order is a general response concern based on experience in radial flow machinery.) The second natural exducer mode (23,400 Hz) is coincident with the inlet vane passage in the operating range (78,000 rpm or 90.5% N_1). This is a high energy mode (high energy required for excitation) and judged to be an acceptable design.

The rotor and attachment were analyzed for probability of survival (POS) under various conditions including steady-state and transient operation. This was accomplished using FEM for the heat transfer/temperature gradients and the stress/POS calcu-

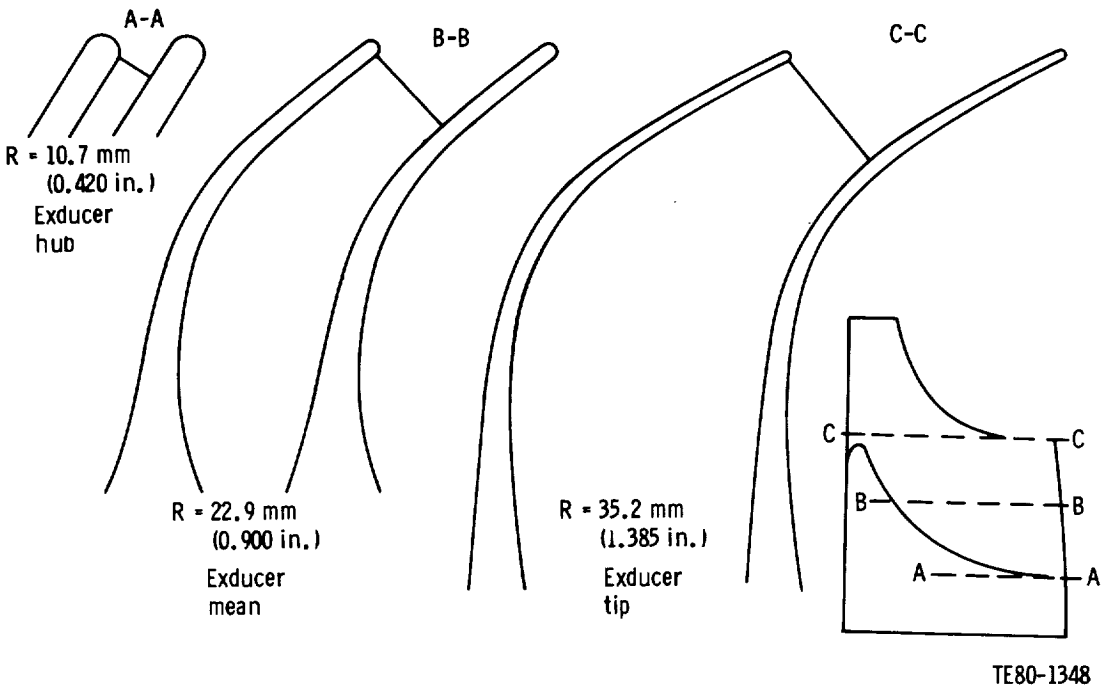

Figure 138. *RPD gasifier turbine rotor airfoil sections.*

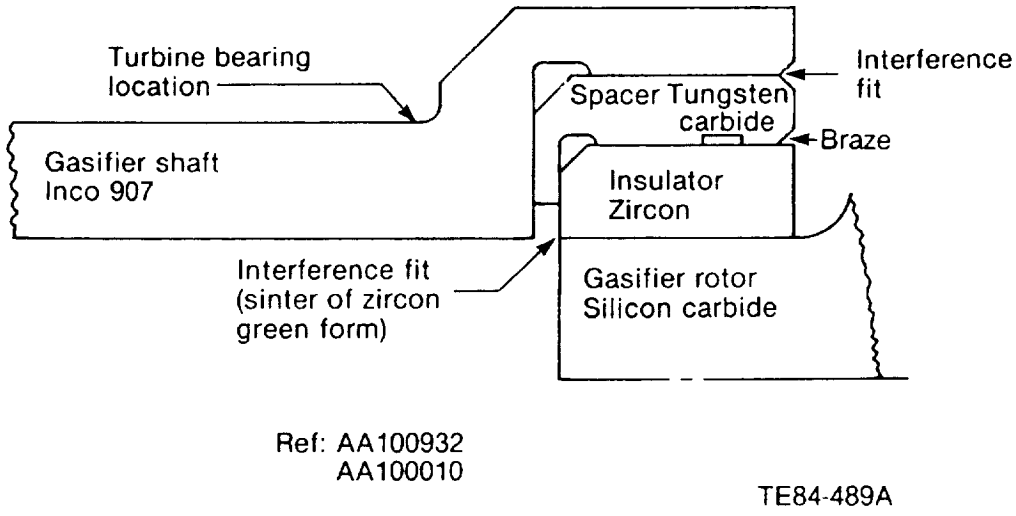

Figure 139. *Design for ceramic rotor/metal shaft attachment.*

Table XXVII.

Results of maximum power steady-state conditions, initial configuration.

Model	Probability of survival	
2-D	Volume	0.8333
Maximum principal stress 170 MPa (24.7 ksi)	Surface	0.9974
	Total	0.8312
3-D	Volume	0.8100
	Surface	0.9955
Maximum principal stress 169 MPa (24.6 ksi)	Total	0.8063

lations. Initially, a comparison was made for axisymmetric 2-D FEM and a 3-D simulation. The 3-D model accurately simulated the airfoil wrap or camber and root fillets. The results at maximum power steady-state conditions, shown in Table XXVII, showed excellent agreement.

The small difference in volume POS is primarily a result of the inclusion of fillets in the blade root of the 3-D model. Based on these results, extensive analyses under various conditions were made utilizing the 2-D axisymmetric FEM (as shown in Figure 141). The following tabulation identifies the various conditions analyzed:

- assembly-interference fit compressor shaft
- room temperature spin
  - as-cast rotor
  - machined rotor with compressor shaft
- engine operation
  - transient accel
  - steady-state
    - 649°C (1200°F) TIT and 50% N_1-light off
    - 954°C (1750°F) TIT and 60% N_1-idle
    - 1080°C (1976°F) TIT and 100% N_1-MOD I configuration
    - 1288°C (2350°F) TIT and 100% N_1-design point

An example of the calculations is shown in Figure 142 for the steady-state design point. (The results of the other analysis cases are shown in Ref 2.) The transient accel case, an interesting example, is discussed later in this report.

2. Alpha-SiC Material, 1.90 mm (0.075 in.) Thick Inducer Airfoil (Thickened Configuration)

The design of a gasifier rotor featuring an impact resistant inducer airfoil was accomplished in 1985. The inducer region of the airfoil was thickened by a maximum factor of two and one-half (× 2.5).

The design criteria were: (1) no increase in the airfoil stress levels and hence no change in the airfoil taper ratio and (2) no change in the flow controlling exducer throat area. The resulting thick-

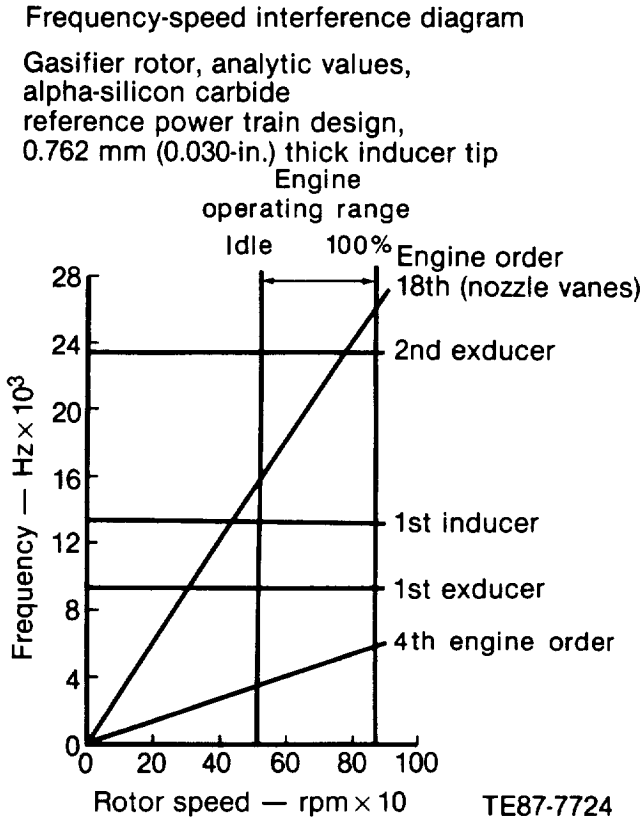

Figure 140. *Calculated airfoil frequencies, SiC material gasifier turbine rotor.*

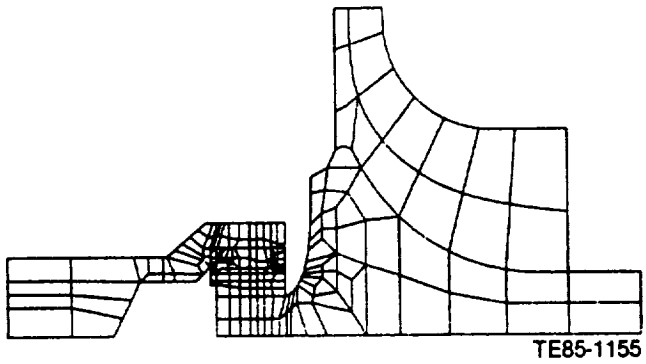

Figure 141. Gasifier rotor/shaft assembly 2-D finite element model.

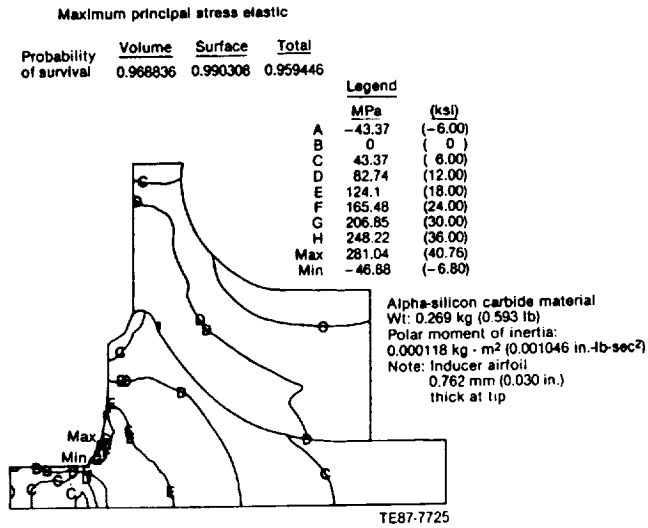

Figure 142. Gasifier rotor maximum principal stress for steady-state, 1288°C (2350°F) and 100% speed.

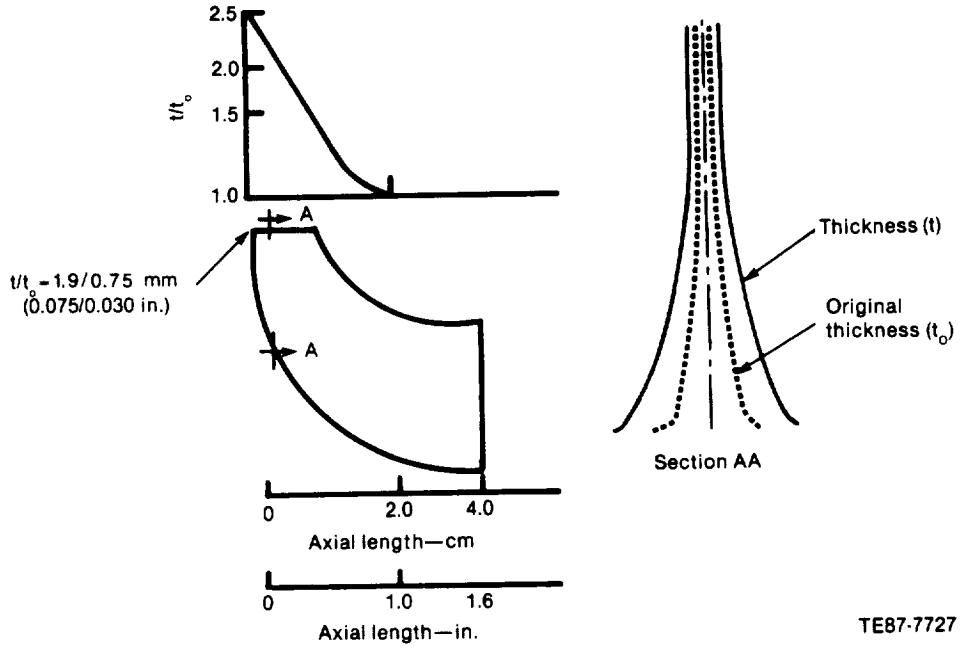

Figure 143. Modified inducer blade thickness.

ness increase is graphically illustrated in Figure 143. In addition to the potential improvement in impact resistance, the stiffened airfoil shifts the first inducer mode well above the operating range as shown in Figure 144.

The thickened airfoil rotor was analyzed for probability of survival under various conditions including steady-state and transient operation. This was accomplished using 2-D FEM for the heat transfer/temperature gradients and the stress/POS calculations. An example of the calculations is shown in Figure 145 for the engine design point. For comparison, the equivalent calculation for the original thickness inducer airfoil is shown in Figure 142. Analysis indicated the small increase in mass of the rotor was a trivial influence on the rotor system dynamics. Thus, no change in the rotor assembly suspension system was required.

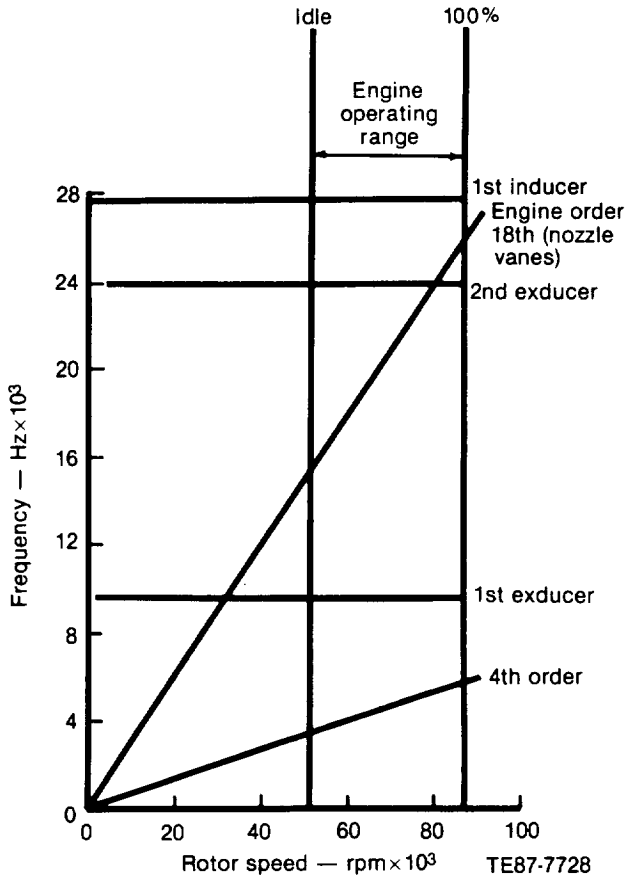

Figure 144. *Calculated airfoil frequencies, SiC material gasifier turbine rotor, thickened inducer airfoil.*

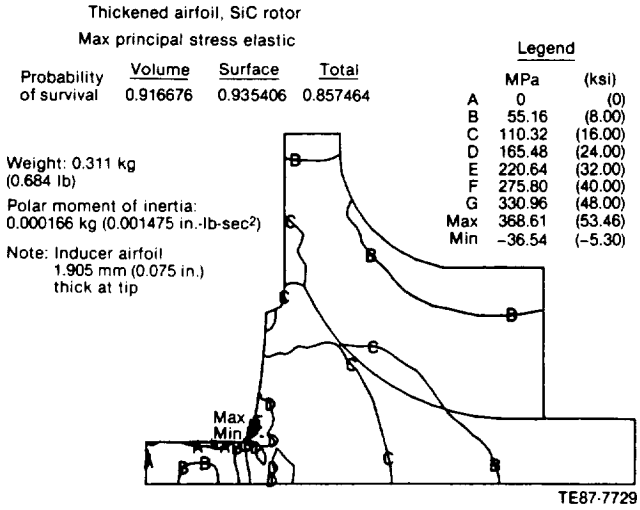

Figure 145. *Gasifier rotor maximum principal stress for steady-state, 1288°C (2350°F) TIT, and 100% speed (design point) engine conditions.*

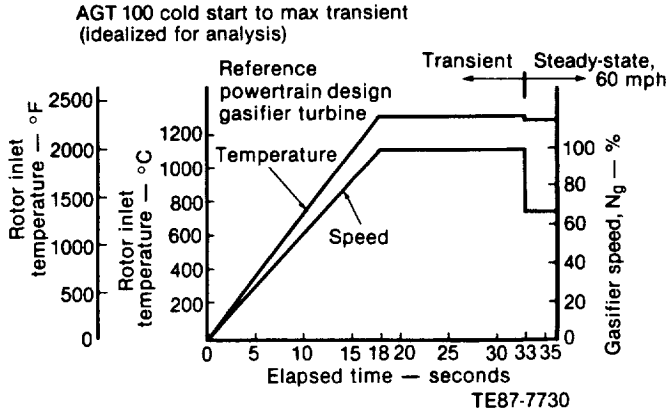

Figure 146. *Gasifier rotor idealized transient, cold start to maximum power.*

The most severe transient condition is a fire-up from ambient to full power. This condition is idealized per Figure 146. This condition is "time sliced" to generate a profile of rotor temperature gradients as a function of time. The results are shown in Figure 147 including identification of the maximum radial gradient in the hub at 33 sec.

The calculated temperature and stress gradients in the rotor at the critical 33 sec point are shown in Figures 148 and 149, respectively. Note that the POS is calculated at 0.4432 for this condition. The results of the analysis of other operating conditions are discussed in Reference 3.

3. Si_3N_4 Material, 0.75 mm (0.030 in.) Thick Inducer Airfoil (Original Configuration)

The rotor/gasifier shaft assembly was also designed utilizing Si_3N_4 material for the gasifier rotor. The material offers approximately 690 MPa (100 ksi) room temperature MOR strength and approximately a 50% increase in fracture toughness compared to SiC. The rotor is a geometric replica of the SiC material rotor described earlier. Two schemes were designed for joining the metal gasifier shaft to the rotor—a proprietary braze attachment supplied by Kyocera and an interference fit by Allison. These schemes are illustrated in Figure 150. Note that the thermal insulator (Ref Figure 139) utilized in the case of the SiC rotor is not required. The thermal conductivity of Si_3N_4 is approximately 20% of SiC.

The density of SASC and SSN are nearly identical (~3.1–3.2 g/cm³). Thus, the mass of the gasifier rotor assemblies are similar. The rotor system dynamic analysis discussed under point 1, alpha-SiC material, is applicable and the previously defined rotor suspension system is directly applicable to the Si_3N_4 material gasifier rotor.

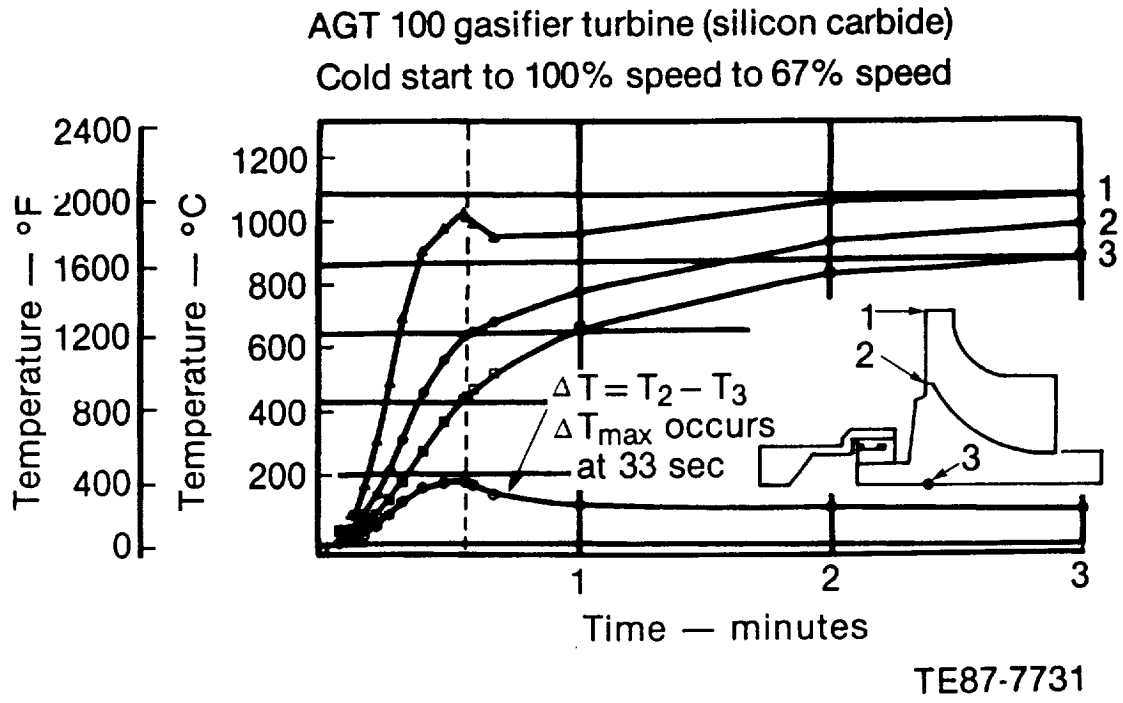

Figure 147. *Transient temperatures, SiC gasifier rotor—Ref Figure 146.*

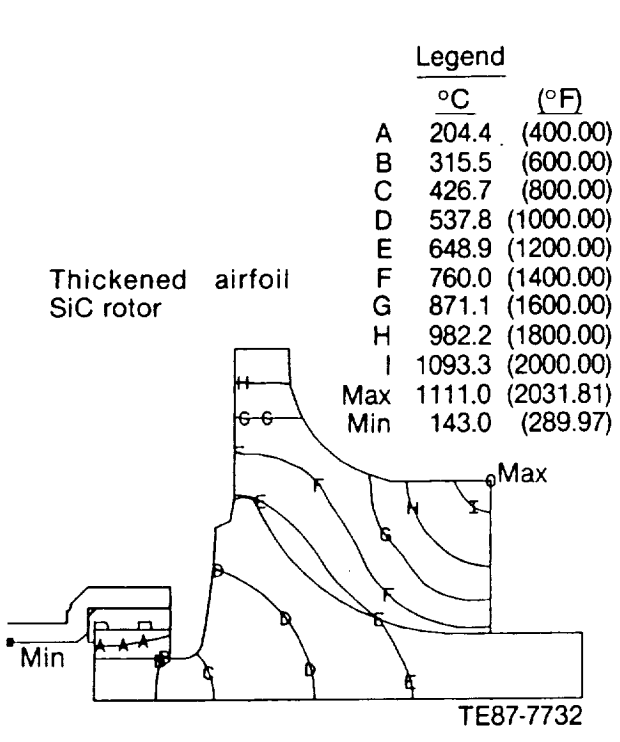

Figure 148. *Gasifier rotor temperature profile for maximum transient condition at 33 sec—Ref Figure 147.*

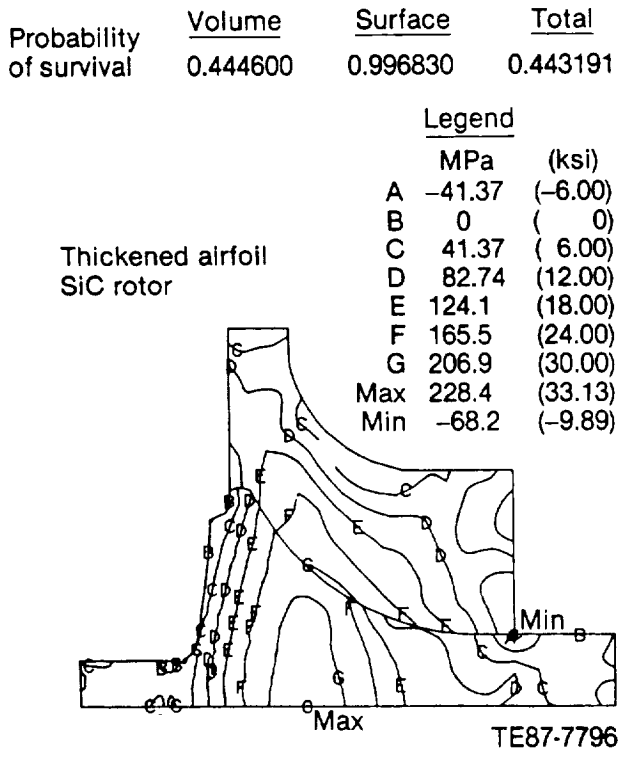

Figure 149. *Gasifier rotor maximum principal stress for transient conditions at 33 sec—Ref Figure 147.*

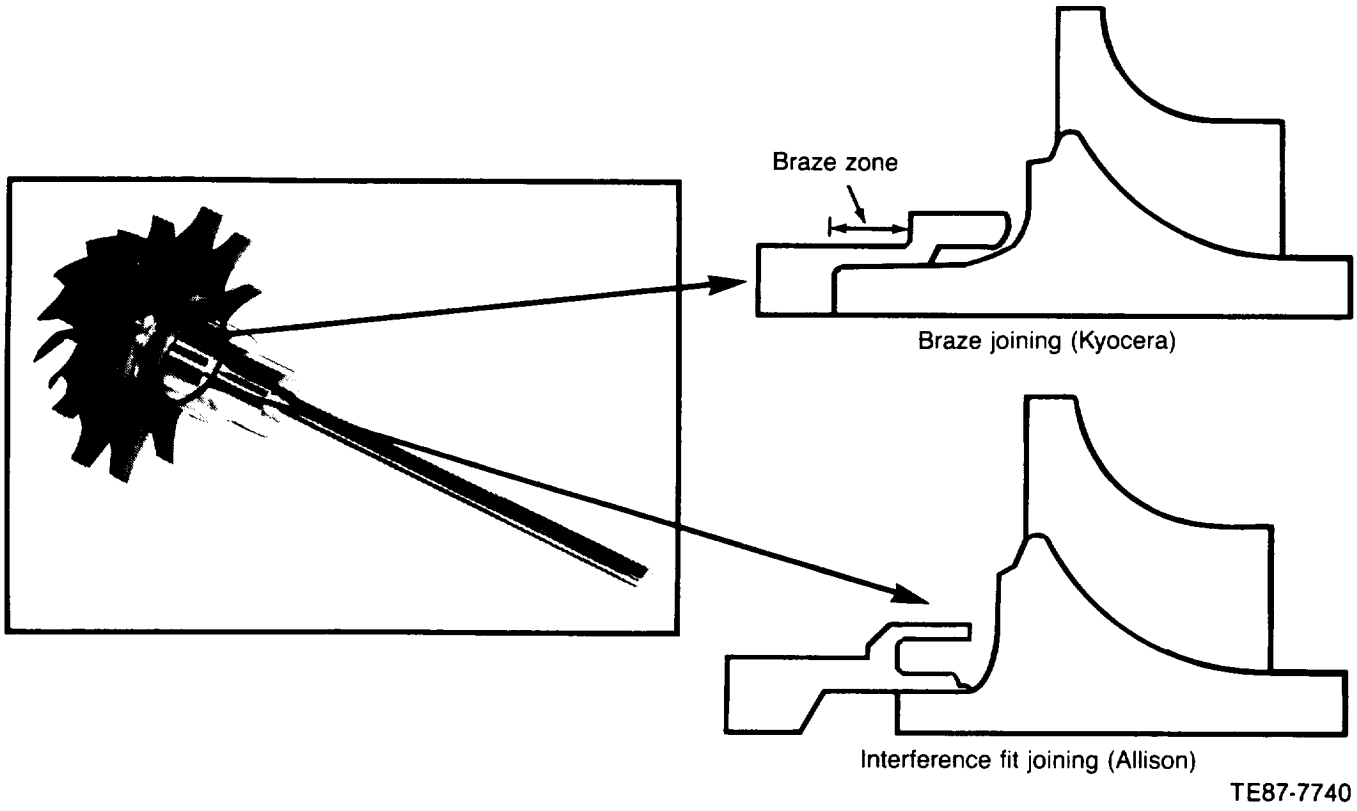

Figure 150. *Braze and interference fit joining of metal gasifier shaft to Si_3N_4.*

The airfoil natural frequencies were calculated utilizing a finite element simulation of the airfoil. The calculated frequencies and corresponding modes are shown in Figure 151. Interference (potential response to vane passage) is predicted for three modes in the operating range. This is in contrast to one mode predicted for the SiC material rotor (Ref Figure 140). The explanation is the material modulus of elasticity; approximately 240 × 10^3 MPa (34.8 × 10^3 ksi) for Si_3N_4 versus 400 × 10^3 MPa (58.0 × 10^3 ksi) for SiC. The reduced modulus generally lowers the natural frequencies of the Si_3N_4 material airfoil. Modulus data for Si_3N_4 material tested later in the program (1985) exhibited values in the 290–300 × 10^3 MPa (42–43.5 × 10^3 ksi) range. Although this would tend to raise the natural frequencies of the gasifier airfoil, the three modes remain in the operating range. The three modes of interest are high energy modes and judged to be an acceptable design.

The rotor and attachment were analyzed for POS under various conditions. The results of the heat transfer and stress analyses at design point (2350°F TIT and 100% speed) for the interference fit shaft are shown in Figures 152–155.

The analysis also calculates the radial stress and total load for the interference fit gasifier shaft. These data are shown in Figure 156. The two

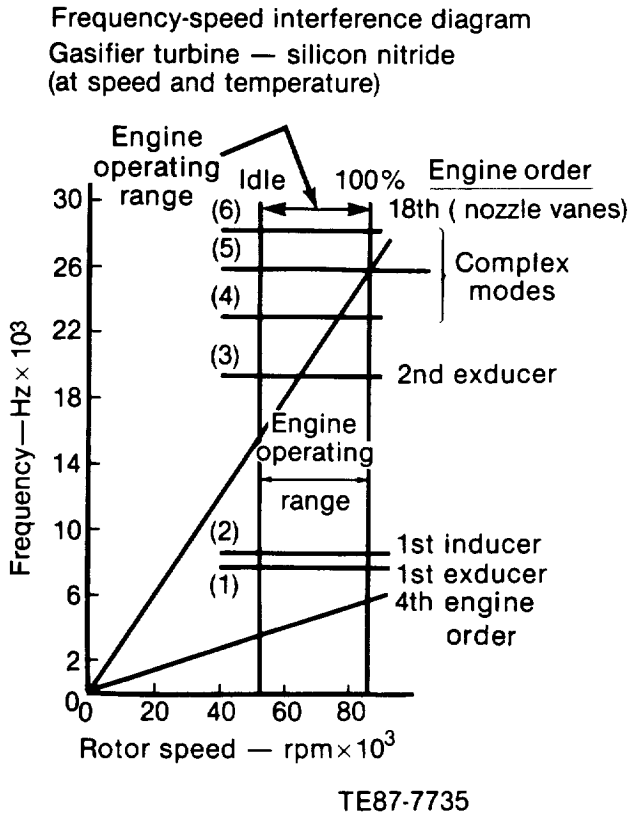

Figure 151. *Calculated airfoil frequencies, Si_3N_4 material gasifier turbine rotor.*

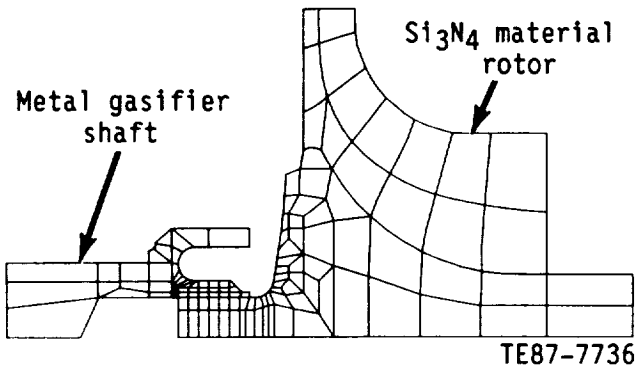

Figure 152. *Gasifier rotor/shaft assembly, 2-D finite element model.*

parameter Weibull unit strength data used in the analyses for Si_3N_4 material are shown in Table XXVIII.

The results of analyses of other engine operating conditions are found in References 4 through 8.

Component Development

SiC Material Rotors, 0.76 mm (0.030 in.) Thick Inducer Airfoil—Early trials indicated that injection molding of the SiC material produced relatively defect-free rotors. Multiple groups were developed that culminated in a group 8 identification from which two engine test rotors were culled.

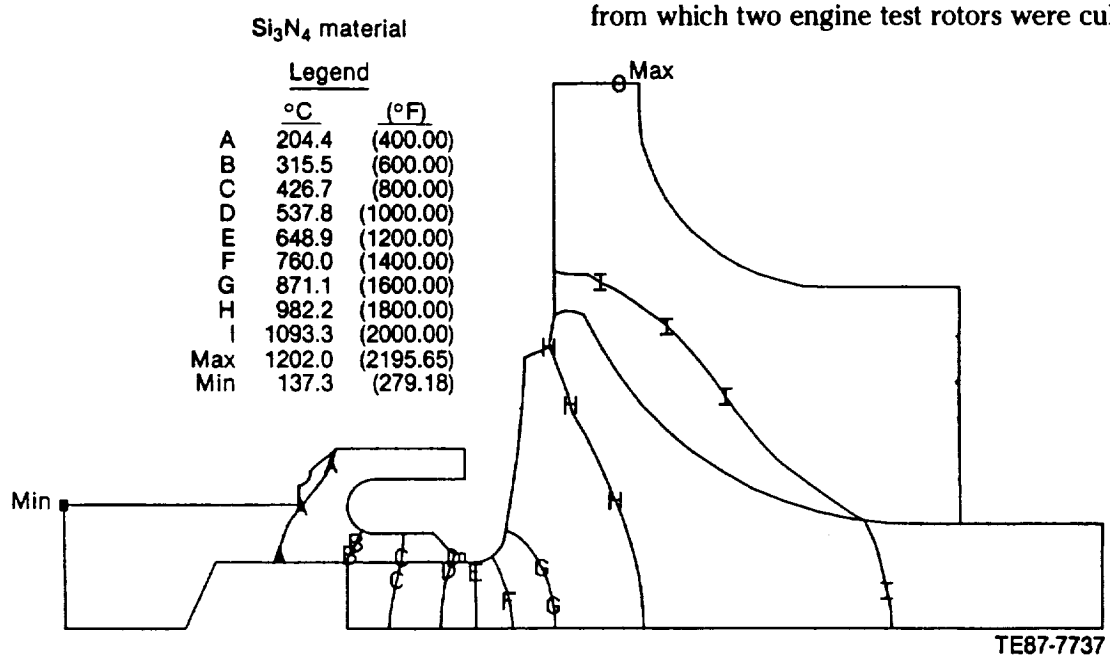

Figure 153. *Gasifier rotor and shaft temperature profile for steady-state, 2350°F TIT, and 100% speed (design point) engine conditions.*

Table XXVIII.
Two parameter Weibull unit strength data.

Temperature— °C (°F)	m_v	σ_{ov}— ksi/in.^{3}	Temperature— °C (°F)	m_s	σ_{os}— ksi/in.^{2}
21 (70.0)	15.61	70.842	21 (70.0)	10.484	61.212
600 (1112.0)	15.61	70.842	600 (1112.0)	10.484	61.212
800 (1472.0)	15.61	65.883	800 (472.0)	10.484	56.928
1000 (1832.0)	15.61	56.674	1000 (1832.0)	10.484	48.970
1200 (2192.0)	15.61	28.336	1200 (2192.0)	10.484	27.545

NOTE:
m_v = material Weibull modulus, volume strength
m_s = material Weibull modulus, surface strength
σ_{ov} = material unit volume Weibull strength
σ_{os} = material unit surface Weibull strength

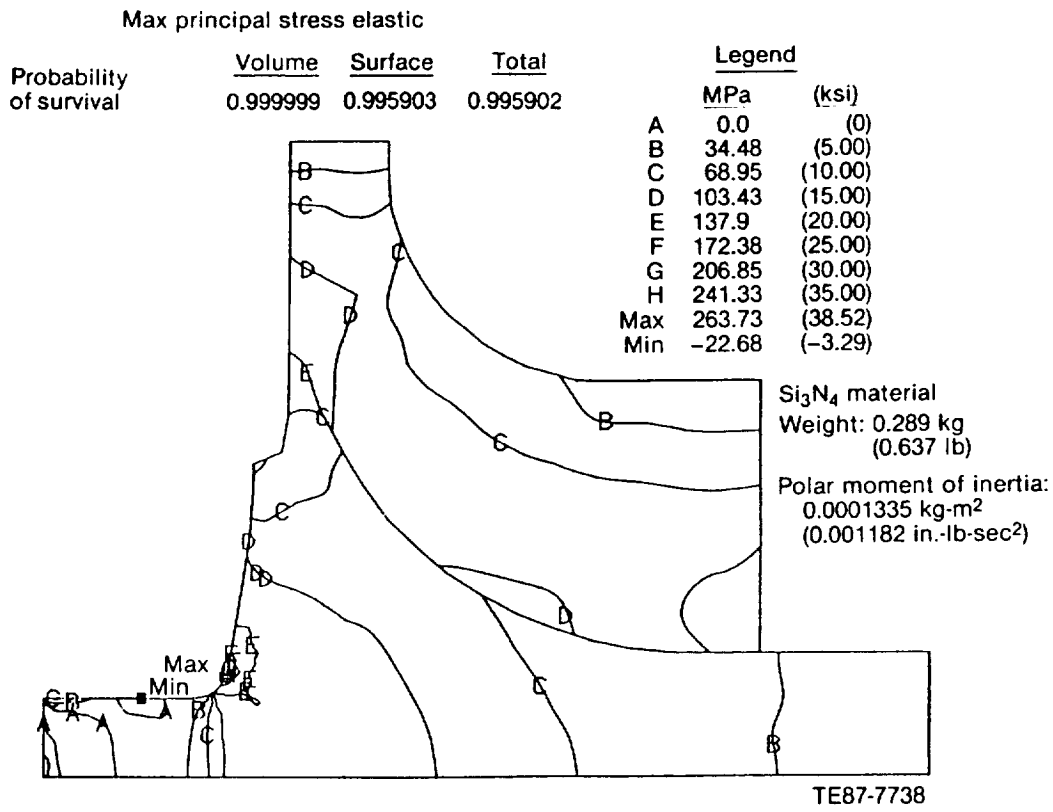

Figure 154. *Gasifier rotor maximum principal stress for steady-state, 2350°F TIT, and 100% speed (design point) engine conditions.*

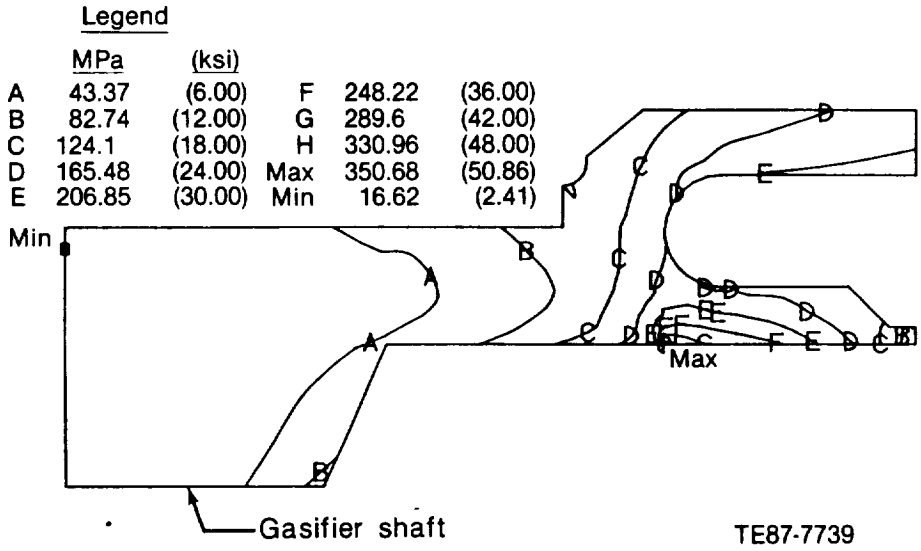

Figure 155. *Si_3N_4 material rotor interference fit shaft, combined equivalent stress for steady-state 2350°F TIT and 100% speed (design point) engine conditions.*

In the 1985 time frame, the final sample of 162, group 8 rotors were received. This brought the total quantity of original inducer thickness (0.76 mm) [0.030 in.] rotors to 425. The shaft end injection was successful in eliminating backface region molding flaws observed in prior processing. This resulted in a

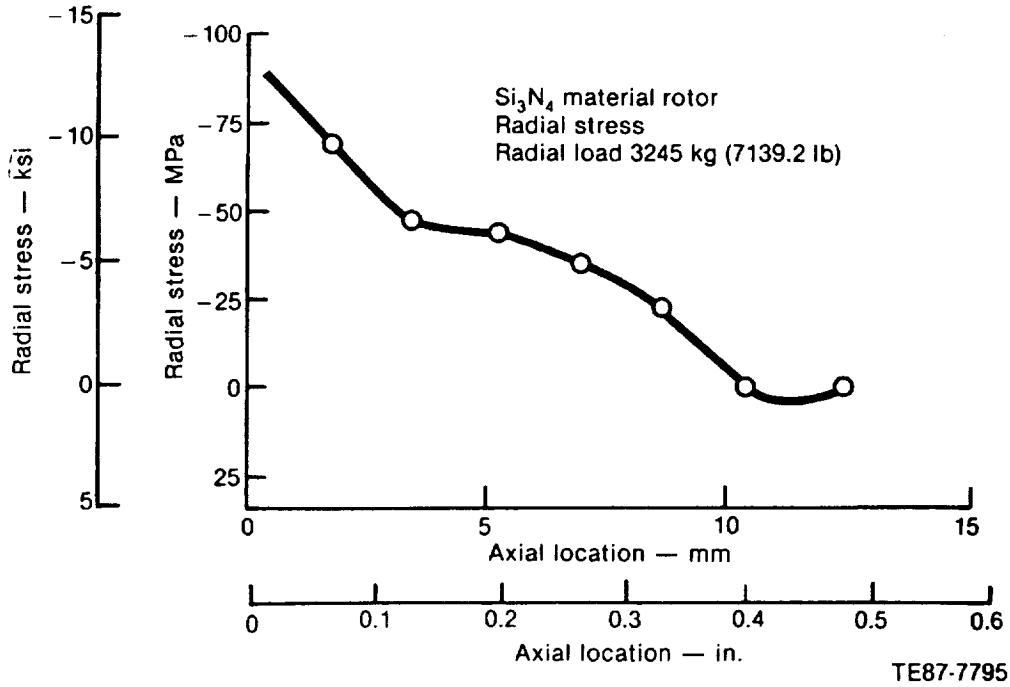

Figure 156. *Radial stress and total load for the interference fit gasifier shaft.*

Table XXIX.
Overall quality level of the rotors.

Quality level (surface)	Number
A	90
B	52
C	20
	162

process yield (defined as green form to rotors suitable for spin proof test) of 52% as compared to only 11% for prior processing techniques.

The overall quality level (NDE) of the rotors is summarized in Table XXIX.

"A" quality is free of visual or FPI indications; "B" quality rotors exhibit blendable indications, and "C" quality is rejected due to the presence of permanent (nonblendable) indications.

A detail listing of the Group 1 through 8 processing standards is shown in Reference 9.

A suspended item (proof and burst) Weibull treatment of the Group 8 spin tests is shown in Figure 157. The data are for 30 successful spin proof tests and 40 burst tests.

The successfully proofed rotors are flagged by an arrow pointing to the right (higher speed range). The data indicate an average burst speed of 116% gasifier turbine design speed (N_1) and a Weibull modulus (scatter) of 12. Calculations indicate that an average MOR bar strength in the 310 MPa (45 × 10^3 lb/in.^{2}) to 345 MPa (50 × 10^3 lb/in.^{2}) range corresponds to this average burst speed.

A sample of 14 of the 30 proof tests were successfully spun to 104,500 rpm or 121% N_1.

At the termination of processing of the alpha-SiC rotors with the original thickness airfoil, the following summary points are applicable:

- Shaft end injection (vs nose end) improved yield and strength as assessed by average spin burst speed.
  1. The process yield improved from 11% to 52%.
  2. Average burst speed and Weibull modulus improved from 110% N_1 and a modulus of 4.8 to 116% N_1 and a modulus of 12.0.
- Engine test qualified rotors were culled from the Group 8 sample.
  1. one tested in engine S/N 2, BU8
  2. one tested in engine S/N 2, BU12
  3. one assembled in engine S/N 2, BU15
  4. one held in reserve
- The Group 8 process standard was the initial standard for processing of the thickened airfoil rotors.

Development

SiC Material Rotors, 1.90 mm (0.075 in.) Thick Inducer Airfoil—Sohio modified the

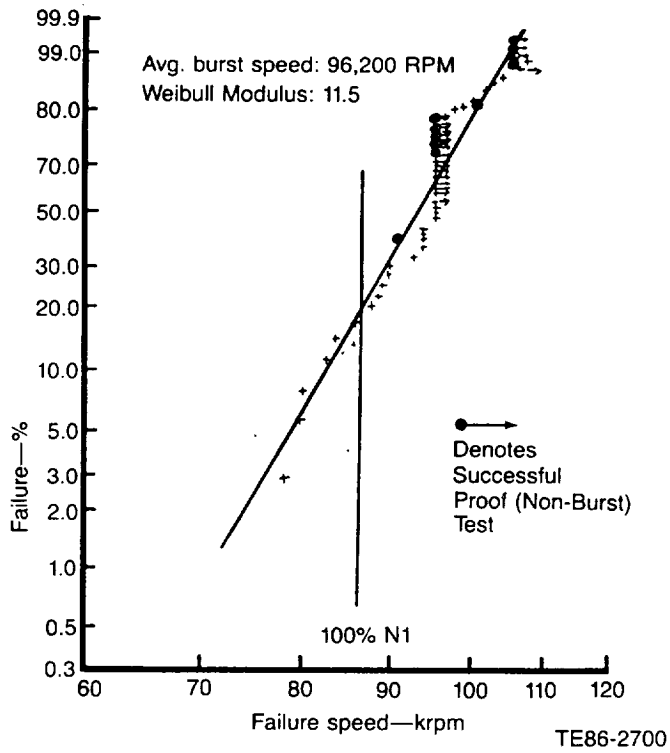

Figure 157. *Cumulative probability of failure as a function of spin speed, Group 8 (1985) SiC gasifier rotors.*

injection-molding tool with new inserts for the thicker airfoil (part number AA101326). A visual comparison of the original configuration inducer airfoil versus the thickened design is shown in Figure 158.

The processing of alpha-SiC rotors by Sohio during CY 1986 utilized only the thickened airfoil injection molding die. The goal of 60 deliverable rotors was achieved on schedule at a rate of 10 rotors per month from April through September. This sample was labeled Group 9 and rotor S/N FX52275 was successfully demonstrated in engine S/N 2, BU19.

At the termination of processing (1986) of the injection-molded alpha-SiC rotors with the thickened inducer airfoil, the following summary points are applicable:

- The processing by Sohio was quickly developed and produced a yield (green form to sintered rotor suitable for spin test) of approximately 72%.
- Postprocessing of sintered rotors by the ASEA glass encapsulation scheme resulted in rotors nearly matching the analytic average burst (MOR = 60 ksi, Weibull modulus = 8) of 103.3 krpm versus 98.2 krpm test observed burst.

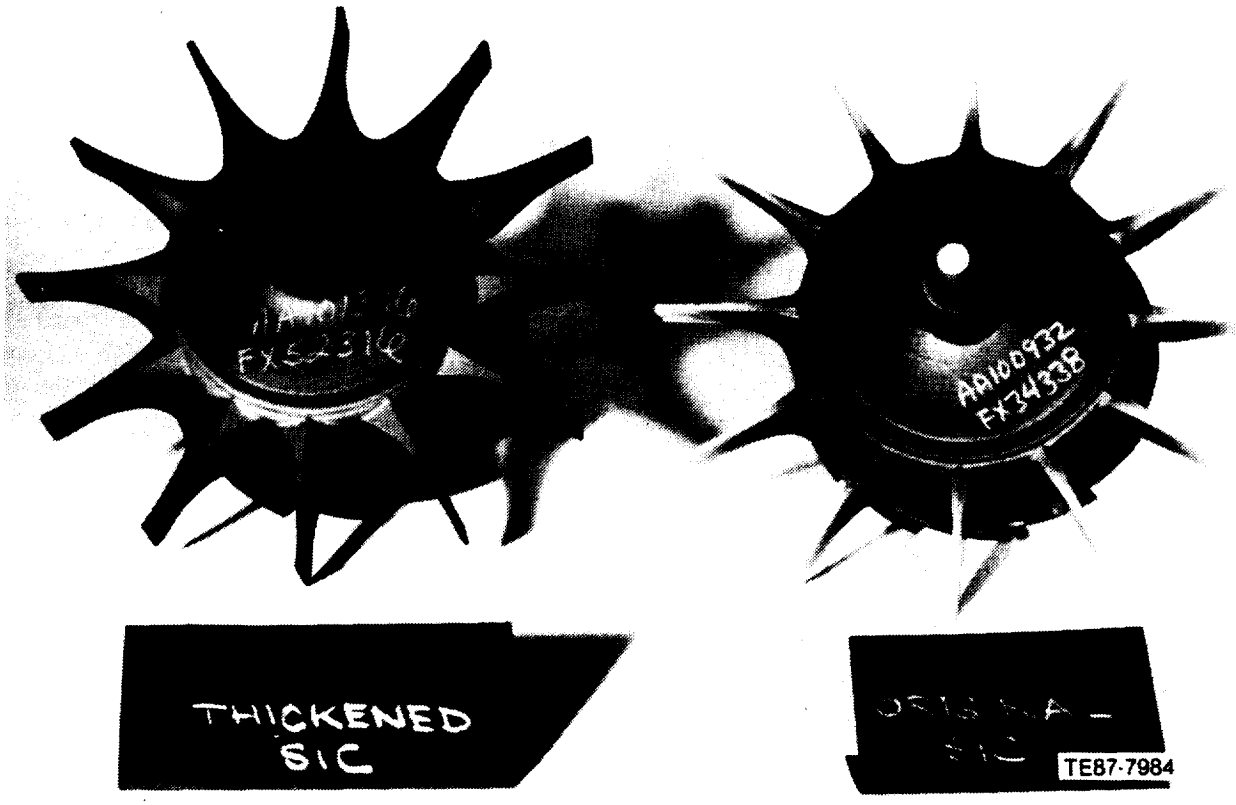

Figure 158. *Original configuration inducer airfoil and the thickened design, alpha-SiC material gasifier rotors.*

- The successful engine test (engine S/N 2, BU19) of rotor S/N FX52275 achieved 70% N1 at the max TIT of 1976°F for a total run time of 5:11 hr. Additional discussion of this test is found in the Component Engine Test section.

Development

Si_3N_4 Material Gasifier Rotors—Si_3N_4 material rotors were procured from two vendors; (1) Kyocera International on a "parts buy" basis and (2) GTE Laboratories on a development basis. The following discussion reviews both.

1. Kyocera—Interference Fit and Braze Joined Compressor Shaft

The two schemes for joining the silicon nitride rotor to the metal compressor shaft are illustrated in Figure 150. Three grades of Kyocera Si_3N_4 were procured, all slip cast processing: SN220M, SN250M, and SN251. The SN220M was initially recommended by Kyocera followed by an improved SN250M. MOR bar properties were not achieved in the rotors, and Kyocera successfully addressed this deficiency with the SN251 grade material. The rotor effort with Kyocera is summarized as follows:

- Rotors and rotor assemblies were fabricated to the following plan:
  a. interference fit
     - 12 bare rotors, SN220M material for interference fit shaft attachment—source for multiple engine tests
     - 12 bare rotors, SN250M material—strength data indicated MOR bar properties not being achieved in rotors
     - 6 ea bare rotors, SN251 addressing above
  b. brazed shaft attachment by Kyocera
     - 10 ea assemblies, SN220M rotor material with braze joined compressor shaft based on turbocharger experience—typically failed attachment flexural load proof test. Braze layer was not uniform thickness. (These 10 replaced by following 10.)
     - 5 ea assemblies, SN250M rotor material with refined braze joining scheme—all passed flexural load proof test and 3 were finish machined.
     - 5 ea replacement, SN220M, for interference fit shaft.
- Eleven rotor shaft assemblies machined
  1. 5 interference fit, SN220M material rotor
  2. 2 interference fit, SN250M material rotor
  3. 3 braze attachment SN250M material rotor
  4. 1 interference fit, SN251 material rotor
- Five assemblies were engine tested, and the details are presented in the Component Engine Test section.

2. GTE Laboratories

GTE, a domestic source of Si_3N_4 material, proceeded to develop the injection molding and processing technology to demonstrate the successful manufacture of gasifier rotors. Based on this, an order was placed in March 1986 for 10 rotors fabricated from the GTE PY6 material.

The 10 were received in 1987, and at the completion of the program two rotors had successfully passed spin proof tests and thus qualified as engine candidates (see Table XXX).

The 10 are being held as potential candidates for future test. The results of the MOR bar tests are discussed in Section II.

Discussion of the engine test of ceramic gasifier rotors is organized by the rotor material; first the alpha-SiC material followed by the Si_3N_4 material. A capsule summary of the tests is shown in Table XXXI and detail discussions follow.

Component Engine Test

Alpha-SiC Material, Rotor Test Number 1—Engine No. 2, BU8 was assembled with the first ceramic gasifier rotor to be tested. This rotor, S/N FX34286, alpha-SiC material and the original inducer airfoil thickness is shown in Figure 159.

This finish-machined assembly successfully passed dimensional, FPI, and static load tests across the rotor/shaft attachment plane.

The assembly was successfully spin tested to 77,000 rpm with a 10 sec dwell. The maximum speed was limited to 77,000 rpm as a result of rig seal rub. The seal clearances were increased for future spin tests.

The airfoil natural frequencies in the rotor speed range were calculated and measured prior to the engine test to identify speed bands of potential airfoil response. The results are shown in Figure 160. The differences in calculated versus measured frequencies were attributed to airfoil thickness deviations from the drawing specification.

Engine testing, summarized in Section IV, was terminated due to an extensive increase in gasifier shaft whip during an acceleration to 55% N_1.

Teardown inspection revealed that the ceramic gasifier turbine had failed, losing approximately

Table XXX.
Two GTE rotors successfully passed open proof tests.

Number	Part number	Serial number	Proof spin speed, krpm (% N_1)
1	AA101302	107	88.0 (102)
2	AA101302	109	90.0 (104.5)

Table XXXI.
Capsule summary, engine test of ceramic rotors.

Group 1. Alpha-SiC material rotors

No.	Engine	Time frame	Test	Result
1	S/N 2, BU8	Nov 1984	Motoring with externally heated air supply	Fractured inducers, original thickness
2	S/N 2, BU12	Aug 1985	899°C (1650°F) TIT & 60% N_1	Fractured inducers, original thickness
3	S/N 2, BU19	June 1987	1080°C (1976°F) TIT & 70% N_1	Successful, thickened inducer airfoils

Group 2. Si_3N_4 material rotors

No.	Engine	Time frame	Test	Result
1	S/N 1, BU16 thru 20	Oct 1985 May 1986	1080°C (1976°F) TIT & 83% max N_1	99:54 hr total, fractured inducers, carbon debris
2	S/N 1, BU21	July 1986	996°C (1825°F) TIT & 70% max N_1	Scroll liftoff destroyed rotor
3	S/N 1, BU22 thru 24	Aug 1986 Dec 1986	1080°C (1976°F) TIT & 80% max N_1	19:21 hr total, dome fracture destroyed rotor
4	S/N 1, BU25	March 1987	1166°C (2130°F) TIT & 72% max N_1	Emergency shutdown, thermal soak back and relative motion, rotor to shaft
5	S/N 1, BU26	May 1987	All ceramic hot section 1093°C (2000°F) TIT & 70% max N_1	Multiple fractures of ceramic components

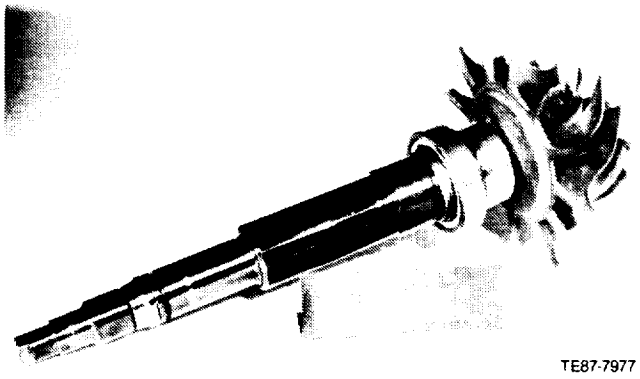

Figure 159. *First ceramic gasifier rotor for engine test, alpha-SiC material (assembly with compressor spacer for spin proof test).*

15 mm (0.6 in.) from all inducer blade tips, as illustrated in Figure 161.

Postfailure investigation of the attachment showed it was structurally sound by clearing FPI and repeating the drawing (machining) dimensions; no slippage was evident in the assembly.

Potential explanations for the inducer airfoil failure were identified. These were then divided into the following remote and potential classifications:

- remote failure modes
  - overspeed—no evidence
  - rub
  - thermal stress gradient—no evidence
  - material flaw—no discernible feature/flaw per fractographic analysis of the 12 failed airfoils, but the surfaces battered by the failure debris
- potential failure modes
  - FOD—any particle(s) passing through the flow path and impacting the ceramic rotor

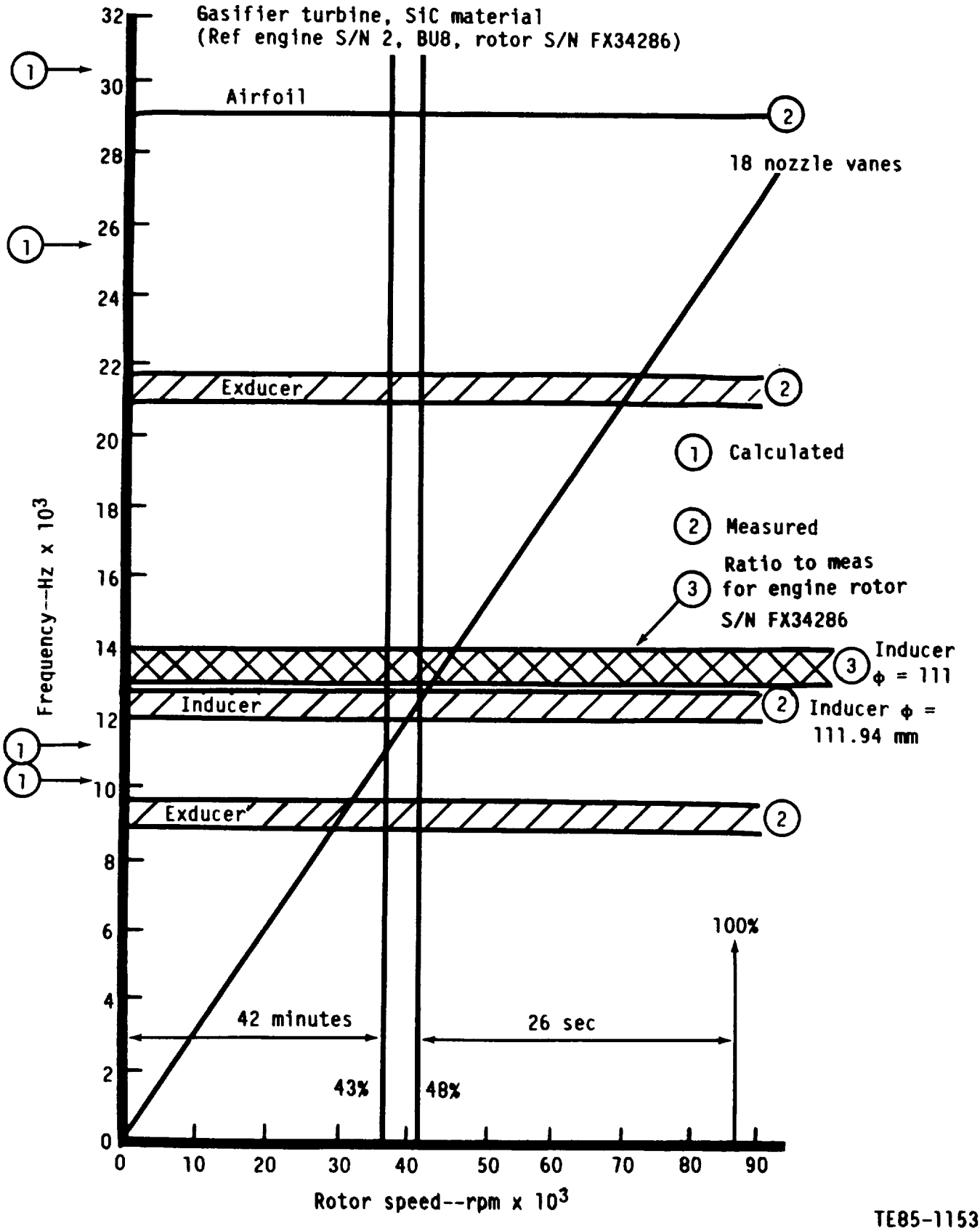

Figure 160. *Speed bands of potential airfoil response.*

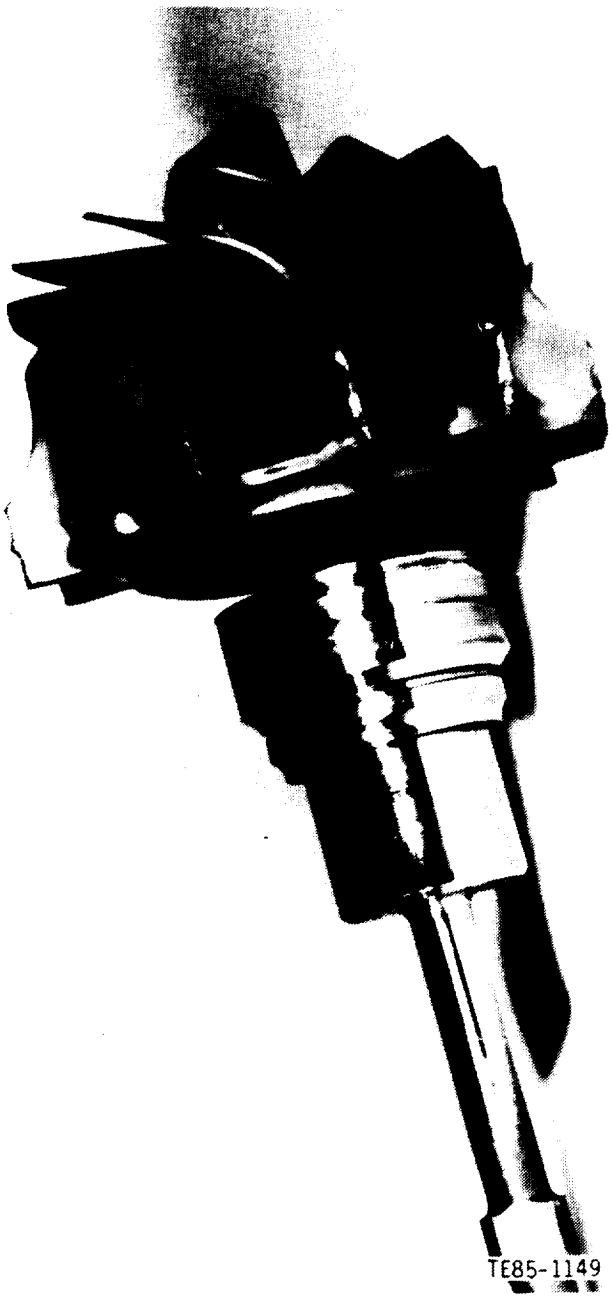

Figure 161. *Failed ceramic gasifier rotor (S/N FX34286), engine S/N 2, TD-8.*

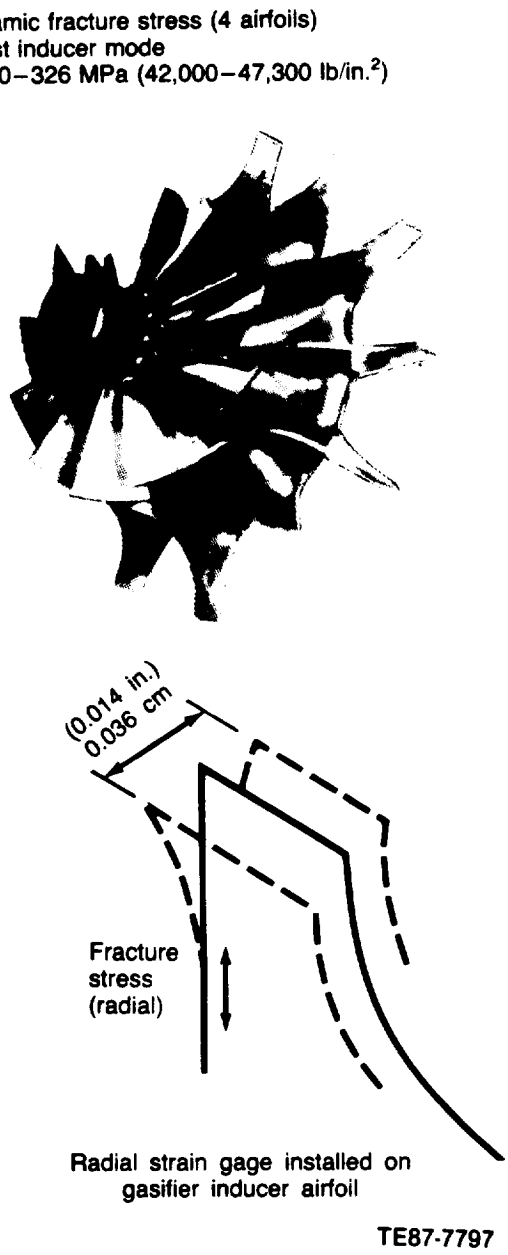

Figure 162. *Ceramic rotor inducer blade dynamic fracture test.*

- vibration (nozzle vane passage)—review of the test results indicates step change in whip response at about 36,000 rpm. (This does not correspond to a coincidence with vane passage frequency per Figure 160.)

In summary, the potential causes for failure of the inducer region of the airfoils in engine S/N 2, BU8 were foreign (loose) object damage and/or forced vibration.

To characterize inducer blade dynamic response further, a test program was conducted. Room temperature tests of a nonrotating rotor consisted of the following:

- determination of first inducer mode response versus excitation frequency through resonance
- determination of the fracture stress at resonance

Four airfoils were instrumented with radially oriented strain gages placed at the maximum stress location and then excited at their natural frequencies as shown in Figure 162.

The excitation was increased until fracture occurred. The airfoils failed between 289.6 MPa (42.0 ksi) and 326.1 MPa (47.3 ksi) with a tip double amplitude of 0.356 mm (0.014 in.) (Figure 162).

Three-dimensional finite element models were used to assess the probability of survival of the airfoil in the first mode for the observed tip deflection. Mean probability of survival, calculated at ± 319.9 MPa (46.4 ksi) (which corresponds with observed tip amplitude at fracture), would seem to indicate that inherent average rotor blade strength was only 71% of the material characteristic strength as determined from MOR test bars. The 71% MOR correlates with the rotor material strength deduced from spin burst characterization tests. It is unlikely that the ± 319.9 MPa (46.4 ksi) level of inducer excitation was present in the engine at the failure event; therefore FOD was concluded to be the probable failure mode.

Alpha-SiC Material, Rotor Test Number 2— Engine No. 2, BU12 was assembled with the second ceramic gasifier rotor to be tested. This rotor, S/N FX34360, alpha-SiC material, was the original inducer airfoil thickness. The assembly successfully passed dimensional, FPI, static load tests, and proof spin test to 73,400 rpm (rig limitation).

The airfoil natural frequencies in the rotor speed range were measured (siren excitation) prior to the engine test and the results are shown in Figure 163.

Engine testing was terminated after an increase in gasifier shaft whip and a decrease in gasifier speed. Teardown revealed gasifier rotor inducer blade tips to be broken off (Figure 164).

The similar failure of the SiC rotors, engine S/N 2 BU8 and S/N 2 BU12 as illustrated in Figure 161 and 164, respectively, prompted a detail comparison of the tests. Table XXXII is a tabulation of the key rotor features for the tests.

Alpha-SiC Material, Rotor Test Number 3— Engine No. 2, BU19 was assembled with the third and final SiC material gasifier rotor to be tested. This rotor, S/N FX52275 featured the thickened inducer

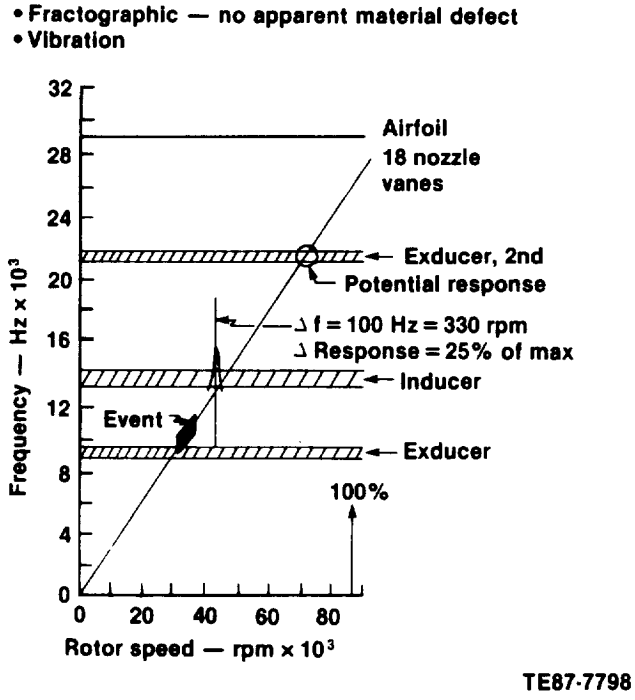

Figure 163. Ceramic gasifier rotor airfoil natural frequencies.

Figure 164. Ceramic gasifier rotor condition at engine teardown.

Table XXXII.

Comparison of SiC material, gasifier rotor engine tests.

Nov 1984 Engine S/N 2, Test 8		Aug 1985 Engine S/N 2, Test 12
	Engine test	
	Engine configuration	
	• Rotor, SiC	
EX142325 FX34286 0.3 mm (0.012 in.) extra clearance to scroll (versus metal rotor)	P/N S/N	EX142325 FX34360 0.3 mm (0.012 in.) extra clearance to scroll (versus metal rotor)
86,200 rpm	• Proof spin casting	94,400 rpm
77,000 rpm	Machined	73,400 rpm
Yes	• Airfoil freq measured	Yes
Turbine end 8.64 g-mm	• Build balance (DWG, Tol = 2.16 g-mm)	—
Ceramic	• Combustor	Ceramic
Metal	• Scroll	Metal
	Test parameters	
• Cold motoring (no combustion)		• Initial cold motoring
• Compressor discharge air electrically heated in external 20 kVA heater; non-rotating regen		• Standard lightoff, combustor operated on start nozzle only
• TIT ~ 500°F max very slow heat rate		• TIT ~ (1650°F) max
1:13 hr	• Test time	0:12 hr cold motoring 1:28 hr burning
0 → 48% NG (0 → 41,200 rpm)	• Speed range (gasifier)	0 → 60% N_G (0 → 52,000 rpm)
	Test parameters	
38.7/42.1% N_1	• Probable failure speed	37.7/43.5% N_1
33,400/36,300 rpm—see Figure 159		(32500/37500 rpm - see Figure 162
	Failures essentially identical	

- Summary
  - Essentially identical inducer failures (post test) at 33,400/37,500 rpm (38.7/43.5%)

    Vibration—does not correspond to vane passage interference

    Thermal Shock—1st failure—impossible
    2nd failure—potential

    FOD—potential

    Redesign airfoil, thickened inducer

    (Reference, Paragraph I, Design section)

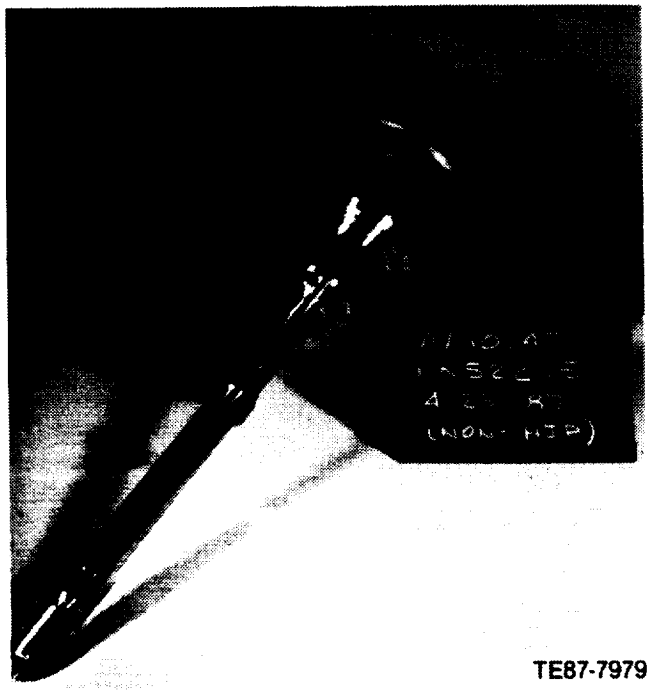

TE87-7979

Figure 165. *Thickened inducer airfoil, SiC material gasifier rotor successfully demonstrated in engine S/N 2, BU19, June 1987.*

P/N AA101471, S/N FX52275
(Sohio SiC, thickened inducer, non-hot isostatic pressing
Gasifier rotor, engine S/N 2, BU19

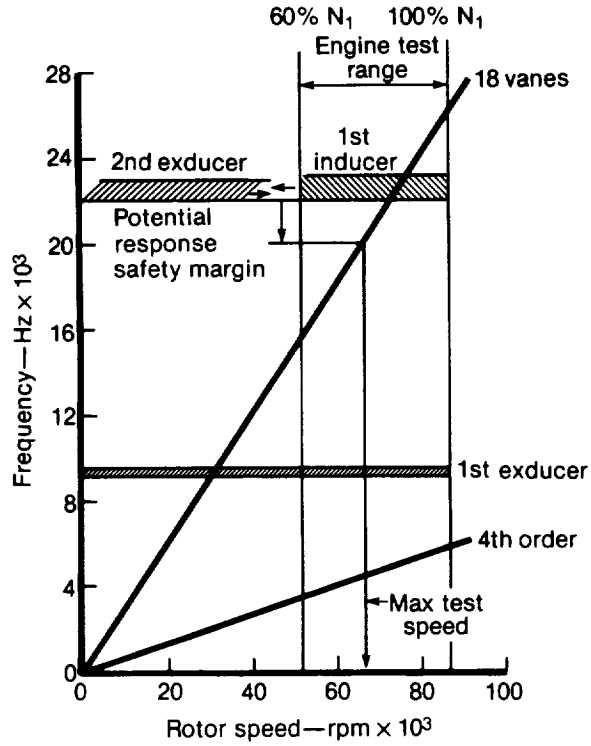

TE87-7741

Figure 166. *Frequency/speed diagram for SiC rotor.*

airfoil as shown in Figure 165. This rotor also featured an RPD-open configuration for the airfoil passage form. The configuration potentially offers improved performance over the Mod-I open form used for all other ceramic gasifier rotor tests including the Si_3N_4 material rotors.

The test, conducted in June 1987, was a successful demonstration of ceramic rotor technology.

Prior to the engine test, the assembly successfully passed dimensional, FPI, and static load tests. The airfoil natural frequencies in the rotor speed range were measured prior to the engine test, and the results are shown in Figure 166.

Shown as cross hatched data were the measured (experimentally determined) frequencies for each of the first three airfoil modes. The scatter encompassed the range of frequencies observed for the twelve airfoils of the rotor. All data are at room temperature. The observed first and second exducer mode frequencies meet the design requirements and agree with analytic calculations. The observed first inducer frequencies are less than the design goal of 28,000 Hz for the thickened inducer airfoil. This condition was a result of the particular position for machining the airfoil in the casting.

Note that the first inducer and second exducer mode frequencies are coincident. To help preclude any potential response, engine testing was limited to a maximum rotor speed corresponding to 90% of the interference frequency of 22,000 Hz. This is shown in Figure 166. Thus, the suggested maximum gasifier rotor speed was 66,500 rpm or 77% N_1.

The test successfully accomplished the exposure of the rotor to the 1080°C (1976°F) TIT and 70% N_1 goal and demonstrated the structural integrity of the thickened airfoil design. The RPD-open airfoil passage form was also demonstrated, thus progressing a step closer to the final RPD configuration. This completes the discussion of the engine testing of the alpha-SiC material gasifier rotors.

Si_3N_4 Material, Rotor Test Number 1— Engine No. 1, BU16 was assembled with the first Kyocera supplied, Si_3N_4 material (SN220M) gasifier rotor. The rotor geometry including the airfoils was identical to the original design (thin inducer) SiC material rotor. The compressor shaft attachment was the Allison interference fit scheme (Figure 150).

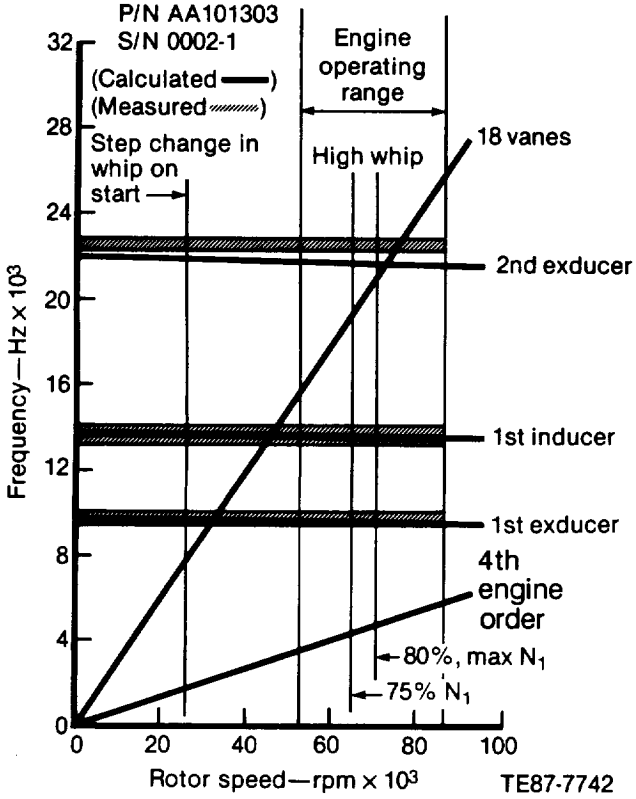

Figure 167. *Frequency speed interference diagram, Si_3N_4 gasifier rotor, engine S/N 1, BU16 through TD20.*

The finish-machined assembly Mod I open clearance configuration successfully passed dimensional and FPI inspection and was proof spin-tested to 50 krpm (rig limitation).

In preparation for the engine test, the rotor airfoil natural frequencies were calculated and bench test measured. The data are shown in Figure 167 and the agreement is excellent.

All engine test objectives were met, including approximately 20 hr of "durability" testing at 60% N_1 speed and 1066°C (1950°F) TIT. Both the inducer and exducer region of the gasifier airfoil successfully cleared potential vane passage response during numerous speed excursions of the rotor up to a maximum of 60,000 rpm (reference Figure 167).

The rotor (S/N 0002-1) successfully ran for 30 hr total during BU16. Post test inspection indicated a flawless rotor identical to the condition at assembly.

The rotor continued testing in engine S/N-1 through BUs 17, 18, 19, and 20. During a routine fire-up on BU20, shaft whip increased dramatically at 30% speed. A borescope inspection revealed a fracture of the turbine inducer airfoils (reference Figure 168). Teardown inspection revealed several large, hard carbon deposits on the inside of the combustor body and evidence of missing deposits. The engine was operated in a "ram" start mode (gasifier pinion removed) and this probably contributed to the carbon deposits. Total time on this rotor was 99:54 hr, including 56 start/stop cycles. The rotor was successfully exposed to 1080°C (1976°F) max TIT and 83% max N_1.

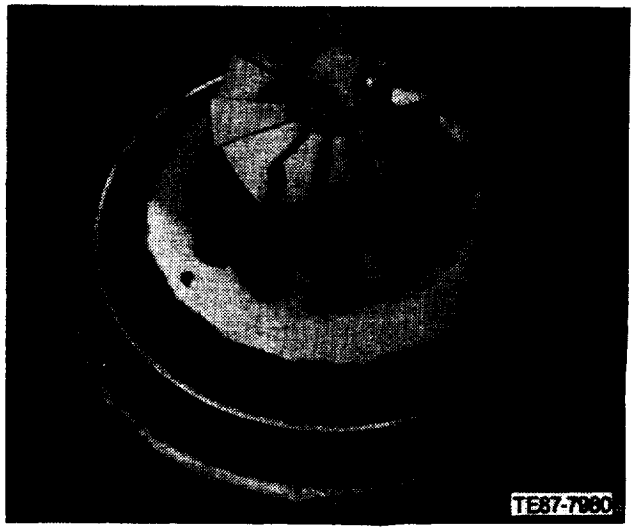

Figure 168. *Si_3N_4 gasifier rotor (S/N 0002-1) at teardown, engine S/N 1 TD-20 for 99.54 hr total on the rotor.*

Postfailure fractographic analysis of the rotor reached the following conclusions:

1. The gasifier turbine rotor failed as a result of FOD. A large piece of carbon build-up on the inner diameter wall of the combustor came loose into the gas flow path, and the resulting impact on the gasifier turbine rotor fractured all of the inducer blade tips.
2. One exducer blade tip of the rotor failed from a preexisting surface flaw. However, this event did not cause the rotor failure.

Si_3N_4 Material, Rotor Test Number 2—Based on the previous high hour (approximately 100) test of a Si_3N_4 gasifier rotor and the FOD rather than structural integrity failure of the airfoils, test engine No. 1, BU21 was assembled with an identical gasifier rotor assembly, S/N 0002-8. The usual inspections were conducted and the airfoil natural frequencies were calculated and experimentally measured. The results are presented in Figure 169 and the agreement is excellent.

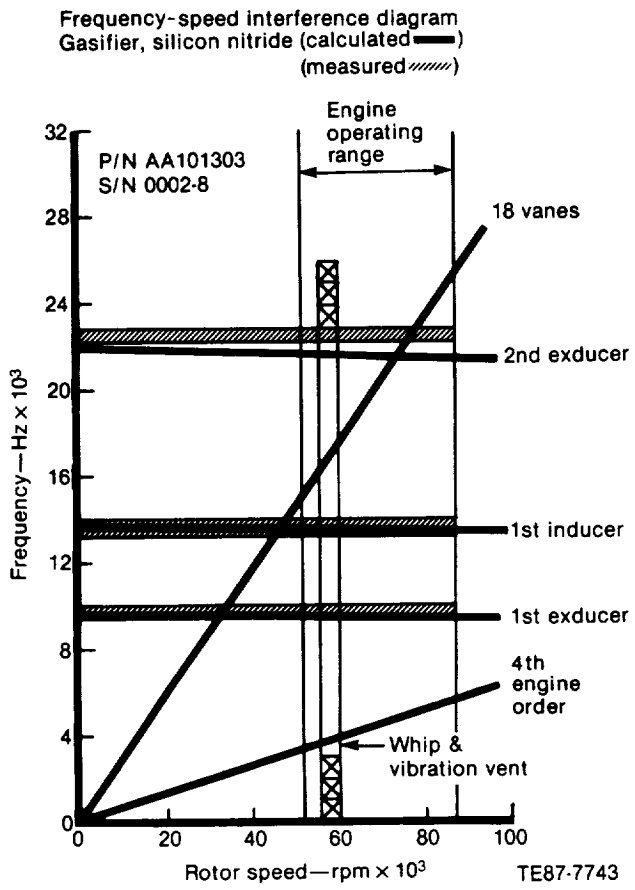

Figure 169. *Frequency/speed diagram for Si_3N_4 gasifier rotor, engine S/N 1, BU21.*

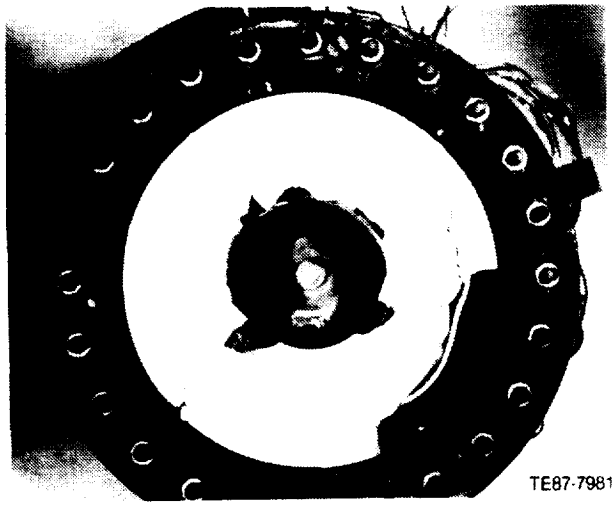

Figure 170. *Engine S/N 1, BU21 teardown condition. Gasifier (Si_3N_4) rotor (center) was broken at the stub shaft and wedged in the scroll.*

During the fourth test cycle, the rotor failed at 70% N, and 996°C (1825°F) TIT. Teardown inspection revealed fracture of the ceramic rotor stub shaft as shown in Figure 170. It caused extensive damage to the gasifier scroll assembly and FOD damage of the power turbine and scroll. Figure 171 illustrates the rotor remnant.

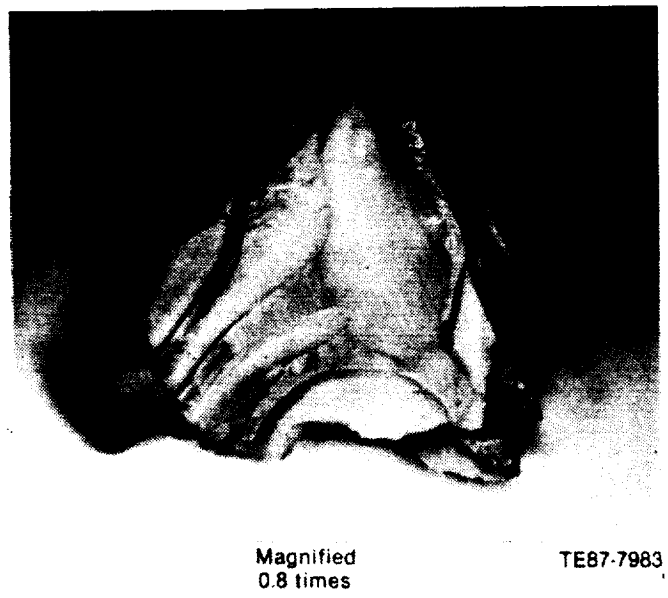

Figure 171. *Engine S/N 1, BU21 teardown condition of Si_3N_4 material gasifier rotor.*

Data analysis indicated that the cavity pressure behind the inner backplate was excessive and caused the gasifier scroll to lift off and tilt into the rotor. It was concluded that the interference (scroll to rotor) probably failed the Si_3N_4 rotor stub shaft at the juncture to the metal compressor shaft. This is consistent with the postfailure fractographic analysis. A failure origin was found at the stub shaft typical of a tensile failure with a well defined mirror region. From the mirror radius and the materials constant obtained from test bars, the failure stress of the stub shaft was 441.3 MPa (64 ksi), which is much higher than the predicted stress at 70% speed. Thus, the Si_3N_4 gasifier rotor was exonerated of a primary structural failure, and the decision was made to rebuild test engine number 1 with an identical Si_3N_4 gasifier rotor for additional, hot environment experience.

Si_3N_4 Material, Rotor Test Number 3— Engine No. 1, BU22 was assembled with the third identical Si_3N_4 material (SN220M) gasifier rotor, S/N 0002-6. This rotor, finished to Mod I open clearance configuration the same as all ceramic gasifier turbine rotors to date (August 1986), was successfully

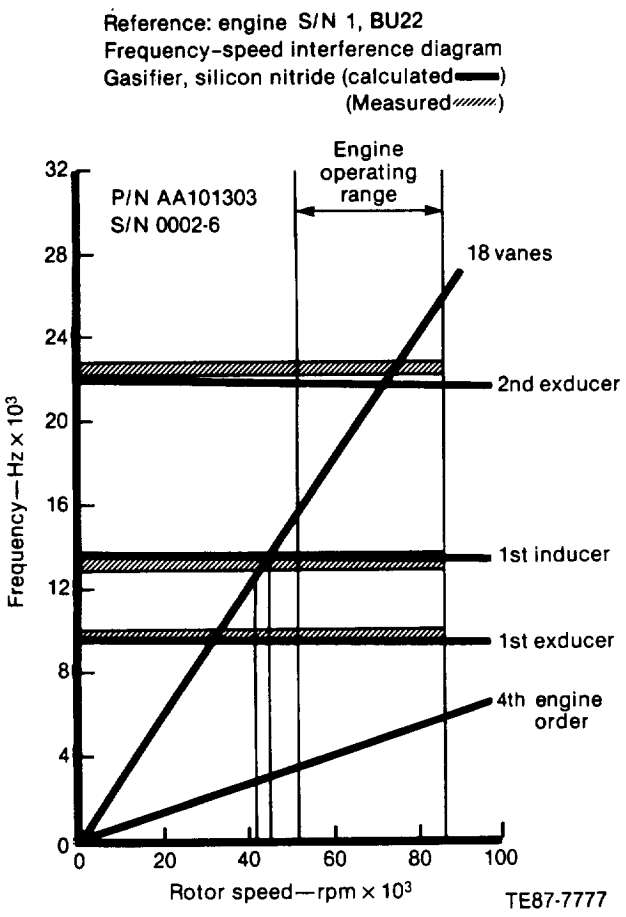

Figure 172. Frequency-speed diagram for Si_3N_4 gasifier rotor, engine S/N 1, BU22.

qualified by FPI, visual, dimensional, and dynamic proof stress of the inducer airfoil. The airfoil natural frequencies were experimentally measured and the data shown on the interference diagram per Figure 172. Further, the inducer portion of the airfoils was dynamically proof stressed by controlled amplitude vibration in the airfoil first inducer mode. This was the first engine rotor to be subjected to this specialized proof test. This was an effort to clear the rotor for engine operation which exposes the inducer section to vane passage response in the 42 to 45 krpm range (Figure 172). Each inducer airfoil was excited to a tip amplitude of 63% of fracture amplitude for a minimum dwell of 1 minute. This resulted in a peak-to-peak tip amplitude of 0.305/0.28 mm (0.012/0.011 in.) and a radial stress component of approximately 207 MPa (30 ksi). The test and a comparison with SiC material airfoil are shown in Figure 173.

The engine test plan was successfully completed and the engine was disassembled to replace the metal gasifier scroll with the Norton SiC scroll proof-tested on engine S/N 2, BU16.

Engine S/N 1, BU23 was configured with the first all ceramic gasifier turbine package. The test plan was successfully completed and the all-ceramic gasifier turbine was operated at 60% N_1 and 899°C (1650°F) TIT.

Engine disassembly revealed that one cross-key slot on the outer backplate had broken. No other damage was noted.

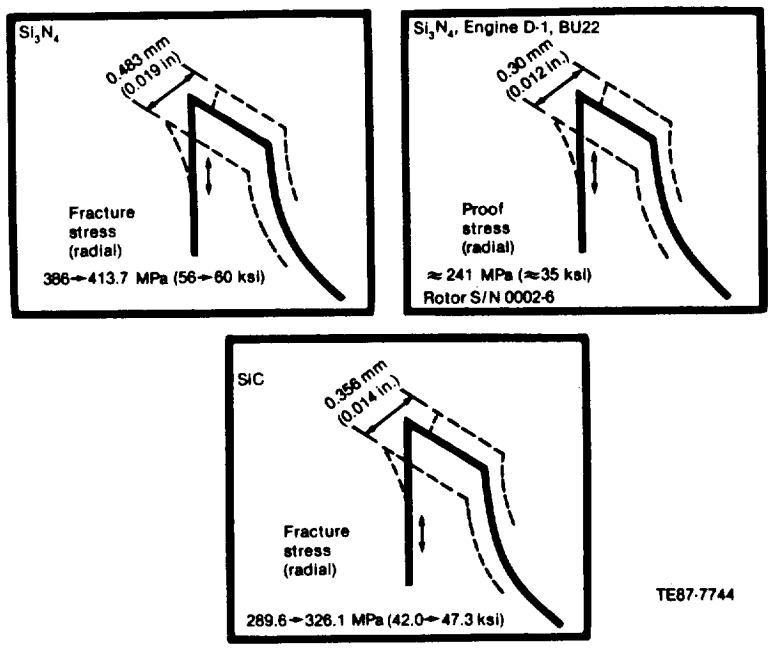

Figure 173. Gasifier turbine first inducer mode resonant fracture and proof test.

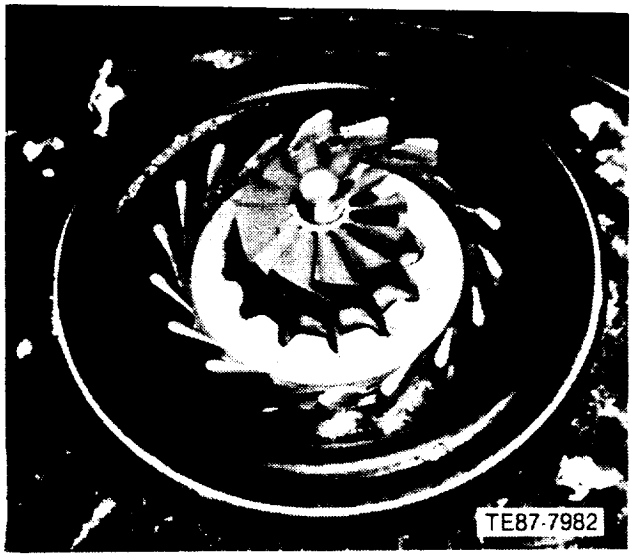

Figure 174. *Si_3N_4 gasifier rotor, engine S/N 1, TD-24, fractured airfoils, inducer region.*

Engine S/N 1 was reassembled as BU24 to continue testing the first all-ceramic gasifier turbine package as was tested on BU23.

Turbine failure occurred during the second cycle at a stabilized condition (1010°C [1850°F] TIT and 60% N_1) 2 min after crossover to the main fuel nozzle. The symptoms were a sudden decrease in rotor speed and an increase in turbine inlet temperature. A manual shutdown was made.

Engine disassembly verified turbine failure. Damaged ceramic hardware included the following:

- all rotor tips broken
- all vanes broken
- outer backplate cross key slot tang broken
- combustor dome chipping
- combustor body chipping

Figure 174 illustrates the fractured inducer airfoils of the gasifier. Total time on this ceramic gasifier rotor was 20 hr 11 minutes.

The key points that support the concept that the gasifier rotor was not the primary failure are as follows:

- The rotor vendor, Kyocera International, had proof spin tested the rotor to 116% speed.
- The inducer region of the airfoils had successfully cleared the dynamic proof test.
  - Data base: 0.5 mm (0.020 in.) double amplitude failure at σ_r = 396.46 MPa (57.5 ksi)
  - Proof test: 0.305/0.28 mm (0.012/0.011 in.) double amplitude at σ_r = 234.4 MPa (34 ksi)
- Critical speed range for vane passage response is 48 to 52% N_1 (Figure 172).
- Failure initiated at 60% N_1.
- Prior tests successfully exercised the rotor through the critical range.

Based on these observations and data, vane passage response failure of the rotor airfoils was considered remote. However, some test time was demonstrated for the all ceramic gasifier section.

Si_3N_4 Material, Rotor Test Number 4— Engine S/N 1, BU25 was assembled for an all-ceramic gasifier turbine test. The three previous tests of Si_3N_4 gasifier rotors used the SN220M grade Si_3N_4 and the decision was made to demonstrate the newer SN250M grade Si_3N_4 rotor material.

This rotor was joined to the compressor shaft by the Allison interference fit scheme and finished to Mod I open clearance configuration, and was successfully qualified by FPI, visual, dimensional, dynamic proof stress of the inducer airfoil, and attachment flexural proof test. The airfoil natural frequencies were experimentally measured and the data shown on the interference diagram per Figure 175. The inducer portion of the airfoils was dynamically proof stressed by controlled amplitude vibration in the airfoil first inducer mode to approximately 63% of the fracture amplitude. Further, the interference fit shaft attachment was subjected to a bending or flexural load of two times the maximum expected engine load resulting from the maximum allowable unbalance. The assembly was revolved through 720° while subjected to the flexural load. This attachment proof test was prompted by the flexural failures of the first group of Kyocera braze attachments.

During the third attempt at increasing the temperature to 1204°C (2200°F) BOT, the engine was shut down by the test stand safety system, which precluded motoring. Shutdown occurred at an indicated BOT of 1166°C (2130°F). This is the maximum inlet temperature experienced in all AGT 100 engine testing.

Subsequent running yielded high vibration and whip at 45% N_1. Testing was terminated and the engine was removed from the test cell for disassembly. Post-test gasifier rotor balance was 10 times the drawing maximum limit compared with conformance to the drawing limit at assembly.

Detail dimensional inspection (Figure 176) of the gasifier rotor at disassembly confirmed movement of the rotor relative to the shaft. This explained the observed change in balance. The data suggested yield and permanent set of the metal

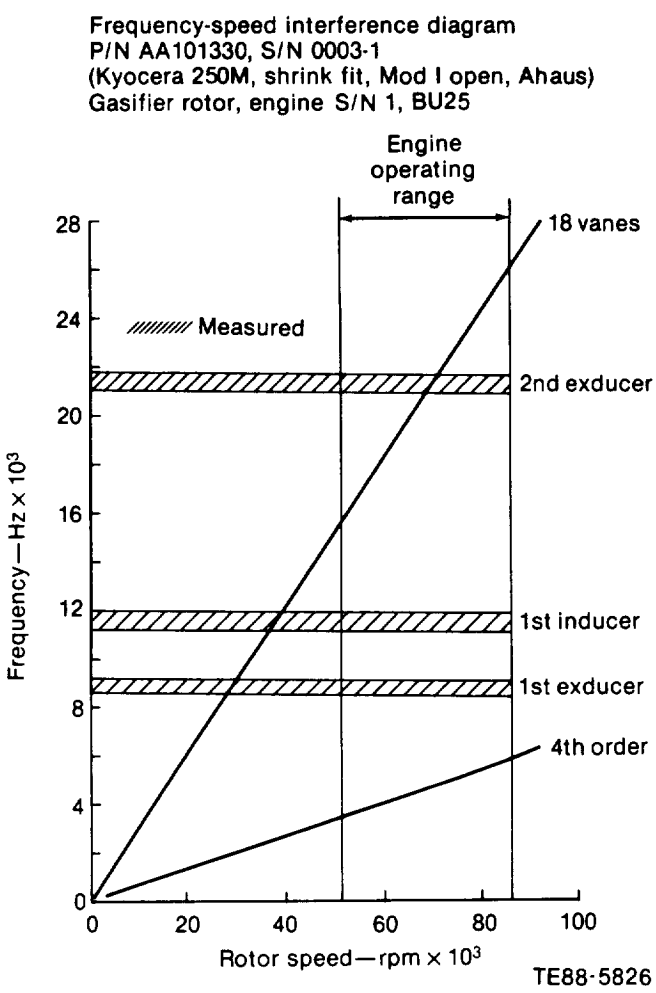

Figure 175. *Frequency-speed diagram for gasifier rotor, engine S/N 1, BU25.*

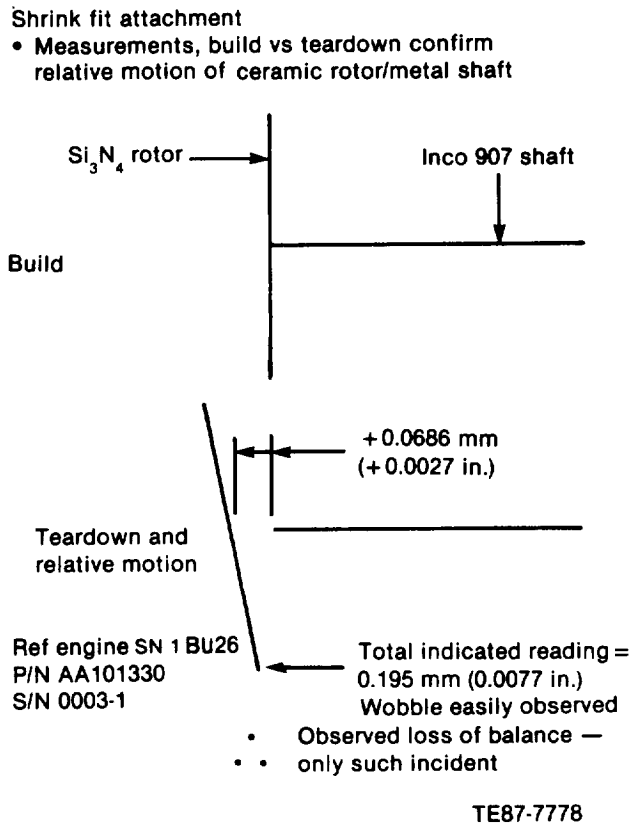

Figure 176. *Post-test dimensional inspection, ceramic rotor/metal shaft interference fit geometry.*

shaft, although the design of the attachment is well below material yield.

The investigation of the relative motion of the Si_3N_4 material rotor to the Inco 903 material gasifier shaft is summarized as follows (Ref engine S/N 1, BU25):

- facts
  - design stress value well below yield (620.6 MPa [90 ksi] versus 1103.2 MPa [160 ksi])
  - quick shutdown—no evidence of excessive heat at attachment, i.e., blueing of shaft
- relative motion, rotor/shaft
  - wobble observed
  - balance change
- compressor shaft locally soft
  - R_c 32 versus 40 required
  - σyd ~ 827 MPa (120 ksi)
- scenario
  - quick shutdown—no cooling of airfoils
  - heat soak, rotor to rotor stub shaft
  - combination of heating of metal shaft and annealed material
  - shaft yielded/permanent set
  - rotor tilt—imbalance, shaft dynamics

A heat transfer analysis of soakback is an additional design consideration—particularly for the interference fit rotor/shaft attachment scheme. Another design consideration is an alternate shaft material exhibiting less thermal growth.

Si_3N_4 Material, Rotor Test Number 5— Engine S/N 1, BU26 was assembled for another all-ceramic hot section test. This was the final build of this engine under the AGT 100 program for the test conducted in May 1987. The gasifier rotor was Kyocera supplied, Si_3N_4 material (SN220M grade) proof spin tested to 134 krpm (155% N_1). This rotor, joined to the compressor shaft by the Allison interference fit scheme and finished to MOD I open clearance configuration, was successfully qualified by FPI, visual, dimensional, dynamic proof stress of the inducer airfoil and flexural proof test of the attachment. The airfoil natural frequencies were experimentally measured and the data shown on the interference diagram per Figure 177.

While increasing to 2000°F and 70% N_1 during the second engine test cycle, a sudden drop in N_1 speed to 46% occurred. Emergency motoring was conducted to prevent thermal shock and bearing overtemperature. Removal of main nozzle revealed a failed gasifier scroll. The failed gasifier scroll prompted a complete teardown and inspection of the engine. This revealed that all ceramic hardware, except the combustor body, combustor dome, and pilot flame tube, was unsuitable for further testing.

The engine record data associated with the shutdown, the interpretation of the data, photo record of the components, postfailure investigation, and possible scenarios are fully discussed under Gasifier Turbine Static Structure.

Relative to the gasifier rotor, the engine record data showed the failure event to be remote from potential rotor airfoil response to vane passage (see Figure 177). However, impact damage to the airfoils is a potential failure mechanism.

Fractographic analysis of the failed rotor stub shaft calculated the fracture stress at 463.34 MPa (67.2 ksi). This stress is nearly identical to the fracture stress calculated for the scroll liftoff case (rotor test 2).

In summary, two key points were developed in the postfailure investigation relative to the gasifier rotor. These were the following:

1. An exact cause of the engine failure was not identified.
2. The rotor airfoil impact survivability is a major concern.

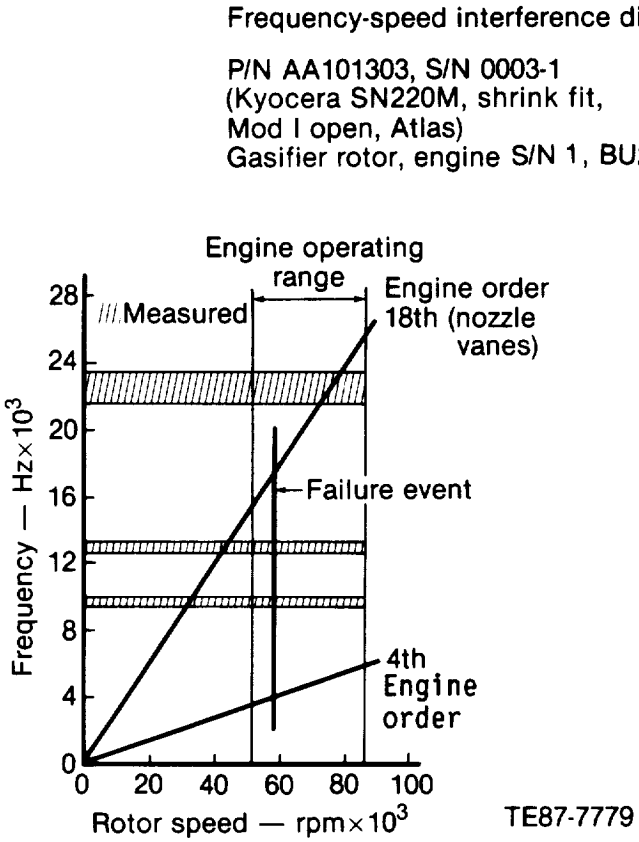

Figure 177. Frequency-speed diagram for Si_3N_4 gasifier rotor, engine S/N 1, BU26.

3.6 GASIFIER TURBINE STATIC STRUCTURE

Introduction

The gasifier turbine ceramic static structure consists of the turbine scroll/shroud assembly, outer backplate, inner backplate, nozzle vanes (18), insulating shim spacer ring, interturbine coupling, and seal rings.

Complete ceramic gasifier turbine static structure assemblies have been tested in 10 engine builds during the AGT 100 engine program. Ceramic or composite ceramic gasifier turbine inner backplates have been installed in 16 engine builds during the program, and partial or complete ceramic nozzle vane sets (18 vanes) have been installed in 17 engine builds.

The static structure assemblies have included components fabricated of monolithic SASC, SiSiC, RB SiC, and SSN. Zirconium oxide insulating rings have been used in all 45 engine assemblies and composite ceramic inner backplates have been tested in seven engine assemblies. The ceramic components have been developed by American suppliers and procured from foreign suppliers on a parts buy basis.

A room temperature static load proof test has been developed to subject the gasifier turbine scroll body/shroud braze joint to RPD structural load conditions. Twenty gasifier turbine scroll assemblies were subjected to the proof load test; 19 passed.

A revised design gasifier turbine scroll with a new outlet configuration and a new companion interturbine coupling were designed and have been fabricated. This configuration simplifies engine assembly.

Since the last annual report, seven incidents resulting in the fracture of one or more gasifier turbine static structure components were investigated and failure scenarios developed. Detailed accounts of these incidents are included later in this subsection.

At the conclusion of the AGT contract, the following occurred:

1. A major engine failure (S/N 1, BU26) in the all ceramic hot section was still under investigation. A primary failure origin has not been identified.
2. Improvement in the Carborundum (CBO) SiC scroll body/shroud braze joint performance had not been demonstrated. However, a new CBO scroll body assembly with an improved braze joint (both material and joint configuration) had been fabricated. The newly fabricated CBO scroll assemblies also incorporate the revised scroll outlet configuration.
3. While 13:45 hr of successful testing had been conducted with the Kyocera Si_3N_4 scroll assembly, a braze joint in that assembly is suspect in the previously mentioned S/N 1, BU26 engine failure. Further evaluation of additional Si_3N_4 scrolls would be necessary to determine their performance.

Objective

The design requirements of the gasifier turbine ceramic static structure are as follows:

- to provide a closed flow path from the combustor outlet, through the gasifier turbine rotor to the power turbine scroll inlet within the space allotted in the general engine layout
- to have flow path geometry that maintains approximately Mach 0.1 velocity in the scroll housing and proper flow direction and Mach No. (approximately 0.7) through a nozzle blade row
- to be fabricated of material(s) that have capability of operating continuously at 1288°C (2350°F) gas temperature
- to provide a close-fitting shroud around the turbine rotor blades under all operating conditions
- to have a design probability of survival of 0.999375 at each failure site in the assembly under steady-state and transient operating conditions

Discussion

Gasifier Turbine Static Structure Design

The gasifier turbine static structure consists of the following four major components, as shown in Figure 178:

- scroll/shroud (bonded assembly)
- outer backplate
- inner backplate
- nozzle vanes (18)

For purposes of reporting, the interturbine coupling and the ceramic insulating shim are included as parts of the gasifier turbine static structure.

The monolithic zirconium oxide thermal barrier ring/shim is positioned between the turbine

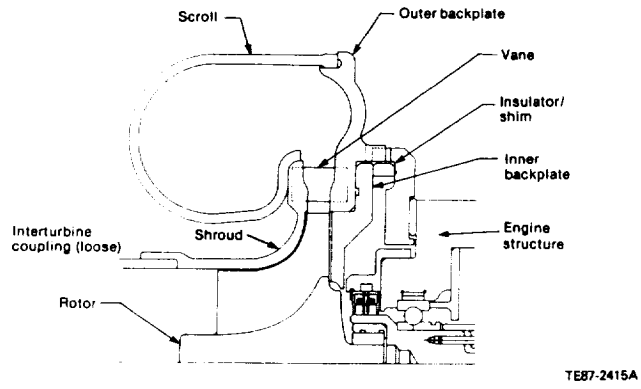

Figure 178. *Cross section of gasifier ceramic turbine static structure.*

static structure and the metal engine structure. Its thickness is varied to adjust turbine rotor blade to shroud clearance.

Analytical design analysis has been conducted on the gasifier turbine static structure using Allison's STRATA FEM program. By using 2-D and 3-D FEM models, operating temperatures, component deflections, stresses, and POS have been calculated for steady-state and transient start-up conditions. Design iterations were completed on the gasifier turbine scroll/shroud assembly and inner backplate to optimize POS and/or deflection. Various materials also have been evaluated with the FEM analysis. Calculated probability of survival for transient and steady-state RPD conditions are shown in Table XXXIII for three design variations of the gasifier turbine scroll fabricated of Norton NC-430 SiC material, CBO SASC material, and Kyocera SSN material. Calculated POS for gasifier turbine outer backplates fabricated of CBO alpha-SiC and Kyocera Si_3N_4 are shown in Table XXXIV and for gasifier turbine inner backplates in Table XXXV. POS for gasifier turbine vanes made of CBO SiC was calculated using a 3-D FEM analysis. The results are shown in Table XXXVI. Because the calculated POS of the gasifier vanes during a transient was less than the goal of 0.999375, a proof test procedure was established for individual vanes to qualify them for engine test.

Since the last annual report, gasifier turbine component design activities included the following:

- Detail prints of Kyocera design of gasifier turbine static structure were approved for fabrication.
- Metal gasifier turbine scroll/outlet elbow configuration were revised to ease engine assembly.
- CBO alpha-SiC gasifier turbine scroll/outlet elbow configuration were revised and new scrolls and couplings fabricated.
- Static load proof tests were designed to evaluate scroll body/shroud braze joint.
- Analytical study determined suitability of Corning CAS-II composite ceramic material for gasifier turbine vanes.

Detail discussion of these activities appears in the following paragraphs.

Kyocera Gasifier Turbine Scroll Design— Kyocera International was asked to quote on fabrication of an alternate design gasifier turbine scroll (AA101200 configuration). Kyocera responded with a revised design that simplified fabrication. Approval of Kyocera's proposal was granted and six Si_3N_4 gasifier scroll assemblies (AA101339) were fabricated. Figure 179 shows a comparison of the Kyocera scroll configuration and the CBO/Norton scroll configuration.

Metal Gasifier Turbine Scroll/Outlet Elbow Modification—The original designs of the gasifier turbine scroll, interturbine coupling, and power turbine scroll require that they be installed in the engine simultaneously. To simplify engine assembly, all (three) metal gasifier turbine scroll assemblies being tested were modified to remove the outlet elbow from the scroll. New interturbine couplings, which take the place of the elbow originally affixed to the gasifier scroll and the short interturbine coupling that connected to the power turbine scroll inlet, were fabricated. Figure 180 shows the configuration of the modified gasifier turbine scroll and the extended interturbine coupling duct.

Revised CBO Alpha-SiC Gasifier Turbine Scroll/Outlet Elbow Configuration—The CBO alpha-SiC gasifier turbine scroll design has been revised to provide a ceramic scroll assembly with the outlet elbow removed in a manner similar to that described in the previous subsection. A new extended length ceramic interturbine coupling was also designed as a companion part to the revised scroll. The total number of joints in the flow path

Table XXXIII.

Calculated POS for transient and steady state RPD conditions.

Inlet temp	AA101052				AA101052 with thick wall				Alternate design scroll			
—°C(°F)	Steady state		Transient		Steady state		Transient		Steady state		Transient	
1288	P_v	0.09780	P_v	0.6446	P_v	0.99776	P_v	0.8717	P_v	0.9989	P_v	0.5880
(2350)	P_s	0.9951	P_v	0.8603	P_s	0.9949	P_s	0.9498	P_s	0.9997	P_s	0.8642
	POS	0.9732	POS	0.5545	POS	0.9726	POS	0.8279	POS	0.9986	POS	0.5081

Characteristic strength for volume is 87.56 MPa (12.7 ksi) and 157.89 MPa (22.9 ksi) for surface; Weibull modulus is 8.66 for volume and surface.

POS comparison of CBO alpha-SiC ceramic scroll.*

Inlet temp	A101626 original design				AA101160 increased thickness				AA101200 alternate designs			
—C°(°F)	Steady state		Transient		Steady state		Transient		Steady state		Transient	
1288	P_v	0.9986	P_v	0.9033	P_v	0.9984	P_v	0.9826	P_v	0.9999	P_v	0.9941
(2350)	P_s	0.9972	P_s	0.9788	P_s	0.9995	P_s	0.9969	P_s	0.9999	P_s	0.9993
	POS	0.9958	POS	0.8842	POS	0.9979	POS	0.9796	POS	0.9999	POS	0.9934

*Characteristic strength is 558 MPa (25,580 lb/in.^{2}) for volume and 706 MPa (48,700 lb/in.^{2}) for surface; Weibull modulus is 8.43 for volume and 8.71 for surface.

POS of Kyocera Sintered Si_3N_4 ceramic scroll.

Inlet temp	AA101160 design configuration			
—°C(°F)	Steady state		Transient	
1288	P_v	1.0000	P_v	0.9999
(2350)	P_s	1.0000	P_s	1.0000
	POS	1.0000	POS	0.9999

Characteristic strength is 406.79 MPa (59.0 ksi) for volume and 595.02 MPa (86.3 ksi) for surface. Weibull modulus is 15 for volume and surface.

Table XXXIV.

POS of gasifier turbine outer backplates.

Inlet temp	CBO Alpha-SiC		Kyocera Si_3N_4	
—°C(F°)	Steady state	Transient	Steady state	Transient
1288 (2350)	0.9999	0.9627	1.0000	0.9999

Characteristic strength of alpha-SiC is 176.51 MPa (25.6 ksi) for volume and 335.77 MPa (48.7 ksi) for surface; Weibull modulus is 8.4 for volume and 8.7 for surface; characteristic strength of Si_3N_4 is 406.79 MPa (59.0 ksi) for volume and 595.02 MPa (86.3 ksi) for surface; Weibull modulus is 15 for volume and surface.

Table XXXV.
POS of gasifier turbine inner backplate.

Inlet temp	CBO Alpha-SiC		Kyocera Si_3N_4	
°C(F°)	Steady state	Transient	Steady state	Transient
1288	0.9998	0.9289	1.000	0.9999

Characteristic strength of alpha-SiC is 176.51 MPa (25.6 ksi) for volume and 335.77 MPa (48.7 ksi) for surface; Weibull modulus is 8.4 for volume and 8.7 for surface; characteristic strength of Si_3N_4 is 406.79 MPa (59.0 ksi) for volume and 595.02 MPa (86.3 ksi) for surface; Weibull modulus is 15 for volume and surface.

Table XXXVI.
POS of SiC gasifier turbine vane.

Inlet temp	CBO alpha-SiC	
°C(F°)	Steady state	Transient
1288 (2350)	0.9999	0.9800

Characteristic strength is 176.51 MPa (25.6 ksi) for volume and 335.77 MPa (48.7 ksi) for surface; Weibull modulus is 8.4 for volume and 8.7 for surface.

between turbines remains the same as the original design, thus the leakage should be unchanged. Revised design scrolls and interturbine couplings, shown in Figure 181, have been fabricated.

Static Load Proof Test of Gasifier Turbine Scroll Body/Shroud Braze Joint—Engine testing of the CBO alpha-SiC gasifier turbine scrolls has shown poor braze joint integrity at the scroll body/shroud interface. To insure that the braze joint can withstand the structural load experienced during

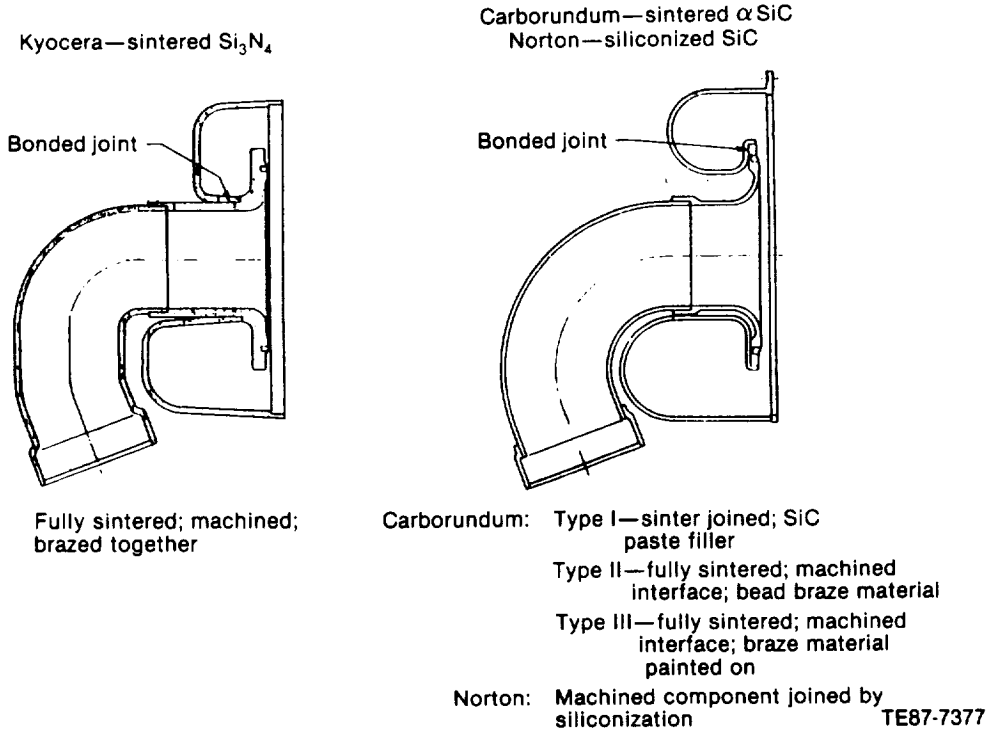

Figure 179. *AGT 100 gasifier turbine scrolls.*

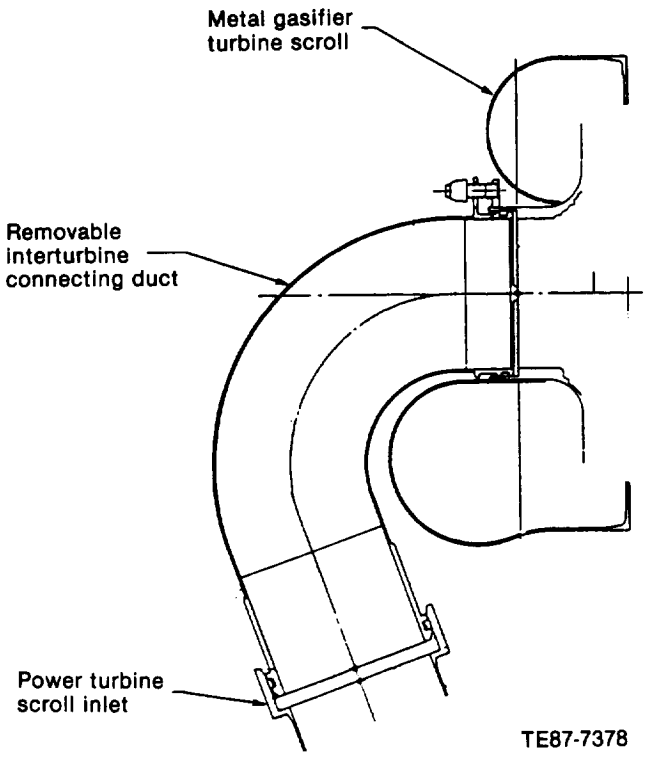

Figure 180. *Modified metal gasifier turbine scroll and removable interturbine connecting duct.*

engine operation a room temperature static load proof test has been designed to expose the subject braze joint to the structural load experienced at RPD engine operating conditions. Test configurations have been designed for (1) the CBO and Norton scrolls with outlet elbows, (2) the Kyocera scroll with outlet elbow, and (3) the CBO scroll without the outlet elbow. The test configurations for the CBO and Norton scrolls are shown in Figure 182. This test has been made a part of the inspection routine for each scroll received. Twenty scrolls have been tested; 19 passed without distress.

Evaluation of Corning CAS-II/SiC Composite Ceramic Material as Gasifier Turbine Vane Material—Engine test experience has shown a need for increased toughness in the ceramic nozzle vane material. Corning Glass Works CAS-II/SiC whisker reinforced glass ceramic material has the potential for increased toughness compared to monolithic ceramics and was evaluated analytically to determine its suitability as a material for the gasifier turbine vane. Operating temperatures, stresses, and POS were calculated for steady-state and transient start-up operating conditions.

The results of the analysis show that the CAS-II/SiC material evaluated is not suitable for use in a gasifier turbine vane component. A high thermal gradient develops at the trailing edge of the vane during the start-up transient because of the low thermal conductivity of the CAS-II material. The severe thermal gradient causes high local stress at the vane trailing edge and low POS.

The material characteristics used in the analysis are shown in Table XXXVII along with typical alpha-SiC properties for comparison. Note that the coefficient of thermal conductivity for CAS-II/SiC is about one tenth that of silicon carbide.

The CAS-II/SiC vane undergoes a maximum thermal gradient at about 13 sec into the start procedure. (A similar vane made of alpha-SiC undergoes a maximum thermal gradient at about 16 sec into the start-up cycle.)

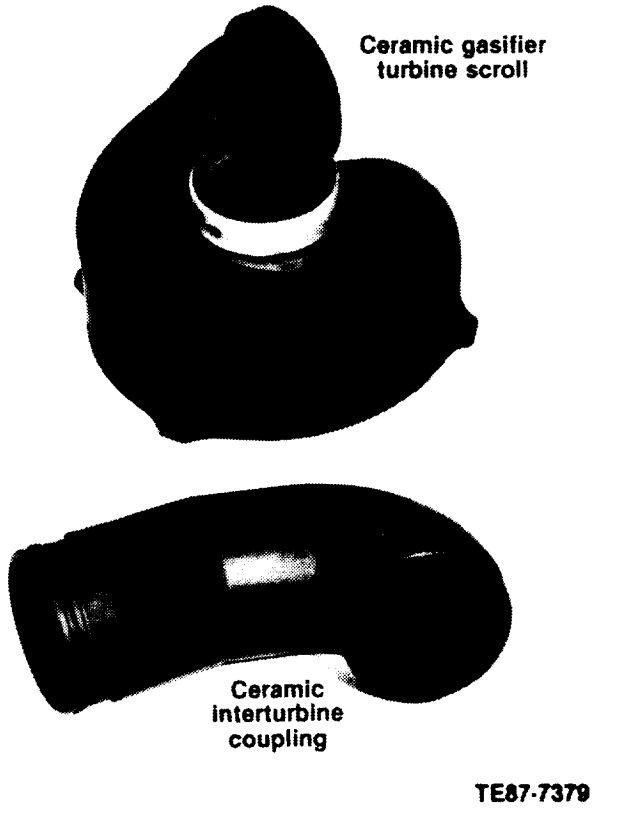

Figure 181. *Gasifier turbine scroll and removable elbow coupling, CBO alpha-SiC material.*

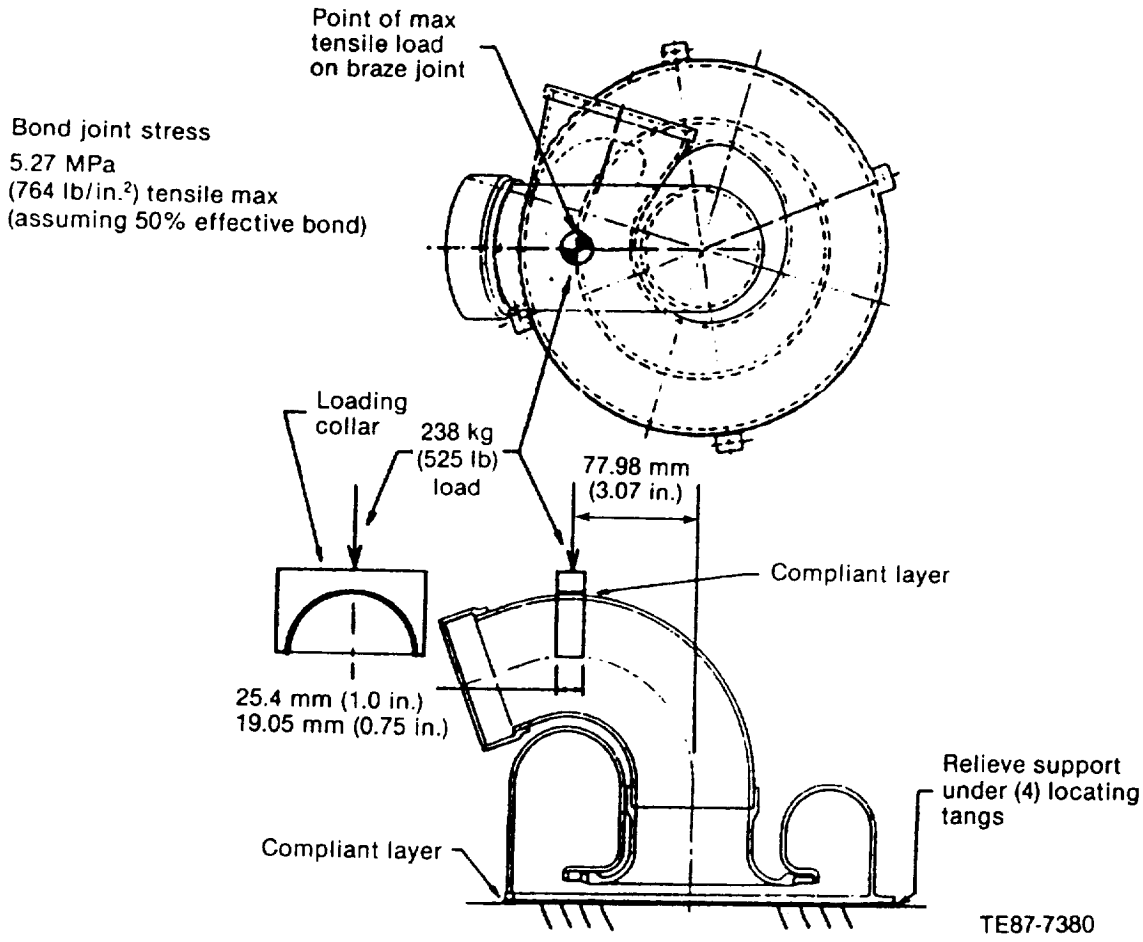

Figure 182. *Static load scroll proof test.*

Table XXXVII.
Material property comparison.

	Alpha-Sic	CAS-II
Thermal conductivity—Btu-in./hr-in.-°F		
77	7.368	0.4556
1112	3.0347	0.2056
1832	2.1181	0.1976
2192	1.8056	0.1875
Thermal expansion—in./in.-°F E-6		
77	1.74	1.74
1112	2.20	2.02
1832	2.59	2.17
2192	2.73	2.27

Table XXXVII. *(Cont)*
Material property comparison.

	Alpha-Sic	CAS II
Weibull modulus	8.71 sur 8.43 sur	9.00 sur 9.00 sur
Characteristic strength—MPa (ksi)		
Surface		
70/77	335.77 (48.7)	311.64 (45.2)
2000/2192	335.77 (48.7)	204.08 (29.6)
Volume		
70/77	176.50 (25.6)	209.60 (30.4)
2000/2192	176.50 (25.6)	137.20 (19.9)

The maximum principal stress and POS for the CAS-II/SiC are shown in Table XXXVIII. Corresponding values for an alpha-SiC vane are also included in Table XXXVIII. The POS of the CAS-II/SiC vane is very low. Both surface and volume effects contribute to the low POS. By comparison, the POS of the alpha-SiC vane nearly equals the design requirement POS (0.999375).

Figure 183 shows the temperature gradient on the pressure side of the vane, and Figure 184 shows the maximum principal stresses on the pressure surface of the vane at 13 sec into the transient cycle.

Engine Test of Ceramic Gasifier Turbine Static Components

One or more ceramic gasifier turbine static structure components in addition to the zirconium oxide insulating shim have been installed in 23 engine assemblies during the AGT 100 program. The zirconia shims have been installed in all 45 engine assemblies tested. The various components comprising the gasifier turbine have been fabricated from a number of ceramic material systems. The turbine vanes and inner backplates may be used interchangeably with mating components of differing materials. However, scrolls and outer backplates must be of materials with similar thermal expansion coefficients because of their close fitting mating features.

Turbine Scroll—Testing has been performed of scrolls fabricated from alpha-SiC, SiSiC, and Si_3N_4. Testing of alpha-SiC gasifier turbine scrolls in the engine has resulted in fractures of the scroll body in the region of the scroll body/shroud braze joint that are related to poor performance of that braze joint.

Table XXXVIII.
Stress summary and POS.

	Alpha-SiC	CAS II
	Maximum conditions	
Principal stress	405.41 MPa (58.8 ksi)	446.78 MPa (64.80 ksi)

Note: These stresses are located at a node 0.094 mm (0.0037 in.) inward of the trailing edge.

	Probability of survival	
Surface effects	0.991	0.0459
Volume effects	0.989	0.5439
Total effects	0.980	0.0249
Design requirement	0.999375	0.999375

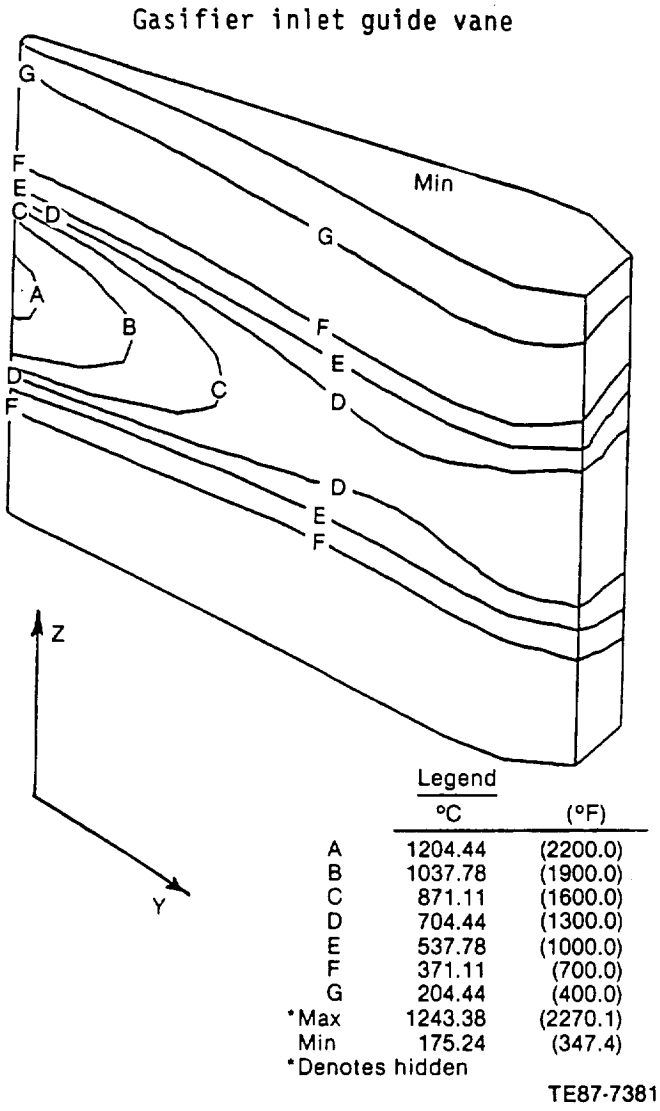

Figure 183. *Thermal gradient, pressure side, at 13 sec into transient cycle.*

Design and processing improvements have been implemented to improve the braze joint performance. Two approaches have been taken. First, greater care has been taken to insure that an improved fit of the mating parts exists and that ample braze material ($MoSi_2$) is supplied to obtain complete coverage of the mating surfaces. Second, a revised scroll body configuration, which omits the rim that surrounds the shroud detail, has been fabricated. (This is the portion of the scroll body that has fractured in engine testing.) In addition, a new braze material, CrVTi, has been used in the revised joint. Scrolls incorporating the improved $MoSi_2$ braze joint and the revised CrVTi joint have been fabricated but have not been engine or rig tested. A total of 20 hr of hot engine test time have been accumulated on CBO alpha-SiC gasifier turbine scrolls. Maximum operating temperature of the scrolls in engine testing was 1080°C (1976°F). In addition, a total of 6.5 hr of test time were accumulated in a static thermal shock test fixture preceding engine testing.

Successful testing has been accomplished with Norton NC-430 SiSiC gasifier turbine scrolls. One Norton scroll, identical in configuration to the CBO alpha-SiC scroll, has accumulated 23.4 hr of hot engine testing reaching a maximum temperature in excess of 1149°C (2100°F) plus 8.3 hr of static rig testing. This scroll remains in good condition and is a candidate for future engine testing. A second Norton scroll has successfully undergone 13.1 hr of testing in a static thermal shock rig to a maximum of

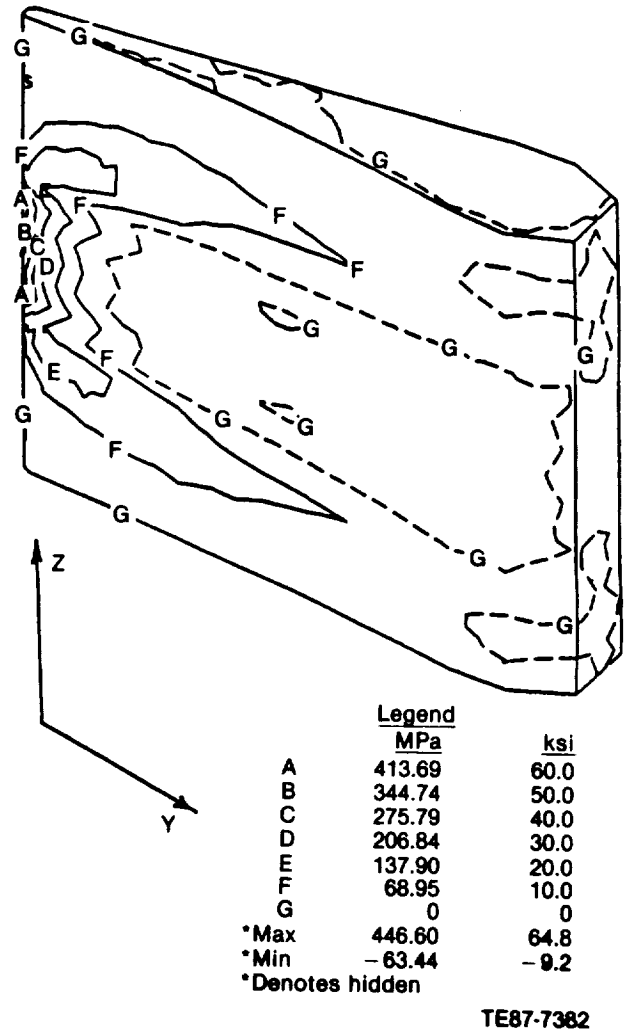

Figure 184. *Principal stress gradient, pressure side, at 13 sec into transient cycle.*

1093°C (2000°F) operating temperature and is qualified for engine testing.

A Kyocera SSN gasifier turbine scroll has also been engine tested. The scroll was successfully tested in two engine assemblies for a total of 13.8 hr reaching approximately 1093°C (2000°F) maximum operating temperature. The scroll fractured in a subsequent test while being tested along with a complete complement of engine hot section ceramic components. The exact cause of that engine failure could not be ascertained because of the significant damage sustained by many of the ceramic components; but the failure investigation concluded that a braze joint in the gasifier turbine scroll body assembly may have been a primary failure origin in that event. Additional testing of the Kyocera Si_3N_4 scroll is required to determine the performance of that scroll assembly.

Vanes—Gasifier turbine vanes fabricated of CBO's alpha-SiC and GTE's AY6 and PY6 Si_3N_4 have been tested during the AGT 100 program. Partial or complete sets of gasifier turbine vanes have been included in 17 test engine assemblies and 8 thermal shock rig assemblies. Early in the program, vanes were proof tested in groups of three in a static test fixture capable of exposing the vanes to transient operating conditions because analysis showed the POS during transient operation to be below design goals (POS = 0.98 versus goal of 0.999375). Following good performance of the vanes in engine tests, the proof test procedure was waived later on in the program. SiC vanes have experienced some minor chipping during engine testing. Si_3N_4 vanes have been successfully tested in the engine and thermal shock rig in both SiC and Si_3N_4 static structure assemblies. One hundred eleven engine test hours have been accumulated on SiC vanes and 46 engine test hours have been accumulated on Si_3N_4 vanes. Gasifier turbine vanes of both materials have shown vulnerability to FOD. When an engine experienced FOD, which typically would damage turbine rotor inducer blades, the vanes would invariably receive damage also.

Outer Backplate—Gasifier turbine outer backplates fabricated by CBO of alpha-SiC and by Kyocera of Si_3N_4 have been engine tested during the AGT 100 program. SiC outer backplates have been tested also in the thermal shock test rig. Early tests of alpha-SiC outer backplates resulted in fractures during engine testing. The fractures were the result of thermal stress plus stress from unplanned loading by associated components. Design changes were implemented resulting in successful testing of a SiC outer backplate to temperatures in excess of 1149°C (2100°F). Similar changes were incorporated in the Si_3N_4 outer backplate design before fabrication of parts began. A Si_3N_4 outer backplate has been successfully tested in two assemblies of the engine. During the third engine test of that outer backplate it was fractured as a consequence of other engine component failures. During the AGT 100 program 43.4 hr of hot engine testing were accumulated on SiC outer backplates with testing in excess of 1149°C (2100°F) during one test. Nineteen hours of hot engine testing were accumulated on Si_3N_4 outer backplates.

Inner Backplates—Over 119 hot engine test hours have been accumulated on ceramic gasifier turbine inner backplates during the AGT 100 program, 51 hr on composite ceramic (BMAS-III/SiC) components, and 68 hr on Si_3N_4 components. Inner backplates fabricated of Corning Glass Works BMAS III/SiC composite ceramic material have been used in seven engine assemblies. The engine test specimens incorporated a "stepped" fiber reinforcement configuration, which has greater shear strength in the subject part configuration. Additional inner backplate components fabricated of LAS, BMAS-II, and MAS matrix materials with flat fiber and random-oriented whisker reinforcement media were evaluated in static tests but not in engine tests. BMAS-III material has a maximum operating temperature of approximately 1093°C (2000°F) and therefore was not engine tested in excess of 1093°C (2000°F). An inner backplate fabricated of CAS-II/SiC material with increased temperature capability was obtained at the conclusion of the AGT 100 program. It was tested successfully in a hot static test fixture to 1093°C (2000°F), but was not available in time for engine testing.

Si_3N_4 inner backplates supplied by GTE were successfully tested in the static thermal shock test fixture and three engine assemblies. Si_3N_4 inner backplates supplied by Kyocera have been used in six engine tests, in one test at temperature in excess of 1149°C (2100°F). Inner backplates have been fractured during engine testing. However, investigation has shown that the inner backplate failures have been secondary in nature; i.e., caused by the failure of another component(s). The last 16 engine builds of the AGT 100 program incorporated a ceramic or ceramic composite gasifier turbine inner backplate.

This reliable component has been used with other turbine static components fabricated of metal and also when proof testing ceramic turbine rotors.

Tables XXXIX and XL summarize the test experience in the AGT 100 program for ceramic gasifier turbine static components. Table XXXIX shows the vendor and ceramic material for each gasifier turbine static component tested in the engine(s). Table XL shows the total test time for various types of components tested in the engine(s) and in the static thermal shock test fixture.

Gasifier Turbine Static Component Failure Analysis

All 14 engine assemblies tested since the last annual report incorporated one or more ceramic gasifier turbine static components. During seven of these engine tests a ceramic gasifier turbine static component failed.

Analyses of the failures and corrective actions taken for six of the seven component failures are summarized as follows. The seventh engine test failure is discussed in greater detail following the six summaries. The component failures are discussed in the order in which they occurred.

Gasifier Turbine Scroll Failure, Engine S/N 2, BU14—Engine S/N 2, BU14 was the third engine test for CBO alpha-SiC gasifier turbine scroll S/N FX 30584. During this test the scroll fractured at the inner rim of the scroll body adjacent to the scroll body/shroud braze joint. Small segments of the rim separated and passed through the turbine vanes and rotor. One larger segment of the rim became lodged in the vane row. The ceramic vanes, ceramic outer backplates, and metal turbine rotor were damaged also. The scroll body rim fracture was determined to be the primary failure in this incident. Effort was undertaken to improve the performance of the scroll/shroud braze joint by increasing the amount of braze material applied to the joint and improving the flatness of the mating surfaces.

Gasifier Turbine Scroll Failure, Engine S/N 2, BU15—A borescope inspection of a CBO alpha-SiC gasifier turbine scroll following a fifth engine thermal cycle revealed a crack in the scroll body inner rim region similar to that observed in engine S/N 2, BU14 (discussed previously). Examination showed the large circumferential crack to have five distinct contact fractures (origins) at the scroll body/shroud interface. The ceramic vanes, outer backplate, and inner backplate installed in this test were undamaged. Examination showed the failure to be caused by intermittent and nonuniform braze coverage. Following this second failure of a scroll/shroud joint, development of the braze technology was intensified. In addition, a static load proof test simulating the structural load imposed by engine operation on the braze joint region of the scroll was designed. All gasifier turbine scrolls tested subsequent to the S/N 2, BU15 engine test were exposed to this proof test.

Gasifier Turbine Inner Backplate Failure, Engine S/N 1, BU21—A GTE SN-1000 Si_3N_4 gasifier turbine inner backplate was fractured during testing of engine S/N 1, BU21. The inner backplate fractured after being impacted on the inside diameter by the turbine rotor. The turbine rotor (ceramic) had been broken from its shaft by loading imposed on it as the gasifier turbine scroll assembly tilted. Modifications were made to the engine components to eliminate gas leakage into the cavity behind the turbine scroll assembly. No modification of the inner backplate was necessary because this failure was secondary in nature.

Gasifier Turbine Outer Backplate Failure, Engine S/N 2, BU16—The six cross-key slot tabs on the reverse side of a CBO alpha-SiC gasifier turbine outer backplate fractured during testing of engine S/N 2, BU16. Loss of function of the cross-key features allowed the ceramic turbine static structure to shift and rub the metal turbine rotor. The rotor rub did not damage the scroll (Norton SiC) beyond future use. The ceramic vanes and inner backplate were undamaged also. The cross-key failures were diagnosed as resulting from overload caused by lack of flexibility of the interturbine coupling. The coupling must allow relative motion between the gasifier and power turbine static structures during engine operation. To increase flexibility at the interturbine coupling, the ceramic piston rings were replaced by ceramic rope packing in all subsequent engine builds.

Table XXXIX.

Chronological summary of gasifier turbine ceramic static structure component engine testing.

Test			Ceramic component				
Engine No.	Build No.	Hot test time—hr	Scroll	Outer backplate	Inner backplate	Vane	Inter turbine coupling
1	1	2.35				CBO Alpha-SiC	
1	2	0.17				CBO Alpha-SiC	
1	11	11.87				CBO Alpha-SiC	
1	12	15.88				CBO Alpha-SiC	
2	5	37.85				CBO Alpha-SiC	
2	6	11.98				CBO Alpha-SiC	
2	7	16.30				CBO Alpha-SiC	
2	9	1.65	CBO Alpha-SiC	CBO Alpha-SiC	Corning BMAS-III step	CBO Alpha-SiC	
2	10	6.20	CBO Alpha-SiC	CBO Alpha-SiC	Corning BMAS-III step	CBO Alpha-SiC	
2	11	1.05			Corning BMAS-III step		
2	13	22.63			Corning BMAS-III step		
2	14	7.00	CBO Alpha-SiC	CBO Alpha-SiC	Corning BMAS-III step	CBO Alpha-SiC	Pure RB SiC
2	15	5.12	CBO Alpha-SiC	CBO Alpha-SiC	GTE SN1000 Si_3N_4	GTE PY6 Si_3N_4	Pure RB SiC
1	21	4.63			GTE SN1000 Si_3N_4		
2	16	16.92	Norton NC-430 SSiC	CBO Alpha-SiC	Kyocera SN250 Si_3N_4	GTE AY6 Si_3N_4	Pure RB SiC
1	22	9.47			Corning BMAS-III step		
1	23	3.55	Norton NC-430 SSiC	CBO Alpha-SiC	Corning BMAS-III step	GTE AY6 Si_3N_4	Pure RB SiC
1	24	2.97	Norton NC-430 SSiC	CBO Alpha-SiC	Kyocera SN250 Si_3N_4	GTE AY6 Si_3N_4	Pure RB SiC
2	17	9.68	Kyocera SN250 Si_3N_4	Kyocera SN250 Si_3N_4	Kyocera SN250 Si_3N_4	GTE AY6 Si_3N_4	Pure RB SiC
1	25	5.07	Kyocera SN250 Si_3N_4	Kyocera SN250 Si_3N_4	Kyocera SN250 Si_3N_4	GTE AY6 Si_3N_4	Pure RB SiC
2	18	14.53			Kyocera SN250 Si_3N_4		
1	26	4.35	Kyocera SN250 Si_3N_4	Kyocera SN250 Si_3N_4	Kyocera SN250 Si_3N_4	GTE AY6 Si_3N_4	Pure RB SiC
2	19	4.75			GTE AY6 Si_3N_4		

SSic = sintered SiC

Table XL.
Summary of gasifier turbine static structure experimental testing.

Component	No. of engine tests	No. of static rig tests	Total hot test hr in engine	Total hot test hr in st. rig
Scroll/outer backplate	10	8	62.50	34.2
Inner backplate	16	8	119.57	34.2
Nozzle vanes	17	8	158.91	38.7
Insulating shim	45	9	415.5	38.7
Interturbine coupling	8	—	54.66	0
Interturbine seal rings	5	0	36.89	38.7

Gasifier Turbine Outer Backplate Failure, Engine S/N 1, BU23—One cross-key slot tab was broken from the gasifier turbine ceramic outer backplate (CBO alpha-SiC) during testing of engine S/N 1, BU23. All components of the gasifier turbine assembly were fabricated of ceramic. The fractured cross-key slot tab was discovered at a routine engine disassembly after completing the first phase of testing of the all ceramic gasifier turbine. The outer backplate was inspected for additional damage. None was found and the outer backplate was declared suitable for additional testing since loss of one cross-key feature did not adversely affect the function of locating the turbine static structure with respect to the rotor. All other ceramic components used in this test were undamaged and suitable for additional testing. Analysis of the cross-key details showed that insufficient clearance existed between the metal cross-keys and the mating slots in the outer backplate if worst case dimensional tolerances existed. To correct this condition, the width of the metal cross-keys was reduced sufficiently to provide a minimum of 0.127 mm (0.0005 in.) clearance.

Gasifier Turbine Ceramic Static Structure Failure, Engine S/N 1, BU24—The same all ceramic gasifier turbine assembly hardware tested in engine S/N 1, BU23 was retested to higher temperature (>1149°C [2100°F]) in engine S/N 1, BU24. During an acceleration to 1149°C (2100°F) BOT a failure occurred in which the ceramic rotor, outer backplate, and vanes were damaged. The ceramic scroll received very minor chipping around the vane pockets but is suitable for additional testing. The primary failure in this test was fracture of the combustor dome. A large chip from the dome separated and passed through the gasifier turbine vanes and into the rotor. The rotor blades and vanes were damaged by the "ping-pong" effect of debris recirculating between the vane row and the rotor inlet until it is ground into small enough particles to be entrained in the gas stream and pass through the turbine rotor. During this test a second cross-key slot tab was broken from the outer backplate. (The first one was fractured during the S/N 1, BU23 test.) This incident was thought to be unrelated to the consequences of the combustor dome failure. Review of the cross-key/slot clearance analysis done previously with more severe boundary conditions failed to show cause for the cross-key slot tab failure. Further investigation revealed possible adverse loading on the cross-keys due to unrelieved thermal growth of the combustor assembly. Engine assembly specifications were revised to provide ample allowance for thermal growth of the combustor and turbine assembly.

Gasifier Turbine Static Structure Failure, Engine S/N 1, BU26—The entire hot section of engine S/N 1, BU26 was assembled with ceramic components: the combustor assembly, both turbine assemblies, interconnecting ducts, the regenerator disk, and the regenerator seal platform. After approximately 4 hr of testing, a failure occurred resulting in fractures of all the ceramic components except the combustor dome, combustor body, the combustor dilution band, the pilot burner ceramic tube, the interturbine coupling, and the regenerator disk. The hot side of the regenerator disk was, however, deeply gouged by debris that lodged between the disk and the regenerator seal. Disassembly of the engine revealed the power turbine components to be fractured into relatively small fragments while the gasifier turbine components were broken into larger pieces that were, in general, still near their original location in the engine. Both ceramic tur-

bine rotors were broken from their respective metal shafts.

The gasifier turbine rotor was lodged in the curved gasifier turbine outlet duct (with blades broken off). The power turbine rotor broke into many small pieces (some unrecovered).

Reconstruction was accomplished of all the fractured components except the power turbine rotor, and the vanes of both turbines. Analysis of the fractured components defined fracture origins in all components except the power turbine inner backplate, power turbine rotor, and the turbine vanes.

The origin of fracture of the power turbine rotor from its stub shaft was determined from the ceramic stub remaining in the metal shaft. The magnitude of the stress at the origin of fracture of both turbine rotors from their shafts was in excess of 462 MPa (67,000 lb/in.^{2}), on the order of ten times normal stress at that location. This indicates that a large unbalance force or other load input was experienced by both rotors.

Summary of Engine Test Data (S/N 1, BU26)—Engine test data (over 300 channels) were acquired by an automatic data system at a rate of three data points per second. The test data for engine S/N 1, BU26 was examined for the period from about 3 minutes prior to the failure event to the conclusion of engine rotation and cool down, about 6 minutes after the first indication of engine distress. The data show that (1) the gasifier turbine rotor experienced an incident 2/3 of a second before any indication of distress by the power turbine rotor, (2) the whip of the gasifier rotor shaft returned to normal level after 2 sec, (3) the whip of the power turbine rotor shaft returned to normal after 2-1/3 sec, and (4) the internal engine pressure (burner inlet pressure) decreased to atmospheric pressure level in 2 sec.

The following observations were assembled after examination of the engine test data and inspection of the engine components:

- The gasifier turbine rotor experienced an incident prior to the power turbine rotor.
- The initial rate of burner inlet pressure loss was similar to that observed due to loss of gasifier turbine vanes in a previous test.
- The rate of burner inlet pressure loss increases at the time of maximum power turbine rotor whip—indicating an additional loss of flow restriction in the engine.
- Debris can become trapped between the regenerator disk and the regenerator seal in 0.8 sec or less after reaching the disk surface.
- Fracture and rub marks on gasifier turbine inner backplate were similar to those of another test where the scroll tilted and the rotor separated from its shaft.
- The gasifier turbine rotor blades were operating at a condition remote from their natural frequencies when the failure occurred.
- Oxidized particles of turbine scroll braze material were observed in engine debris—indicating braze distress prior to failure.

The extent to which engine components were damaged in this failure event has complicated the development of a definite failure scenario. The scenario discussed first is the one best supported by the physical evidence seen at engine disassembly and by engine test data.

Heavy emphasis was given to engine data that showed a decrease in the gasifier turbine rotor speed (and airflow and compressor discharge pressure) prior to any change in the speed of the power turbine rotor.

S/N 1, BU26 Engine Failure Scenario—The following is a scenario for S/N 1, BU26 engine failure:

- Particle(s) enter gas turbine (GT) vanes and rotor causing rotor inducer blade and nozzle vane damage.
- Debris from GT rotor blades and vanes enters power turbine (PT) causing PT rotor to breakup.
- PT static structure was broken up by debris from PT rotor as the rotor broke up.
- Debris from both turbines is blown into regenerator disk by out rush of P_3 air.
- Pieces of debris wedge between regenerator disk and regenerator seal causing seal platform to deflect and fracture.
- Displaced seal platform crossarm contacts GT scroll outlet elbow loading the GT scroll and outer backplate to failure.
- The GT scroll shroud (which did not fracture) was displaced and contacted the GT rotor (blades) causing rotor to separate from its shaft.

- GT rotor contacts inner backplate on inside diameter causing inner backplate to fracture.

The scenario set forth is straightforward once the initiating damage to the gasifier turbine rotor has occurred. Unlike other test experiences where gasifier turbine rotor blades were damaged by identified foreign objects, such foreign objects have not been precisely identified in the S/N 1, BU26 incident. Possible foreign objects are the following:

- particles of insulation from within the engine
- carbon buildup in combustor body
- particles of the braze material used to bond the gasifier turbine scroll together
- chips off of gasifier turbine vanes or scroll body
- chips off of ceramic combustor assembly components

Particles of carbon deposits and chips from ceramic combustor components can be eliminated because neither existed in this engine test. It was judged that particles of insulation were not likely to have caused a turbine blade failure also.

The gasifier turbine scroll/outer backplate/vane assembly used in S/N 1, BU26 had been tested for over 13 hr in two previous engine tests at TITs up to 1093°C (2000°F). Inspections after those tests revealed no chipping of the vanes, scroll, or outer backplate. It is therefore believed that the vanes would have performed satisfactorily in this test. FPI of the scroll following each of those tests revealed no indications except at the braze joints. These indications were thought acceptable because of the porous nature of the braze. However, examination of the scroll inlet/scroll body braze surfaces following separation in the S/N 1, BU26 test revealed oxidation to be present over approximately one-third of one plane of the joint. This prompted additional examination of the braze joint that revealed very small chipping at the exposed edge of the scroll body/inlet adapter joint and also the scroll body/shroud braze joint. This evidence suggests that the braze joints were in distress and a likely source of particles large enough to initiate turbine rotor damage. Once turbine rotor blade damage was initiated, additional destruction of the rotor blades was self-perpetuating.

Alternate Failure Scenario—Four alternate scenarios describing how the S/N 1, BU26 failure event might have been initiated are as follows:

- adverse load on gasifier turbine scroll inlet caused by malfunctioning BVG mechanism or unrelieved thermal growth of combustor components
- sudden loss of P_3 cavity pressure, which would cause gasifier and/or power turbine scrolls to tilt or lift
- loss of gasifier turbine rotor inducer blade(s)
- failure of power turbine rotor blades/hub

The fact that the gasifier turbine scroll inlet transition was separated from the scroll body raised the question "Did the combustor assembly exert an unplanned load on the scroll?" Post-test experience has shown that when the combustor loaded the gasifier scroll, chipping occurred on one or both ends of the combustor body and on the combustor dome. There was no chipping on either the combustor body or dome after the S/N 1, BU26 test. Instrumentation showed no unscheduled excursion of the BVG mechanism before or at the time of the hot section failure.

The spring-loaded combustor assembly retention details were adjusted to provide ample clearance in this engine build. While the gasifier turbine ceramic outer backplate was fractured in this test, the type of fracture associated with adverse loading from the combustor assembly due to thermal growth (contact loading in the cross-key slots) was not evident in this test. In summary, the post-test examination of the components did not show signs of adverse loading on the gasifier turbine scroll by the combustor assembly that have been observed in previous tests. Hence, it is believed that adverse loading on the gasifier turbine scroll, causing it to fracture and or be displaced, did not occur in this test.

An analysis was completed to determine if sudden loss of burner inlet pressure (P_3) would cause either of the turbine scrolls to tilt or lift off their mounting surfaces, which would result in scroll/rotor contact. Sudden release of P_3 pressure could occur if the regenerator seal platform or power turbine exhaust coupling fractured. This scenario can be set aside for two reasons. First, test data

show that the loss of pressure did not precede the loss of speed experienced by the gasifier turbine rotor but instead was concurrent with it. In addition, calculations show that the gasifier turbine scroll would not tilt until P_3 pressure was reduced to 129.62 MPa (18.8 psia) or lift until P_3 pressure was reduced to 113.07 MPa (16.4 psia). The calculations showed that the power turbine scroll would not tilt or lift even when P_3 was exhausted to atmospheric pressure.

Loss of one or more gasifier turbine rotor blades could have initiated the S/N 1, BU26 failure event. Previous test experience has shown that loss of inducer blades may or may not be accompanied by an instantaneous change in rotor whip. In the S/N 1, BU26 test, gasifier rotor whip decreased slightly 1/3 sec after the rotor speed decreased and returned to the original whip level about 1-1/2 sec later. This scenario is not given high probability for the following reasons. Similar gasifier turbine rotors have performed well in engine test unless subjected to FOD. The subject gasifier turbine rotor had passed (1) cold spin test to 130% speed, (2) dynamic vibrating testing of inducer blades to 50% of fracture stress, and (3) complete X-ray, FPI, and dimensional inspection prior to engine testing. At the time of engine failure, the rotor operating condition was remote from the natural frequency of the rotor blades.

The ceramic power turbine components, static and rotating, were broken into much smaller pieces than were the gasifier turbine components. This might suggest that the power turbine assembly suffered a more intense failure than the gasifier turbine, i.e., that a power turbine rotor burst may have been the initiating event. At least one fragment of power turbine rotor did pierce the scroll body and penetrate the entire thickness of an encapsulated insulation blanket inside the engine. S/N 1, BU26 was the first test of a ceramic power turbine rotor. Hence, no past test experience can be drawn from to diagnose this failure. This scenario is not thought to be correct because (1) test data show that events leading to failure of the power turbine assembly followed events involving the gasifier turbine and (2) the power turbine rotor passed a spin test to 130% design speed, dynamic testing of inducer blades to 50% of fracture stress, and X-ray, FPI, and visual inspection. As has been stated previously, heavy emphasis has been given to engine test data in ordering the sequence of events in this engine failure.

Absolute diagnosis of the event or events which precipitated the S/N 1, BU26 engine failure may never be determined. In other previous ceramic component failures, definition of an origin of failure of the ceramic component usually defined a case of hardware misfit or flaw in the ceramic material. In the S/N 1, BU26 engine assembly care was taken to address all assembly and thermal growth interferences that have been experienced in previous tests. No new component misfits have been identified during this failure investigation.

3.7 POWER TURBINE ROTOR

Introduction

Ceramic power turbine rotors were designed and fabricated with the knowledge gained in gasifier rotor development. The power turbine rotor development was delayed until after the gasifier had been successfully demonstrated in engine testing. Once this had occurred, the power turbine rotor, which runs under less severe conditions, could undergo faster development. Thus, power turbine development parallels that for the gasifier rotor, subsection 3.5.

Finite element heat transfer and stress analyses were performed on both of the power turbine rotor configurations (one for each ceramic material being developed) to determine peak stresses and POS at various operating conditions, resulting in an acceptable POS for Si_3N_4 rotors. A 3-D finite element model was used to predict the airfoil dynamic response. Various proof tests supported the analyses and were used to qualify rotors for engine test.

Objective

One objective of the AGT 100 program was to develop a ceramic power turbine rotor assembly (or assemblies) to complete an all-ceramic hot section. The design included selecting appropriate materials and configuration to attain a desired POS of 0.976. The development included fabrication and proof testing of the components to provide qualified parts for engine testing. The RPD of this rotor is at 1113°C (2035°F) rotor inlet temperature and 68 krpm (1721 ft/sec tip speed).

Discussion

Geometry Definition

The layout for the ceramic power turbine section of the engine was completed, and detail drawings have been published reflecting the configurations defined in the layout. The detail drawings for

cast rotors were provided to the applicable vendors: Kyocera for Si_3N_4 and Sohio Engineered Materials for SiSiC.

There are two versions of the airfoil contours for the power turbine rotor: the original, or "thin" airfoil, and those with thickened inducers. Inducer failure during engine testing with ceramic gasifier turbine rotors suggested FOD as one of the possible failure modes. Both the gasifier and power turbine rotors' inducers were thickened as a result of this finding. Figure 185 shows the scheme with which the power turbine rotors' inducers were thickened in order to make them more FOD resistant.

Both the thin-bladed and the thick-bladed rotors have the same basic hub contour (wheel passage). Finished rotors for engine test are cut to one of two clearances: design clearance, or RPD, and open clearance, or RPD-open, which is 0.3048 mm (0.012 in.) less material (more clearance) all around. The various wheel passages are compared graphically in Figure 186.

The basic geometry of the power turbine rotor is very much like that of the gasifier turbine rotor, only on a larger scale. The rotor is a radial inflow turbine with 12 blades. The inducer outer diameter is approximately 157.48 mm (6.2 in.) as a casting. This is machined down to 147.46 mm (5.8 in.) when the contour is cut to design clearances. The backface is shaped in a 90 mm radius blended into a 3 mm (0.118 in.) radius, connecting the balance ring with the stub shaft. The stub shaft is 13.5 mm (0.531 in.) in diameter. The shaft attachment configurations are exactly like those for the gasifier rotor, except for the 1.5° taper in the stub shaft of a SiSiC rotor, which is required for wettability of the glass-bonding material used in its attachment scheme.

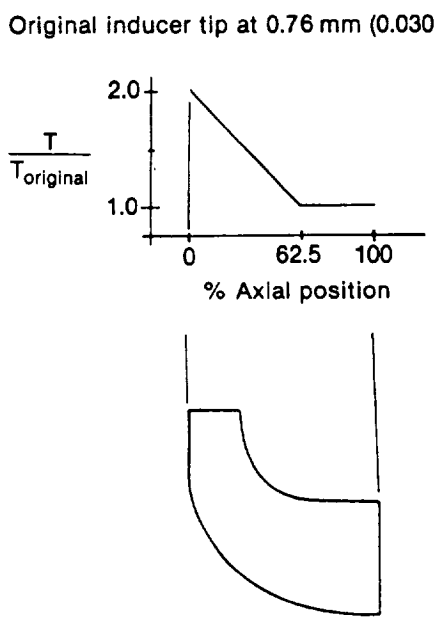

Figure 185. Thickened power turbine rotor thickened inducer airfoil.

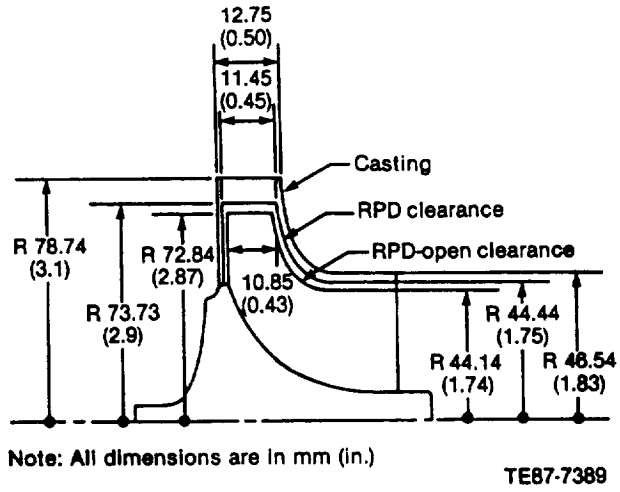

Figure 186. Comparison of power turbine rotor stages.

Siliconized Silicon Carbide (SiSiC) Rotor Fabrication

A total of 40 thickened airfoil SiSiC rotors were ordered from Sohio during the AGT 100 program. Sohio was supplied the appropriate cast rotor drawings, as well as blade books and master charts, so that preproduction work could progress on thick-bladed rotors. It was agreed that Sohio would provide Allison with rotors fabricated with thin blade tooling until the tool inserts for the thickened airfoil rotors were available. Due to various problems experienced by the vendor making the inserts, the inserts were not received in time for Sohio to produce thickened inducer rotors. Therefore, only thin airfoil rotors (AA101300) were delivered to Allison. In all, 37 rotors (P/N AA101300) were made from the metal master and delivered prior to the end of the contract.

These rotors were used by Sohio as subjects in a process development matrix. Early deliverables had very poor surface finish, were highly porous with voids, and had broken airfoils. The poor surface finish made routine FPI impractical. The density variations (voids, porosity) in the rotors resulted in hub bursts during spin test, and the general condition of the surface and incomplete composition precluded the possibility of the first siliconized rotors being engine candidates. As the process developed, however, less excess silicon build-up was evident on the surfaces, densities were more uniform and closer to theoretical (2.80–2.81 g/cm^3), and rotors were intact. However, none of the rotors reached 100% power turbine rotor speed (N_2) in spin testing.

These facts, as well as the thin inducer blades, precluded an SiSiC rotor becoming an engine candidate during the course of AGT 100.

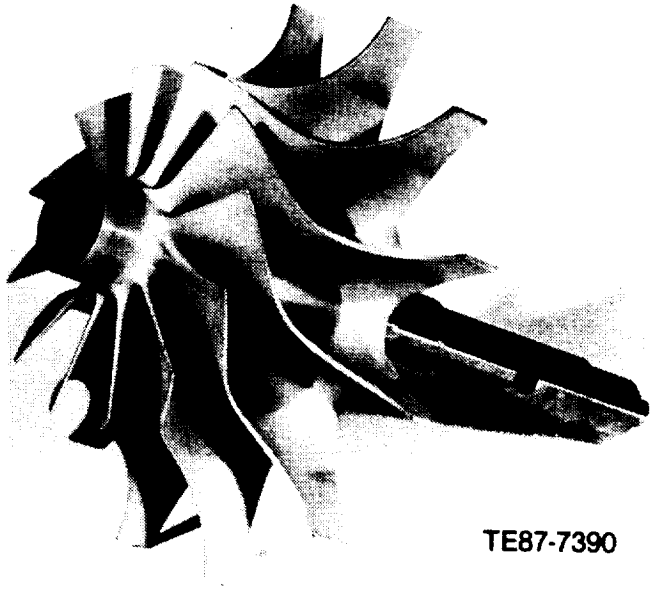

Figure 187. *Power turbine rotor S/N 0002-1 prior to test.*

Silicon Nitride (Si_3N_4) Rotor Fabrication

Twelve thickened-airfoil Si_3N_4 power turbine rotor castings were purchased from Kyocera in their SN220M Si_3N_4 material. Allison contracted Plumb Mold to fabricate the power turbine aluminum master die. This tool is 114% size to account for the shrinkage experienced during sintering. The tool drawing, the airfoil contour, and the basic wheel contour descriptions were supplied to both Plumb and Kyocera. Unlike the SiSiC rotors, only thickened airfoil Si_3N_4 rotors were fabricated for the power turbine. All ordered rotors were received with certification of proof spin to 130% of power turbine design speed (design = 68 krpm), and were inspected for dimensional conformance, cracks (FPI), and voids and porosity (real-time microfocus X-ray). One rotor was actually tested in an engine. This rotor, S/N 0002-1, is pictured in Figure 187 prior to test. Figure 188 is a photographic comparison of a Si_3N_4 casting with a SiSiC casting.

Stress Analyses

The design methodology for ceramics includes finite element analysis coupled with two-point Weibull failure analysis to determine POS for each design given specific material characteristics. The stress and POS analyses were performed using 2-D, axisymmetric finite element models constructed of 12-noded elements. The various operating conditions at which the power turbine rotor was analyzed are described as follows:

- assembly stress—0.0254 mm (0.001 in.) radial interference between metal shaft and rotor stub
- proofing stress—room temperature, 88.5 krpm
- mechanical stress—room temperature, 68 krpm
- maximum power (steady state)—1113°C (2035°F) TIT, 68 krpm
- acceleration transient—0 to 64% N_2, slice at 33 sec

The cases analyzed are summarized in Table XLI, along with their resultant maximum principal stresses and POS. Each analysis was performed for both SASC and Si_3N_4. The SiSiC runs were made using material data for SASC because it was the best data available for a widely characterized material, both test bars and test bars cut from rotors. The two materials will probably behave similarly under the specified conditions so the material properties for the SASC can be substituted for the SiSiC properties until better information becomes available.

Figures 189 and 190 show the finite element geometry plots for the two rotor configurations, and Figures 191 and 192 are the isostress plots for the maximum principal stresses in the Si_3N_4 power turbine rotor at steady state (maximum power) and during the transient acceleration to 64% speed. All of the Si_3N_4 cases analyzed yield acceptable POS, exceeding the 0.976 required by the reliability standards. However, none of the SiC cases yielded sufficient POS to meet design goals.

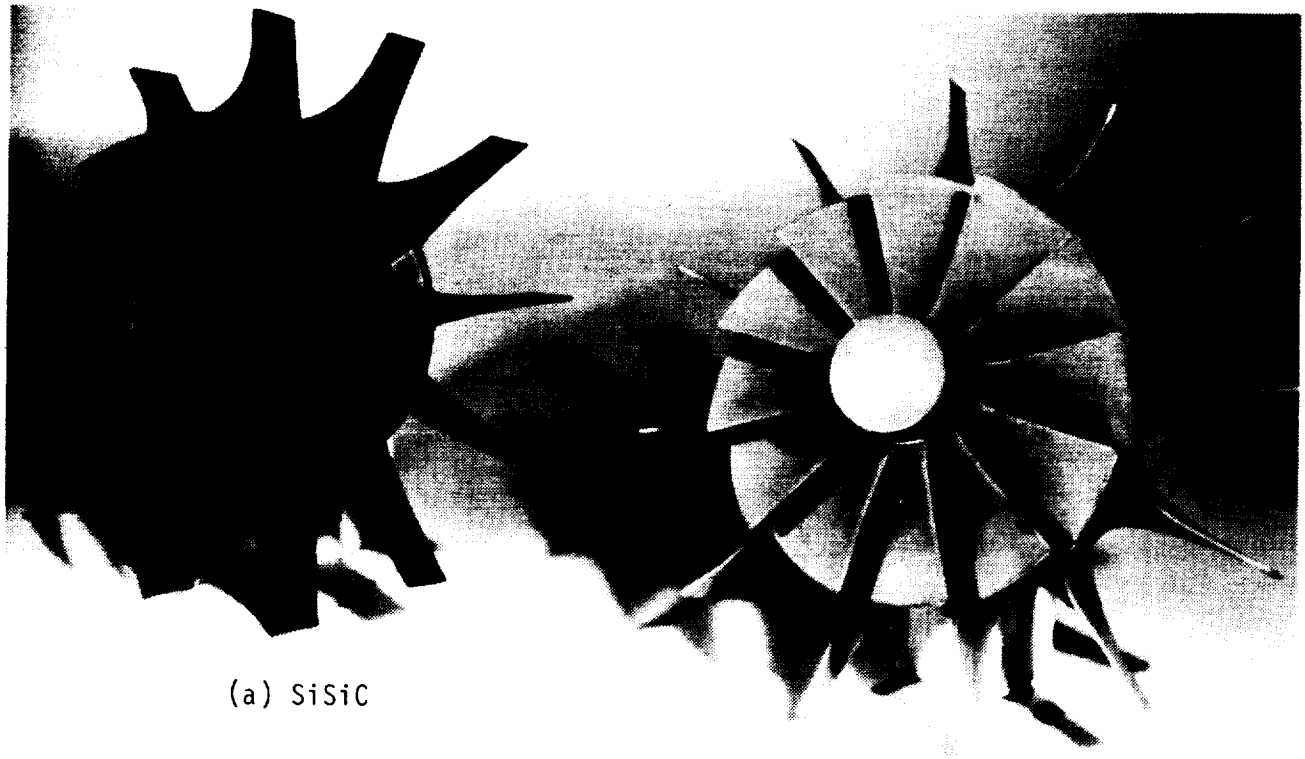

Figure 188. *Comparison of a Si_3N_4 power turbine rotor casting with a siliconized silicon carbide power turbine rotor casting.*

Table XLI.
Summary of PT rotor analyses.

Rotor type POS	Operating conditions	Maximum principal Stress—ksi	POS
Si_3N_4			
RPD assembly	Mechanical	30.3	0.999851
Cast rotor	Proofing	48.5	0.828921
RPD assembly	Assembly	24.9	0.999994
RPD assembly	Steady state	35.2	0.999526
RPD assembly	Transient acceleration	64.3	0.999287
SiC			
RPD assembly	Mechanical	30.6	0.938303
RPD assembly	Assembly	6.9	1.000000 (rotor) 0.999865 (insulator) 0.999865 total
RPD assembly	Steady state	66.0	0.901034 (rotor) 0.998748 (insulator) 0.899906 total
RPD assembly	Transient acceleration	65.6	0.728420 (rotor) 0.998340 (insulator) 0.727211 total

Airfoil Dynamic Response Testing and Analysis

The thickened rotor airfoil contour was analyzed to predict its natural frequencies encountered within the engine operating range. The frequencies were also determined experimentally to confirm these values. The dynamic proof test was devised as a precaution to evaluate the dynamic response of each rotor's inducer airfoils prior to engine test since this response was identified as a potential failure mode in gasifier rotor failures during engine test.

The testing procedure involved excitation of the airfoils using an air siren to their four modal frequencies. A 3.175 mm (0.125 in.) Fontonic Sensor was used with the air siren for frequency identification. Damping was accomplished by the frequency sweep method. When necessary, each blade was failed by increasing air pressure with a 60-hole air siren rotor, without need of any dwell time.

The frequency analysis of an as-cast rotor using a finite element model with nominal blade thickness predicted modes 10–20% lower than those observed in test. Airfoil thicknesses were checked for two axial sections and one radial section and were found to be thinner than defined on the master charts,

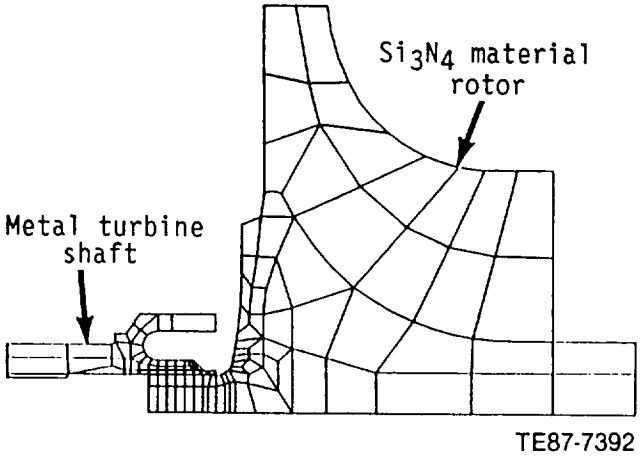

Figure 189. *Power turbine assembly, rotor/shaft assembly, 2-D finite element model, Si_3N_4 rotor.*

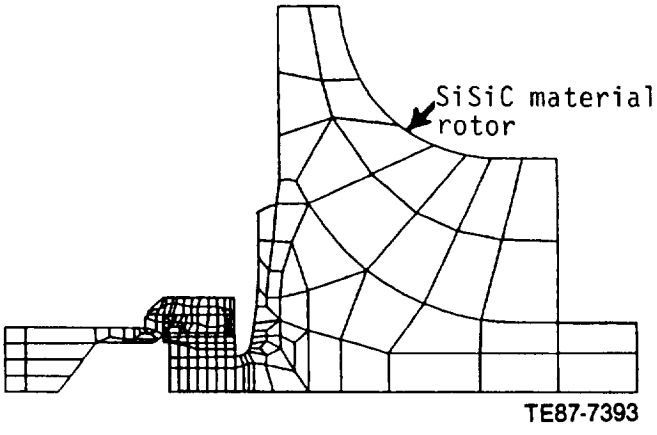

Figure 190. *Power turbine assembly, rotor/shaft assembly, 2-D finite element model, SiSiC rotor.*

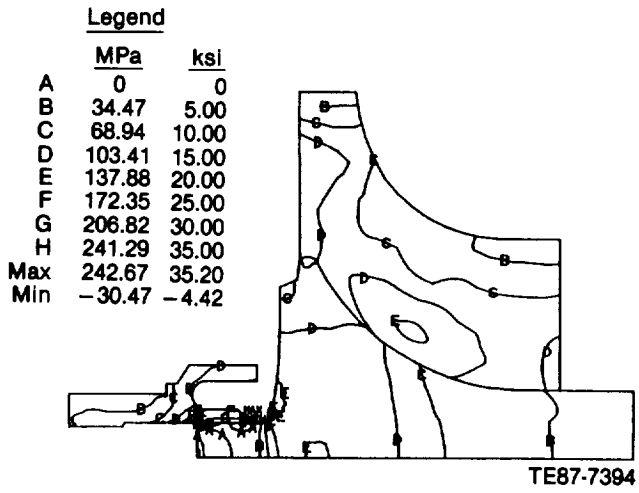

Figure 191. *Isostress plot for the maximum principal stresses in the Si_3N_4 power turbine rotor at steady state maximum power.*

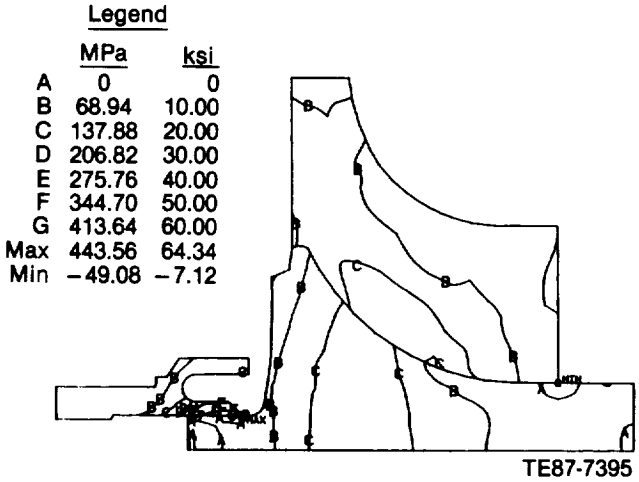

Figure 192. *Isostress plot for the maximum principal stresses in the Si_3N_4 power turbine rotor during the transient acceleration to 64% speed.*

Table XLII.
Modal frequencies for an RPD-open clearance power turbine rotor.

Mode	Analytically predicted—Hz	Measured range—Hz	% difference from mean value
1st inducer	12,123	12,341–12,522	2.3
1st exducer	5,390	5,466–5,881	4.8
2nd exducer	14,079	14,335–14,747	2.5
3rd exducer	19,610	20,016–20,703	2.8

especially closer to the airfoil's root. The radial section indicated that the exducer curvature was more severe than defined by the master charts. Part of the difference in frequency in the exducer modes might be explained by the increased curvature of the actual rotor exducers. The thickness measurements, however, were in the opposite directions of explaining the differences between analytical and test results. A machined engine candidate RPD rotor was then modeled and tested. Table XLII summarizes the values determined analytically and experimentally. The excellent correlation confirmed the engine rotor's frequency-versus-speed diagram (shown in Figure 193) and allowed engine test plans that avoided potentially harmful operating conditions to be formulated. No additional effort to correlate the as-cast blade frequency results was deemed necessary.

An assessment of blade fracture amplitude, which empirically determined the blade tip deflection required to fail an as-cast rotor airfoil by vibrating each airfoil to failure at inducer resonance, was also performed. Strain gages were used to measure the failure stress level and to determine its location radially along the inducer. Finite element models were used to correlate the blade tip deflection versus failure site stress level relationship. Iterative POS analyses indicated that an actual rotor must have a material characteristic strength of 424.03 MPa (61.5 ksi) to have half of its blades failed at a tip deflection of 0.406 MPa (0.016 in.), the measured test result. The actual rotor strength of 424.03 MPa (61.5 ksi) compares well with the characteristic strength from billet test bars of 421.96 MPa (61.2 ksi). Further finite element analysis in conjunction with a material characteristic strength of 420.58 MPa (61 ksi) was used to determine the relationship between blade tip deflection amplitude and POS for an RPD-open airfoil configuration. Based on these results, as shown in Figure 194, the peak-to-peak proofing amplitude was set at 0.280 mm (0.011 in.) to be proofing at a stress level of approximately 60% of the fracture stress and still proof it in a range where it is predicted to have a high POS. The actual dynamic stress levels experienced in the engine are expected to be less than this proofing stress.

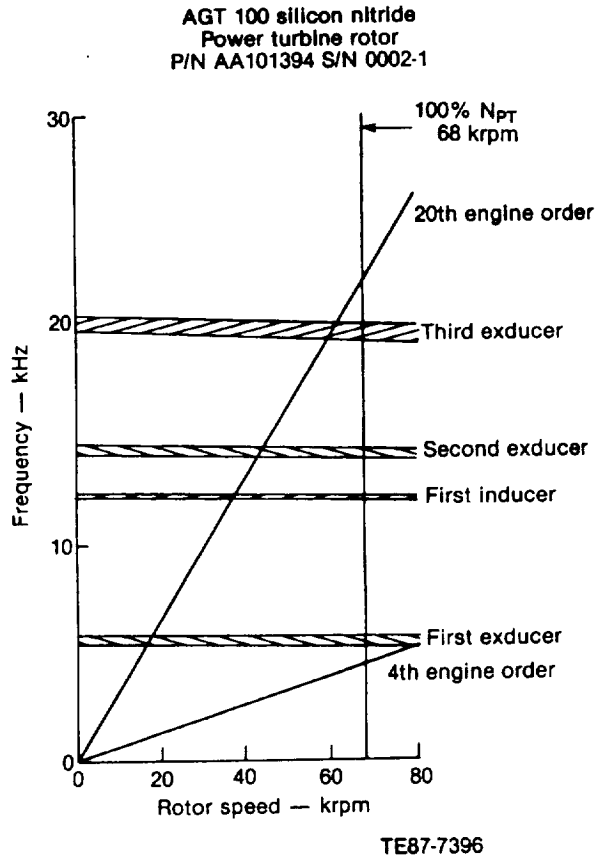

Figure 193. *Engine rotor's frequency versus speed diagram.*

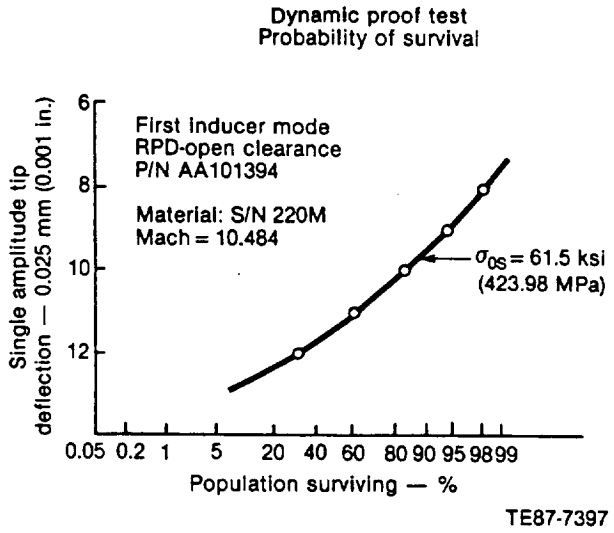

Figure 194. *Results of power turbine rotor finite element analysis used to determine the relationship between blade tip deflection amplitude and POS for an RPD-open airfoil configuration.*

Proof Testing

In addition to the dynamic response proof test, each ceramic power turbine rotor undergoes both cold spin to 130% speed and bend test to check soundness of the attachment joint prior to finish machining and, ultimately, engine test. Each of these tests is briefly described in the following.

Spin Testing—The ceramic rotors are spin-tested at room temperature to prove their structural integrity prior to finish-machining. Although the test is not performed at the design temperature of 1113°C (2035°F), the rotor is driven to 130% overspeed, or 88.5 krpm. The overspeed condition raises the maximum stress to approximately simulate the higher stress level experienced in running at design temperature and speed by applying enough mechanical stress to account for both mechanical and thermal stress associated with engine running.

The Si_3N_4 rotors were spun by the vendor, Kyocera, to the specified speeds prior to their delivery to Allison. No unproofed rotors were delivered, and, according to Kyocera representatives, all rotors that were subjected to proof spin at the factory passed the test. Sohio's SiSiC rotors were spun byThe Balancing Company. None of these rotors achieved 100% power turbine speed, and they were not proofed. Burst results for these rotors can be found in Table XLIII.

Bend Test—Each semi-finished rotor assembly is subjected to a bending proof test of its attachment joint prior to being finish machined. This proof test is accomplished by hanging a dead weight onto a shaft attached to the rotor to create a moment across the attachment plane. The moment is analogous to that experienced by the rotor assembly in operation, plus a safety factor. The assembly is rotated through 360° to ensure the joint's integrity all around. The proofing moment is specified on the semi-finished assembly drawings as 3.56 N-m (31.5 lb-in.).

3.8 POWER TURBINE STATIC STRUCTURE

Introduction

The ceramic power turbine static structure consists of the following components:

- scroll/shroud assembly
- outer backplate
- inner backplate
- vanes (20)
- insulating/shim spacer ring
- power turbine exhaust coupling and seal rings

Complete ceramic power turbine static structures have been tested in two engine assemblies. Partial sets of power turbine vanes have been tested in five additional engine assemblies. Monolythic zirconium oxide power turbine insulating rings have been used in all 45 engine assemblies tested during the program.

Power turbine static structure components fabricated of SiC and Si_3N_4 materials were planned for this program. However, silicon carbide scroll/shroud assemblies were not yet available for test at the conclusion of the program.

The SiC scroll body design was modified after the first several castings were made to improve moldability of the component and to improve the configuration of the scroll body/shroud braze joint. The configuration of the Si_3N_4 scroll assembly was developed by the supplying vendor (Kyocera). It is patterned closely after the gasifier turbine scroll,

Table XLIII.

Summary of SiSiC PT rotor spin tests.

Rotor S/N	Density—g/cm³	Burst speed—krpm	Comments
1-11	2.80	54.8	
8-11	2.81	48.1	
151(8A)	2.75	46.0	Hub burst
156(8A)	2.80	24.0	Core still intact when test stopped at 46.5 krpm
282	2.81	25.0	Airfoil release; core stayed intact
288	2.81	20.8	Inducer release; core stayed intact
FX56036	2.80	47.0	Released 9 airfoils simultaneously
FX56037	2.78	34.96	Tip release suspected
FX56040	2.77	47.5	Released 7 airfoils simultaneously
FX56042	2.76	41.5	Single airfoil release
FX56043	2.76	49.76	Single airfoil release followed by 6 more
FX56058	2.79	55.9	Multiple fracture—origin may be at root of airfoil No. 1 with secondary at root of airfoil No. 6
FX56059	2.80	47.6	Released 7 airfoils simultaneously
FX56060	2.79	52.4	Multiple fracture—origin at middle of backface between blades 11 and 12
FX56061	2.80	27.0	Single fracture—origin at root of either airfoil No. 6 or 11
FX56064	2.80	29.0	Multiple fracture—origin at root of airfoil No. 3

which they supplied midway in the program. The power turbine exhaust coupling was revised to increase its length. This modification increased flexibility between the turbine outlet and the regenerator seal platform inlet.

At the conclusion of the program, testing of an engine assembly comprising of an "all ceramic" hot section concluded with a failure of one or more ceramic components. Consequential damage occurred to all other ceramic components except the combustor assembly. Initial findings do not point to a primary failure occurring in the power turbine static structure. Additional testing is required to assess the performance of the Si_3N_4 components. To bring the SiC power turbine scroll assembly to test readiness, additional development of the fabrication and brazing processes is required.

Objective

The design requirements of the power turbine ceramic static structure are the following:

- to provide a closed flow path from the interturbine coupling to the regenerator seal platform inlet within the space provided inside the outer combustion case
- to have a flow-path configuration that maintains approximately 0.1 M_N velocity in the scroll housing and proper flow direction and velocity (approximately 0.7 M_N) through the nozzle vane row to accommodate the turbine rotor design
- to be fabricated of material(s) that meet the design operating conditions: 1138°C (2080°F) inlet temperature, 3500 hr service life, and 0.999375 POS at each failure site
- to provide a close fitting shroud around the turbine rotor blades under all operating conditions
- to provide design flexibility to accommodate changes in nozzle flow area with only minor revision to detail parts (allowing rematch of turbines for various design conditions)

Discussion

Power Turbine Static Structure Design

The function of the power turbine static structure is to receive gases exhausted from the gasifier turbine, direct them through the power turbine

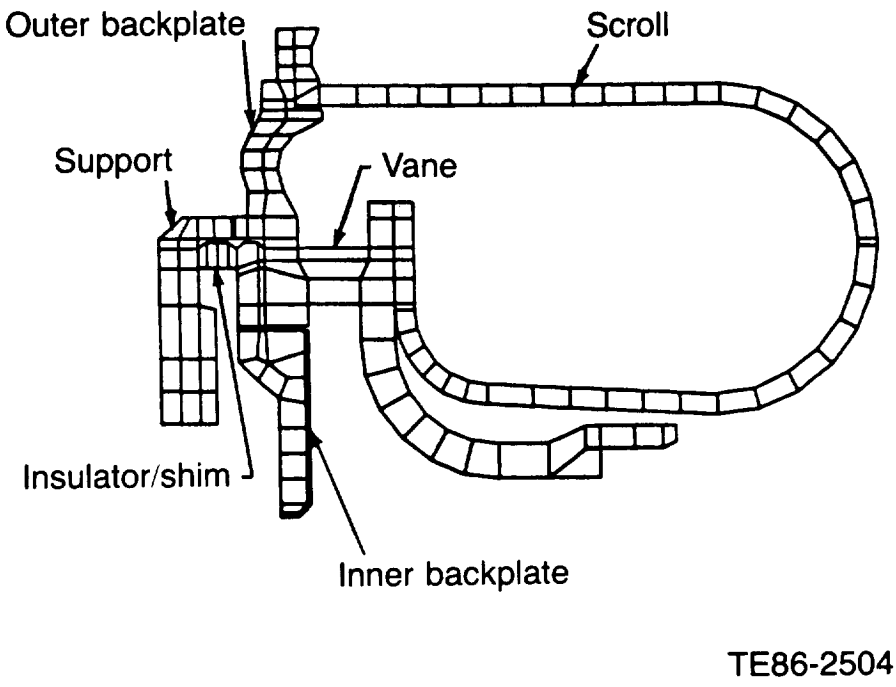

Figure 195. *Power turbine static structure finite element model.*

rotor, and exhaust the expanded gases to the regenerator exhaust heat recovery system. The power turbine static structure consists of the following four major components:

- scroll/shroud (bonded assembly)
- outer backplate
- inner backplate
- nozzle vanes (20)

The power turbine static structure also consists of the following associated components:

- zirconia insulating/shim ring
- power turbine exhaust coupling
- exhaust coupling seal rings (2)

The power turbine components are very similar in design to the gasifier turbine static structure components with the power turbine components being about 8% larger in linear size. The zirconia thermal barrier/shim ring positioned between the inner backplate and metal engine structure is varied in thickness to adjust the turbine rotor-to-shroud clearance. Turbine rotor-to-shroud backplate clearance is adjusted by machining the surface of the inner backplate adjacent to the rotor blades.

The power turbine static structure was designed, and drawings prepared, to be fabricated of SiC and Si_3N_4 materials. The detail components made of both materials are dimensionally interchangeable. However, as in the gasifier turbine, because of the difference in the thermal expansion properties of the two materials, the outer backplate and scroll must be of the same material to maintain proper fit and a SiC inner backplate may not be used with a Si_3N_4 outer backplate because of interference.

Analytical design analysis has been conducted on the power turbine static structure using Allison's STRATA finite element method program. Using 2-D axisymmetric models of the components, as shown in Figure 195, operating temperatures, component deflections, stresses, and POS have been calculated for steady-state and transient start-up conditions. Calculated POS for power turbine static structure components fabricated of SiC material at RPD steady-state (2080°F TIT at power turbine) and a start-up transient are shown in Table XLIV. The POS of the outer backplate and scroll, at steady-state conditions, is at or near the design reliability goal of 0.999375. POS of the inner backplate and insulator/shim is sufficiently high for these components to be good candidates for experimental engine testing. They require further design refinement or improved material characteristics, however, to meet reliability goals.

Table XLIV.

Probability of survival for alpha-SiC power turbine static components, at steady-state and start-up transient.

Scroll				Outer backplate			
Steady-state		Transient		Steady-state		Transient	
Pv	0.99927	Pv	—	Pv	0.99999	Pv	—
Ps	0.99992	Ps	—	Ps	0.99999	Ps	—
POS	0.99919	POS	0.99961	POS	0.99999	POS	0.95457
Inner backplate				**Insulator/shim**			
Steady-state		Transient		Steady-state		Transient	
Pv	0.99621	Pv	—	Pv	0.99946	Pv	—
Ps	0.99960	Ps	—	Ps	0.99404	Ps	—
POS	0.99582	POS	0.99923	POS	0.99350	POS	0.99999

For alpha-SiC material-characteristic strength is 558 MPa (25.58 ksi) for volume and 706 MPa (48.7 ksi) for surface; Weibull modulus is 8.43 for volume and 8.71 for surface.

Pv = Probability of survival for characteristic volume strength
Ps = Probability of survival for characteristic surface strength
POS = Probability of survival overall

Table XLIV also shows the POS of the scroll, inner backplate, and insulator/shim to be very high during the transient while the outer backplate POS reaches a minimum of 0.95457 at about 70 sec into the cycle. The calculated POS of the inner backplate and insulator/shim remain high during the first 120 sec of operation, then decrease to lower values at steady-state operation.

Following initial attempts to fabricate an alpha-SiC power turbine scroll body at CBO, design modifications were made to the scroll body to address two concerns. In the initially fabricated parts severe cracking occurred in the crotch where the inlet transition section merges into the scroll body. Many castings were being damaged (and lost) in this same region because of difficulty in separating the casting from the mold. To address this problem, the fillet radius in the crotch was increased from about 0.01 mm (0.00039 in.) to 0.025 mm (0.00098 in.) and relocated nearer the inlet end of the inlet transition as shown in Figure 196. The decreased length of the inlet makes it less likely to droop during the sintering process.

The second modification to the power turbine scroll body addressed a problem in the region of the braze joint between the scroll body and the shroud. The original scroll body casting had a discontinuous surface at the joint to the shroud. The revised design provides a continuous surface to which the shroud is brazed.

Development of this component was suspended near the end of the program when it became evident that fully machined samples could not be obtained in time for engine testing. This decision was also influenced by the fact that Si_3N_4 power turbine static structure components had become available for testing. Detail analysis of a Si_3N_4 gasifier turbine static structure showed that Si_3N_4 is a viable alternative material for that application with very good POS as noted in the section on the gasifier turbine static structure (see Tables XXXIII through XXXVI). Based on the results of that analysis, detail drawings were prepared for Si_3N_4 power turbine static structure components. The Si_3N_4 components are dimensionally interchangeable with like SiC parts. However, based on the results of the gasifier turbine analysis, use of a Si_3N_4 outer backplate with a SiC inner backplate would not be acceptable because of the difference in thermal expansion rates of the two materials.

The vendor (Kyocera) quotation for Si_3N_4 components contained a proposal for an alternate construction of the power turbine scroll/shroud assembly similar to that of the Kyocera Si_3N_4 gasifier

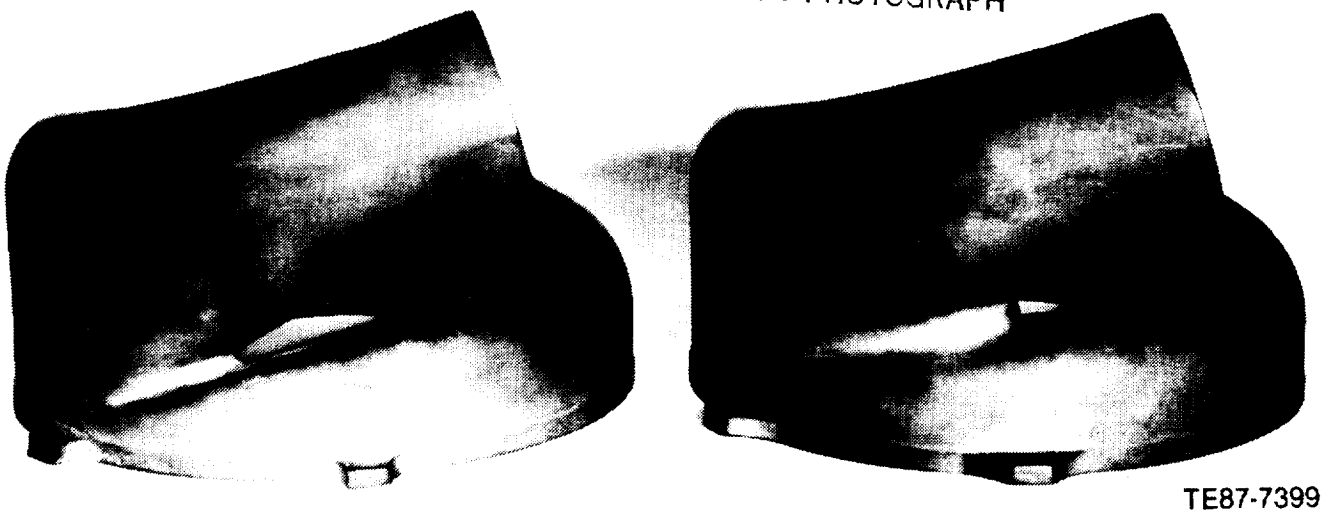

Figure 196. *Fillet radius increased from 0.01 mm to 0.025 mm and relocated.*

turbine scroll/shroud. The shroud is a separate part that is bonded to the scroll body to complete the scroll assembly. A comparison of the CBO SiC scroll design and the Kyocera Si_3N_4 scroll design is shown in Figure 197.

Engine Test of Ceramic Power Turbine Static Structure Components

Complete ceramic (Si_3N_4) power turbine static structure assemblies have been installed and tested in two engine assemblies, engine S/N 2, BU18 and engine S/N 1, BU26. The first test of the ceramic power turbine static structure constituted a proof test of the static structure in an engine environment. The second test was in an engine assembly that included all other hot section ceramic components designed for use in the AGT 100 engine. Partial sets of ceramic power turbine vanes were tested (in metal scroll assemblies) in five engine assemblies early on in the program. Complete sets of vanes were included in the last two engine tests with associated ceramic power turbine components. The zirconium oxide insulator/shim rings have been used in all 45 engine tests during this program.

SiC power turbine vanes were installed in the first AGT 100 engine assembly in 1982. However, fabrication of other (SiC) ceramic power turbine components was deemphasized so effort could be concentrated on gasifier turbine components. In late

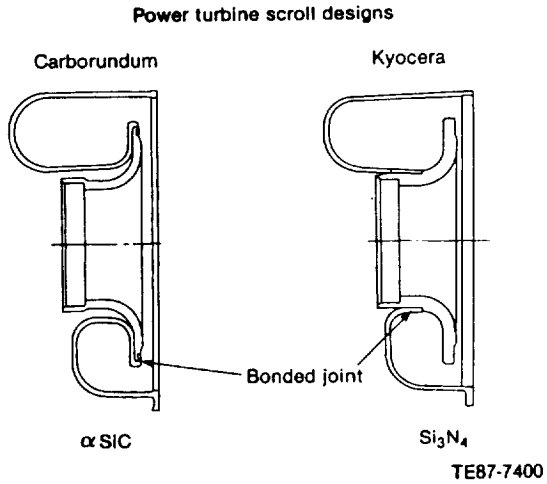

Figure 197. *Power turbine scroll designs.*

1985, after gasifier turbine components were available for test, new emphasis was placed on obtaining ceramic versions of all engine hot section components so that gasifier turbine operating temperatures could be increased beyond 2200°F. At the end of 1986, power turbine scrolls, outer backplates, and inner backplates fabricated of Si_3N_4 (Kyocera SN 250 and SN 220) material became available for test. Si_3N_4 power turbine vanes had been procured earlier in the program.

Vanes—SiC vanes supplied by CBO have been installed in five engine assemblies and tested for a total hot test time of 68.7 hr at temperatures up to 971°C (1780°F). It is estimated, but not documented, that an additional 68.5 hr of hot engine test time have been accumulated on a pair of SiC power turbine vanes installed in a metal turbine scroll assembly. The SiC vanes performed satisfactorily, but showed a tendency to chip during assembly and engine operation.

GTE Si_3N_4 (AY6) power turbine vanes were installed in the two engine assemblies in which ceramic power turbine scrolls and backplates were also tested. The first of the two tests was a proof test of the Si_3N_4 vanes (and associated ceramic power turbine static components) in an engine environment at temperatures up to 971°C (1780°F). This test in engine S/N 2, BU18 included 11 start-up cycles and a total hot test time of 14.53 hr. Inspection of the 20 vanes following the test revealed very small FPI indications at the trailing edge of 4 vanes. No chips or segments of the four vanes were missing. The four vanes were removed from further testing and replaced by new vanes.

The 16 surviving vanes from the test in engine S/N 2, BU18 and 4 new vanes were reinstalled in the proof tested ceramic scroll and outer backplate and tested in engine S/N 1, BU26. (This engine build incorporated an all ceramic "hot section.") Testing of engine S/N 1, BU26, continued at power TIT up to 899°C (1650°F) for 4.5 hr, at which time a major component failure occurred in the engine hot section and all the power turbine vanes were fractured (along with other power turbine components). The vanes were damaged beyond the point of identifying fracture origins. Failure of the power turbine vanes is thought to be secondary, i.e., a consequence of another failure, because engine test data show that the gasifier turbine was in distress before any indication of failure in the power turbine assembly. Primary failure of the power turbine vanes would not support the sequence of events suggested by the test data. A complete discussion of the engine S/N 1, BU26 failure analysis appears in the section dealing with gasifier turbine static structure. In testing and assembly handling, the Si_3N_4 vanes have shown less tendency to chip than the SiC vanes.

Scroll/Outer Backplate/Inner Backplate—Ceramic power turbine static structure assemblies have been tested in two engine assemblies. The first test in engine S/N 2, BU18, was a proof test of the entire ceramic power turbine static structure. The scroll and backplates were fabricated of Si_3N_4 (Kyocera SN250, SN220). The engine was assembled with a metal gasifier turbine assembly and a metal power turbine rotor. The power turbine rotor was specially machined to ensure that rotor-to-scroll/backplate rub did not occur. The power turbine components were exposed to temperatures up to 971°C (1780°F) for a total of 11.5 test hours hot and experienced 11 start-up cycles. Post-test inspection of the scroll and inner and outer backplates revealed no distress in any of the three components. To conserve time in completing assembly of the engine (S/N 1) in which this static structure assembly would next be tested in combination with a ceramic power turbine rotor, an identical new inner backplate was installed in engine S/N 1 during the normal engine assembly sequence while the proof test in engine S/N 2 was being completed. Use of an unprooftested inner backplate with a ceramic rotor was considered low risk based on the very good test performance of similar inner backplates in the gasifier turbine.

The second test of the Si_3N_4 power turbine static structure was in engine S/N 1, BU26. Also installed in engine S/N 1, BU26, was a ceramic power turbine rotor and a complete ceramic gasifier turbine assembly. After 4.5 hr of testing of this engine assembly a major failure event occurred in the engine hot section during which all ceramic power turbine static structure components were severely damaged. The maximum temperature experienced by the power turbine components during this test was about 899°C (1650°F), some 72°C (130°F) cooler than the static structure components were exposed to in the proof test. Both turbine rotors were operating at 70% of design speed when the failure occurred.

The power turbine scroll and outer backplate were reconstructed and failure origins identified. The scroll failed from tensile loading at its outside diameter where it mates with the outer backplate. The failure origins in the outer backplate were near its inside diameter bore with the fractures traveling toward its outside circumference. The fractures in the outer backplate were also caused by tensile loads. No overload contact type of failures were observed in any of the six cross-key slot features on the outer backplate where it contacts the metal engine structure. Possibly the scroll failed from loads exerted by the outer backplate as it expanded radially upon fracturing.

The ceramic power turbine inner backplate broke into many pieces, a fair share of which could

not be identified in the post-test debris. Reconstruction of the outer portion of the inner backplate was accomplished and analysis showed that the fractures progressed from the inside of the component to the outside. This type of failure has been seen in gasifier turbine failures where the turbine rotor separated from its shaft and impacted the inside bore of the inner backplate. (The power turbine rotor was broken from its shaft and disintegrated during the failure event.)

It may be optimistic to state that the ceramic power turbine static structure was performing satisfactorily in this test and became the victim of the consequences of another component failure. Engine test data from the subject test show the gasifier turbine (rotor) to be in distress before the power turbine. It is on this basis that the statement is made "that the failure of the power turbine components was secondary to another failure." The investigation of this engine failure is described earlier in this document.

The accumulated hot engine test time for the ceramic power turbine static structure components is shown in Table XLV. In Table XLVI the engine assemblies are listed in which ceramic power turbine static structure components were installed during the AGT 100 program. The vendor from which the components were procured and the material from which they were fabricated are also shown in Table XLVI.

Table XLV.

Summary of power turbine static structure experimental testing.

Component	No. of engine tests	Total hot test hours in engine
Scroll/outer backplate	2	18.88
Inner backplate	2	18.88
Nozzle vanes	7	87.53
Insulating shim	45	415.50
Power turbine exhaust coupling	2	18.88
Exhaust coupling seal rings	27	306.51

Table XLVI.

Chronological summary of power turbine ceramic static structure component engine testing.

Test			Ceramic component				
Engine No.	Build No.	Hot test time—hr	Scroll	Outer backplate	Inner backplate	Vane	Exhaust coupling
1	1	2.35				CBO Alpha-SiC	
1	2	0.17				CBO Alpha-SiC	
2	5	37.85				CBO Alpha-SiC	
2	6	11.98				CBO Alpha-SiC	
2	7	16.30				CBO Alpha-SiC	
2	18	14.53	Kyocera SN250 Si_3N_4	Kyocera SN220 Si_3N_4	Kyocera SN220 Si_3N_4	GTE AY6 Si_3N_4	COORS RB SiC
1	26	4.35	Kyocera SN250 Si_3N_4	Kyocera SN220 Si_3N_4	Kyocera SN220 Si_3N_4	GTE AY6 Si_3N_4	COORS RB SiC

3.9 REGENERATOR SYSTEM

Introduction

The regenerator met Mod I engine goals of 93.5% to 96% effectiveness, 4.7% to 5.6% leakage, and 5.5% total pressure drop at up to 982°C (1800°F) max temperature.

Advances in regenerator state of the art were made with the following:

- a successful ceramic pressure bulkhead and exhaust gas duct
- very low flow distortion with low pressure loss achieved with porous media

An aid to future disk material development was the calculation of required matrix strength versus thermal expansion.

Deficiencies of the current system were the following:

- limited low leakage life of hot side seal due to thermal distortion at 982°C (1800°F)
- hot seal wearface limited to 982°C (1800°F)
- disk limited to 2000 engine accelerations with 1232°C (2250°F) peak exhaust temperature
- disk spiral wrap process quality difficult to control resulting in 20% failure rafe

System Description

Figure 198 shows the Mod I regenerator system developed during this program. The Mod I system was introduced in 1981 to replace the RPD system for operation up to 982°C (1800°F) regenerator inlet temperature instead of the 1066°C (1950°F) RPD requirement. The Mod I system used a cooled Inco 625 inboard seal in lieu of the ceramic seal of the original RPD system. Features of the Mod I system shown in Figure 198 are as follows:

- disk
  - aluminum silicate (AS) spiral-wrapped Corning regenerator disk
  - room temperature vulcanizing (RTV) silicone rubber mounted, tungsten carbide coated 1050 steel ring drive gear
  - graphite bearing
- outboard (cold) seal—430 stainless steel platform with graphite wearface and Inco X750 static seal leaves
- inboard (hot) seal—Inco 625 nickel alloy platform with NiO/CaF_2 crossarm wearface, graphite rim wearface, and L605 cobalt alloy static seal leaves
- bulkhead—lithium aluminum silicate (LAS) slip cast pressure bulkhead and exhaust duct

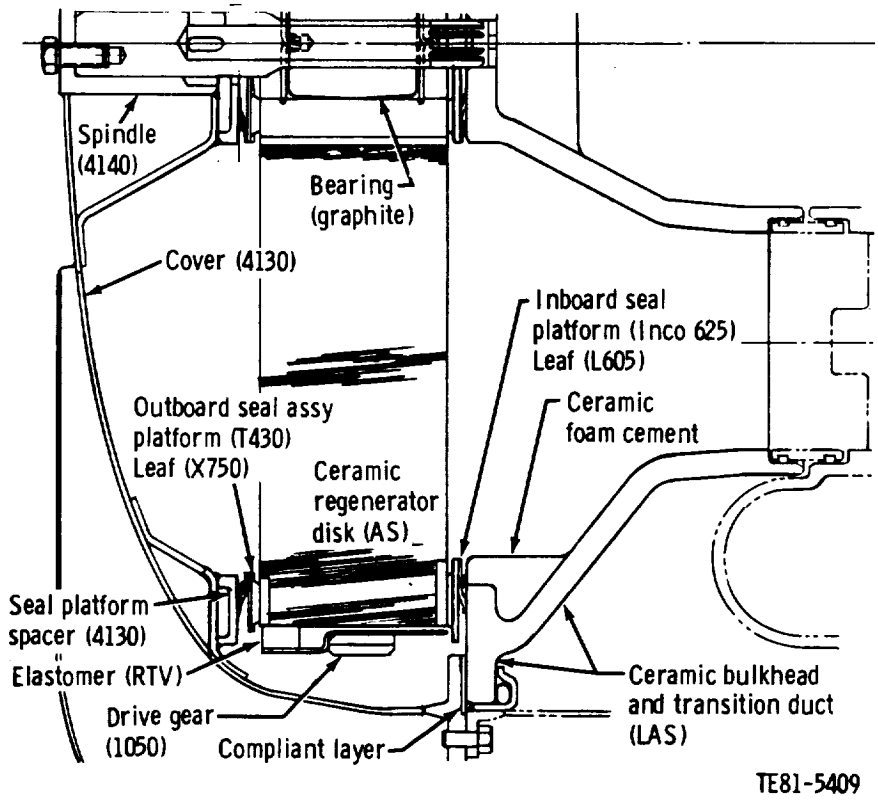

Figure 198. Mod I regenerator.

Table XLVII.
Disk properties.

	SI units	English units
Corning 9461 AS—spiral wrapped		
Nominal wall thickness	0.06 mm	0.0024 in.
Cells/unit area	233/cm^2	1500/in.^{2}
% open area	77	77
Surface area/volume	9.5 cm^2/cm^3	1860 ft^2/ft^3
Tangential bending strength	2.43 MPa	351 lb/in.^{2}
Radial compressive strength	0.58 MPa	84 lb/in.^{2}
NGK CO3P MAS—extruded triangular		
Nominal wall thickness	0.13 mm	0.0051 in.
Cells/unit area	143/cm^2	920/in.^{2}
% open area	62	62
Surface area/volume	41 cm^2/cm^3	1240 ft^2/ft^3
Tangential bending strength	1.59 MPa	230 lb/in.^{2}
Radial compressive strength	1.63 MPa	236 lb/in.^{2}
Common exterior dimensions		
Outer diameter	467.4 mm	18.4 in.
Thickness	74.7 mm	2.94 in.
Hub bearing inside diameter of solid hub insert	44.5 mm	1.75 in.

- housing—formed and welded 4130 steel housing with bearing support spindle, which also delivers cooling air to inboard seal and 4.5% porous flow distribution plate

Regenerator Disk

Configuration

Both Corning spiral-wrapped AS and NGK-extruded magnesium aluminum silicate (MAS) disks were hot rig tested, but only the AS disk was able to withstand 871 to 982°C (1600 to 1800°F) temperatures.

Properties of the disks are shown in Table XLVII.

Figure 198 illustrates how RTV silicone rubber is used to attach a sheet metal gear adapter to the ceramic disk. The gear employed 392 teeth with 14.5° pressure angle and was plasma-spray-coated with tungsten carbide to eliminate wear.

Thermal Analysis

Temperature distributions in the Corning disk at idle and 100% power were calculated and reported in Allison TDR-AD0441-013, 22 June 1983. These temperatures were used for stress analysis.

Stress Analysis

A stress analysis on the Corning disk, including the effects of temperature, pressure, gear loads, bearing loads, and seal friction loads, was reported in Allison TDR-AD-440-033, 1 August 1983. Peak radial stress was 0.31 MPa (45 lb/in.^{2}) compressive and peak tangential stress was 1.01 MPa (146 lb/in.^{2}) compressive. Both occurred at 100% power due to high pressure, since thermal stresses are low in the low expansion Corning AS material. In addition, a stress study was done to predict what material strength would be required for various higher expansion rates as a guide for material developers. For example, a material with thermal expansion of 3.1 mm/mm/°C (1.72 in./in./°F) would develop a tangential stress of 4.58 MPa (665 lb/in.^{2}). The results are given in Allison TDR AD0440-037 (Ref NASA CR-179484, September 1986, p. 87). Figures 199 and 200 demonstrate how two types of disk stress are affected by variation in thermal expansion at different engine operating conditions.

Analysis of the drive gear predicted 1.1 mm (0.044 in.) radial deflection due to gear loads (Ref NASA CR-165346); however, only 0.35 mm (0.014 in.) deflection was measured (Ref NASA CR-165504, p. 68).

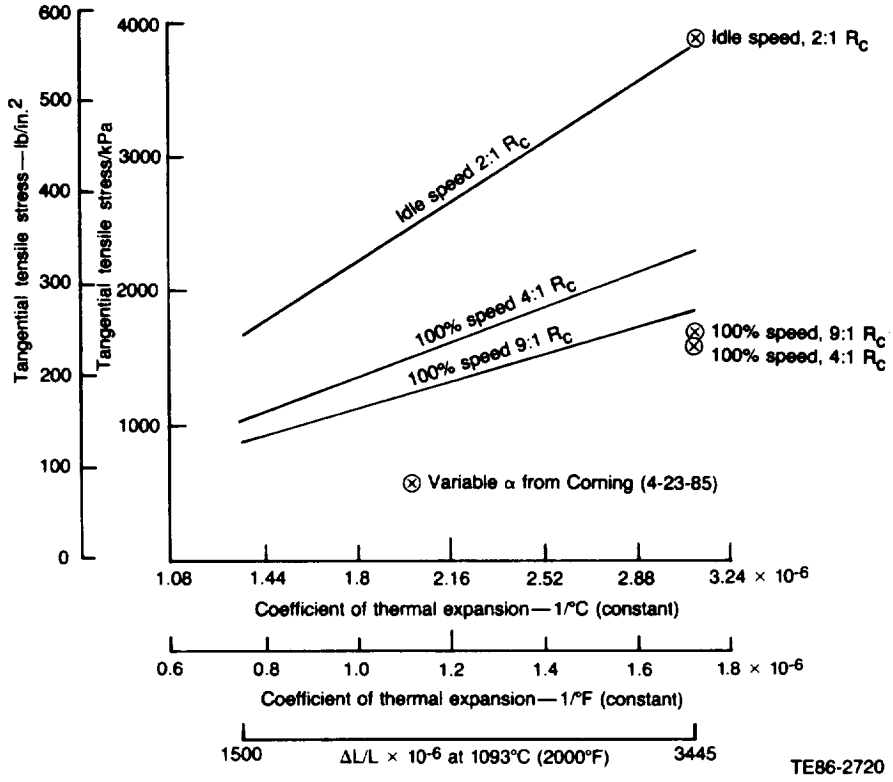

Figure 199. *Regenerator tangential tensile disk stress as affected by variation in thermal expansion at different engine conditions.*

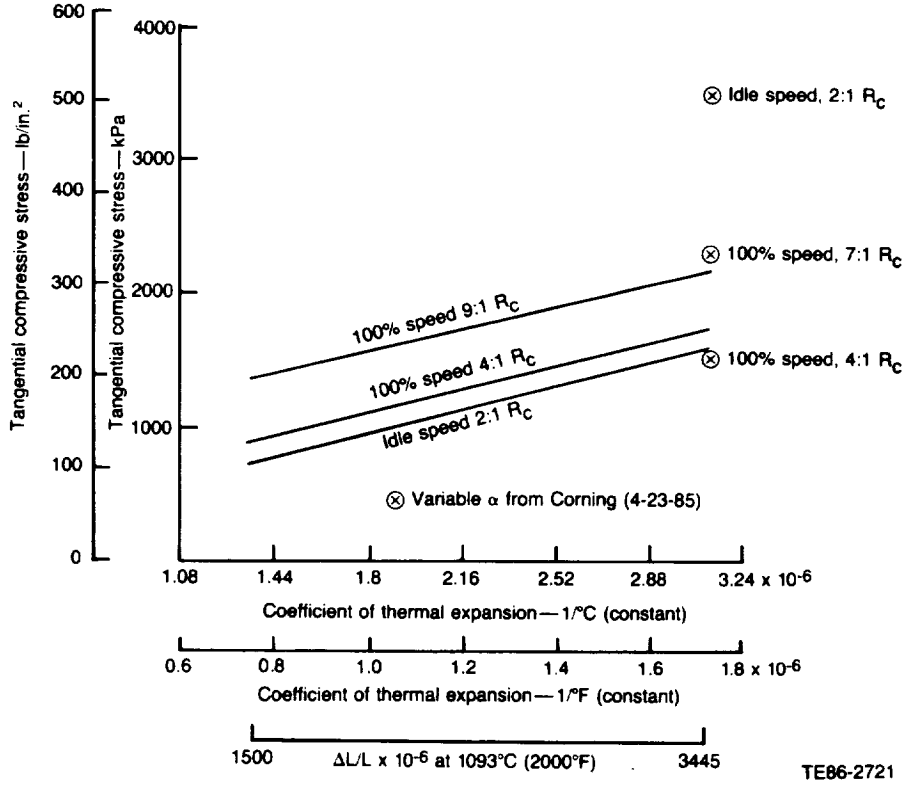

Figure 200. *Regenerator tangential compressive disk stress as affected by variation in thermal expansion at different engine conditions.*

Laboratory Tests of Disk Matrix

Laboratory tests were run on candidate disk matrix materials to determine their suitability including the following:

- radial and tangential bending strength ($MOR_{R\&T}$)
- permeability
- cyclic thermal exposure (CTE) duplicating engine accelerations

The effects of wall thickness, permeability, and CTE on strength were determined. CTE caused loss in strength of all materials as had been shown in the previous NASA/DOE ceramic engine program. The strongest Corning AS disk showed a loss from 2.44 to 1.98 MPa (354 to 287 lb/in.^{2}) after 20,000 cycles to 1177°C (2150°F). Figure 201 shows this loss in strength and depicts the thermal cycles. An extruded Corning MAT sample with high static temperature capability showed a loss from 1.83 to 0.76 MPa (226 to 110 lb/in.^{2}) in 1000 cycles to 1093°C (2000°F). CTE was found to be the life limiting factor for all materials. The best material, Corning AS, was limited to 2000 accels to predicted AGT 100 temperatures of 1232°C (2250°F) where 100,000 are required. It was necessary to reduce temperature rise rate from 1160°C/sec to 361°C/sec (2100°F/sec to 650°F/sec) to eliminate cyclic damage (Ref NASA CR-174798, p. 50). NGK-MAS samples showed 40% strength loss with 5000 cycles to only 1010°C (1850°F). Samples of modified CO9 NGK-MAS extruded rectangular matrix received in February 1987 showed dramatic improvement in as-received bending strength and permeability, but cyclic thermal tests were not completed. Long axis MOR was 3.32 MPa (482 lb/in.^{2}) compared to earlier values of 2.05 MPa (297 lb/in.^{2}) for CO9P and 0.97 MPa (141 lb/in.^{2}) for CO8.

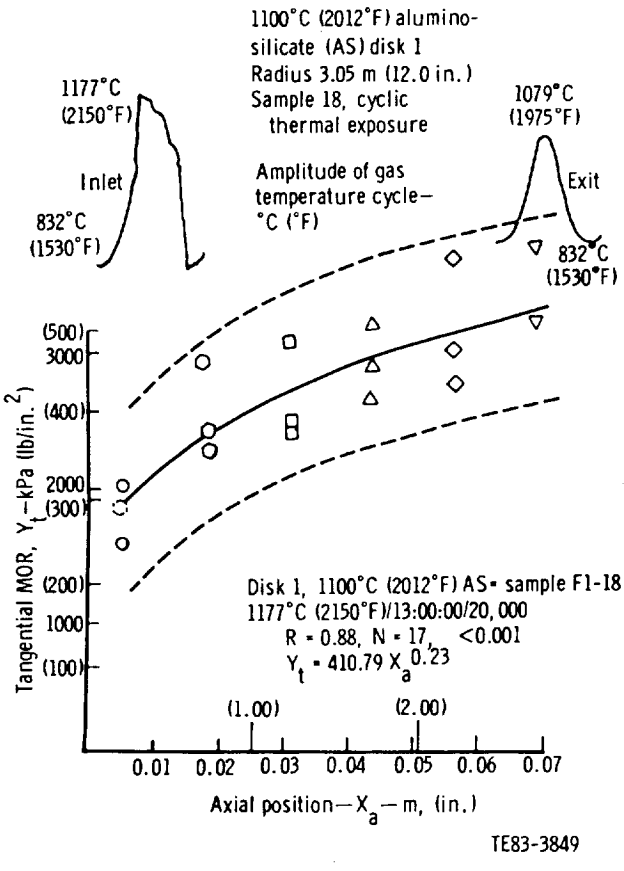

Figure 201. *Corning AS regenerator disk shows loss of strength after 20,000 thermal cycles.*

Figure 202 (Ref NASA CR-175018, p. 50) shows the dependence of Corning AS disk strength on disk permeability, which leads to an Allison limit on permeability. A striking result from the permeability tests was the fact that wrapped Corning AS matrix was 17 to 128 times more permeable in the tangential direction than in the radial direction. Radial bending strength (affected by tangential porosity as well as the wrap geometry) is only one-third that of tangential bending strength. Since tangential permeability involves only the corrugated strips while radial permeability involves both corrugated and flat strips of the spiral wrap, the corrugated strips were much more porous and weaker (Ref NASA CR-179484, p. 87).

Regenerator Rig Tests

Allison employs a regenerator rig that fully duplicates engine flow, pressure, and temperature conditions. Regenerator testing of 791 hr was accomplished. Mod I regenerator performance goals were achieved early in 1983 with effectiveness of 93.5% at 100% power conditions and 96% at idle, leakage ranging from 4.7 to 5.6%, and total pressure drop of 5.5% with up to 982°C (1800°F) inlet gas temperature (Ref NASA CR-174629, p. 41).

The rig run constitutes a proof test for new parts. Two of 10 Corning AS disks failed and both NGK disks tested failed. The first Corning disk to fail, when examined in the laboratory, proved to be the weakest ever tested with tangential bending strength ranging from 1.08 to 1.37 MPa (157 to 199 lb/in.^{2}) where average is 2.42 MPa (351 lb/in.^{2}). Average flat wall thickness was only 0.038 mm (0.0015 in.) where the average of all disks was 0.053 mm (0.0021 in.) (Ref NASA CR-174798, p. 50). The failure consisted of a 38 mm (1.5 in.) circumferential crack 25 mm (1.0 in.) from the outer diameter. A radial crack connected that circumferential

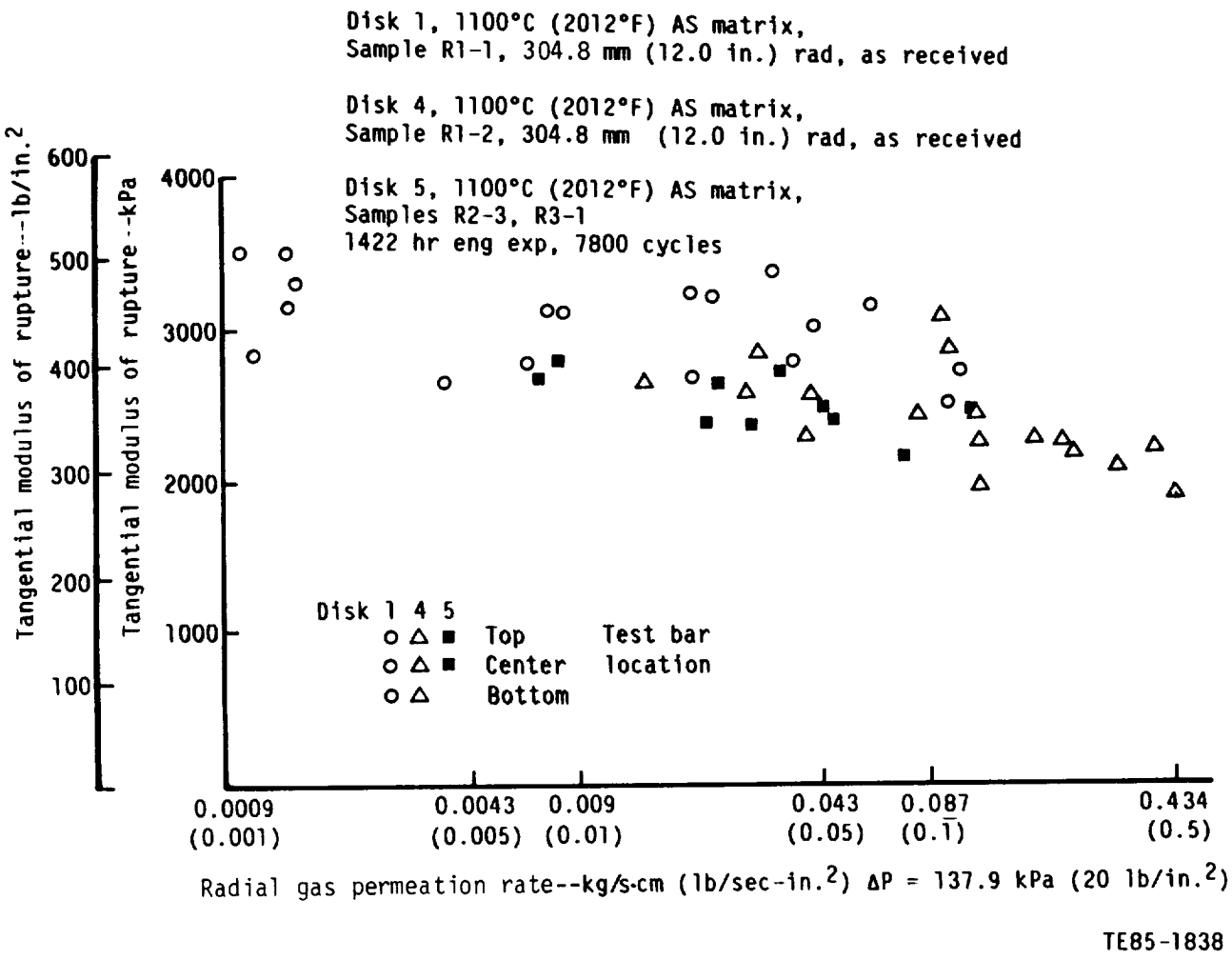

Figure 202. *Corning AS regenerator disk strength depends on disk permeability.*

crack to a second circumferential crack at a 77 mm (3.0 in.) radius, which extended 150°. Despite these extensive cracks, the disk was still operable. Failure occurred after 70 hr of operation. The failure was attributed to the low strength caused by the thin flat walls. No reason could be found for the second Corning disk failure, which must have resulted from a local defect near the hub. Failure was after 16:44 hr of operation. This disk met the low leakage (low porosity) specification, was stronger than average, and had thicker walls than average.

Extruded NGK-CO3P MAS disks impregnated to reduce unacceptable leakage of about 1% began cracking at 871°C (1600°F) in rig operation. Laboratory cut-up examination revealed an extensive branching crack pattern after 46 hr of operation to no more than 871°C (1600°F) as shown by Figures 203, 204, and 205 (Ref NASA CR-175018, p. 50). Failure was blamed on the high thermal expansion of the impregnated MAS, 1.2 × 10^{-6} 1°C. A new NGK-MAS is now available with half the expansion of the failed impregnated material and with acceptable porosity and higher strength, but is expected to be marginal in thermal stress at AGT 100 engine conditions.

Engine Tests

A Corning AS disk was run to 100% engine pressure and speed and 910°C (1670°F) without incident. A total of 572 engine disk hours were accumulated with 267 hr on the high time disk. No disk failures occurred in engine tests.

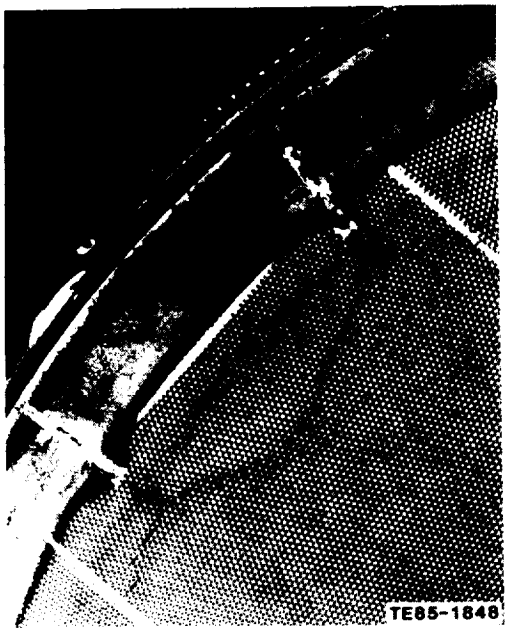

Figure 203. Hot face crack indications on regenerator rim of S/N G-2.

Disk Extrusion

Extrusion of disk matrix offers many advantages and potential solution of some disk problems:

- potentially less strength loss from temperature transients due to preferential grain alignment minimizing thermal stress caused by anisotropic grain expansion
- greater strength due to:
  - improved geometry
  - reduced porosity due to compaction, grain alignment, and elimination of paper carrier burnout
  - elimination of thin walls due to wicking in wrap process
  - lower incidence of wall distortion
- ultimate lower cost, especially when a one-piece extrusion is achieved
- higher effectiveness and lower pressure drop due to consistency in hole size

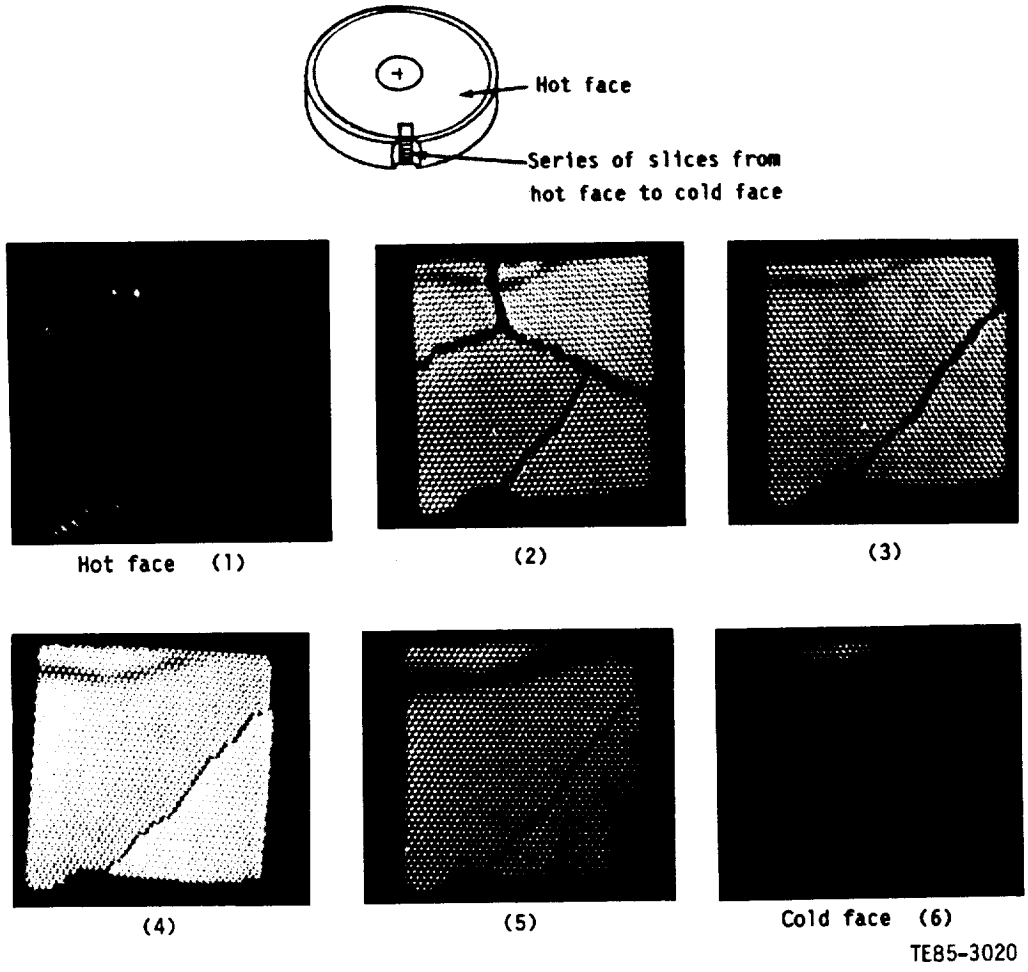

Figure 204. Matrix samples cut from disk S/N G-2 showing crack propagation.

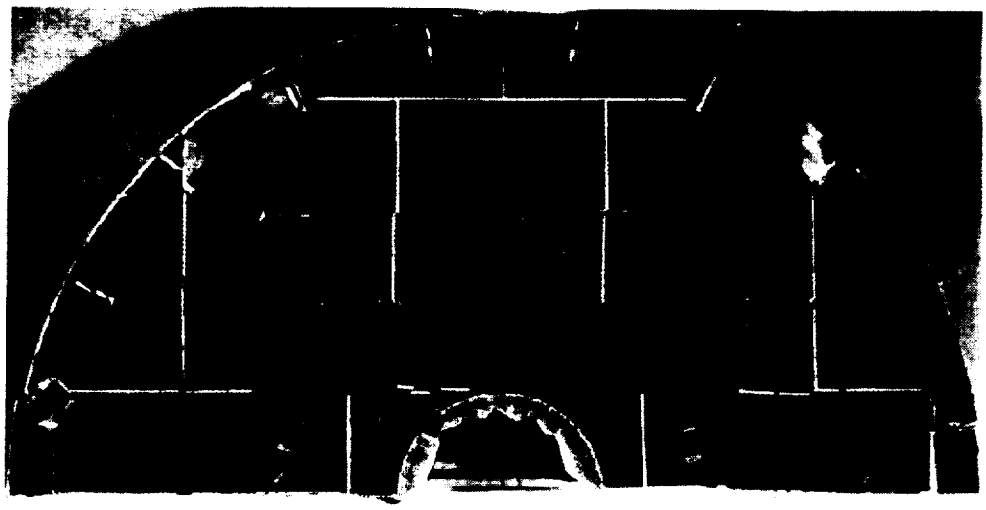

TE85-1849

Figure 205. *Extensive cracking of NGK extruded MAS regenerator disk S/N G-2.*

Allison has funded an extrusion development for the ultra low expansion Corning AS material at Corning. Progress has been very slow due to minimal manpower and funding. Effort is now concentrated on a 2:1 aspect ratio rectangular matrix with a goal of 202 cells/cm^2 (1300 cells/in.^{2}) and 0.11 mm (0.0044 in.) walls. Calculations show that such a rectangular matrix would equal the effectiveness and pressure drop of a triangular matrix with 233 cells/cm^2 (1500 cells/in.^{2}) and 0.0815 mm (0.0032 in.) thick walls. With fewer cells and thicker walls the rectangular matrix offers easier extrusion than the triangular matrix but is not as strong in diagonal loading.

Regenerator Seals

Configuration

Figure 198 shows the inboard (hot) regenerator seal and outboard (cold) seal in the assembled regenerator. Both seals are one-piece assemblies with wearfaces rubbing against the regenerator disk mounted on one side of a structural metal platform and 0.064 mm (0.0025 in.) thick metal foil static sealing leaves on the other side. The thin static seal leaves are backed up against pressure loads by hinged thicker support leaves. These details may be seen in Figure 206. Planform of two cold seals, showing the wearface side, may be seen in Figure 207. The rim extends a full 360° on hot seals. The seal wearface is pressure loaded against the disk. Nominal loads are 0.07–0.10 MPa (10–15 lb/in.^{2}). Figure 207 shows grooves in the cold seal wearfaces necessary to control these loads in the face of major disk rotational effects. Leaves are installed on both sides of the hot seal crossarm to channel cooling air that is introduced at the hub through the disk bearing shaft and at the rim. Rim segments of the hot seal are not rigidly attached to the crossarm and are installed with initial inner diameter tension. This tension or preload is a patented feature to counter rim buckling due to radial temperature gradient across the rim. The cold seal wearface and rim wearface of the hot seal are specially developed and impregnated graphite for low friction without induced torsional disk vibration, at a maximum operating temperature of 621°C (1150°F). Wear life has not been established for the AGT 100 but is expected to be satisfactory based on short-term measurements and on other engines. The hot seal crossarm wearface is plasma-sprayed 90 NiO/10 CaF_2 providing a maximum operating temperature of 982°C (1800°F) with acceptable friction and wear. Axial disk differential pressure loads are reacted by the cold seal. Structural platforms are 430 SS for the cold seal and Inco 625 for the hot seal. Sealing leaves are Inco X750 for the cold seal and L605 cobalt alloy or Rene 41 nickel alloy for the hot seal selected for both hot strength and nongalling wear.

Effort was concentrated from 1982 through 1987 on the Mod I regenerator previously described. From 1979 through 1981 a prototype unit was designed and tested but was replaced when the AGT 100 engine was redesigned. Initial effort to develop a 1066°C (1950°F) ceramic hot seal was abandoned to concentrate effort on engine development.

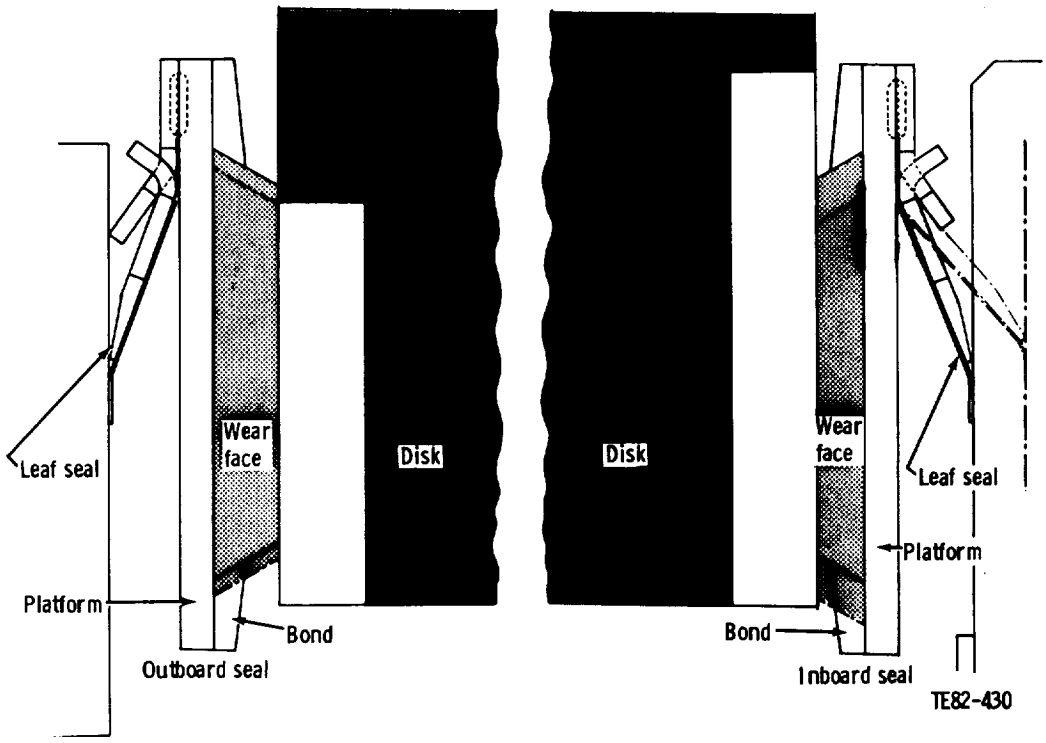

Figure 206. *Regenerator seal cross section details.*

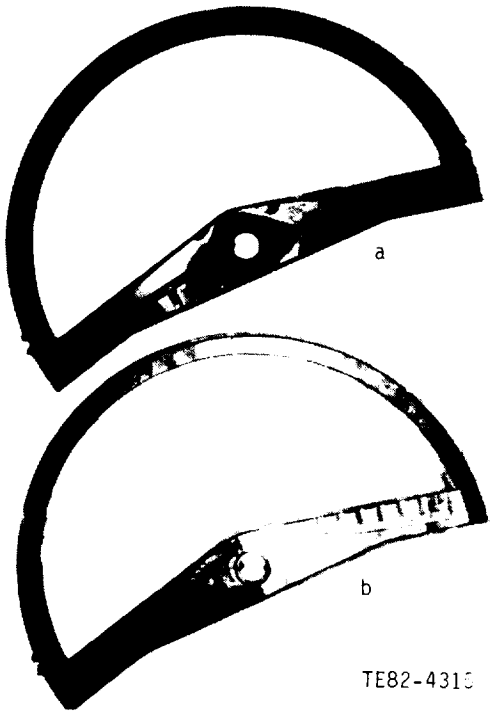

Figure 207. *Planform of two regenerator cold seals, showing loading grooves.*

Regenerator Rig Test Results

A regenerator rig that fully simulates engine flows, pressures, and temperatures was used for both seal and disk testing. From this rig, leakage, effectiveness, pressure drops, drive torque, gas temperatures, and material temperatures were available. A static seal leaf leakage rig was also used to locate leak points.

Leakage

The static seal leaf leakage rig showed that most leakage occurred at the rim to crossarm leaf joints and at the center crossarm leaf joint. O-ring segments installed under the sealing edge of the leaf acting as a spring were found to reduce total regenerator leakage from 10% to 8% (Ref NASA CR-168056, p. 26). These O-ring segments were retained on the cold seal but were replaced by L605 metal helper springs on the hot seal with slight loss in benefit. In April 1983 Mod I leakage goals were met with leakage ranging from 4.7% to 5.6% using a newly specified low leakage disk and nominal seal pressure loading. Figure 208 illustrates some examples of regenerator leakage throughout the engine operating range as defined by inlet air pressure with various seals and disks but not the lowest quoted here (Ref NASA CR-174629, p. 41). These seals grad-

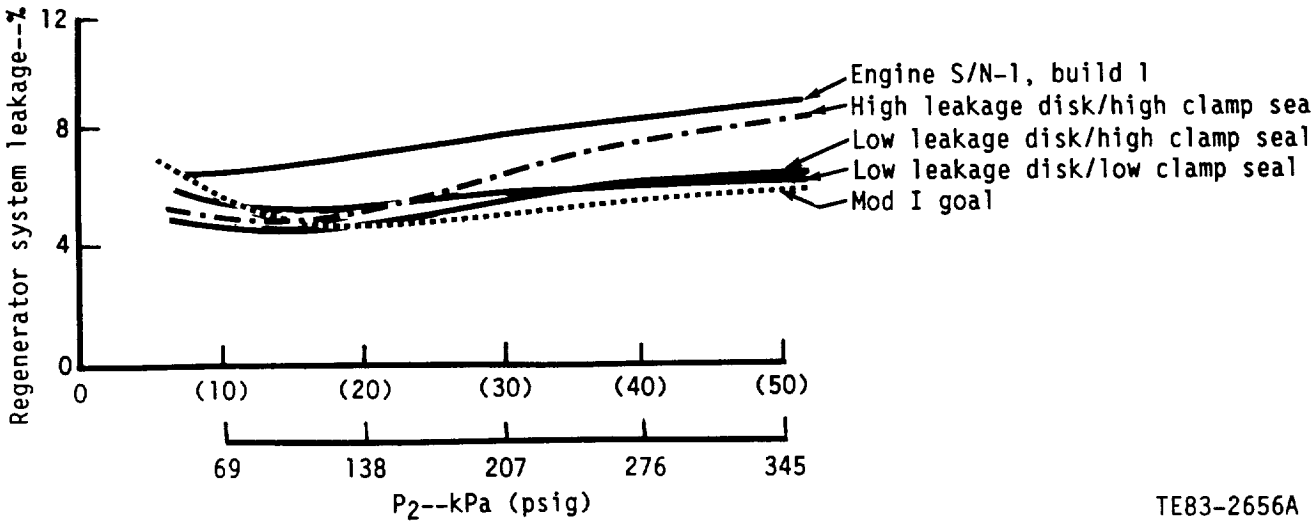

Figure 208. *Examples of regenerator leakage throughout engine operating range.*

ually deteriorated with both rig and engine usage until 11% to 18% leakage was measured in 1985 (Ref NASA CR-179484, p. 85). The deterioration resulted from thermal distortion due to inadequate cooling and from handling. Allison's long time vendor for regenerator seals gave up this work and learning difficulties experienced by a new vendor prohibited reproduction of 1983 seal quality by program's end in 1987. The best leakage achieved with the new vendor was 15%, although they had succeeded in consistently producing somewhat similar Allison 404 engine regenerator seals with the required 4% leakage. It is believed that failure to use a weld chiller for leaf attachment caused platform distortion that could not be corrected. Precise processing is critical to produce a low leakage seal. The essential features are a flat thermally stable wearface and smooth nondistorting static leaves. These essential features could be assured with a low expansion ceramic platform and an independent, cooled, protected metal static leaf seal.

Wear

Seal running times have not progressed beyond the 300 hr early high wear phase; but, based on long-term running in the 404 engine, wear rates are consistent with the 3500 hr life goal.

Torque

Typical drive torques from idle to maximum power conditions for high pressure loaded and nominal pressure loaded seals were as follows:

	Idle-torque	Max power-torque
High pressure loaded seals	31 Nm (24 ft-lb)	170 Nm (125 ft-lb)
Nominal pressure loaded seals	16 Nm (12 ft-lb)	68 Nm (50 ft-lb)

Seal pressure loading is governed by the loading groove pattern of the cold seal as shown by Figure 207. Nominal loading is 0.07-0.10 MPa (10-15 lb/in.^{2}) while high loading is 0.07-0.30 MPa (10-45 lb/in.^{2}). Rim load remains constant at the lower value.

Seal Cooling

The metal hot side seal operating at 982°C (1800°F) gas temperature requires platform and leaf cooling to prevent thermal stresses from causing yield and distortion resulting in leakage. The current cooling concept has not been adequate. An improved concept was not pursued to completion to concentrate effort on engine development. The current concept uses only the 0.0083 MPa (0.12 lb/in.^{2}) differential pressure available between regenerator inlet and outlet air to channel inlet air from the seal rim and hub areas to an exhaust point on each half of the crossarm. This cooling air is returned to the burner. A more effective cooling system would employ full cycle pressure differential but would sacrifice the air to turbine exhaust flow. Figure 209 shows seal crossarm platform temperatures with and without cooling air using the current concept.

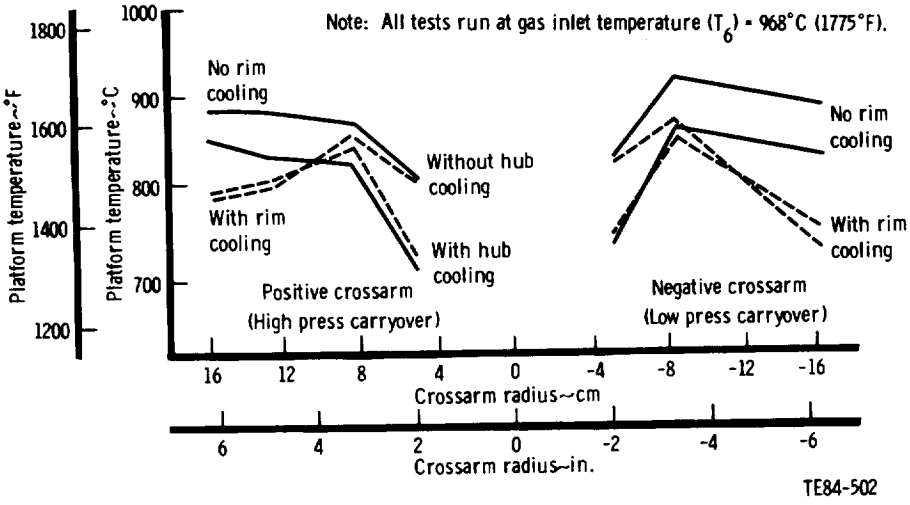

Figure 209. *Seal crossarm platform temperatures with and without cooling air.*

This figure shows that little cooling is achieved at the 8 cm (3 in.) radius while hub and rim areas are overcooled (Ref NASA CR-174798 p. 46). The improved concept would concentrate cooling where needed and prevent excessive temperature gradients that cause distortion and leakage. A longer term solution would employ an uncooled ceramic platform and a separate static leaf structure protected from heating through the platform, thus easing the cooling load.

Rim Preload

The patented hot seal rim preload used to prevent a radial temperature gradient from causing rim buckling and leakage was monitored during testing to verify the required preloads. These preloads impose tensile prestress on the rim inner diameter, which is relieved at running conditions.

Laboratory Wearface Friction and Wear Tests

A laboratory friction and wear rig was utilized to test samples of candidate seal wearface material against subscale rotating disks in an oven environment. These tests, in static air, provide a means of selecting the best candidate material but constitute a more severe environment than the actual regenerator where airflow removes wear debris and carries away friction heat. In this program samples of graphite loaded polyimide, graphite composite, and ceramic were tested. Tables XLVIII, XLIX, and L show friction and wear (Ref NASA CR-174629, p. 36). DuPont Vespel SP22 was selected from Table XLVIII as the best candidate for a combined platform and wearface for cold side seals. Later in 1984 Pure Polybon L was shown to have lower friction and equal wear as seen in Table L. The ceramic shown in Table XLIX was an unsatisfactory candidate for the hot side seal crossarm.

Polyimide-Rubber Cold Side Seal

A cold side seal with potential for very low leakage, simple fabrication, and easily controlled quality was designed and tested. This seal would ultimately have only 2 pieces: (1) a composite graphite fiber-polyimide combined platform and wearface and (2) a one-piece molded silicone rubber static seal leaf. Figure 210 compares this polyimide seal to the standard metal seal and an interim metal-rubber version (Ref NASA CR-174629, p. 34). The polyimide test seal incorporated several epoxy bond joints to use readily available stock. An epoxy joint failed at an estimated 354°C (670°F) exhaust gas temperature, which should not have exceeded 299°C (570°F). The excessive temperature that caused the polyimide seal failure was caused by excessive hot seal leakage that raises exhaust gas temperature. A successful polyimide-rubber cold seal would require a dependable low leakage hot seal. A metal seal with a silicone rubber seal leaf suffered hardening and debonding of the rubber. This was also attributed to the abnormally high exhaust temperature. PMR 15 polyimide now available, and NASA-developed PMR-II-700 polyimide, soon to be available, offer higher temperature capability than the Vespel SP22, which failed.

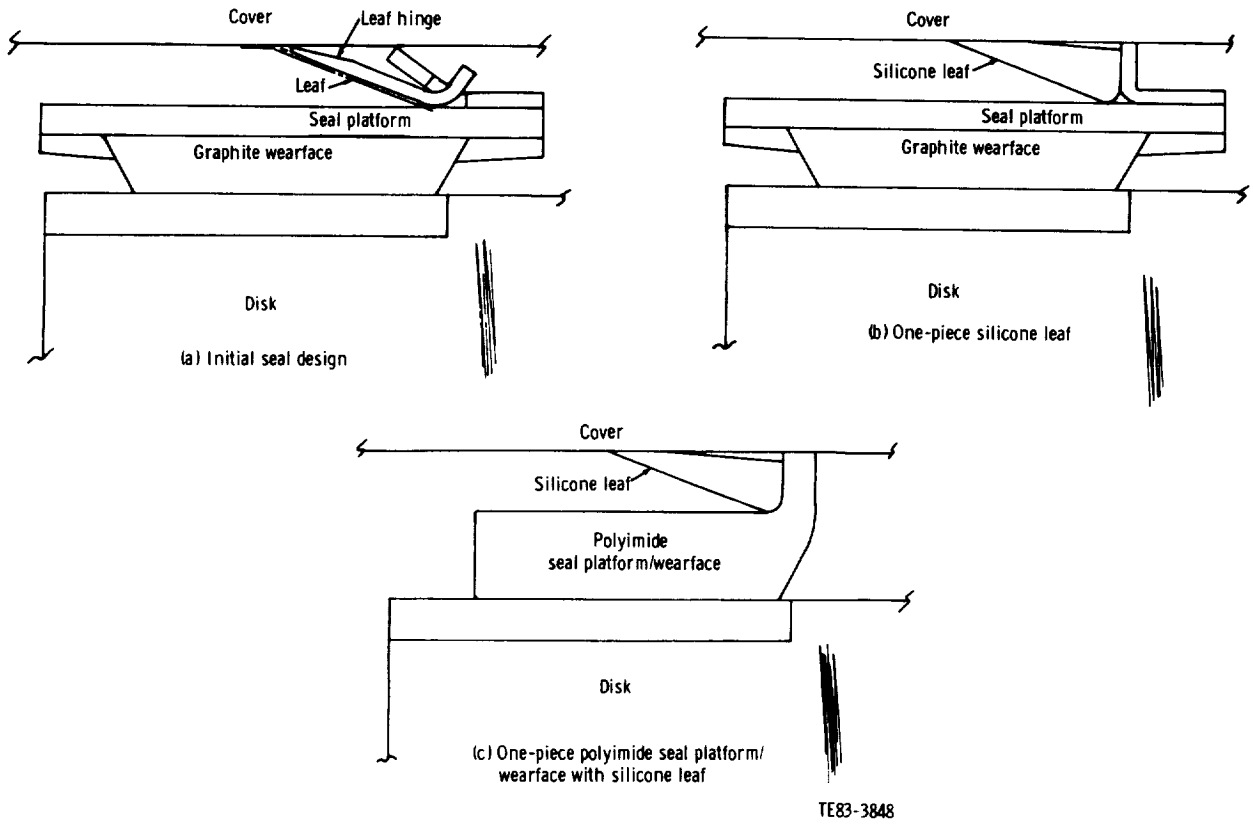

Figure 210. *Polyimide regenerator seal evolution.*

Table XLVIII.
Friction/wear screening test results (6 hr at 103 kPa [15 lb/in.^{2}] contact pressure).

Material	Test conditions: Sliding velocity— m/s	(ft/sec)	Temperature— °C	(°F)	Results: Coefficient of friction	Wear—mm (in.)
DuPont Vespel SP21	0.05	(0.17)	204-316	(400-600)	0.12/0.25	
	0.2	(0.75)	204-316	(400-600)	0.15/0.21	0.03 (0.001)
	0.5	(1.75)	204-316	(400-600)	0.08/0.19	
DuPont Vespel SP22	0.05	(0.17)	204-316	(400-600)	0.12/0.20	
	0.2	(0.75)	204-316	(400-600)	0.09/0.19	0.03 (0.001)
	0.5	(1.75)	204-316	(400-600)	0.08/0.16	
Amoco Torlon 4275	0.05	(0.17)	204-316	(400-600)	0.12/—	
	0.2	(0.75)	204-316	(400-600)	0.14/—	failed at 260°C (500°F)
	0.5	(1.75)	204-316	(400-600)	0.06/—	
Amoco Torlon 4301	0.05	(0.17)	204-316	(400-600)	0.14/—	
	0.2	(0.75)	204-316	(400-600)	0.10/—	failed at 260°C (500°F)
	0.5	(1.75)	204-316	(400-600)	0.09/—	
Pure Polybon M (TO454)	0.05	(0.17)	204-316	(400-600)	0.07/0.12	
	0.2	(0.75)	204-316	(400-600)	0.07/0.08	0.08 (0.003)
	0.5	(1.75)	204-316	(400-600)	0.05/0.07	

Table XLIX.
Friction/wear screening test results.

Material	Test conditions: Sliding velocity—m/s (ft/sec)	Test conditions: Temperature—°C (°F)	Results: Coefficient of friction	Results: Wear—mm (in.)
Ceramic (SGC-1)	0.05 (0.17)	427 (800)	0.12	After 6 hr
(34 kPa [5 lb/in.^{2}]		760 (1400)*	0.50	0.064 (0.0025)—wearface
contact pressure)		1038 (1900)*	0.94	0.14 (0.0055)—disk
	0.2 (0.75)	427 (800)	0.11	
		760 (1400)*	0.20	
		1038 (1900)*	0.83	
Graphite composite	0.2 (0.75)	93 (200)	0.05	After 8 hr
(H/CCD/009-10)		316 (600)	0.19	0.043 (0.0017)—wearface
(138 kPa		538 (1000)	0.16	0.005 (0.0002)—disk
[20 lb/in.^{2}]		649 (1200)	0.33	
contact pressure)		760 (1400)	**	

* high vibration
** excessive vibration
max velocity possible—0.1 m/s (22 ft/min)
max velocity—0.09 m/s (17 ft/min)

Table L.
Friction/wear screening test results
(6 hr at 103 kPa [15 lb/in.^{2}] contact pressure).

Material	Test conditions: Sliding velocity—m/s (ft/sec)	Test conditions: Temperature—°C (°F)	Results: Coefficient of friction, μ	Results: Wear—mm (in.)
DuPont Vespel SP22	0.05 (0.17)	204–316 (400–600)	0.12–0.20	
	0.2 (0.75)	204–316 (400–600)	0.12–0.20	0.03 (0.001)
	0.5 (1.75)	204–316 (400–600)	0.12–0.20	
Pure Polybon M	0.05 (0.17)	204–316 (400–600)	0.12–0.20	
	0.2 (0.75)	204–316 (400–600)	0.12–0.20	0.08 (0.003)
	0.5 (1.75)	204–316 (400–600)	0.12–0.20	
Pure Polybon L	0.05 (0.17)	204–316 (400–600)	0.12–0.20	
	0.2 (0.75)	204–316 (400–600)	0.12–0.20	0.03 (0.001)
	0.5 (1.75)	204–316 (400–600)	0.12–0.20	

Ceramic Pressure Bulkhead and Duct

Configuration

A slip cast Corning code 9458 LAS pressure bulkhead and exhaust gas duct was developed and satisfactorily tested. Figure 211 shows this bulkhead, which sustains full engine differential pressure of 0.345 MPa (50 lb/in.^{2}). This material has ultra low expansion of only 240 parts per million at 900°C (1652°F). Wall thickness is 10 mm (0.40 in.). A foamed ceramic cement filler is used around the inner diameter of the rim to blend a cast undercut and to insulate the rim. The rim flange is installed between compliant high temperature packings.

Stress Analysis

Figure 212 shows the finite element model used to predict stress and deflection. Predicted failure rate was 1 in 925 (Ref NASA CR-167875, p. 25). Measured stresses and deflections agreed closely with pre-

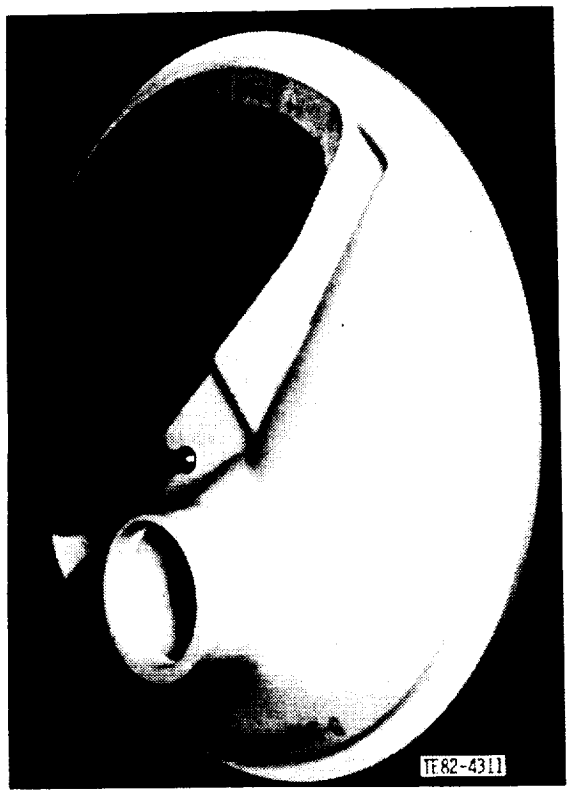

Figure 211. Ceramic bulkhead—exhaust duct.

dicted values. Maximum deflection was 0.43 mm (0.017 in) in the center of the crossarm. Four iterations were required to perfect this design.

Proof Tests

All parts were proof tested to full engine pressure with no failures. Deflections and strains were measured on each part.

Engine Tests

One bulkhead successfully completed an engine test to full pressure and 910°C (1670°F) exhaust gas temperature. A Mod I engine bulkhead would require an exhaust gas temperature capability of 982°C (1800°F). Three bulkheads were damaged before adequate clearance with the turbine exit duct was established.

Regenerator Housing

Configuration

The regenerator housing is constructed of formed and welded 1.8 mm (0.070 in.) thick 4130 steel.

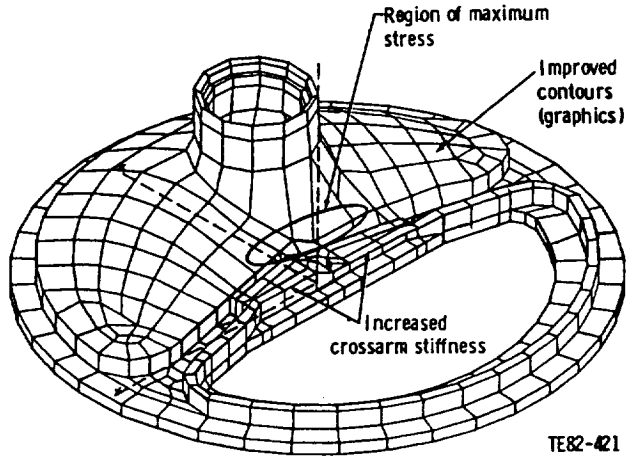

Figure 212. Finite element model of bulkhead—exhaust duct.

Figure 198 shows how the housing serves as a mount and subassembly of all regenerator parts. Figure 213 is a photo of the housing showing air and gas passages prior to installation of a 4.5% porous flow distribution plate in the air inlet passage. This plate incorporates photo etched 0.94 mm (0.037 in.) diameter holes on 3.5 mm (0.136 in.) centers. The plate is preceded by a 50 mesh 30% open wire screen also for flow distribution. Part of the flow is allowed to bypass the flow distribution screen and plate. The cover also mounts the drive pinion gear which drives the regenerator ring gear.

Flow Modeling

A series of 8 cold flow models were built to arrive at an optimum inlet air flow distribution. The final configuration with forementioned flow distribution porous plate and screen was calculated to lose only 0.2% regenerator effectiveness at full power due to flow distribution with a cost of only 0.56% pressure drop (Ref NASA CR-168325 p. 19).

Stress Analysis

Two-dimensional stress analysis predicted a maximum stress of 276 MPa (40 ksi) and deflection of 5.1 mm (0.020 in.) with 1.5 mm (0.060 in.) thick material. Tests with the eventual 1.8 mm (0.070 in.) thick material showed only 0.13 mm (0.005 in.) maximum deflection of full pressure (Ref NASA CR-168056, p. 21). Significant weight reduction could be made in this conservative design.

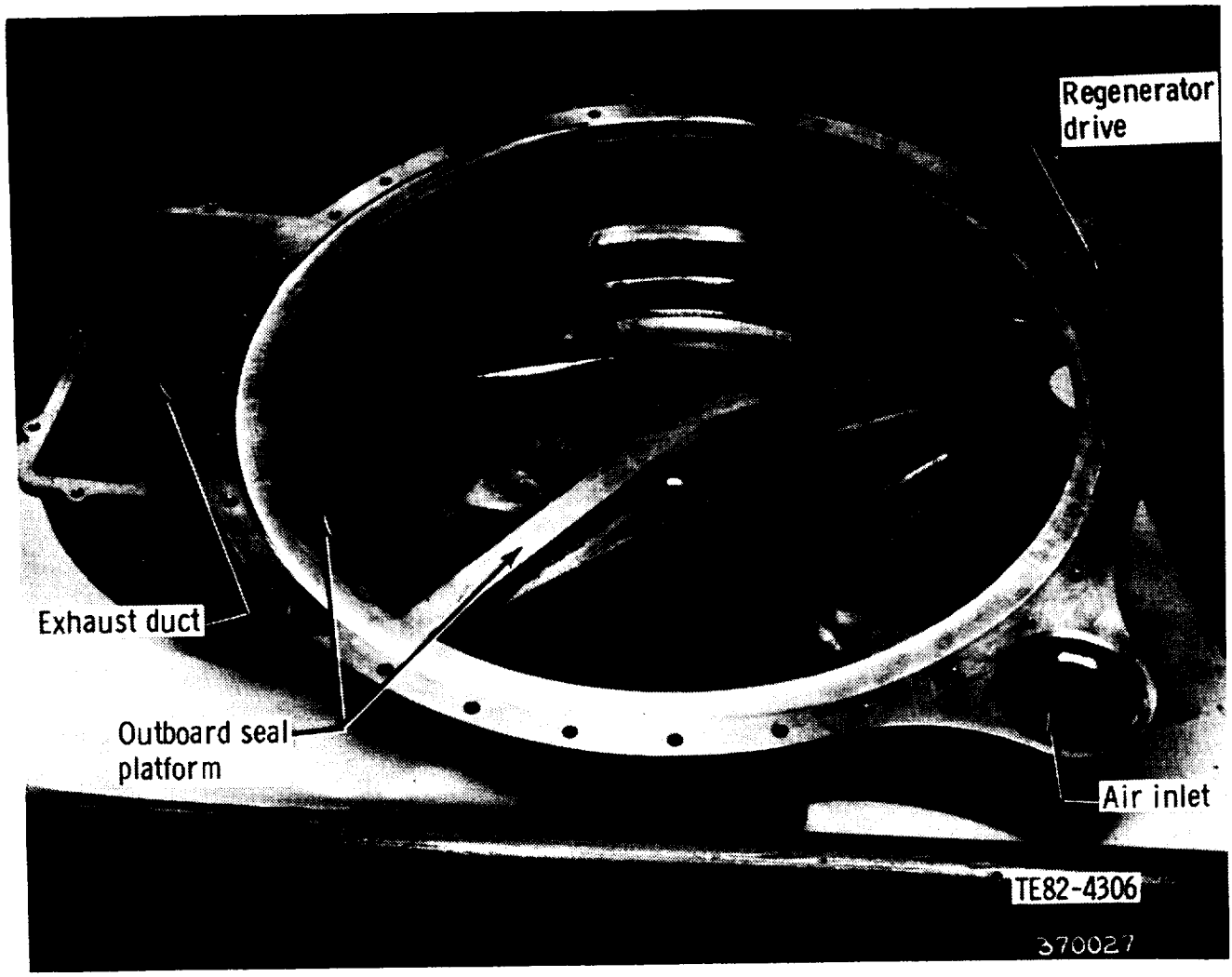

Figure 213. *Regenerator housing.*

IV. ENGINE ASSEMBLY AND TEST

4.1 SUMMARY

The engine assembly and test phase of the AGT technology project began in July 1982 with the assembly of the first AGT 100 engine, and continued through the life of the program. Two experimental AGT 100 engines, with the serialized designation of S/N 1 and S/N 2 respectively, were obtained to support this phase of the program. A total of 45 engine assemblies or buildups (BU) were evaluated for a combined engine total test time of 572 hr. Table LI summarizes the engine testing.

4.2 OBJECTIVES

Engine testing was planned and executed to address the following objectives:

- engine mechanical development
- aerodynamic performance evaluation
- ceramic component development

The first two objectives were pursued at a level necessary for establishing the AGT 100 as a credible testbed machine for the evaluation of ceramic components and to identify engine interaction of components. Test objective emphasis, distribution, and timing throughout the entire engine test phase can be seen in the chronological engine assembly presentation of Figure 214. With the AGT 100 project focused on ceramic component technology generation, the testbed was uniquely qualified to identify engine-related structural ceramic component problems and/or improvements required for the hot section of the engine.

A basic test philosophy maintained by Allison was that the ceramic components should successfully pass a proof test prior to being introduced into an engine. This was a prudent procedure at this stage of ceramics development, designed to minimize the chance of an extensive, expensive, engine failure. However, the proof tests frequently do not totally simulate actual engine operating conditions (stresses, dynamics, thermals, leak paths, clearances, transients, etc). To do so might require equipment as costly as experimental engines, and entail significant development of the rigs themselves. Ultimately, the engine test becomes the final proof test. Because of this, engine testing of new ceramic turbine section components or assemblies was pursued in an individual, building block fashion in a control-variable approach. This approach, as actually applied, is shown in Figure 215, which summarizes the chronological ceramic component introduction into the engine test program. Ceramic component engine operating times, featuring high-time parts and total part times, are shown in Table LII.

Several ceramic components have been present in all accumulated engine testing: combustor body, dilution band and pilot tube, regenerator disk and seal platform, and the thermal barrier shim rings. This accomplishment reflects the expertise and confidence, in both designing for and fabricating from ceramic materials, that was gained during the preceding CATE project. The most challenging components to design, fabricate, and verify have been the turbine rotors and turbine static structures. Consequently, initial engine testing was accomplished with metal surrogates.

Table LI.
Summary of engine testing.

	Engine builds	Engine total test time—hr
Engine S/N 1	26	305
Engine S/N 2	19	267
Program total	45	572

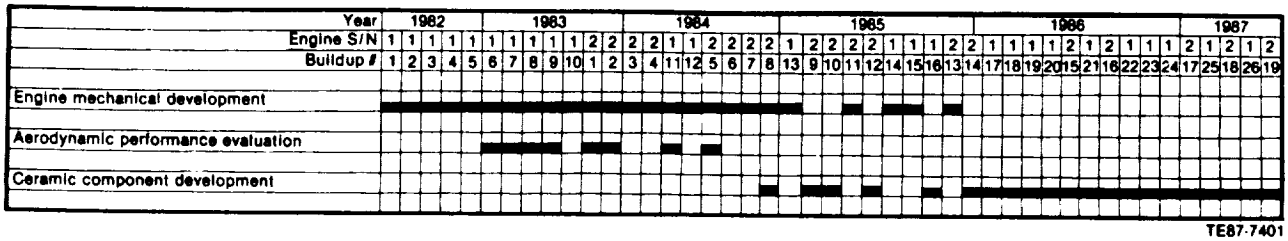

Figure 214. *Engine test schedule.*

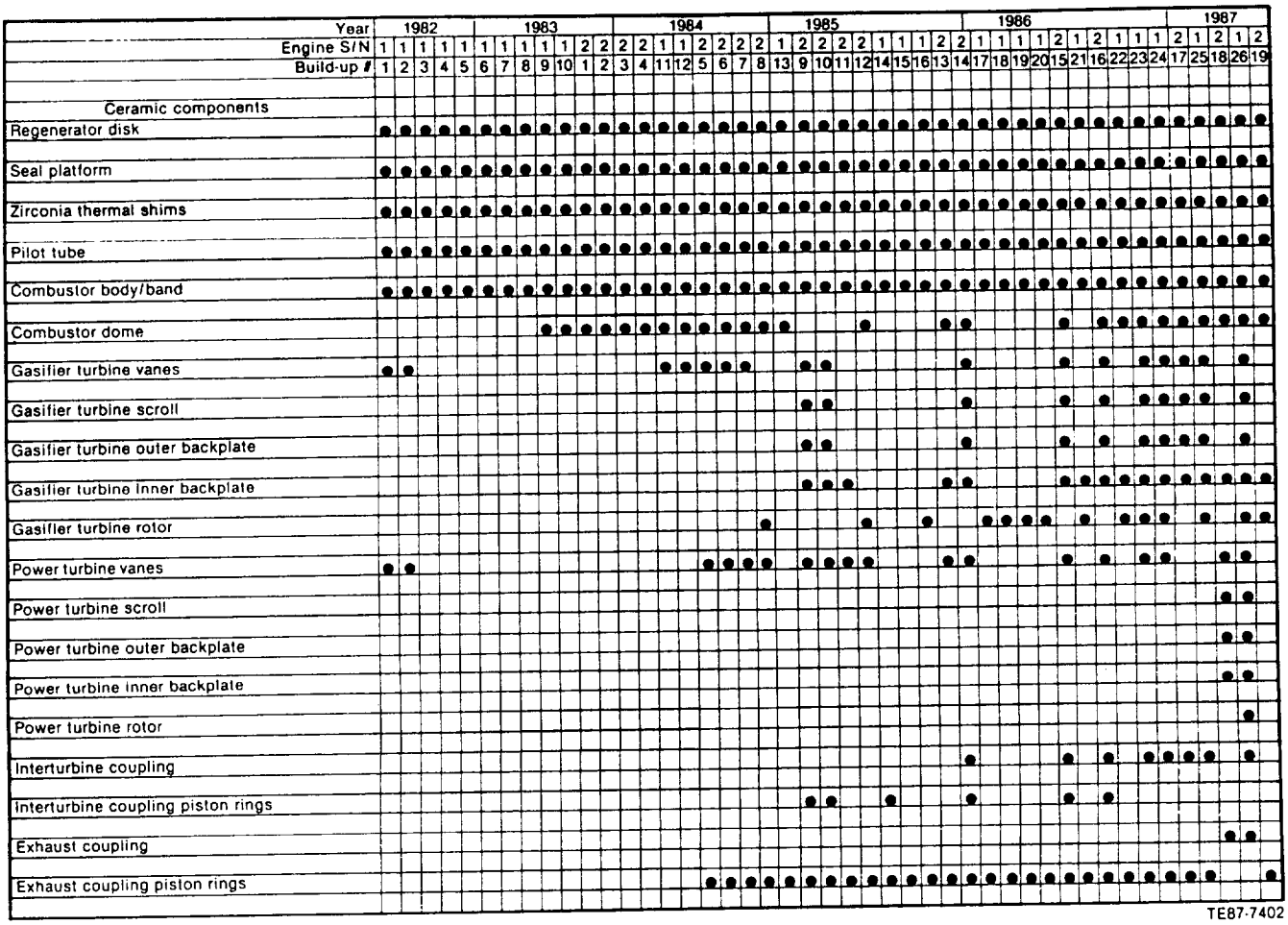

Figure 215. *Summary of ceramic component introduction into engine testing.*

Table LII.
Ceramic component operating times.

	Ceramic component	Engine test times—hr	
		High-time part	Total time
Combustor:	Dome	135	401
	Body	214	572
	Pilot tube	119	572
	Dilution band	247	572
Turbine:	Vane	71	192
	Rotor	100	142
	Scroll	30	77
	Inner backplate	53	152
	Outer backplate	22	77
Regenerator:	Disk	267	572
	Seal platform	161	572
Misc:	Shim, gas turbine	126	572
	Shim, power turbine	126	572
	Coupling, int turb	37	69
	Coupling, PT exhaust	18	24

The second engine was not brought on line until 1983. This kept parts rework to a minimum while the first engine accomplished normal shakedown activities that revealed important clearances and adjustments to geometries, lubrication, and instrumentation systems. In 1984 the first engine tested ceramic gasifier rotor was introduced. Initial engine testing of an entirely ceramic gasifier static structure began in 1985, with continuing design and processing refinements, new materials applications, and testing of these components, as well as the ceramic gasifier rotor, through the 1986 and 1987 programs. The first power turbine ceramic static structure and ceramic rotor were not introduced until 1987. Emphasis throughout the program was placed on ceramic technology development as applied to the gasifier turbine section of the engine. Once this technology and experience had matured to a significant level, it would be transferred to the less severe operating requirements of the power turbine components. The building block, control-variable approach culminated in an all-ceramic hot section engine test in 1987.

Following is a historical summary of the engine test program with highlights from each engine build. Included are primary test objectives, test time, maximum speed and temperature obtained, major successes and/or failures, engine problems and fixes, and major ceramic components.

S/N 1, BU1

- objective: mechanical shakedown run with motoring and fire-up
- ceramic combustor (body, pilot flame holder, and dilution band), regenerator (disk and seal platform), turbine vanes (2 gasifier and 2 power turbine), and thermal-barrier shims
- motored to 60% N_1 and 60% N_2
  100% N_1 = 86,256 rpm gasifier turbine
  100% N_2 = 68,156 rpm power turbine
- nozzle light-off unsuccessful
  conclusion: relatively high power turbine speed resulted in reduced flow capacity
- high deflection on gasifier shaft
  conclusion: iron ring seal sleeve yielded and rubbed rotor shaft

S/N 1, BU2

- objective: mechanical shakedown run
- same ceramic parts as S/N 1, BU1
- replaced iron seal ring with carbon seal
- nozzle light-off successful with motoring only the gasifier
- 980°C (1800°F) TIT and 68% N_1
- self-sustained engine operation not attained
- gasifier rub with inducer blade tips uniformly broken
  conclusion: unseating and cocking of both scrolls due to air loads exceeding spring retention force
- secondary damage to all ceramic vanes and slight scoring of regenerator disk

S/N 1, BU3

- objective: mechanical shakedown run, self-sustained operation at 60% N_1
- same ceramic components as S/N 1, BU2 minus gasifier and power turbine vanes
- gas path rub pins removed, scroll retaining loads increased, gasifier turbine clearance improved, and interturbine instrumentation added
- 980°C (1800°F) TIT and 60% N_1
- brief period of self-sustained operation
- gasifier rotor rub at inner backplate inner diameter (i.d.)
  conclusion: inner backplate coning at i.d. due to thermal transient

S/N 1, BU4

- objective: stabilized operation at 60% N_1
- same ceramic components as S/N 1, BU3
- modified gasifier inner backplate
- platinum rub pins installed
- 1004°C (1840°F) TIT and 58% N_1
- power turbine to inner backplate rub
  conclusion: distortion of power turbine outer backplate due to thermal transient moved inner backplate axially into rotor

S/N 1, BU5

- objective: stabilized operation at 60% N_1
- same ceramic components as S/N 1, BU4
- gasifier and power turbine clearances increased while design work on parts configuration modifications was under way
- 995°C (1820°F) TIT and 60% N_1
- broken ceramic regenerator seal platform
  conclusion: power turbine exhaust coupling piston ring end-gap not sufficient for ring thermal expansion

- 4:38 hr accumulated run time for S/N 1, BU1 through BU5 (run time is combination of burn time and motoring time)

S/N 1, BU6

- objective: stabilized operation at 70% N_1 and hydraulic starter system verification
- same ceramic components as S/N 1, BU5, seal platform replaced
- increased air hold-down loads on turbine scrolls
- backplates coated with zirconia for heat insulation to reduce thermal distortion
- gasifier shroud coated with abradable material and clearances reduced between shroud, rotor, and backplate
- gasifier flow area reduced 7% to decrease steady-state TIT
- power turbine exhaust coupling and piston ring reduced in diameter
- starter replaced with continuous duty hydraulic motor
- engine started satisfactorily and self-sustained at 71% N_1 and 854°C (1570°F) TIT
- engine removed from stand for hot-end inspection prior to testing at higher speeds
- 5:15 hr total run time

S/N 1, BU7

- objective: 90% N_1 and 90% N_2
- no change in engine parts from S/N 1, BU6
- engine self-sustained and obtained 90% N_1 and 90% N_2 and 1038°C (1900°F) TIT
- engine removed from stand for planned inspection
- cracked ceramic combustor body and cracked carbon ring seal at gasifier bearing location identified during teardown inspection
- 5:37 hr total run time

S/N 1, BU8

- objective: obtain performance data throughout speed range—including 100% N_1
- same ceramic components as S/N 1, BU7 with exception of new combustor body
- all carbon ring seals replaced
- oil flow to gasifier turbine bearing increased
- vanes of compressor impeller thinned to increase high-speed airflow as demonstrated on compressor rig
- build clearance of both turbines decreased
- diagnostic instrumentation added to the engine
- performance data acquired from fire-up to 100% N_1 with the maximum speeds of 94% N_1 and 89% N_2 at which thermal stability was attained at 1038°C (1900°F) TIT
- apparent gas path fire downstream of power turbine
- disassembly disclosed: failed carbon ring seals at gasifier and power turbine locations, cracked oil instrumentation tube, chipped areas on ceramic combustor body due to combustor-to-scroll compliant layer dislodging and requiring removal during testing, minor damage to gasifier turbine rotor blade tips from ceramic combustor chips, and worn areas on combustor body in dilution band area
- 6:17 hr total run time

S/N 1, BU9

- objective: performance mapping, durability experience, and air leakpath checks
- same ceramic components as S/N 1, BU8, with the exception of a new combustor assembly with a ceramic dome employed for the first time
- redesigned regenerator drive system with a plan-o-centric gear drive
- excessive vibration at 80% N_1
- regenerator drive system configuration returned to pre BU9 status for vibration investigation
- testing terminated with excessive flow-path leakage from broken seal platform at power turbine exhaust coupling location
  conclusion: probable excessive friction in coupling did not allow realignment during thermal growth
- 14:42 hr total run time

S/N 1 BU10

- objective: vibration investigation and leak path check
- same ceramic components as S/N 1, BU9 except new regenerator seal platform installed
- excessive vibration at speeds above 80% N_1
- correcting gasifier pinion shaft runout and indexing the shaft did not help vibration problem

- leak-path check performed
- disassembly revealed broken ceramic seal platform at the power turbine coupling position
  conclusion: greater thermal misalignment than coupling could accommodate
- gasifier rotor significantly out of balance
- 1:48 hr total run time

S/N 2, BU1

- objective: explore mechanical operation and performance throughout speed range
- same configuration as S/N 1, BU9, except flow capacities of both turbines matched to original 1080°C (1976°F) TIT (engine S/N 1 was rematched in BU6 and BU8)
- ceramic regenerator reworked to accommodate new power turbine exhaust coupling design
- motoring tests to 50% N_1 successful
- performance data acquired from 60%–70% N_1 and 30%–70% N_2
- engine removed due to substantial flow-path leak
- severe wear on regenerator hot seal
  conclusion: excessive plasma spray material rubbed regenerator disk rim cement producing highly abrasive dust
- 12:43 hr total run time

S/N 2, BU2

- objective: explore mechanical operation and continue shakedown of new engine
- same hardware as S/N 2, BU1 except regenerator and seal assembly replaced with one from S/N 1
- pilot nozzle flamed out after combustion light-off and carboning eventually plugged pilot orifice
- burner variable geometry schedule modified due to combustor flashback at 80% N_1
- test terminated due to air leakage past graphite ball seals at scroll hold down springs closest to burner (severe oxidation)
- 25:16 hr total run time

S/N 2, BU3

- objective: mechanical shakedown, run locked clutch test, and measure soakback temperatures on shutdown
- ceramic components same as S/N 2, BU2
- graphite ball seals replaced with metal (HA188) ball seals
- undesirable vibration and shaft displacement at 90% N_1
- further investigation revealed shaft displacement had changed, indicating a permanent balance change
- locked clutch test and soakback information successfully acquired
- 23:47 hr total run time

S/N 2, BU4

- objective: perform mechanical loss test
- bladeless rotors, no impeller, no burner, no regenerator
- at full speed, losses higher than estimated, at part speed, losses match design estimates
- 18:17 hr motoring time

S/N 1, BU11

- objective: obtain performance data and evaluate hardware design changes
- same ceramic components as S/N 1, BU10 with the addition of two ceramic gasifier vanes
- squeeze film damper replaced spring bar mass isolator at No. 2 bearing
- improved spring bar mass isolators at turbine end of gasifier and power turbine shafts
- performance data obtained at 60%–100% N_1, with TIT between 1099°C (1920°F) and 1071°C (1960°F)
- spent 1:07 hr at 100% N_1 with low vibration-maximum whip was 30% of limit
- some combustor flashback due to thermal insulation in airflow path
- testing terminated due to stuck relief valve in oil pump
- brass separator of No. 2 bearing cracked
- 16:02 hr total run time

S/N 1, BU12

- objective: accumulate additional test time and continue shakedown
- same ceramic parts as S/N 1, BU11
- heavier separator installed in No. 2 bearing
- added external oil pump while redesign of engine oil pump was under way
- gasifier speed limited to 86% N_1 due to hot/cold section pressure unbalance
  conclusion: Haynes 188 ball seals not seated properly

- durability test performed at 60% and 70% N_1
- ceramic combustor dome chipped at metal locating pin
- gasifier turbine carbon seal severely oxidized
  conclusion: increased seal clearances permitted hot turbine gases to backflow through the seal
- 17:34 hr total run time

S/N 2, BU5

- objective: test first Asahi SiC ceramic combustor body and obtain additional performance data
- same ceramic components as S/N 2, BU4 with two gasifier and two power turbine ceramic vanes and Asahi ceramic combustor body (previous tests used Carborundum combustor body)
- performance data obtained from 55% to 88% N_1
- vibration velocity limits exceeded at 90% N_1
- some combustor instability
- 41:36 hr total run time

S/N 2, BU6

- objective: investigate combustor instability with each type of main fuel nozzle
- same ceramic components as S/N 2, BU5
- thermal insulation properly positioned so as to not impede airflow past the combustor
- combustor instability occurred with each fuel nozzle
- 12:19 hr total run time

S/N 2, BU7

- objective: determine if stability differences exist between the two combustor bodies and perform lubrication system test
- same ceramic components as S/N 2, BU6, except CBO combustor body reinstalled
- some instability continued, switched to JP5 fuel to reduce coking on main fuel nozzle
- bearing temperature versus oil flow rate data obtained at 65% and 85% N_1
- No. 4 bearing failure ended test
  conclusion: inadequate oil cooling caused partly by oil coking aggravated during lubrication test
- combustor dome broken at outer diameter (o.d.) flange
- chip out of one ceramic gasifier vane at midchord on one end
- 17:27 hr total run time

S/N 2, BU8

- objective: test first ceramic gasifier rotor (CBO, alpha-SiC)
- same ceramic components as S/N 2, BU7, except ceramic gasifier rotor added and ceramic vanes removed
- no combustor, heated air provided by 60 kW electric heater
- engine motored to 43% N_1 and 250°C (482°F)
- test terminated when whip and vibration increased excessively during accel at 48% N_1
  conclusion: ceramic rotor inducer blade tip failure
- 1:13 hr motoring time

S/N 1, BU13

- objective: perform leakage tests
- ceramic components: combustor (body, dilution band, dome, and pilot tube), regenerator (disk and seal platform), thermal barrier shims, and exhaust coupling piston rings
- performed turbine airflow rate calibration and hot engine run with tracer gas and flow calibrated turbines
- identified need of modifying regenerator seals
- high gasifier whip at 84% N_1
- test terminated with exhaust gas over temperature
  conclusion: ring gear separated from regenerator disk due to improper installation
- 70:59 hr total run time

S/N 2, BU9

- objective: test first gasifier turbine ceramic scroll package
- ceramic components: combustor (pilot tube, body, and dilution band), thermal-barrier shims, two power turbine vanes, interturbine and exhaust coupling piston rings, and gasifier scroll assembly (CBO alpha-SiC scroll, CBO SiC vanes, Corning BMAS III Stepped inner and CBO alpha-SiC outer backplates)

- ran one cycle to 943°C (1730°F) and 58% N_1
- engine removed from stand for scheduled inspection
- no problems observed
- 2:24 hr total run time

S/N 2, BU10

- objective: additional testing of ceramic scroll package
- same ceramic parts as S/N 2, BU9
- ran 5 more cycles similar to test of S/N 2, BU9
- engine removed for scheduled inspection of ceramic parts
- gasifier turbine outer backplate (CBO, alpha-SiC) developed radial crack through locating slot
- 6:55 hr total run time

S/N 2, BU11

- objective: investigate whip and vibration levels throughout speed range
- same ceramic parts as S/N 2, BU10 except replaced scroll assembly with metal parts (ceramic inner backplate)
- assembly procedure ensured final assembled condition of gasifier rotor to be within print limits
- power turbine shaft seized at 20% N_2
  conclusion: improper seating of scroll locating shim allowed buildup of excessive pressure that moved inner backplate against rotor
- 1:19 hr total run time

S/N 2, BU12

- objective: engine test second ceramic CBO alpha-SiC gasifier rotor
- same ceramic components as S/N 2, BU11 except ceramic rotor added and ceramic inner backplate replaced with metal part
- ran one thermal cycle to 898°C (1650°F) TIT and 60% N_1
- increase in gasifier shaft whip and decrease in gasifier speed
- teardown revealed gasifier rotor inducer blade tips broken off
- 1:40 hr total run time

S/N 1, BU14

- objective: study engine vibration and test power transfer clutch
- same ceramic components as S/N 1, BU13 minus the ceramic combustor dome
- engine oil changed from Dextron II to MIL-L-23699
- vibration limit reached at 84% N_1
- power transfer clutch performed successfully
- numerous combustor flameouts
  conclusion: excessive flow through fuel metering valve
- engine removed from stand to fix oil leak
- 21:07 hr total test time

S/N 1, BU15

- objective: continuation of S/N 1, BU14 testing
- engine from BU14 removed from stand to fix oil leak and returned as BU15
- after 5 minutes at 60% N_1, high vibration and bearing temperature
- teardown revealed a failure of the No. 1 position carbon seal
- 1:29 hr total run time

S/N 1, BU16

- objective: engine test first Kyocera Si_3N_4 ceramic gasifier rotor (SN220M)
- same ceramic components as S/N 1, BU15 with addition of gasifier rotor
- completed: 2 cycles to 60% N_1, 898°C (1650°F) TIT
  1 cycle to 70% N_1, 898°C (1650°F) TIT
  2 cycles to 70% N_1, 1079°C (1975°F) TIT
- approximately 20 hr durability testing at 60% N_1 and 1065°C (1950°F) TIT
- 30:00 hr total run time

S/N 2, BU13

- objective: test first pilotless combustor, additional testing of power transfer clutch and to monitor rotor dynamics
- ceramic components same as S/N 2, BU12 except added Corning BMAS-III gasifier inner backplate and removed ceramic rotor
- extensive instrumentation added to monitor dynamics
- successfully completed pilotless combustor and power transfer clutch testing
  conclusion: dynamic response is indicative of rotor unbalance
- 31:12 hr total run time

S/N 2, BU14

- objective: increase test time of the gasifier ceramic scroll, turbine vanes, and inner backplate that had been previously tested in S/N 2, BU9 and BU10
- same ceramic components as S/N 2, BU10 plus a ceramic combustor dome, interturbine coupling, and a new CBO alpha-SiC gasifier outer backplate
- 3 successful cycles to 80% N_1 and 1080°C (1976°F) TIT
- primary ceramic failure of scroll at inner rim occurred during 4th cycle
- secondary failure: all ceramic vanes broken, ceramic outer backplate cracked, scroll inlet flange cracked and shroud broken, metal gasifier rotor inducer tips broken and/or abraded off
- 11:07 hr total run time

S/N 1, BU17

- objective: increase test time of first Kyocera Si_3N_4 rotor (SN220M) successfully run in S/N 1, BU16
- same ceramic components as S/N 1, BU16
- 3 successful cycles to 80% N_1 and 1080°C (1976°F) TIT
- test stopped due to compressor oil seal failure
- 6:05 hr total run time

S/N 1, BU18

- objective: accumulate test time on first Kyocera Si_3N_4 rotor (SN220M)
- same ceramic parts as S/N 1, BU17
- new compressor oil seals installed
- 1 successful cycle to 80% N_1 and 1080°C (1976°F) TIT
- testing terminated with failure of compressor aft oil seal
- 3:09 hr total run time

S/N 1, BU19

- objective: accumulate test time on first Kyocera Si_3N_4 rotor (SN220M)
- same ceramic parts as S/N 1, BU18
- new compressor oil seals installed with increased diametral clearances
- successful endurance running at 60% and 70% N_1 and 1037°C (1925°F) TIT
- compressor oil seal failed again during oil pressure variation test to No. 2 bearing and squeeze film damper
  conclusion: dimensional problem with wave spring in seal ring and forces acting on ring during high vibration
- 45:30 hr total run time

S/N 1, BU20

- objective: accumulate test time on first Kyocera Si_3N_4 rotor (SN220M) and determine if gasifier pinion shaft adversely affects whip
- same ceramic parts as S/N 1, BU19
- removed splined coupled gasifier pinion shaft and ram started engine
  conclusion: gasifier pinion had little affect on whip
- endurance running performed at 60% and 70% N_1, and 1080°C (1976°F) TIT
- carbon deposits from combustor dislodged and broke ceramic gasifier turbine rotor
- 15:33 hr total run time
- total time on first Kyocera Si_3N_4 rotor (SN220M) was 99:54 hr, including 56 start/stop cycles

S/N 2, BU15

- objective: engine test a new ceramic gasifier scroll assembly
- same ceramic components as S/N 2, BU14, new parts as follows:
  - gasifier scroll, SiC, CBO
  - gasifier outer backplate, SiC, CBO
  - gasifier inner backplate, Si_3N_4, GTE SN1000
  - gasifier vanes (18), Si_3N_4, GTE PY6
- 3 successful cycles to 60% N_1 and 899°C (1650°F) TIT
- combustor flameout at 982°C (1800°F) TIT due to erratic burner variable geometry positioning
- borescope inspection revealed cracks in ceramic turbine shroud
- 6:33 hr total run time

S/N 1, BU21

- objective: evaluate second Kyocera Si_3N_4 ceramic gasifier rotor (SN220M)

- same ceramic components as S/N 1, BU20 with the addition of ceramic gasifier rotor and a GTE SN1000 Si_3N_4 gasifier inner backplate from S/N 2, BU15
- 3 successful cycles to 60% N_1 and 899°C (1650°F) TIT
- rotor failed during 4th cycle at 70% N_1 and 996°C (1825°F) TIT
  conclusion: excessive cavity pressure caused gasifier scroll lift off and tilt into the rotor
- 6:00 hr total run time

S/N 2, BU16

- objective: engine test Norton SiSiC gasifier scroll
- same ceramic components as S/N 2, BU15 except new gasifier scroll assembly and Kyocera SN250 Si_3N_4 gasifier inner backplate
- 3 successful cycles to 60% N_1 and 899°C (1650°F) TIT
- 3 successful cycles to 80% N_1, and 1079°C (1975°F) TIT
- high whip and rotor rub of scroll and inner backplate at 90% N_1
- outer backplate broken, scroll and inner backplate not cracked and reusable
- 19:42 total run time

S/N 1, BU22

- objective: engine test of third Kyocera Si_3N_4 ceramic gasifier rotor (SN220M)
- ceramic components: combustor assembly, regenerator disk and seal platform, thermal barrier shims, exhaust coupling piston rings, Corning BMAS-III gasifier inner backplate, and gasifier rotor
- 3 successful cycles to 60% N_1 and 899°C (1650°F) TIT
- 3 successful cycles to 80% N_1 and 1080°C (1976°F) TIT
- test plan successfully accomplished, engine removed from stand
- 12:18 hr total run time

S/N 1, BU23

- objective: engine test the first all-ceramic gasifier turbine package
- same ceramic components as S/N 1, BU22 with the addition of the ceramic scroll run in S/N 2, BU16
  - CBO SiC combustor assembly
  - Norton SiSiC gasifier scroll
  - CBO SiC gasifier outer backplate
  - Corning BMAS-III gasifier inner backplate
  - GTE AY6 Si_3N_4 gasifier vanes
  - third Kyocera SN220M Si_3N_4 gasifier rotor
  - Pure Carbon RB SiC interturbine coupling
  - 3M Nextel rope (piston ring) seals
- 3 successful cycles to 60% N_1 and 899°C (1650°F) TIT
- test plan successfully accomplished, engine removed from stand
- teardown revealed one broken cross-key slot on gasifier outer backplate
- 4:30 hr total run time

S/N 1, BU24

- objective: evaluate the all ceramic gasifier turbine in engine environment at 1204°C (2200°F) TIT
- same ceramic parts as S/N 1, BU23 except replaced inner backplate with Kyocera SN250 Si_3N_4 part
- successful cycle to 60% N_1 and 1149°C (2100°F) TIT
- turbine failure at 60% N_1 and 1010°C (1850°F) TIT during second cycle
  conclusion: combustor dome cracked, debris destroyed vanes and rotor and cracked another cross-key slot in the outer backplate
- 3:53 hr total run time

S/N 2, BU17

- objective: engine proof test new all-ceramic gasifier turbine static structure
- gasifier ceramic static components: Kyocera Si_3N_4 SN250 scroll, inner and outer backplate; GTE AY6 Si_3N_4 vanes; and Pure Carbon RB SiC interturbine coupling
- 3 successful cycles to 60% N_1 and 899°C (1650°F) TIT
- 3 successful cycles to 70% N_1 and 1080°C (1976°F) TIT
- during subsequent running at 95% N_1, combustor flashback occurred resulting in a shutdown

- ceramic combustor dome cracked
  conclusion: thermal growth through oversize fillets in metal mating parts responsible for failure
- 11:11 hr total run time

S/N 1, BU25

- objective: evaluate all ceramic gasifier turbine in engine environment at 1204°C (2200°F) TIT
- ceramic gasifier static structure transferred from S/N 2, BU17 and fourth Kyocera Si_3N_4 rotor (SN250M introduced)
- test facility induced emergency shutdown at 1166°C (2130°F) TIT and 72% N_1
- subsequent running yielded high vibration and whip at 45% N_1
- gasifier rotor cocked with respect to the shaft
- 6:13 hr total run time

S/N 2, BU18

- objective: engine proof test first ceramic power turbine static structures
- ceramic power turbine components: Kyocera Si_3N_4 scroll, inner and outer backplate; GTE AY6 Si_3N_4 vanes; Coors SiC power turbine exhaust coupling; and Pure Carbon RB SiC interturbine coupling
- 3 successful cycles to 60% N_1 and 899°C (1650°F) TIT
- 3 successful cycles to 70% N_1 and 1080°C (1976) TIT
- test plan successfully completed and engine removed from stand
- 4 power turbine vanes showed FPI indications
- 17:41 hr total run time

S/N 1, BU26

- objective: engine test first all ceramic hot section
- ceramic components: gasifier turbine parts from S/N 1, BU25 plus fifth Kyocera Si_3N_4 rotor (SN220), power turbine parts transferred from S/N 2, BU18 plus first Kyocera Si_3N_4 power turbine rotor (SN220)
- cycle No. 1: test facility shutdown while operating at 70% N_1 and N_2, and 1093°C (2000°F) TIT
- cycle No. 2: engine failure while increasing to 70% N_1 and N_2, and 1093°C (2000°F) TIT
- all ceramic components except combustor assembly and interturbine coupling were broken
- 6:01 hr total run time

S/N 2, BU19

- objective: engine test third CBO alpha-SiC gasifier turbine rotor (thickened airfoils)
- only gasifier turbine ceramic parts: CBO rotor and GTE AY6 Si_3N_4 inner backplate
- 3 successful cycles to 60% N_1 and 899°C (1650°F) TIT
- observed oil smoke from engine vent at 70% N_1 and 1080°C (1976°F) TIT
- oil leak between seal housing and No. 1 bearing support
- 5:11 hr total run time

V. GENERAL ENGINE DESIGN AND DEVELOPMENT

5.1 SUMMARY

Following initial concept studies and design reviews, an engine configuration was identified that had the potential of satisfying the powertrain system objectives. Hardware was subsequently procured to provide for the development testing of two complete test-bed engines. The following subsections provide summary details regarding the design and development of the nonceramic aspects of the AGT 100. More complete details are found in several of the general references at the end of this document. Sections II and III of this document address the ceramic components.

5.2 GEARBOX/POWER TRANSFER CLUTCH

Introduction

A gearbox was designed to satisfy all necessary gearbox functions as well as form part of the compressor air inlet flow path and incorporate the compressor discharge scroll. The gearbox was comprised of three aluminum castings: an inner gear case, an intermediate gear case, and a cover.

A power transfer clutch, enclosed within the gearbox, was developed and tested for transferring power from the gasifier turbine to the power (output shaft) turbine during low power requirement.

Objective

The gearbox had to perform the following four functions: (1) house gear trains to reduce the high power turbine speed down to that of a standard automotive transmission and increase starter speed up to the high gasifier turbine speed necessary during start; (2) provide drives for the accessories and oil pump; (3) serve as a main structural component of the engine; and (4) house the power transfer clutch.

Discussion

The gear train design layout is shown in Figure 216. A three-quart sump is provided at the bottom to supply the single element lube pump. Sixteen gears are arranged to interconnect the components and services shown in Table LIII.

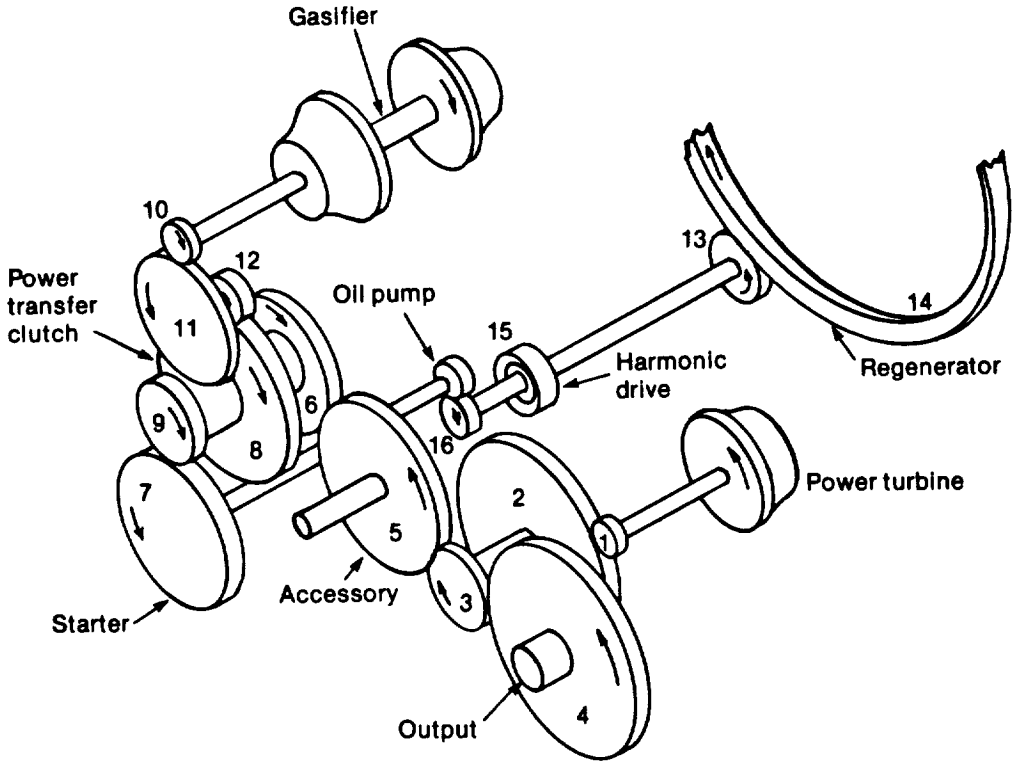

Figure 216. AGT 100 gear train.

Table LIII.
Engine design speed of AGT 100 gearbox components.

Components	Engine design speed (100% rpm)
Gasifier turbine rotor	86,256
Power turbine rotor	68,156
Engine output shaft	3,061
Power transfer clutch	5,636
Regenerator disk	22.5
Starter	3,074
Vehicle accessory drive	4,552
Lube pump	3,074
High-pressure fuel pump	3,074

The power transfer unit permits the engine to operate at a higher maximum cycle temperature even at low power conditions by providing a means for excess gasifier turbine power to be mechanically coupled through a slipping clutch to the output gear train. This results in reduced fuel consumption.

The clutch is located between gears 6 and 8 (see Figure 216). A hydraulically controlled disk design, the clutch turns at a maximum speed of 5636 rpm. Cooling oil is scheduled as a function of control oil pressure so that parasitic losses resulting from clutch pumping are reduced during periods when heat rejection is low. A balance piston is incorporated into the design to eliminate speed sensitivity. A complete description of the power transfer clutch is reported in Ref 1, p 214–16.

5.3 BEARINGS AND SEALS

Introduction

Rolling element bearings were selected for the AGT 100 engine primarily to minimize radial and axial running clearances, thereby obtaining the highest possible performance. Air-buffered carbon seals were chosen for critical, high temperature sealing locations in the gasifier and power turbine rotor system.

Objective

The objective of this program was to select commercially available bearings and seals that would meet and survive the rigid condition of a small automotive gas turbine.

*DN = bearing bore diameter in millimeters × speed in rpm × 10^{-6}

Discussion

The 20 rolling element bearings in the engine are located as shown in the AGT 100 bearing schematic (see Figure 217). Bearings 1–5 are the high-speed mainshaft bearings and are considered the critical bearings in the engine. Bearings 1 and 4 are common AFBMA class 5 quality, made from M50 tool steel to accommodate the soak-back temperatures of engine shutdown. The other bearings, 2, 3, and 5, are also class 5 quality, but are made from SAE 52100 steel. The highest DN* value of 2.15 occurs at the No. 1 position. This is consistent with Allison experience on the industrial gas turbine (IGT) commercial engine program and has been demonstrated for positions 1 and 2 on the compressor test rig. For a complete analysis see Ref 5, pp 79–81.

5.4 INSULATION

Introduction

Allison successfully tested various insulation schemes in the AGT 100 engine and static rigs. Although not engine tested by program conclusion, a moldable insulation scheme demonstrated significantly improved effectiveness during rig testing compared with the lower conductivity multipiece insulation methods used in all engine tests. The moldable insulation also showed no loss of material integrity and is potentially the leading engine insulation candidate.

Objective

Insulation is necessary in the AGT 100 gas turbine engine for two reasons. First, it protects engine components and parts from excessive heat, which would prevent their functioning as designed. Second, it inhibits heat loss to the outside environment, thus maximizing the engine's overall thermal efficiency.

Discussion

The estimated heat rejection (expressed as percent of fuel input energy) of the original multipiece insulation system is shown in Figure 218. Two combinations of insulating materials are shown with essentially the same characteristic. The physical properties of the insulation material are presented in Ref 5, pp 77–78.

The original design used the best insulation that could be found for low conductivity. To locate the optimum insulation in various parts of the engine, and to permit assembly, many individual

1	Gasifier turbine bearing
2	Compressor front bearing
3	Pinion bearing
4,5	Power turbine bearing
6,7,14,15	Idler shaft bearing
8,9,10,11	Clutch bearing
12,13	Accessory shaft bearing
16,17	Output shaft bearing
18,19,20	Regenerator drive shaft bearing

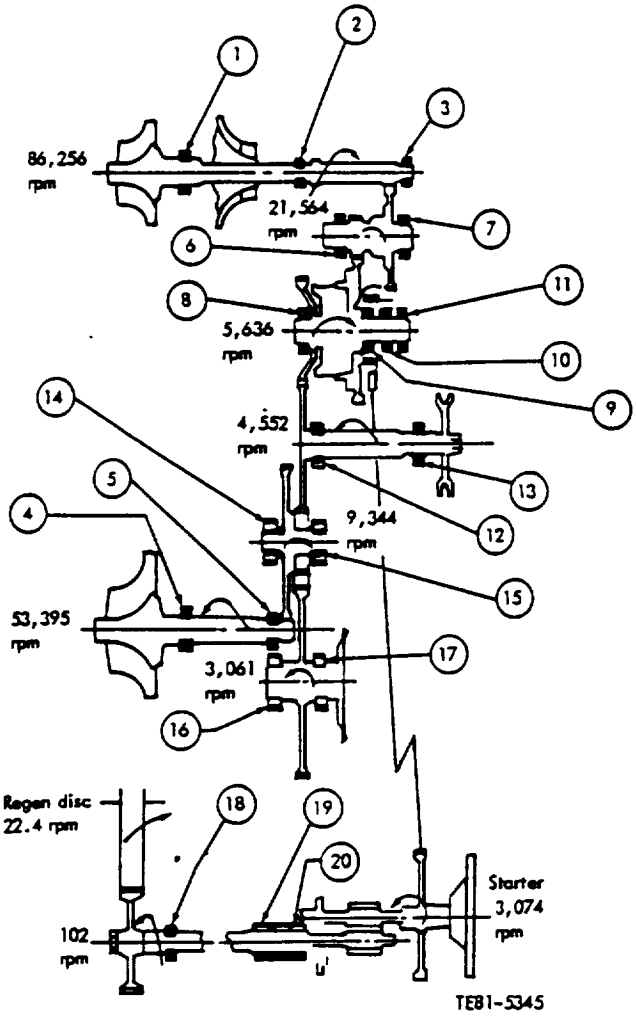

Figure 217. *Bearing schematic.*

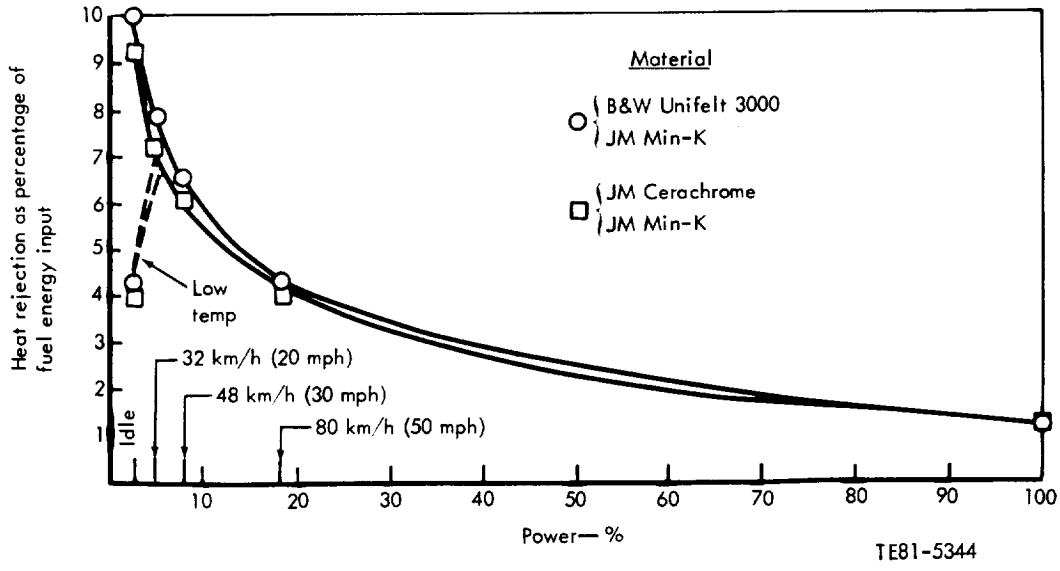

Figure 218. *Calculated heat rejection.*

pieces were designed to fit snugly together. Two problems were revealed during the early testing: (1) the pieces did not fit snugly as designed and (2) the insulation lost its strength and integrity during running and allowed considerable amounts of material to be loose in the engine. The first problem resulted in much larger heat loss than expected (and as a result, much higher metal temperatures than desired). The second problem resulted in large pieces of insulation going through the turbines, which the ceramic parts could not tolerate. This second problem was approached through the use of metal foil encapsulation. This solution has helped the loose insulation problem, but has worsened the heat loss (effectiveness) through the insulation by increasing the gaps between pieces.

As higher temperatures were achieved in the engine, the insulation problem became even more critical. A new look was taken at the overall insulation needs and approaches that might be taken to improve the insulation performance within the engine.

One of the most promising materials is a moldable, alumina based, insulation developed by Manville for/with GM Engineering Staff. This insulation is not yet commercially available and is identified only as "Formula 5907-126-N." Permission by Manville to supply and work with Allison in evaluating this material was obtained from the Engineering Staff.

This moldable insulation was applied to the inside of the outer combustion case of the thermal shock rig. The thermal shock rig was then assembled in the usual manner without any of the original engine insulation.

The material was completely intact at the end of the testing. The wall and dome were still protected by continuous insulation with no cracks or voids. No loss of material integrity was indicated.

Surfaces in the areas of the higher air velocities were inspected for erosion but none was found. Variation in the thickness of the hardener coat was obvious because of coloration differences—but no erosion was seen in any area.

Of primary importance in this test was the insulation's effectiveness. The original insulation was extremely low in conductivity but lost greatly in effectiveness because of many large gaps between the 11 pieces that were used within the outer combustion case. These gaps became even more severe when the insulation had to be encapsulated in metal foil to prevent flaking.

The conductivity of the new (moldable) insulation is not as good as the old, but since it is a single piece with no gaps, joints, etc, its effectiveness is much greater.

Table LIV compares the three outer skin temperatures as measured during BU8 and BU9 while operating at a BOT of 1093°C (2000°F).

Figure 219 shows the old encapsulated insulation in the engine. Figure 220 shows the new moldable insulation.

Table LIV.
Thermal shock rig temperature comparison—BU8 and BU9.

	BU8 (old)—°F	BU9 (new)—°F
Burner inlet temperature	1378	1344
Burner outlet temperature	2001	2004
Skin 1	945	648
2	766	422
3	807	603

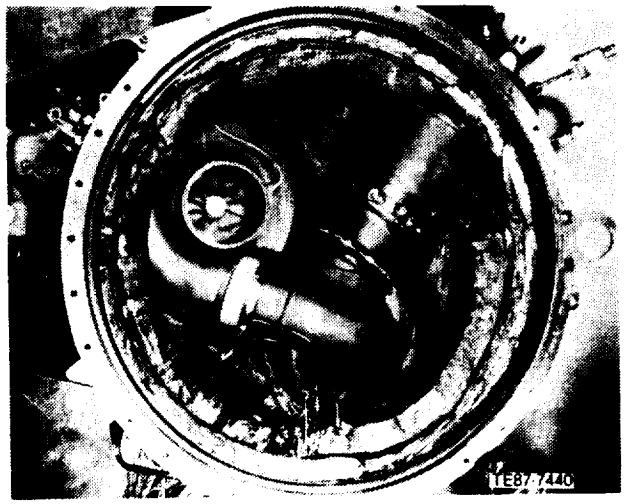

Figure 219. *AGT 100 encapsulated insulation.*

Figure 220. *AGT 100 moldable insulation.*

5.5 OIL SYSTEM

Introduction

An oil system capable of satisfying operational requirements was designed and engine tested, including oil pressure actuated clutch demonstration.

Objective

The objective of the oil system design was to provide a regulated oil supply for lubrication and cooling of the individual bearings and gears within the engine and a modulated oil pressure for the power transfer clutch.

Discussion

The oil system, as designed, is shown in Figure 221. The regulator valve is an integral part of the pump body and the pressure is controlled by a preselected regulator spring. The oil filter and bypass is an engine mounted standard automotive filter with built in bypass.

The clutch valve body modulates the oil pressure and flow to the power transfer clutch for operation as well as cooling. This modulation is controlled by the engine digital controller. All bearing oil flows are controlled by a fixed orifice at the bearing.

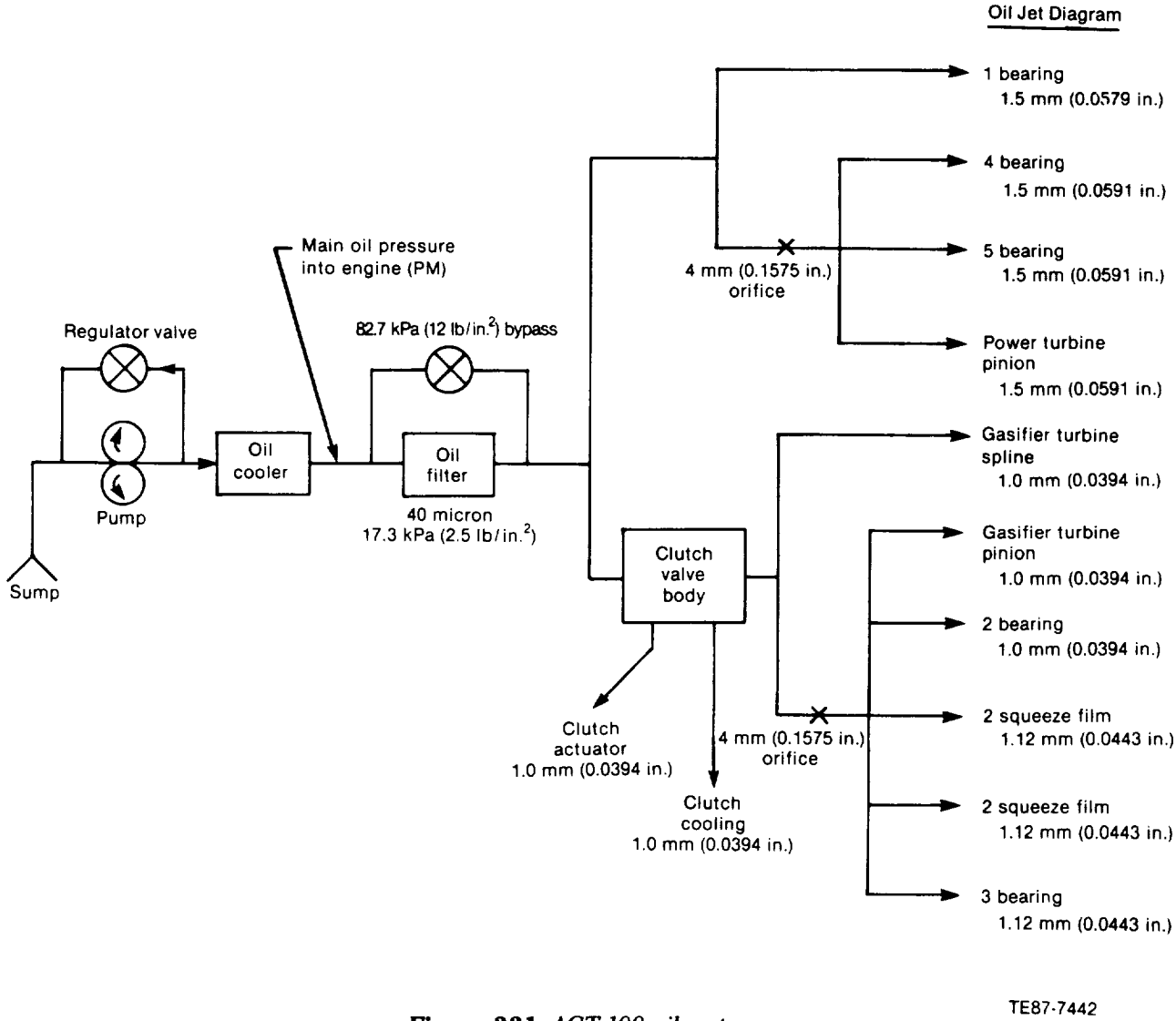

Figure 221. AGT 100 oil system.

5.6 CONTROLS

Introduction

A digital electronics control was designed, fabricated, and successfully used for the operation of the AGT 100 engine on the test stand. This employed the GMCM digital chip set used in Delco Electronics controllers.

Objective

The objective of the AGT 100 Control System is (1) to manage the fuel system for engine speed control, (2) to manage variable geometry for emission control, (3) to manage variable geometry for inlet guide vane control, (4) to manage power transfer clutch for engine operating temperature and power control, (5) to provide for engine protection either by modulating fuel flow or complete shutdown, and (6) to contain self-analysis capabilities for fault isolation within the control system.

Discussion

The electronic control unit (ECU) used for the AGT 100 engine testing is a modified digital control unit from another program. Figure 222 shows the overall system schematic, including the ECU, an operator control console, and required engine connections.

This control console allows manual open loop control of gasifier speed, inlet guide vanes, and power transfer clutch. Switches, lights, and meters are also provided to monitor the engine performance and to allow the control console operator to manipulate various engine conditions. Fuel flow and

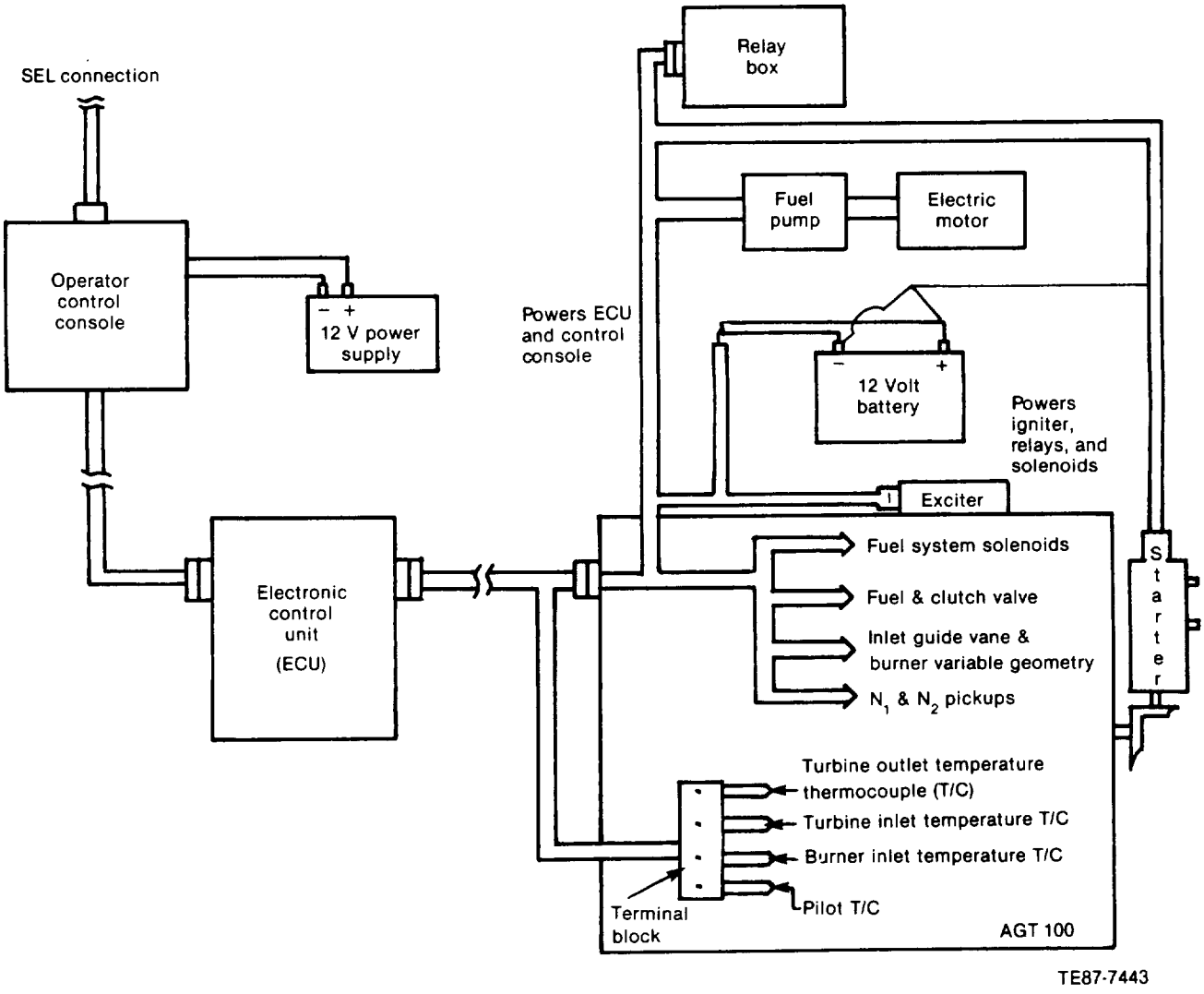

Figure 222. *Overall system schematic.*

burner variable geometry (BVG) position are the only engine parameters that use closed loop control, where the amount of fuel flow and the BVG position are determined by the ECU software program and not manually set by an operator.

The control software is set up to be particularly cautious and protective of the engine while giving maximum flexibility to the control console operator. For a complete analysis of the control system see Ref 1, pp 236–48.

5.7 VEHICLE SYSTEM DEVELOPMENT

Introduction

A GM front-wheel-drive automatic transaxle was selected for use with the AGT 100. The installation drawing, cost, and producibility studies were all coordinated with Pontiac Motor Division (PMD) of GM to take advantage of their expertise in these areas. Due to an early change in program emphasis, work in this area was terminated before task completion.

Objective

The objective of this part of the program was to select a transmission that would match the characteristics of the AGT 100 to obtain the best fuel economy and vehicle performance. Other objectives included determination of engine/vehicle interface, cost, and engine producibility using known manufacturing techniques.

Discussion

The transmission includes a three-element torque converter with torque converter clutch mounted on the engine output centerline. Application of the torque converter clutch provides a direct mechanical drive from input to output. Also mounted on the transmission input centerline is an engine-driven variable displacement pump and a turbine-driven chain drive sprocket. By means of the chain drive, power is transferred to a four-speed range gear set mounted concentric with the output centerline. Full power from the range gear set flows through the sun gear of a single planetary final drive reduction gear and into a concentric differential from which the power is split to the right and left output wheel drive couplings. Unique to the front-wheel-drive transmissions is that the differential and final drive gears are located within the transmission. The two-planetary gear and clutch arrangement provides four speeds forward and one speed reverse (Ref 1, p 249).

Changes early in the program precluded actual transmission and vehicle installation and testing. Producibility studies were also terminated early in the program; however, some materials specifications were determined by these studies.

5.8 REFERENCE POWERTRAIN DESIGN

Introduction

The RPD was a preliminary engineering design of the powertrain system that had the best potential for meeting the goals and objectives of the project. The RPD was to incorporate timely emerging technologies and be updated as project activities progressed.

Objective

The objective of this part of the program was to establish and maintain an RPD as a continuing activity as well as component development effort. Two experimental powertrain versions were to be designed, fabricated, and tested. Mod I, the first, was a stepping stone to Mod II, the final project version consisting of all hot gas path ceramic parts.

Discussion

Prior to this contract, Allison and PMD conducted a gas turbine powertrain concept study (contract DEN3-28). In July 1979 Allison published the results of the concept study (Ref 10). In this study, several configurations were evaluated and a two-shaft regenerative engine, coupled with a conventional automatic transmission, was recommended as providing the potential for meeting the established goals (Ref 10 and 11).

The AGT 100, shown in Figure 124, is thus a two-shaft, regenerative gas turbine engine. In all respects, this engine design is tailored for high-volume application to fuel-efficient passenger cars. Its two-shaft configuration allows the use of conventional manual or automatic transmissions and maximum turbine tip speed (approximately 503 m/s [1650 ft/sec]) commensurate with available ceramic material properties (strength and variability). Careful attention was given to component arrangement for both vehicle installation and management of potentially high heat losses. All hot-section components are grouped together, bound on one end by the regenerator, on the other end by the gearbox, and enclosed by a well-insulated cylindrical case. High-cycle temperature is possible through the use of ceramic hot-section parts, including the combustor (three separate parts), the static structure for

each radial turbine (scroll, inner backplate, outer backplate, vanes), the radial turbine wheels, flowpath couplings (two parts), coupling piston rings (two each coupling), regenerator seal platform/bulkhead, and regenerator disk. This high-cycle temperature capability, coupled with high aerodynamic component efficiencies, produces low fuel consumption and a 30% energy efficiency improvement over a comparable spark ignition powered vehicle.

The general arrangement of the initial RPD design was covered in Ref 1, p 11. However, results of a design review indicated some areas of concern with this configuration. These were cost, weight, heat losses, and bearing DN number. The rearrangement of the engine was covered in Ref 12, p 7.

5.9 AERODYNAMICS

Combustor

Introduction

Allison has designed and tested a variable geometry combustor system capable of operating on multiple fuels and meeting federal Environmental Protection Agency (EPA) emission standards.

Objective

The combustor must control the mixing of the fuel and air to obtain maximum combustion efficiency at minimum pressure drop and to control the emissions generated within the engine so that the power plant meets the following standards: nitrous oxide (NO_x) = 0.4 g/mile, hydrocarbon (HC) = 0.41 g/mile, carbon monoxide (CO) = 3.4 g/mile, and a total particulate level of 0.2 g/mile using diesel No. 2 fuel. The combustor must also have the ability to use alternate fuels.

Discussion

Combustor Design—The design of the combustor for the AGT 100 RPD closely followed the design of previous AGT low-emission combustors. The fuel and a portion of the inlet air are combined in a swirling mixture within a prechamber. The fuel is vaporized within the prechamber because of the high temperature of the prechamber walls and the inlet air. When the fuel and air leave the prechamber, they enter the main burning zone highly premixed and prevaporized.

To keep the exhaust emissions below a specified level, the burning zone temperature must be carefully controlled to stay within narrow limits. This control is accomplished by adjusting the division of primary and dilution zone air through the use of variable geometry. A complete report on the combustion system was reported in Ref 1, pp 171–90 and Ref 5, pp 55–61.

Alternate Fuel Demonstration—An engine was operated on methanol to further demonstrate alternate fuel capability (Ref 4). Results of this test indicate that the AGT 100 combustion system is quite capable of methanol fuel operation. The start and main nozzles were easily ignited, and main nozzle operation succeeded without lean blowout or rich flashback problems. Chemical sampling revealed that main nozzle emissions on methanol were an order of magnitude below those on diesel and jet fuels, which were in turn significantly below those typical of diffusion flame combustors. Figure 223 presents emission data on this combustion system. Successful operation was demonstrated on DF-2, JP-5, and methanol. These results show the potential for an ultra-low emissions automotive gas turbine engine operating on methanol.

Compressor

Introduction

Extensive compressor rig testing was conducted to develop and verify compressor performance. Several design variations of both the static and rotating components were run. Significant progress was demonstrated in improving the performance of the redesigned engine's compressor, pri-

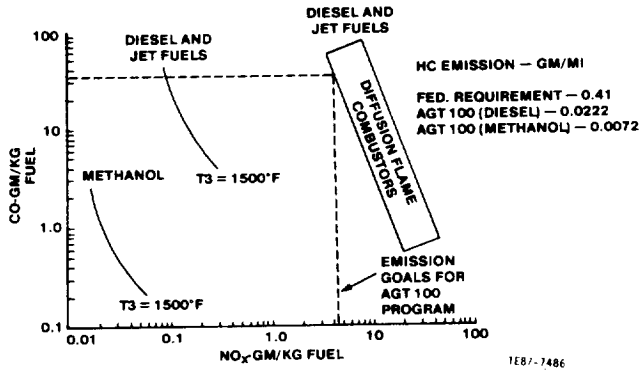

Figure 223. AGT 100 combustion system emission performance.

marily due to impeller blading design modifications and a shroud material change. These improvements came in a stepwise manner consisting of thinning the baseline impeller blades, revising the design to the Type IA compressor, replacing an aluminum shroud with steel, and finally revising the design to the Type II compressor configuration.

Objective

The objective of the compressor aerodynamic effort was to design, develop, and demonstrate a compressor capable of meeting the established component goals for airflow rate, pressure ratio, and efficiency over the operating speed range of the engine. These goals were established from design studies aimed at satisfying overall driving cycle efficiency goals as well as relatively high power requirements for suitable driveability and high altitude operation of the targeted vehicle, even though most operation was to be at relatively low power settings. The efficiency goals of the AGT 100 compressor were judged to be quite aggressive, based on a review of the state of the art. The goal operating points are summarized in Table LV.

Discussion

A single-stage centrifugal compressor was selected for the AGT 100 engine. The initial impeller design had 16 full blades, 16 splitters, and 50° of backsweep. Minimization of the inducer tip relative Mach number, meeting the minimum hub radius constraint required to satisfy rotor critical speeds, and other aerodynamic considerations led to the selection of design point specific flow of 143 kg/(sec m^2) (29.3 lbm/[sec ft^2]) and an inducer hub/tip radius ratio of 0.45.

The impeller internal design parameters were assessed using a computer program that provides for an axisymmetric radial equilibrium flow solution, including the effects of enthalpy and entropy gradients. The flow path shape, blading angles, and blading thicknesses were iteratively adjusted to alter diffusion rates, loading distributions, and stress levels.

Blade elements and blade normal thicknesses were linear between equal meridional locations on the hub and shroud. The hub inducer suction surface diffusion was limited to 45 m/s (148 ft/sec). The shroud exhibited essentially linear diffusion from inlet to exit. At design point the impeller choke flow margin was 5.3%. The impeller was set to this relatively small choke margin to enhance low speed performance.

The original diffuser had 21 wedge-shaped vanes and employed a vaneless space length equal to 8% of the impeller exit radius. The flow path through the diffuser vane had a constant axial dimension with 8.5 deg divergence between vane walls achieving a 4.04:1 diffuser area ratio.

A collector (scroll) was required around the diffuser to gather the compressed air for transfer to

Table LV.
AGT 100 compressor operating points.

	Idle	48 km/h (30 mph)	80 km/h (50 mph)	Design point, standard day, max power
Equivalent flow, $W/\sqrt{\Theta}/\delta$, kg/s (lbm/sec)	0.105 (0.231)	0.107 (0.235)	0.134 (0.295)	0.347 (0.764)
Equivalent speed, $N/\sqrt{\Theta}$, rad/s (rpm)	4405 (42065)	4405 (42065)	5290 (50513)	9027 (86200)
Equivalent speed, percent of design	48.8	48.8	58.6	100
Pressure ratio total/static	1.41:1	1.54:1	1.84:1	4.5:1
Efficiency goal, $\%\eta_{T-S}$	74.9	80.1	81.6	82.8
Inlet guide vane induced preswirl, deg from axial	60	0	0	0

the single entry port regenerator. The collector was designed to maintain a circumferentially constant static pressure at design point with low exit velocity to minimize losses in the ducting to the regenerator.

To meet the established performance goals, efficiency loss with reduced speed had to be minimized. Variable inlet guide vanes (IGVs) were included to enhance low power efficiency goals. Cycle simulations indicated that the vanes improved steady-state fuel economy below 48 km/h (30 mph).

A compressor rig was designed for development and verification testing. The initial rig design used engine compressor parts extensively. A full complement of instrumentation was included, with design and location based on previous test experience.

Five rig builds and tests were accomplished prior to the first engine build. The first rig build's primary goal was to determine operational characteristics of the rig and impeller-to-shroud running clearances. The compressor was mapped through 100% corrected speed without any significant problems on the first build. During the first five builds, various design components were tested. These included bifurcated radial and nonsymmetric axial inlet ducts, different IGV designs, various blade thickness impellers, and various diffuser throat areas. Performance data after rig stabilization was found to be affected by rig insulation layers and rear bearing oil temperature. Modifications were made to address the situation.

Airflow, pressure ratio, efficiency, and surge margin were determined at various speeds on the five builds. Data review indicated problem areas were limited to impeller performance. Analysis indicated blade thickness reduction was needed to reduce inducer choking effects. Following this modification, corrected flow and pressure ratio exceeded design point values, but indicated efficiency was below design point.

After these first five builds, aerodynamic development was directed toward the design of two compressor configurations (designated Type 1A and 1B) for evaluation of impeller passage diffusion effects. Both designs featured flow path changes to alleviate a potential "tight" knee region and thinner airfoils. Also, design studies for evaluation of alternate compressor configurations, including design point prewhirl and reduced inducer blading, were conducted. Prior to rig testing of these compressor configurations, the compressor rig underwent an extensive redesign for the following reasons: (1) a major redesign of the engine occurred after the original rig was designed, (2) discrepancies between the redesigned engine and the original rig performance data using the same impeller were noted, and (3) a need to minimize heat transfer effects for accurate performance assessment was identified. The redesigned rig used engine design compressor components, was heavily insulated, and moved the rear bearing farther away from the impeller to reduce performance sensitivity to oil temperature. A feature allowing axial clearance to be adjusted was also added. Subsequent rig tests demonstrated that the redesigned rig successfully addressed the issue of eliminating the heat transfer effects of the rear bearing oil temperature and ambient air on indicated efficiency. Testing of the baseline engine compressor hardware on the redesigned rig yielded data agreeing with previous engine test data; flow and indicated efficiency were down while surge margin and range were up compared with original rig testing of the same baseline impeller. The Type 1A compressor configuration was then tested. Comparison with the baseline configuration showed a significant increase in flow, pressure ratio, and efficiency at high speed, with little difference at part speed; however, the design goal was not met.

Since the combined effect of reduced diffusion and thinner blades proved favorable, a further modification of the Type 1A impeller was devised to investigate the effects of impeller blade friction. The splitter blades and every other full blade were cut back to reduce impeller blading, thereby reducing blade friction while increasing blade loading. Rig testing revealed increased high speed flow with decreased efficiency at all speeds. Thus, losses incurred by increased blade loading outweighed gains due to reduced blade friction. The modified Type 1A compressor was also tested at 50%, 70%, and 80% corrected speed to investigate the effects of clearance and variable IGV settings. Closing down axial clearance by 0.010 cm (0.004 in.) and closing the IGVs to 40 deg to introduce prewhirl both resulted in substantial performance improvement: 2% at both 50% and 70% corrected speed and 1.3% at 80% corrected speed, respectively.

A comprehensive analysis of all data obtained on the AGT 100 compressors was undertaken to determine modifications required to improve performance. Two key modifications were identified: (1) isolating the impeller from undesirable heat recirculation through the diffuser and shroud and (2) employing new design concepts addressing small size compressors. The static structure metal temperatures in the original rig were significantly lower at high speed than the corresponding temperatures in the redesigned rig. This was attributed to the

difference in thermal conductivity of the static structure materials: steel in the original rig and aluminum in the redesigned engine and rig. A design modification was made to replace the redesign rig's aluminum shroud and diffuser wall with a low conductivity steel shroud insert. A new impeller (Type II) was designed to better control blade loading, choke flow characteristics, and inducer incidences, the driving force behind the redesign being to gain high speed performance. Primary differences were in blade thickness and angle definition, leading edge sweep, and reduced number of blades. The peak efficiency estimation for the new Type II design with a steel shroud was 80.5% at full speed, compared to a measured 75% for the Type 1A design with an aluminum shroud. The predicted gain was based on previous test experience, as well as intuition regarding the advantage of the revised blading techniques.

Initial testing of the steel shroud insert was done with the Type 1A impeller. The steel shroud provided a substantial (2.5% to 3.5%) efficiency gain and up to 3.7% choke flow gain across the entire compressor map up to 90% N_1, the highest speed reached. This finding confirmed the suspected need to reduce heat circulation for improved performance.

The steel shroud insert and Type II compressor were tested together next. Problems were encountered obtaining desired clearances due to an apparent shroud-to-impeller cocking and/or translating condition. Resulting average clearances were consequently set greater than desired to prevent impeller rub. Nevertheless, its performance was essentially the same as that of the Type 1A compressor with steel shroud up to 90% N_1, the highest speed reached. Based on clearance sensitivity studies performed earlier, the Type II compressor with steel shroud is estimated to have as much as 2% more efficiency than any other AGT 100 series compressor when running at the desired clearance values.

Turbine

Introduction

Gasifier and power turbine aerodynamic designs that took several factors into account were defined. Emphasis was placed on high efficiency over a broad operating speed range for both turbines.

Initial rig testing of the power turbine demonstrated that it effectively met or exceeded RPD goals without the need to expend development effort. While the initial gasifier turbine rig tests were not quite as successful, they were encouraging. Initial rig test goals were exceeded and RPD goals were nearly met. The cause of the deficiency was limited to the gasifier vanes, and a vane design modification improving efficiency was identified.

Objective

The objective of the turbine aerodynamic effort was to design, develop, and demonstrate gasifier and power turbines capable of meeting the established component goals for power and high efficiency over their respective broad operating speed ranges. Meeting the high efficiency goals for the turbines was challenging because of the turbine's small size, ceramic construction, and relatively low Reynolds number. The aerodynamic designs for achievement of the component goals had to be consistent with stress, heat transfer, vibration, mechanical design requirements including low inertia for rapid transient response and adequate clearance to prevent rub, and low cost for automotive market competitiveness.

Initial RPD parameters for various engine operating points for the gasifier turbine and power turbine are summarized in Tables LVI and LVII, respectively.

Discussion

Single-stage radial inflow turbines were selected for both the gasifier and power turbines in the AGT 100 engine. Each turbine had a scroll to evenly distribute the flow path gases through 360 deg around the rotor inlet from a single delivery point. Evenly spaced vanes directed the gases from the scrolls into the rotors. An interturbine duct directed the gases from the gasifier exit to the power turbine scroll inlet. Likewise, an exhaust duct delivered the gases from the power turbine exit to the regenerator inlet. Design emphasis was on high efficiency, low inertia, low rotor exit Mach number, and low cost.

Although the turbines operated at the maximum power point only a small fraction of the time, this point represented the most severe steady-state structural design condition. The maximum power condition, therefore, was selected as the design point to ensure a systematic integration of fabrication, aerodynamic, heat transfer, stress, and vibration design disciplines.

Several factors were involved in the selection of "optimum" flow path parameters. First was the realization that part power was emphasized at the

Table LVI.
Reference powertrain design gasifier turbine parameters for various engine operating points.

Speed, km/h (mph)	Idle	32 (20)	48 (30)	80 (50)	102 (70)	Maximum power*	Maximum power sea level**
Turbine power—kW (hp)	5.03 (6.74)	6.04 (8.10)	6.99 (9.37)	14.50 (19.45)	26.53 (35.58)	64.49 (86.48)	71.35 (95.68)
Inlet temperature—°C (°F)	683 (1261)	982 (1799)	1172 (2142)	1266 (2238)	1241 (2265)	1288 (2350)	1288 (2350)
Equivalent flow—kg/s (lbm/sec)	0.128 (0.282)	0.136 (0.299)	0.141 (0.309)	0.162 (0.357)	0.172 (0.377)	0.176 (0.387)	0.178 (0.391)
Equivalent work—kJ/kg (Btu/lbm)	16.40 (7.05)	15.79 (6.79)	16.00 (6.88)	23.24 (9.99)	30.49 (13.11)	39.80 (17.11)	42.08 (18.09)
Equivalent speed—%	63.5	54.4	51.9	62.2	75.8	100.00	100.00
Expansion ratio (total-to-total)	1.262	1.252	1.259	1.407	1.560	1.847	1.873

*Ambient temperature: 29°C (85°F), altitude: 152 m (500 ft)
**Ambient temperature: 15°C (59°F), altitude: sea level

Table LVII.
RPD power turbine parameters for various engine operating points.

Speed, km/h (mph)	Idle	32 (20)	48 (30)	80 (50)	102 (70)	Max power*	Max power (SL)**
Turbine power—kW (hp)	1.48 (1.98)	2.56 (3.44)	4.30 (5.76)	9.31 (12.49)	21.10 (28.30)	64.98 (87.14)	74.09 (99.36)
Inlet temperature—°C (°F)	634 (1174)	979 (1795)	1106 (2022)	1128 (2062)	1113 (2035)	1113 (2035)	1109 (2028)
Equivalent flow—kg/s (lbm/sec)	0.159 (0.350)	0.168 (0.369)	0.175 (0.385)	0.224 (0.493)	0.261 (0.574)	0.314 (0.691)	0.322 (0.707)
Equivalent work—kJ/kg (Btu/lbm)	5.07 (2.18)	70.2 (3.02)	10.30 (4.43)	15.96 (6.86)	26.45 (11.37)	46.87 (20.15)	49.24 (21.17)
Equivalent speed—%	24.5	32.8	47.0	53.0	74.6	99.9	100.0
Expansion ratio (total-to-total)	1.075	1.099	1.149	1.237	1.441	1.990	2.064

*Ambient temperature: 29°C (85°F), altitude: 152 m (500 ft)
**Ambient temperature: 15°C (59°F), altitude: sea level.

expense of full power performance. However, caution was exercised to avoid any severe efficiency reduction at maximum power, resulting in unacceptable vehicle response. A second major factor was the selection of aerodynamic and geometric parameters consistent with structural design for fabricability, long life, and low cost. This second factor became particularly important with respect to achieving adequate life of the ceramic wheel. A third important consideration in design related to selection of flow path parameters that are conducive to low inertia.

RPD and Mod I (reference Section 5.8) flow paths were designed for both turbines. Since interchangeability of metallic and ceramic hardware was an important design factor, consideration was given to supplying Mod I designs that would provide maximum compatibility with their respective RPD turbine with minimum aerodynamic penalty. However, because of differing cycle conditions between Mod I and RPD, exact duplication of the RPD flow paths was not possible.

The initial RPD and Mod I flow paths for both turbines featured symmetrical vanes with endwall contouring and low inertia rotors. Ducts were designed with emphasis on minimizing losses. The flow path selections were verified through sensitivity studies of critical design parameters including specific speed, tip diameter, vane exit angle, exducer hub/tip radius ratio, and exducer area.

Turbine test rigs were operated to develop and verify performance for both the gasifier and power turbine. The test rigs were thoroughly instrumented for interstage and overall performance measurements. Rig design emphasis was placed on duplicating the critical engine turbine flow path geometry. The rig hardware flow path geometry was identical to the hot RPD engine turbine aerodynamic definition.

The first power turbine rig test results were excellent. Data analysis showed the power turbine performance was close to RPD design expectations over a broad operating range. Measured efficiencies exceeded RPD goals, with the greatest excess at the maximum power point. Generally good agreement was found between design and test for flow, exit swirl, and Mach number throughout the operating range. Since the power turbine effectively achieved RPD goals, no RPD development effort followed. The rig data were used to modify the Allison radial turbine performance computer code to provide a close match on flow rate, work, and efficiency. The modified program was then used to specify vane width and estimate performance for engine builds.

To achieve higher output shaft power for the power turbine during reduced maximum temperature engine testing, an alternate power turbine design was pursued. The turbine flow capacity at maximum power was originally selected for 68,000 rpm conditions, consistent with the RPD engine. Consequently, the power turbine was not speed matched to the gasifier turbine for the reduced temperature testing of the engine. This accounted for an efficiency reduction of approximately 15%. The alternate design involved rematching the turbine by reducing its speed and adjusting the turbine flow capacity with a vane width reduction. Actual flow and expansion ratio goal magnitudes were selected to match maximum power operation as interpreted from S/N 1 BU8 data, with increased power resulting from increased efficiency.

Initial gasifier turbine rig test results exceeded initial build goals but fell short of RPD goals. Achievement of RPD goals required an efficiency improvement of 1.5% at maximum power and 1.8% at 48 km/h (30 mph). Specific areas for improvement of the gasifier turbine were identified using experimental data to assess losses at various stations through the turbine. The study resulted in a loss breakdown structure showing the vane to be deficient, while the rotor and scroll performed quite satisfactorily. As was the case for the power turbine, the Allison radial turbine performance computer code was modified to match rig data, and then used to specify vane width and estimate performance for engine builds.

Compared with the power turbine vane, the gasifier turbine vane had more trailing edge blockage, less width, and greater downstream turning, all of which contributed to greater losses. A new gasifier turbine vane was proposed to improve performance by as much as 1.5%. It was nonsymmetrical (cambered) for less downstream turning and had reduced trailing edge diameter and increased vane width while requiring fewer vanes. Rig testing with the new vane, along with rotor and vane endwall clearance studies, was planned. Scroll, outer backplate, and vane hardware was procured, but rig testing was not carried out before program completion.

5.10 ROTORDYNAMICS

Introduction

During the AGT 100 program, effort was expended on rotordynamics of the gasifier rotor

assembly. The effort included analytical studies, detailed hardware balance programs with increasing degrees of refinement, operation of a special rig to study the gasifier's characteristics, and consultation with outside sources specializing in balancing and rotordynamics.

While two early engine builds with metal turbine rotors successfully attained 100% speed and another, more recent one appeared to be capable based on rotor shaft vibration (whip) data up to near 95% speed, several other builds were speed limited by whip levels encountered. The last six builds incorporating ceramic turbine rotors were not limited in speed by whip over the speed ranges tested, and they demonstrated low whip levels up to as much as 85% speed. They represented the entire group of ceramic rotor builds to be balanced with the most recent balance techniques.

The engine rotordynamics did not significantly affect ceramic component development, the central focus of the AGT 100 program. The speeds associated with desired thermal conditions could be routinely reached with either metal or ceramic turbine rotor gasifier assemblies.

Objective

The objective of the rotordynamics effort was to obtain a gasifier assembly configuration capable of 1) routinely reaching 100% speed after initial balancing and 2) providing for balance stability throughout its useful life in a vehicular application. These objectives were to be met without exceeding established steady-state and transient vibration limits while simultaneously meeting all other design requirements such as acceleration time, airflow rate, fatigue life, overspeed burst margin, component efficiency, and bearing and seal performance and life.

Discussion

The rotordynamics effort on the AGT 100 gasifier assembly (Ref Figure 224) consisted of a combination of analytical studies and physical hardware experience. The effort was initiated by analytically predicting resonant response frequencies and modes of the proposed gasifier assembly at which relatively high response amplitudes occur. These high responses are manifested as vibration. Since excessive vibration can have undesirable consequences such as reduced bearing life, reduced fatigue lives, and increased clearance requirements to prevent

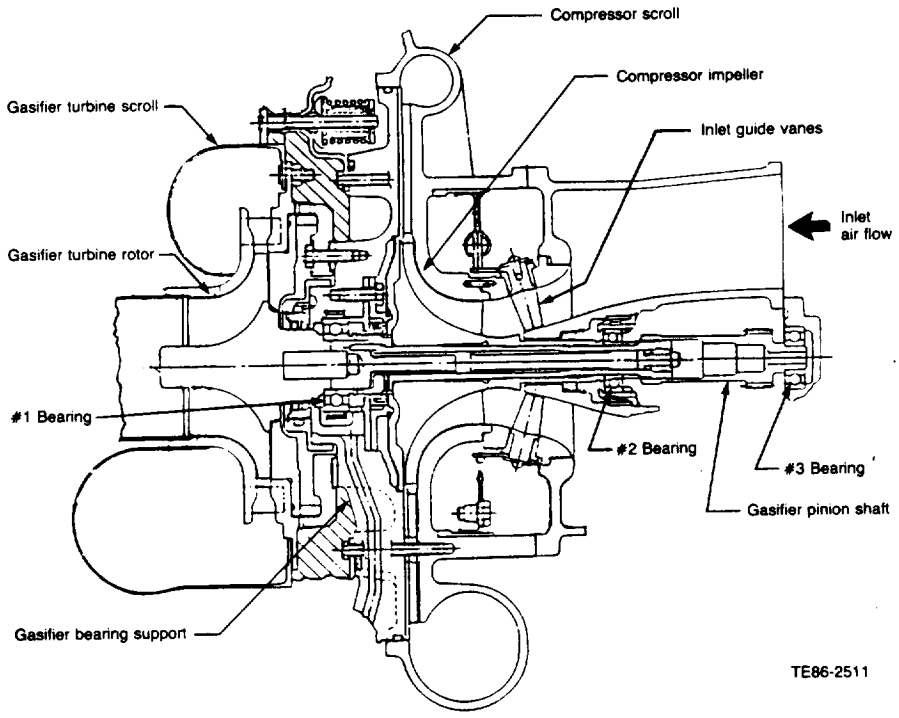

Figure 224. *Gasifier engine section.*

rub, it is desirable to remove response frequencies from the normal operating speed range of the rotor system. The response frequencies are a function of mass, stiffness, damping, and geometry of the rotor assembly and support structure (rotor system). Computer programs have been developed for predicting rotor response frequencies, and can include effects such as gyroscopic stiffening, interaction between imbalance and deflection, phase angle changes, and interface uncoupling. They have also proven to be effective for predicting response modes to verify designs and modifications prior to hardware procurement. Both beam and axisymmetric finite element models of the AGT 100 gasifier assembly were analyzed. The baseline support structure had spring rates of 10.5 MN/m (60,000 lb/in.) and 7.0 MN/m (40,000 lb/in.) at the turbine end (No. 1) and compressor end (No. 2) bearings, respectively. This resulted in no predicted modes in the operating range between idle and 100% speed, with sufficient margin on each end of the range. The first (25% N_1) and second (50% N_1) modes were rigid body modes below idle speed, exciting the turbine end and compressor end bearing supports, respectively. The third (123% N_1) mode was a shaft bending mode above the operating speed range (Ref Figure 225 for finite element model and predicted mode shapes). Essentially the same response frequencies were predicted for the ceramic versus metallic turbine rotor gasifier assemblies.

Initial operation of the engine at 100% gasifier speed (S/N 1 BU8) exhibited gasifier shaft vibration levels approaching the established velocity limit at the compressor end. The predominant vibrational frequency coincided with gasifier rotational speed. Subsequent builds (S/N 1 BU9 and S/N 2 BU3) produced overall vibration levels over the established limit when operating in the upper engine speed range. The predominant vibrational frequency again coincided with gasifier speed.

Carbon seal rub was found on some of the shaft sealing surfaces following engine tests that demonstrated vibration levels above the limit. These carbon seal clearances were increased as an interim measure to prevent rub, pending the demonstration of reduced vibration levels at high engine speed.

An investigation was initiated to study the engine test vibration problem, which was believed to be due to imbalance and/or resonance. The investigation included an extensive balance study, gasifier assembly analytical modeling, and special instrumentation added on S/N 1 BU11 to measure bearing motion.

In addition to removing resonant modes from the operating speed range to prevent undesirable engine vibration, the gasifier rotor assembly had to be adequately balanced. In general, the degree of balance required increases with both increased operating speed and decreased rotational mass. A high degree of balance was required for the AGT 100 gasifier rotor since it had a high operating speed range and low mass.

The gasifier rotor assembly was made of several components that had to be disassembled after balancing before installation and reassembly in the engine. Therefore, to retain the balanced condition when installed in the engine, it was important that a significant balance change not occur due to disassembly and reassembly of the components. A balance repeatability study was conducted to determine how much balance change occurred between successive builds of the gasifier rotor assemblies.

Balance repeatability within the 2.16 g-mm (0.003 oz-in.) limit at each bearing plane was demonstrated for the balanced gasifier rotor assembly from engine S/N 1 before BU11. This was accomplished by balancing the assembly, then disassembling and reassembling the rotor assembly twice,

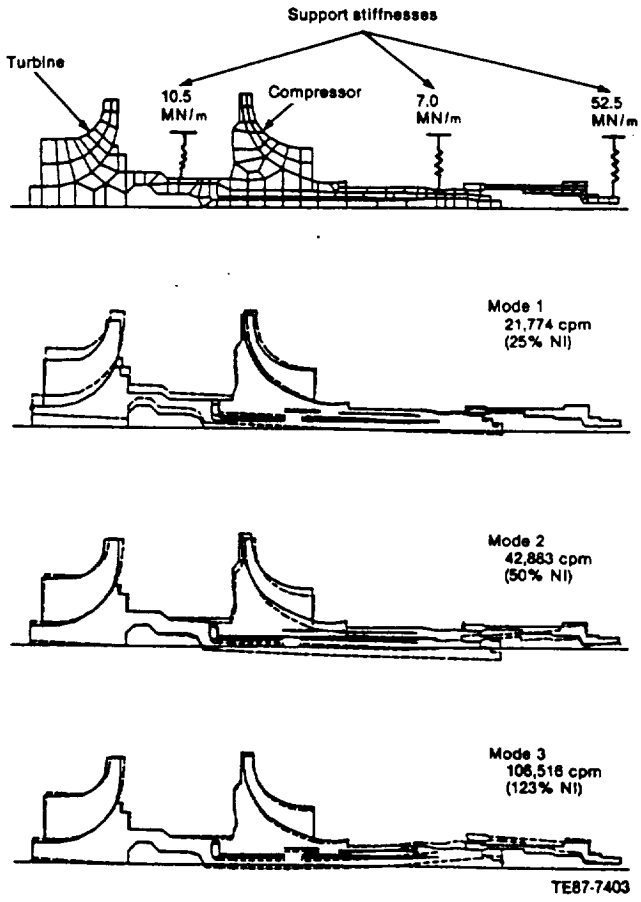

Figure 225. *Gasifier assembly finite element model and predicted mode shapes.*

and checking the imbalance after each assembly. The balancing and checking was done using dummy bearing races instead of the actual engine bearings because of the requirements imposed by the balance machine.

Turbine shaft elongation during assembly was measured, and a shaft elongation versus axial load test was performed. Maintaining a high clamp load between rotor assembly components during engine operation aids in maintaining balance. The elongation measurements and the elongation versus load test confirmed that the desired load was being built into the assembly by the assembly procedure used.

During the balance study using S/N 1 components, measurements were taken to determine fit and flatness of interfaces. The spacer and spline designs were modified to improve their interface. Also, the amount of allowable interference between the turbine and impeller shafts under the No. 2 bearing was reduced to improve the axial clamp load distribution.

The analytical model of the metal gasifier turbine rotor assembly was employed to study the observed engine test vibration response and to aid in identifying corrective action. Assembly response frequencies and mode shapes were determined for various spring rates of the support structure. The spring rates corresponded to conditions in which the mass isolators supporting the shaft bearing were either active or inactive (bottomed). Bottoming of the forward mass isolator was assumed to change its spring rate to approximately 35.0 MN/m (200,000 lb/in.). This action produced a predicted response frequency near 90% gasifier speed, the speed at which vibration limits were exceeded during engine testing.

To reduce the magnitude of gasifier assembly response to imbalance and avoid a critical speed in the operating range caused by the forward mass isolator bottoming, a squeeze film damper was evaluated at the compressor end bearing location. The squeeze film damper adds damping by introducing a fluid layer between two solid surfaces of the support structure. Analytical modeling showed that a damping coefficient of C = 10 produced a 30% critical speed margin and offered a significant reduction in response magnitude for a given imbalance. Based on the analysis results, a squeeze film damper was designed. It was initially employed on S/N 1 BU11, where vibration levels were low during all test operations, including 1:07 hr at 100% gasifier speed.

A balance study was also conducted using the gasifier rotor assembly from engine S/N 2 before undertaking BU5. As with S/N 1 rotor components, fit and flatness measurements were taken, the spacer and spline designs were modified, the turbine shaft to impeller shaft fit under the No. 2 bearing was reduced, and shaft elongation testing was conducted using S/N 2 rotor components. The balance was within the 2.16 g-mm (0.003 oz-in.) limit at each bearing plane for the first two repeatability trials following rotor assembly balancing. However, on the third trial the imbalance at the No. 1 bearing plane slightly exceeded the limit. However, because of the addition of the squeeze film damper on this engine, it was decided to proceed with final balance and installation of the rotor assembly in the engine—S/N 2 BU5.

During engine S/N 2 BU5 testing, the vibration limit at the air inlet splitline reached the established limit when the engine attained 90% gasifier speed. The vibration data indicated that the source of vibration was imbalance.

As with S/N 1 rotor assembly, the S/N 2 rotor assembly was balanced on dummy bearing races. Calculations indicate that a slight shift in the position of the rotational axis may have severe consequences on balance. A rotational axis shift of 0.0025 mm (0.0001 in.) at the No. 1 bearing has been calculated to produce a balance change of approximately twice the unbalanced limit of 2.16 g-mm (0.003 oz-in.). Such a shift may have occurred when replacing the dummy bearing races with engine bearings due to slight differences in runout and outside-to-inside diameter eccentricity. Unbalance may have been introduced by this mechanism even if the assembly balance was repeatable.

To detect this kind of change, a balance fixture, as shown in Figure 226, was designed and fabricated. This fixture allowed the gasifier assembly to be check balanced as assembled on engine bearings while installed in the engine bearing support. The fixture was to be used for checking imbalance both before and after engine testing. It was intended to provide a means of ensuring adequate gasifier assembly balance before engine testing, for checking gasifier assembly balance on teardown, and for gaining insight into any imbalance problems encountered during engine testing. The primary advantages offered by the balance fixture were that it could be used for check balancing the gasifier rotor assembled on engine bearings instead of dummy races and that no disassembly or reassembly was required between check balancing and engine testing.

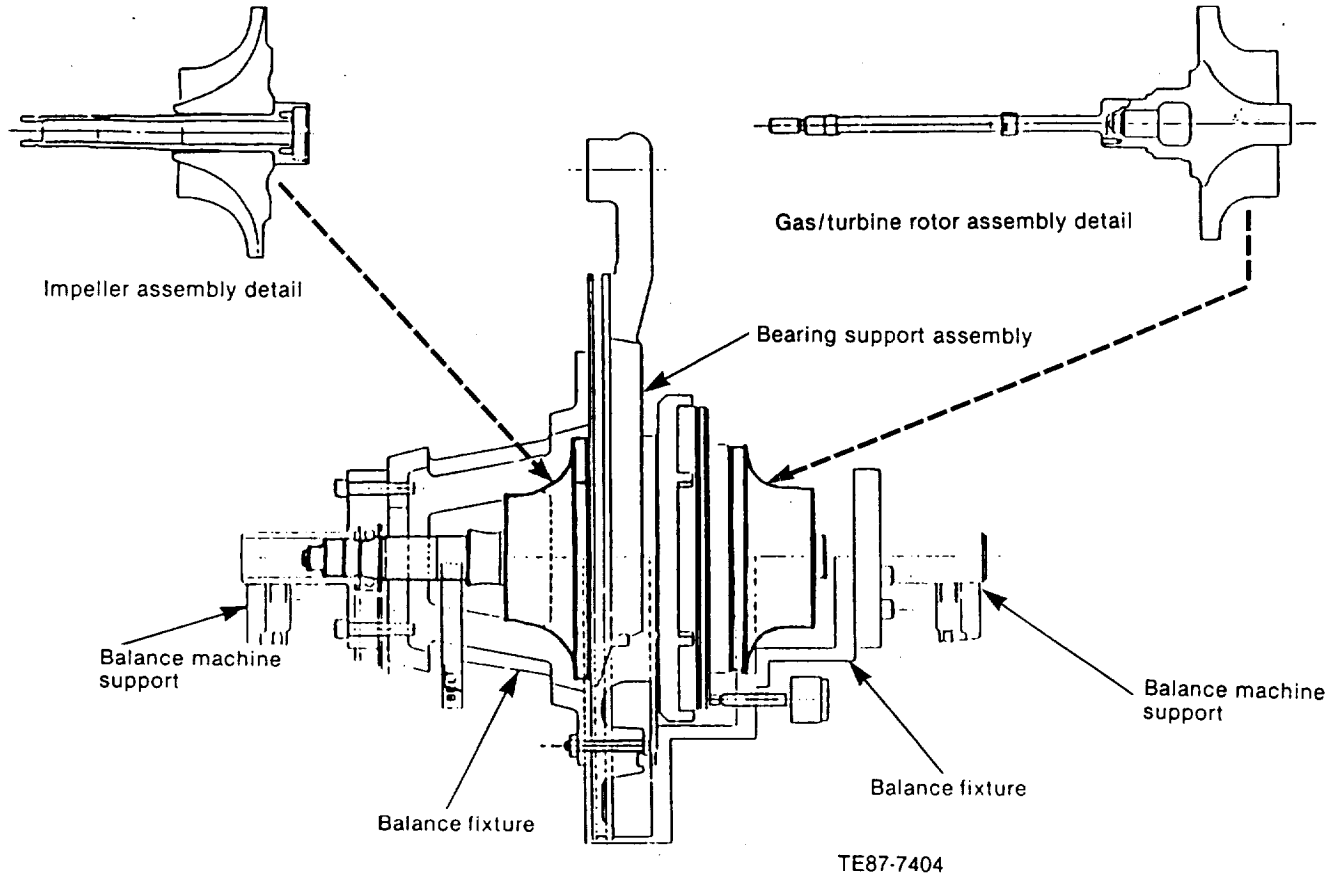

Figure 226. *Gasifier assembly in balance fixture.*

The gasifier assembly was not disassembled between S/N 2 BU5 and TD-7. Thus, the TD-7 gasifier assembly was the one that encountered limited vibration on BU5 near 90% gasifier speed. (No attempt was made to run at 100% gasifier speed on BU6 and BU7.) A check balance of the TD-7 gasifier assembly in the balance fixture revealed that it was within imbalance limits at the front bearing and approximately 12 times the imbalance limit at the rear bearing. This suggested that the gasifier assembly either was not within balance limits when initially installed in the engine and/or experienced a balance change during engine testing. If the imbalance was due to the former cause, use of the balance fixture on future builds could allow the problem to be detected before engine testing.

The balance repeatability of the S/N 2 TD-7 gasifier assembly was checked in the balance fixture after balancing with temporary weights. The balance was found to repeat within approximately one balance limit for each of two consecutive disassembly/reassembly sequences subsequent to the initial temporary balancing. This result demonstrated balance repeatability on the engine bearings.

In addition to in-house efforts to address the balance procedure and balance repeatability, Allison enlisted the Balancing Company, Inc (BALCO) to study the gasifier assembly balance procedures. BALCO specializes in balancing rotors and was requested to recommend methods for ensuring adequate balance during engine testing.

Allison supplied BALCO with a gasifier assembly for use in its balance investigation. BALCO's activity included balance repeatability studies and assessment of the feasibility of balancing the assembly on engine bearings. This activity included balance studies when disassembling and reassembling the gasifier, tightening and loosening the tie bolt nut, changing tie bolt nuts, axially shocking the assembly with a hammer, rotating the impeller relative to the turbine, rotating the bearing races, and varying the balancing speed with the gasifier unit assembled with the entire No. 1 engine bearing.

The results of the repeatability studies were consistent with Allison's balance studies and practice. Balance repeatability was determined to be within the allowable balance limit (2.16 g-mm) at each bearing plane for the disassembly/reassembly sequence using a given set of hardware. Balance repeatability was considered important because of the requirement of disassembling the rotor after balancing for subsequent installation in the engine bearing support. A large change in balance was detected when the No. 1 engine bearing replaced the No. 1 dummy bearing. This balance change was not unexpected and has led to the investigation of alternate balancing methods that eliminate the use of the dummy races in the balancing procedure.

BALCO also indicated that the gasifier mechanical design appeared sound with regard to balance and that the permitted amount of imbalance was reasonable; however, they recommend elimination of disassembly after balancing. An extensive redesign of the gasifier support structure would have been required to accommodate such a change. Thus, initial balancing of the gasifier assembly at that time normally required disassembly of the gasifier section with removal from the bearing support. This was necessary due to the magnitude of imbalance typically present and the corresponding necessity to gain access to the balance correction planes. However, after initial balancing and reassembly in the bearing support, additional minor balance corrections could be made without further disassembly by removing small amounts of mass from the accessible impeller and turbine rotor flow paths.

Other BALCO balance study conclusions were as follows:

- Axial shock of the assembly produced small changes in balance but was not effective in seating the components.
- Balance changed significantly with tie bolt nut torque but was generally repeatable when fully torqued.
- Balance changes produced by exchanging tie bolt nuts were essentially insignificant when fully torqued, indicating that balance changes with torque were not due to individual nut anomalies.
- Rotation of the No. 1 engine bearing inner race 180° produced balance changes on the order of twice the balance limit at the No. 1 bearing plane, indicating that even high quality engine bearings must maintain their position relative to the other components subsequent to balancing.
- Balance continued to change significantly when the entire No. 1 engine bearing was used until stabilization occurred above approximately 1800 rpm, indicating a minimum acceptable speed required for balancing on the entire ball bearing when no axial load was applied.

Up until this point in the program, all builds balanced the two major gasifier detail assemblies (impeller assembly and gas turbine rotor assembly) about their detail axes, built the gasifier assembly on dummy bearing races, balanced it, and then reassembled the gasifier assembly with engine bearings in the engine. Imbalance introduced by a change in the rotational axis caused by variations between the dummy bearings and engine bearings, or build nonrepeatability effects, was left uncorrected. Additionally, the unbalanced state of the gasifier assembly as installed in the engine was unchecked and unknown. Despite this early, nonrigorous balance technique, two engine builds successfully ran to 100% N_1: S/N 1 BU8 and BU11. However, several of other builds using this identical procedure were not successful in attaining full gasifier speed.

In an effort to improve gasifier assembly balance, the balance procedure was revised. Use of dummy bearings was eliminated, and the gasifier assembly was balanced and checked as assembled for engine test. The balance procedure changes incorporated the balance fixture as a key part of the balance process. The balance procedure consisted of the following steps:

1. The impeller assembly and gasifier turbine rotor assembly were individually balanced as detail parts upon initial usage.
2. The impeller/turbine orientation requiring the least amount of balance correction was selected.
3. The gasifier assembly, assembled in the bearing support and balance fixture, was temporarily corrected with balance weights.
4. The gasifier assembly was disassembled for access to the balance correction planes. Corrections determined in step 3 were performed.
5. The gasifier assembly was reassembled in the bearing support and balance fixture for a final check balance. Small corrections were made in the blade channels if required.

The revised balance procedure subsequently proved to successfully produce gasifier assemblies possessing a high degree of rigid body dynamic balance about their actual engine test rotational axes.

Because initial builds employing the balance fixture had to be check balanced on a balance machine with insufficient capacity rating for the supported mass, indicated imbalance was somewhat suspect. Testing showed that variations in machine drive belt tension and pedestal height, as well as the process of removal/reinstallation of the gasifier assembly itself, had significant effects on the indicated imbalance. Suspected limitations of this low capacity balance machine were confirmed and it was no longer used for assembly balance.

Conveniently, a new balance machine with ample capacity was placed in operation at this time. Similar tests were performed on the larger capacity machine, and it was found to be virtually unaffected by any of the factors previously identified as affecting the smaller capacity machine. All subsequent balance work with the balance fixture was performed on the larger capacity machine, starting with engine S/N 1 BU14.

A significant balance milestone was thus attained—the amount of gasifier assembly rigid body dynamic imbalance, as installed in the engine prior to test, could now be determined. This was accomplished through the use of the new balance procedure, the balance fixture, and the new balance machine. As a result, it was possible to obtain and verify rotor imbalances well within print allowable limits (2.16 g-mm) for gasifier assemblies as assembled for engine testing. One gasifier assembly (S/N 1 BU14) was successfully rigid body balanced to the capabilities of the balance machine by making small final balance corrections in the accessible blade channels. (The main balance correction planes were inaccessible when the gasifier assembly was final assembled in the bearing support.) This level of rigid body balance improvement had little effect on vibration and/or whip limits, and engine testing was still limited to speeds below 100% N_1.

To help verify the analytic model of the gasifier assembly, a rap test was performed to compare measured response frequencies with predicted values. This was done for an engine gasifier assembly supported on soft mounts. The measured first and second bending mode frequencies compared closely with predicted values, helping confirm the model's ability to correctly predict modes.

To gain additional insight into the nature of the vibration and whip, one test engine (S/N 2 BU13) was equipped with additional instrumentation to measure squeeze film deflection, case motion, rotor rotational response, coupling shaft whip, and shaft rotation/whip phasing. The analysis resulting from this engine test indicated that the vibration levels encountered were primarily due to rotor imbalance and not significantly amplified by rotor or case resonance.

As the gasifier assembly balance was determined to be well within limits as a rigid body before engine testing, it became apparent that this type of balance of the gasifier assembly was not sufficient to eliminate vibration/whip problems. Therefore, new aspects relative to balancing were explored, including: (1) the effect of the gasifier pinion shaft on the gasifier assembly balance, (2) the determination of a method to balance the assembly while minimizing internal force couples, and (3) the feasibility of performing a high speed balance.

The first aspect addressed the potential imbalance that may arise because the gasifier pinion shaft was balanced only as a detail part, not with the gasifier assembly as a whole unit. To determine the effect of the gasifier pinion on balance, engine tests were performed in which the pinion was indexed in 120° increments, rebalanced as a detail, and completely removed. No significant changes in whip were found compared with baseline tests for any of the pinion changes made, indicating that pinion imbalance was not the primary cause of excessive whip.

The latter two aspects were intended to correct vibration/whip problems that may have arisen because the gasifier assembly was not perfectly rigid and may have been deflecting at high speeds due to internal force couples not detectable by rigid body, low speed balancing. The gasifier assembly bow produced could in turn produce additional imbalance. For example, at 100% N_1 (86,256 rpm) an internal imbalance of only 2.5 g-mm resulting from an imbalance in any plane produces a corresponding unbalanced force of 21 kg (47 lb) in that plane; thus, significant forces could be developed by relatively small imbalances. The employed balance procedure was not capable of removing such internal imbalances but only ensured that they cancel in such a way that the net reaction at the bearing was zero. Because of the fixed and localized nature of the balance correction planes, the distributed nature of the source imbalance, and the inability of any balance machine to identify the source of the imbalance, internal force couples were likely to be present after low speed balancing. Thus, the latter two items were considered for minimizing or counteract-

ing the undesirable effects of such force couples.

While performing a high speed balance was determined to be impractical, a low speed balance procedure was devised that was intended to have a similar result by significantly reducing built-in imbalance couples. The primary feature of the new balance procedure was that the two major gasifier assembly parts (gasifier turbine and impeller assembly details) were balanced in a revised manner adding as little imbalance in the gasifier assembly as possible. This required accounting for any change in the rotational axis of detail parts between the assembly's balance setup and its final assembled condition. To accomplish this, precise measurements were made to determine necessary temporary weights to be added while the details were balanced to account for the axis shifts. Any final assembly corrections were then made in a plane where the imbalance was believed to be centered. Another feature of this balance procedure was that the two assembly balance indicated imbalanced planes had increased axial separation and were positioned where the remaining source unbalance was likely to be located. When done properly, this procedure also helps to eliminate unbalance couples from being built-in during the balance operation. The balance procedure designed to minimize unbalance couples was first used on S/N 1 BU18.

The final assembly balance correction was made on the impeller during the first two builds employing this technique. Whip limits were reached near 75%–80% N_1 with the impeller not showing any significant change from previous tests. The turbine detail was much more difficult to balance properly than the impeller detail, and consequently was more likely to be the predominant source of final assembly imbalance. Significant couples were believed to be unintentionally built into these first two builds since the predominant source of final assembly imbalance was the turbine while the correction was made on the impeller. As a result, subsequent builds made the final assembly balance correction on the turbine instead of the impeller. These builds spanned several months until the end of the program and progressively included other modifications described in the following paragraphs.

The builds generally showed a different whip response character compared with the previous balance method, in which couples were not minimized. Whip was low and essentially constant between start and approximately 60% N_1 for both ceramic and metal turbines. Ceramic turbines continued to show less whip increase up to approximately 85% N_1, the highest speed reached. Metal turbines tended to have a rapid whip increase between 65–80% N_1, sometimes composed largely of a one-third subharmonic rather than synchronous whip frequency (see Figure 227 for response comparisons). One build successfully passed through a near limit whip peak around 77%, with whip continuing to decrease up to 95% N_1. Additionally, the gasifier assembly balanced with this low speed method for the rotordynamics rig successfully ran to 100% N_1 with low whip.

Concurrent with the efforts to improve gasifier assembly balance, a special rig was fabricated to study the gasifier's rotordynamics. This yielded several advantages, including freeing the engine for other tests, performing design change evaluations quickly, and increasing measurement capabilities. The goals were to determine the assembly's sensitivity to imbalance in various planes, the mass isolator and squeeze film damper behavior, rotor mode shapes, and other factors. A modified engine gasifier assembly was used. Provisions were made for adding weights in three different axial planes for conducting imbalance sensitivity studies and performing high speed balancing. The compressor impeller was debladed, allowing the rig to be driven by supplying externally pressurized air to the turbine wheel. The rotor assembly was supported by engine hardware at each bearing, with a special rig fixture joining and supporting the engine pieces. Analytically predicted resonant frequencies for the rig gasifier assembly were essentially the same as for the engine gasifier assembly.

Initial operation of the rig ran to 100% N_1 with very low and constant amplitude whip. The gasifier assembly was low speed balanced before this test using the same procedure for minimizing unbalance couples as used for engine tests. This finding indicated that high speed balancing of engine rotors was unnecessary. Imbalances thought to be typical of earlier engine tests were then added individually in the three available planes. Operation to 100% N_1 was successfully attained for each condition, with all three producing a whip increase near 100% N_1. When the three imbalances were simultaneously combined to form unbalance couples, a response was obtained similar to that typically observed during engine tests before minimizing couples (see Figure 228 for response comparisons). Speed was limited to 80% with the whip response exhibiting one-third subsynchronous content attributed to bottoming of the squeeze film damper (SFD). Clamping the compressor end bearing support to increase its stiffness and varying SFD oil pressure over a wide range showed little effect on the response. The two

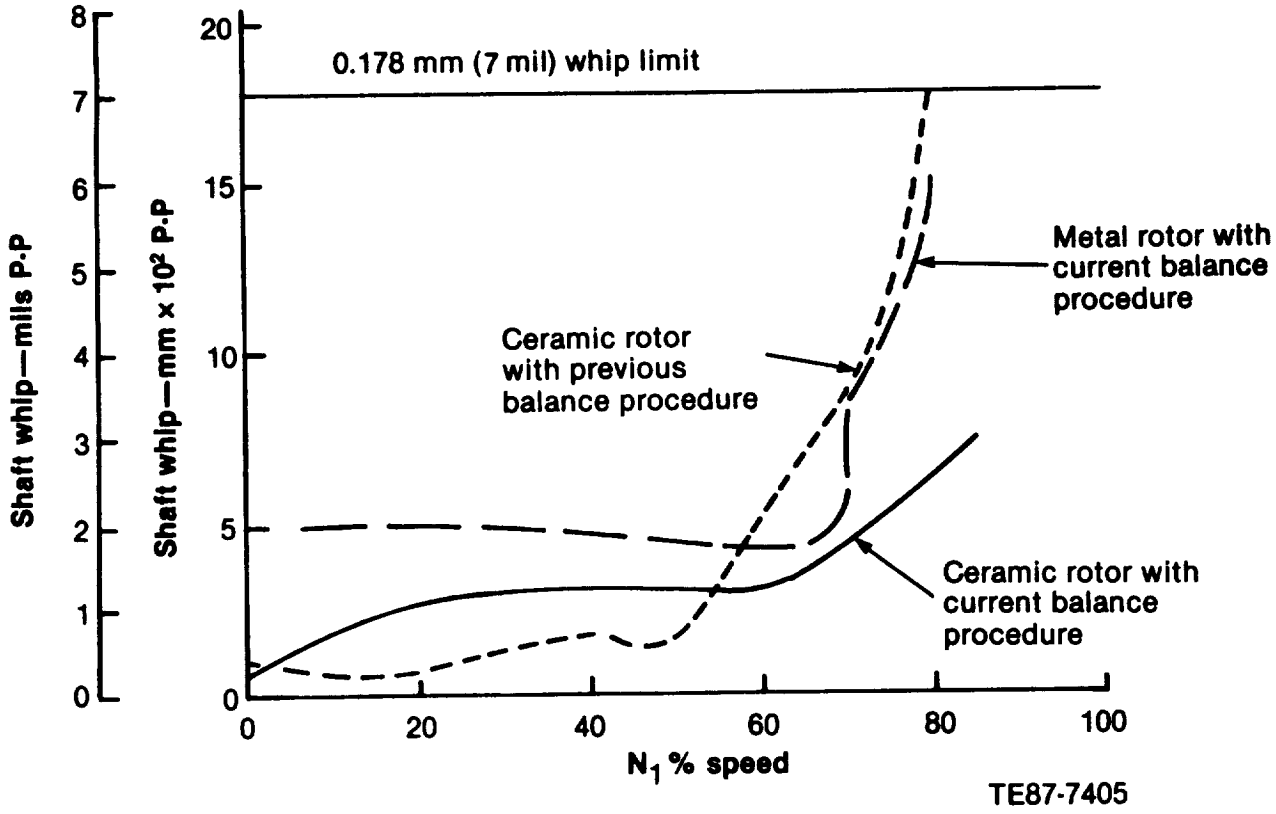

Figure 227. Typical gasifier shaft whip versus speed.

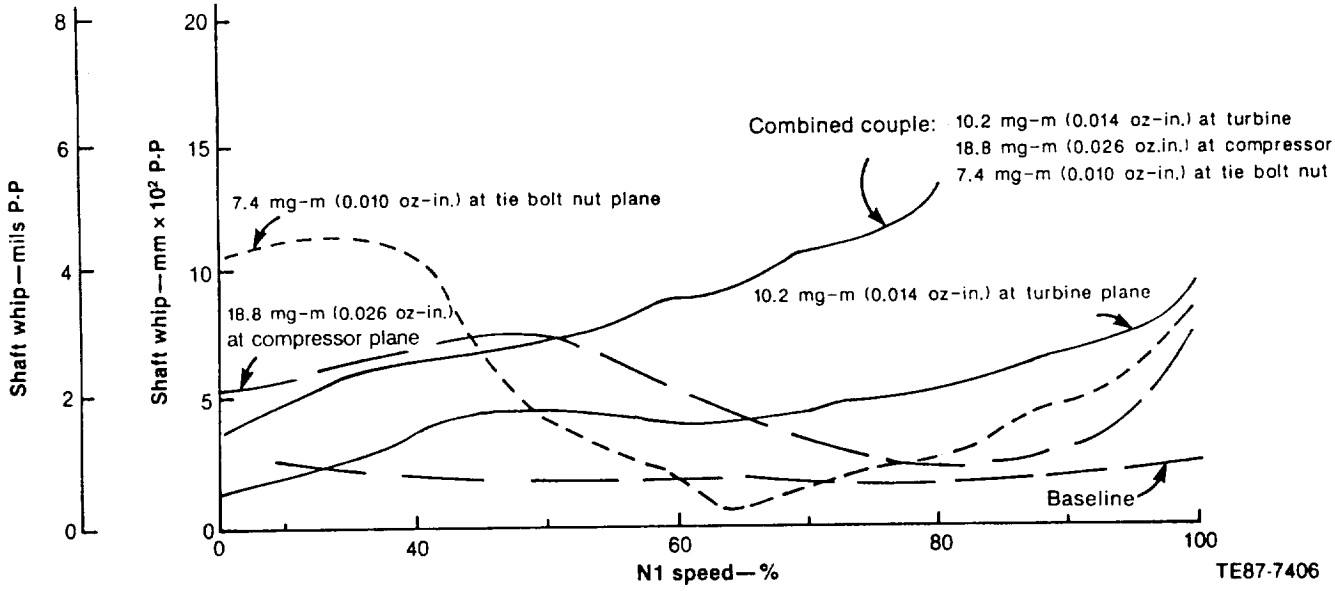

Figure 228. Rotordynamics rig response to various imbalance conditions.

rigid body modes were identified in the predicted speed ranges, and the first bending mode shape was present as design speed was approached. After removing the unbalances, a run was made that showed little difference compared with the baseline run, implying no significant balance change occurred. The gasifier was disassembled and reassembled to replace a damaged No. 2 bearing inner race. Repeating the baseline run showed little response change, as did a run with significantly

reduced tie bolt clamp load.

Because of the success in running the rotordynamics rig to 100% speed while the engine was continuing to experience difficulties, attempts were made to identify relevant differences. These included thermal condition and centrifugal force effects, since the rig was run much cooler than the engine and the impeller was debladed. Analysis showed no significant loss of axial clamp load was predicted that might allow components to shift in the engine gasifier assembly. No significant loss of radial fit at key pilot diameters was predicted for the metal turbine rotor gasifier assemblies, except for partial loss of impeller pilot contact. The partial loss of this fit was not predicted for the rotordynamics rig's impeller. Consequently, this difference received a lot of attention even though no loss of engine impeller fit was predicted at 80% speed and the maximum possible balance change at 100% speed due to the partial pilot release was small.

Because the engine impeller's interference fit was optimized for cyclic life considerations and the bore was already above yield stress, the fit was not increased to maintain total pilot contact. Revised pilot schemes to add a forward pilot and maintain full pilot contact throughout the operating range were investigated, but none were found that met both predicted response mode and stress design criteria. Alternate impeller materials were considered and rejected. Also proposed was a unitized impeller assembly with integral impeller and shaft that would completely eliminate the pilot while incorporating some minor components and placing both bearings on the same shaft. However, this design was predicted to have its first bending mode in the engine operating range.

Instead of preventing partial release of the original impeller pilot, an alternate scheme adding diametral pilot at the front of the impeller was pursued. This design was intended to prevent the impeller from tilting if there was a tendency to tilt. Such a design modification was made to both engine impellers by adding a press fit pilot ring, but no significant change in response was observed.

Several other hardware changes were made to improve the gasifier's response. Tie bolt clamp load was substantially increased to help prevent component shifting and axial splitline separation due to imbalance bending moments. A forward pilot between the tensile and compressive load paths was adjusted slightly looser ensuring the proper clamp load path. The No. 2 ball bearing was replaced with a roller bearing, allowing for greater axial travel capability if the outer race locks up in its support due to growth. Modifications were made to allow for interchangeable No. 2 ball bearing supports, including the original spring bar design and various SFD designs. The SFD designs included centered and uncentered versions of an original clearance design, and a centered version of an increased clearance design recommended by a NASA consultant. Additionally, modifications were made to provide controlled oil delivery pressure to the SFD from an external source.

Concurrent with the hardware modifications, analytic work was done in response to concern that the first bending mode may have been lowered into the operating range by axial splitline separations due to potential excessive bending moments. The analysis was conducted to define the relationship of initial imbalance to bending moments in the gasifier assembly. Combining this with calculations of bending moments required to open axial splitlines, imbalance at various locations required to open individual splitlines could be predicted. Reasonable imbalances were incapable of opening splitlines. Additionally, complete separation through 360° of the splitlines most likely to open was not predicted to alter response mode frequencies. Thus, lowering of the first bending mode into the operating range due to axial splitline separation was not considered responsible for the observed engine whip character.

Engine testing was conducted with the modifications previously mentioned and additional dynamic instrumentation. These gasifiers were balanced with the previously described technique designed to minimize imbalance couples. Although some differences were found with various combinations of the modifications mentioned, no convincing solution was found for the engine's gasifier assembly with metal turbines.

Although one build with an original clearance centered squeeze film damper successfully passed through a response peak slightly below whip limits around 77% N_1 and went on to 95% N_1 with decreasing whip, subsequent attempts to repeat the test were whip limited. Data from the tests with extra instrumentation, which demonstrated the high whip response typically encountered with metal turbines, were more indicative of a shifting and/or increasing imbalance rather than a resonant condition.

REFERENCES

1. First Semiannual Report, 1 October 1979 to 30 June 1980, NASA CR-165178, Allison EDR 10327, Section IV.
2. 1984 Annual Report, 1 January 1984 to 31 December 1984, NASA CR-175018, Allison EDR 12070, Section 9.2.
3. Progress Report No. 74, 1 November to 31 December 1986, Section 9.1.
4. 1985 Annual Report, NASA CR-179484, Allison EDR 12344, Section 9.3.
5. Third Semiannual Report, 1 January to 30 June 1981, NASA CR-165504, EDR 10741, Section 9.2.
6. Fourth Semiannual Report, 1 July to 31 December 1981, NASA CR-167875, EDR 10977, Section 4.3.
7. Seventh Semiannual Report, 1 January to 30 June 1983, NASA CR-174629, Allison EDR 11577, Section 9.2.
8. Eighth Semiannual Report, 1 July to 31 December 1983, NASA CR-174798, Allison EDR 11682, Section 9.2, Table XXII.
9. 1985 Annual Report, NASA CR-179484, Allison EDR 12344, Table XVIII.
10. Johnson, R. A., "Conceptual Design Study of an Improved Gas Turbine (IGT) Powertrain," NASA CR-159604.
11. "Advanced Gas Turbine (AGT) Powertrain System Initial Development Progress Report," NASA CR-159804.
12. Second Semiannual Report, 1 July to 31 December 1980, NASA CR-165346.

1. Report No.	2. Government Accession No.	3. Recipient's Catalog No.
CR-182127		

4. Title and Subtitle	5. Report Date
Advanced Gas Turbine (AGT) Technology Project	August 1988
	6. Performing Organization Code
7. Author(s)	8. Performing Organization Report No.
Engineering Department, Allison Gas Turbine Division	13295
	10. Work Unit No.
9. Performing Organization Name and Address	11. Contract or Grant No.
Allison Gas Turbine Division of General Motors Corporation P.O. Box 420 Indianapolis, IN 46206-0420	DEN 3-168
	13. Type of Report and Period Covered Contractor Final Report October 1979 - June 1987
12. Sponsoring Agency Name and Address	14. Sponsoring Agency Code
U.S. Department of Energy Office of Transportation Systems Washington, D.C. 20545	DOE/NASA

15. Supplementary Notes

Final report, prepared under Interagency Agreement DE-A101-85CE50111
Project Manager P. T. Kerwin, Transportation Propulsion Division,
NASA Lewis Research Center, Cleveland, OH 44135

16. Abstract

This Final Report provides overall summary documentation of the Advanced Gas Turbine Technology Project conducted by the Allison Gas Turbine Division of General Motors under contract to the NASA Lewis Research Center. This advanced, high risk work was initiated in October 1979 under charter from the U.S. Congress to promote an engine for transportation that would provide an alternate to reciprocating spark ignition (SI) engines for the U.S. automotive industry and simultaneously establish the feasibility of advanced ceramic materials for hot section components to be used in an automotive gas turbine. As this program evolved, dictates of available funding, Government charter, and technical developments caused program emphases to focus on the development and demonstration of the ceramic turbine hot section and away from the development of engine and powertrain technologies and subsequent vehicular demonstrations. Program technical performance concluded in June 1987.

The AGT 100 program successfully achieved project objectives with significant technology advances. Specific AGT 100 program achievements are:

- o Ceramic component feasibility for use in gas turbine engines has been demonstrated.
- o A new, 100 hp engine was designed, fabricated, and tested for 572 hr at operating temperatures to 2200°F, uncooled.
- o Statistical design methodology has been applied and correlated to experimental data acquired from over 5500 hr of rig and engine testing.
- o Ceramic component processing capability has progressed from a rudimentary level able to fabricate simple parts to a sophisticated level able to provide complex geometries such as rotors and scrolls.
- o Required improvements for monolithic and composite ceramic gas turbine components to meet automotive reliability, performance, and cost goals have been identified.
- o The combustor design demonstrated lower emissions than 1986 Federal Standards on methanol, JP-5, and diesel fuel. Thus, the potential for meeting emission standards and multifuel capability has been initiated.
- o Small turbine engine aerodynamic and mechanical design capability has been initiated.
- o An infrastructure of manpower, facilities, materials, and fabrication capabilities has been established which is available for continued development of ceramic component technology in gas turbine and other heat engines.

17. Key Words (Suggested by Author(s))		18. Distribution Statement
Automative gas turbine	Alternate propulsion systems	unclassified, unlimited
Ceramic components	Vehicular propulsion	
Structural ceramics	Improved fuel economy	
Engine configuration	Alternate fuels	
rotors	Emissions	

19. Security Classif. (of this report)	20. Security Classif. (of this page)	21. No. of Pages	22. Price*
UNCLASSIFIED	UNCLASSIFIED	188	

* For sale by the National Technical Information Service, Springfield, Virginia 22151